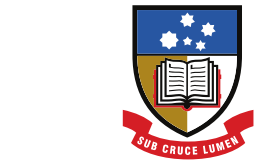

THE UNIVERSITY of ADELAIDE

Mechanical Theory for Particle Detachment in Porous Media

Heng Zheng Ting

A thesis submitted for the degree

of Doctor of Philosophy

School of Electrical and Mechanical Engineering

Faculty of Sciences, Engineering and Technology

February 2023

This page is intentionally left blank

Abstract

The detachment of particles from surfaces is prevalent in numerous environmental, chemical, biological and industrial applications. Some examples include the resuspension of dust in indoor environments, the removal of contaminants from manufactured components, the delivery of pharmaceutical drugs and the transport of bacteria in underground aquifers. Specific to the petroleum industry, the detachment of clay particles induced by hydrocarbon production leads to the plugging of rock pores and hinders the rate of production. The phenomenon of particle detachment is therefore of wide scientific and practical interest. However, the current understanding is often limited to simplified cases of perfectly spherical particles, which limits their applicability for real-world applications.

This thesis aims to further understand and characterise the detachment of non-spherical particles, accounting for parameters such as the particle size, shape, aspect ratio, orientation angle, distribution of parameters and favourable/unfavourable conditions. The study focuses on kaolinite particles as a specific application due to the ubiquity of the mineral in petroleum reservoirs.

The numerical study comprises the modelling of the detaching hydrodynamic forces in creeping flow and the resisting Derjaguin-Landau-Verwey-Overbeek (DLVO) adhesion force. The former and latter are executed using computational fluid dynamics (CFD) and surface element integration (SEI), respectively. A laminar steady-state model based on the CFD package ANSYS/CFX was used throughout the study. Similarly, SEI is a theoretical method that scales the DLVO adhesion force between two parallel plates to that of cylinders and oblate spheroids considered in this study. The torque balance model was used as the main criterion for studying rolling detachment, incorporating both

adhesion and hydrodynamic forces; Hertz contact theory was used to evaluate the torque lever arm. Sliding and lifting detachments were also considered, where necessary.

The numerical studies are further complemented by direct visualisation experiments of engineered polystyrene microparticles (radii of 1.5 to 5 μm) in spherical and spheroidal shapes. Kaolinite particles were also studied to evaluate the effectiveness of the model in characterising natural particles. The particles were deposited in a rectangular microfluidic glass channel and subjected to fluid flows of different pH, salinities and flow rates to assess their detachment rates. The detachment rates of the sphere particles evaluated from the experiment were validated against the established theory for sphere particle detachment before subsequent visualisations of non-spherical particles were conducted.

By comparing the experimental and the simulation results, a new fundamental understanding of the detachment of non-spherical particles was gained. It was shown for the first time that the detachment of spheroidal particles with decreasing aspect ratio is nonmonotonic: there is a particular aspect ratio where detachment rates reach a minimum, before increasing again. Rolling and sliding detachment are most likely to occur for oblate spheroids and cylinders, respectively. In addition, a two-stage detachment process was observed for both engineered latex particles and natural kaolinite under unfavourable conditions. The observation supports the theory of particle detachment from the primary and secondary minima. Separately, the experimentally observed gradual detachment behaviour of kaolinites was reproduced in our modelling, which accounted for the variations in particle parameters using probabilistic distributions. Lastly, spheroidal particles were observed to be deposited at an angle in the visualisation experiments. At low orientation angles, particles with the smallest aspect ratio (flattest) are the hardest to detach, but this trend is reversed at high orientation angles. Consequently, the investigation has advanced the existing understanding of the detachment of particles, which is more relevant to real-world applications.

Contents

Abstract ..... **i**

Contents ..... **iii**

List of Figures ..... **v**

Declaration ..... **vii**

Acknowledgements ..... **ix**

Papers included in this thesis by publication ..... **xi**

Nomenclature ..... **xiii**

Chapter 1 Introduction **1**

1.1 Aim 4

1.2 Details of the publication 4

Chapter 2 Background **7**

2.1 Modelling of kaolinite geometry 8

2.2 Balance of forces and torques 9

2.3 Hydrodynamic drag, lift and moment 9

2.4 Adhesion force 10

2.5 Hertz contact theory 14

2.6 Summary of the simulation workflow 14

2.7 Direct visualisation experiments 15

Chapter 3 Literature Review **19**

3.1 Kaolinite detachment 19

3.2 Impact of shape on particle detachment 20

3.3 Challenges in the laboratory modelling of particle detachment 22

3.4 Detachment of particles under unfavourable conditions 23

3.5 Criteria for the initiation of rolling detachment 24
3.6 Deposition orientation angle between the particle and substrate 25
3.7 Research gaps 27
3.8 Research objectives 28

Chapter 4 31

Impact of shape on particle detachment in linear shear flows 31

Chapter 5 49

Detachment of irregular-shape particles under unfavourable conditions: visualisation and modelling 49

Chapter 6 83

Image interpretation for kaolinite detachment from solid substrate: Type curves, stochastic model 83

Chapter 7 99

Detachment of inclined spheroidal particles from flat substrates 99

Chapter 8 Conclusions and Future Work 137

8.1 Conclusions 138
8.2 Future work 140

References 143

Appendix A Supplementary Data for Chapter 5 153

Appendix B Supplementary Data for Chapter 6 161

Appendix C Supplementary Data for Chapter 7 169

List of Figures

Fig. 1.1. Scanning electron microscopy (SEM) image for kaolinite, chlorite and illite.. 2

Fig. 1.2. Flow chart that shows the main factors considered in the detachment of non-spherical particles and their relation to the numerical and laboratory methodology. 3

Fig. 2.1. The various mechanisms involved in the flow and transport of colloidal particles in a porous rock at the microscale..... 7

Fig. 2.2. Setup of the particle and the substrate.. 8

Fig. 2.3. Comparison of the DLVO force profile under favourable and unfavourable conditions. 12

Fig. 2.4. Workflow diagram of the modelling process for particle detachment. 15

Fig. 2.5. Laboratory setup for the direct visualisation of particle detachment 17

This page is intentionally left blank

Declaration

I certify that this work contains no material which has been accepted for the award of any other degree or diploma in my name in any university or other tertiary institution and, to the best of my knowledge and belief, contains no material previously published or written by another person, except where due reference has been made in the text. In addition, I certify that no part of this work will, in the future, be used in a submission in my name for any other degree or diploma in any university or other tertiary institution without the prior approval of the University of Adelaide and where applicable, any partner institution responsible for the joint award of this degree.

The author acknowledges that copyright of published works contained within this thesis resides with the copyright holder(s) of those works.

I give permission for the digital version of my thesis to be made available on the web, via the University's digital research repository, the Library Search and also through web search engines, unless permission has been granted by the University to restrict access for a period of time.

25 February 2023

This page is intentionally left blank

Acknowledgements

This work would not be possible without the support and encouragement of my supervisors, my family, my friends and my colleagues. Thanks be to God, for His faithful providence throughout my PhD. Through the highs and lows, I am reminded that my PhD, though challenging and demanding, is only a part of the greater things to come.

I am immensely grateful for the knowledge, guidance, time and patience of my supervisors, Dr. Zhao Tian and Prof. Pavel Bedrikovetsky. I thank Zhao for constantly putting out the many fires of panic whenever research inevitably does not go as planned. You have taught me much in learning how to navigate the uncertainties and challenges of doing research. And to Pavel, thank you for showing me how enthusiasm, perseverance and hard work can produce great things in research (and the many tea and fruit cakes along the way).

A big thank you to the staff at the University of Adelaide. To Dr. Themis Carageorgos and Dr. Alex Badalyan for always being so helpful in everything laboratory related. Many thanks to Scott Letton and Brandon Pullen from the workshop for designing and manufacturing the required laboratory devices, and to Benjamin Wade from Adelaide Microscopy for the training and help in acquiring the SEM images.

Special mention to my colleagues and friends, Shipu Han and Paul Bayron for the support and camaraderie as we all embark on the PhD journey. To Yutong Yang, you have been such an insightful and reliable help in my research investigations.

Finally, an enormous thanks to my family. Mom and Dad for inspiring me to do a PhD in the first place, and their constant support, encouragement, and wisdom to see me through. Of course, thanks to my wonderful siblings for keeping me company in Adelaide and the many fun and joy that ensue.

This page is intentionally left blank

Papers included in this thesis by publication

Published

1. **Ting, H.Z.**, Bedrikovetsky, P., Tian, Z.F. and Carageorgos, T. 2021, 'Impact of shape on particle detachment in linear shear flows', *Chemical Engineering Science*, 241.

2. **Ting, H.Z.**, Yang, Y., Tian, Z.F., Carageorgos, T. and Bedrikovetsky, P. 2022, 'Image interpretation for kaolinite detachment from solid substrate: Type curves, stochastic model', *Colloids and Surfaces A: Physicochemical and Engineering Aspects*, 650.

Accepted for Publication

3. **Ting, H.Z.**, Yang, Y., Tian, Z.F., Carageorgos, T. and Bedrikovetsky, P. (in press), 'Detachment of inclined spheroidal particles from flat substrates', *Powder Technology*.

Submitted

4. **Ting, H.Z.**, Tian, Z.F. and Bedrikovetsky, P. 2023, 'Detachment of irregular-shape particles under unfavourable conditions: visualisation and modelling' Submitted to: Particuology

This page is intentionally left blank

Nomenclature

a	Semi-major axis of a particle
A_h	Hamaker constant
b	Semi-minor axis of a particle
e	Charge of an electron
E	Interaction energy per unit area between two parallel infinite planes
E^*	Effective Young's modulus
E_y	Young's modulus of elasticity
f_d	Drag shape factor
f_l	Lift shape factor
f_M	Moment shape factor
$f_{d,\varphi}$	Drag shape factor due to orientation angle
$f_{l,\varphi}$	Lift shape factor due to orientation angle
$f_{M,\varphi}$	Moment shape factor due to orientation angle
F_a	Adhesion force
F_d	Drag force
F_{DLVO}	DLVO interaction force
F_f	Friction
F_g	Gravity
F_l	Lift force
h	Distance between the particle centre and the substrate
$\boldsymbol{k}$	Unit vector directed towards the positive z-axis
k_B	Boltzmann constant
l_d	Drag lever arm
l_n	Normal lever arm
M	Hydrodynamic moment
n	Number concentration of the i-th ion species

$\boldsymbol{n}$	Unit outward normal from surface element
N	Normal force
r	Sphere radius
r_e	Volume equivalent sphere radius
T	Temperature
U	Interaction potential
v	Area-averaged flow velocity
v_o	Particle centre velocity
z	Ion valency

Greek

α	Particle aspect ratio (b/a)
φ	Orientation angle
$\dot{\gamma}_o$	Shear rate
γ	Reduced surface potential
ε_o	Permittivity of vacuum
ε_r	Relative permittivity of water
μ	Dynamic viscosity of the fluid
μ_s	Coefficient of static friction
κ	Inverse Debye length
ρ	Fluid density
σ	Atomic collision coefficient
ζ	Zeta potential
ν	Poisson's ratio

Abbreviations

AFM	Atomic force microscopy
CFD	Computational Fluid Dynamics
DI	Deionised
DLVO	Derjaguin-Landau-Verwey-Overbeek Theory
DMT	Derjaguin-Muller-Toporov model
DT	Dominik and Tielens model
EDL	Electric Double Layer
JKR	Johnson-Kendall-Roberts model
PVA	Polyvinyl alcohol
SEI	Surface element integration
SEM	Scanning electron microscopy
SFA	Surface force apparatus
VDW	van der Waals

This page is intentionally left blank

Chapter 1

Introduction

The phenomenon of particle detachment is present in various aspects of daily life. From the erosion of sand particles from the seabed to the migration of bacteria in subsurface aquifers and the removal of dust particles from monitor screens. The detachment of particles is, therefore, of wide scientific and practical interest in many fields such as pharmaceutical, biological, environmental, manufacturing, and chemical science. Due to its widespread study in different disciplines, the nomenclature ‘detachment’ is also often expressed as re-entrainment, release, mobilisation, removal or resuspension in the literature.

In petroleum engineering, particle detachment is a mechanism for the generation of fines (small particles) and subsequent fines migration [1]. Most fines comprise clay particles that adhere to the rock surfaces by adhesion forces [2]. The drilling and extraction process alters the subsurface flow and chemical conditions, such as increased flow velocity and reduced salinity. The changes could detach fines that later clog smaller pores in subsurface rocks. Subsequent oil production is hindered. Fines migration is estimated to be responsible for approximately US$ 100 billion in economic losses per year, due to reduced production rates and subsequent remediation efforts [3].

One common industry example of engineering problems caused by particle detachment is the formation of wellbore skin near injectors during secondary recovery. Rather than enhancing oil production, poorly designed injection schemes that have neglected the consideration of formation properties caused the mobilisation of fines and consequently disrupted hydrocarbon production [4].

Although particle detachment is generally detrimental to petroleum production, it could also be deliberately induced by low-salinity waterfloods [5]. As subsurface rocks are rarely homogeneous, petroleum flows preferentially through regions of high permeability, bypassing substantial volumes of petroleum still trapped in low permeability zones. With the understanding that reduced salinity can decrease the adhesion force of fines to rock surfaces, injection of low-salinity water has allowed the detachment of fines that leads to the selective blocking of high-permeability zones, forming a more uniform flood front [6, 7]. However, industrial application of the technique remains limited as the underlying mechanisms are still debated; reliable predictions on the outcome of the waterflooding remain elusive.

Therefore, the systematic study of particle detachment is crucial for the advancement of technologies, regardless of whether particle detachment is desirable or undesirable for their specific applications. In fact, given the broad relevance of particle detachment in various research fields, particle detachment has emerged as a subject of rigorous studies in recent years. For example, in the development of wear resistant coatings [8], self-cleaning surfaces [9], particle filtration/separation [10] and drug design [11, 12]. However, despite the diverse applications, the study of particle detachment is relatively underdeveloped compared with particle attachment.

The study of particle detachment is necessarily multidisciplinary, requiring expertise in fields such as adhesion science, fluid mechanics, contact mechanics, simulations, microscopy and microfluidics. The multidisciplinary nature of the subject makes it challenging to develop a consistent modelling framework [13].

Fig. 1.1. Scanning electron microscopy (SEM) image for (a) kaolinite and (b) chlorite and illite. Chlorite is shown as flaky particles, while illite resembles thin ribbon strips [14].

Furthermore, current understanding of particle detachment is largely limited to the assumption of a perfect sphere, with much uncertainty remaining for irregular particles [13]. This lack of understanding limits its application to real-life scenarios where most of the particles are non-spherical.

For example, in petroleum applications, common sources of particles are clays such as kaolinite, chlorites, and illites [2]. Referring to Fig. 1.1, these clay particles do not resemble spheres, but rather flaky particles that can be represented as plates or thin ribbon strips that can be represented as rod geometries for modelling purposes. Clay particles also tend to cluster because of the adhesion force between the particles, forming aggregates on the rock surface. Similarly, in other investigations such as the detachment of bacteria and viruses, pharmaceutical drug carriers, and blood cells/blood clots, understanding the impact of their non-spherical geometries and aggregation on detachment is crucial.

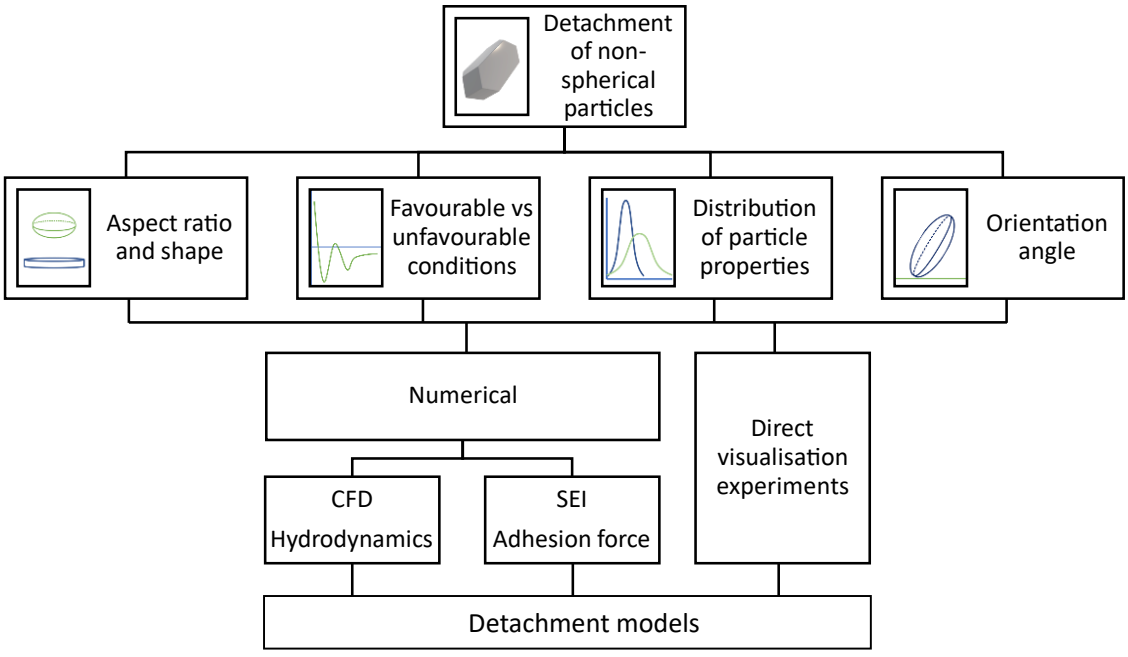

Fig. 1.2. Main factors considered in the detachment of non-spherical particles and their relation to the numerical and laboratory methodology.

Fig. 1.2 shows the outline of the study. Four fundamental aspects of the detachment of non-spherical particles were investigated. The aspect ratio/shape, distribution of particle properties and orientation angle arise from the physical geometry of non-spherical particles. The favourable and unfavourable conditions (explained in more detail in Section 2.4.1) relate to the chemical conditions of the surrounding fluid. The impact

in Section 2.4.1) relate to the chemical conditions of the surrounding fluid. The impact of the four factors on the adhesion and hydrodynamic forces was studied systematically using numerical methods of surface element integration (SEI) and computational fluid dynamics (CFD), respectively. The contributions of these two forces towards the subsequent detachment are quantified using the detachment models (Section 2.2) and compared with the results from the direct visualisation experiments.

1.1 Aim

The aim of this project is to further understand and characterise the fundamental phenomenon of particle detachment, accounting for non-spherical particle shapes, aspect ratio, particle size distribution, orientation angle and favourable/unfavourable conditions. An emphasis is placed on the detachment of kaolinites in petroleum reservoirs as a specific application, although the findings easily extend to other particles too.

The objectives of the project are listed below:

i. *To systematically quantify the impact of particle shape and deposition angle on both the hydrodynamic and adhesion forces in the context of particle detachment from the surface.*

ii. *To assess the effectiveness of the torque balance model and its applicability for predicting the detachment behaviour of both engineered and natural particles through comparison with direct visualisation experiments.*

iii. *To evaluate and understand the mechanism for particle release from the secondary minimum of unfavourable conditions.*

iv. *To further understand and characterise the dominating mechanisms affecting the detachment of natural kaolinite particles, accounting for the observed gradual detachment behaviour*.

1.2 Details of the publication

This thesis comprises four journal articles. Each article is presented as a chapter. The following section details the synopsis of the works and how they address the aims of this project.

1.2.1 Synopsis of Paper 1

The first paper describes the detachment of non-spherical particles under favourable conditions. Previous studies assumed that the impact of shape on hydrodynamic force is negligible. However, our study suggests that when considering the impact of the aspect ratio of the particles, the detachment of oblate spheroids and cylinders with increased flow velocities is non-monotonic. Nonmonotonicity arises from the hydrodynamic drag exerted on the particles. Approximating irregular particles as spheres can underestimate and overestimate the critical detachment velocity. To facilitate future modelling, hydrodynamic shape factors were also presented for the traditional Stokes law to extend its application from spheres to cylinders and oblate spheroids.

1.2.2 Synopsis of Paper 2

The second paper discusses particle detachment under unfavourable conditions, which is more commonly encountered in natural environments than under favourable conditions. The paper presents some discussions of commonly used alternatives to the torque balance model and found that the torque balance model, with its simplified assumptions, appears to be the more convenient way of modelling. The more complicated alternatives, though more rigorous, have several parameters that are unknown for specific applications, often relying on empirical coefficients, which limit their utility. For the first time, a two-stage detachment phenomenon is observed through direct visualisation experiments for both engineered polystyrene latex particles and naturally occurring kaolinites. The two-stage behaviour was attributed to the detachment of particles from the primary and secondary minima.

1.2.3 Synopsis of Paper 3

The third paper advances from the direct visualisation study of engineered polystyrene particles to natural kaolinite. By using stochastic inputs to account for the variation of size and shape in kaolinite particles, the stochastic torque balance model agrees with the gradual detachment behaviour as observed in the direct visualisation laboratory. The semi-major axis, aspect ratio, lever arm ratio and zeta potential are found to affect the detachment of kaolinites in decreasing significance under the given conditions.

1.2.4 Synopsis of Paper 4

The fourth paper investigates the significance of particle deposition angle (pitch) about the subsequent detachment of particles from substrates. Stretched polystyrene latex particles with well-defined geometries and sizes were synthesised and subsequently visualised in microfluidic flow experiments. The particles were observed to deposit at an angle to the substrate, contrary to previous assumptions that the particles would lie flat on the substrate. The previous trend reported in Paper 1 where particle detachment generally reduces with decreased aspect ratio is only true when the particle adopts a side-on configuration (no orientation angle). The trend is reversed when the particle reaches an end-on configuration. Furthermore, under the salinity and pH conditions used in the study, spheroidal particles, regardless of their aspect ratios, detach at virtually the same velocities as spheres when the orientation angle is around 30 ° to 40 °.

Chapter 2

Background

The study of particle detachment remains a very relevant topic for all aspects of industry and academic studies. In the study of colloidal transport in porous media, such as filtration and formation damage, several mechanisms are often involved. As shown in Fig. 2.1, some examples are advection, diffusion, straining, detachment and reattachment. The present study focuses mainly on detachment. However, consideration of attachment is sometimes important to determine the initial conditions.

Fig. 2.1. The various mechanisms involved in the flow and transport of colloidal particles in a porous rock at the microscale [15, 16]

2.1 Modelling of kaolinite geometry

Although the fundamental theories for particle detachment are generally applicable to any colloid particles, this study focuses on their application to kaolinite, which is the most common source of fines in the petroleum rocks [15, 17]. The current understanding of the detachment of natural particles is limited, as the established models are limited to the study of perfect spheres. In nature, particles are rarely spherical, such as the plate-like structure of kaolinite shown in Fig. 1.1.

In this study, a kaolinite particle is approximated as either an oblate spheroid or a cylinder with varying aspect ratio, α and size. The size of the particle is quantified by the volume equivalent sphere radius, r_e. The simplification is shown in Fig. 2.2, where the aspect ratio is defined by the semi-major axis, a, and the semi-minor axis, b, of the shape ($\alpha = b/a$). For the cases where the kaolinite is attached at a non-zero angle to the substrate, the deposition orientation angle, φ is introduced.

Fig. 2.2 shows an oblate spheroid particle attached to a substrate. The particle is subject to a linear shear flow with a shear rate, $\dot{\gamma}_o$ near the wall boundary. The four main forces that act on the particle in a single-phase flow consist of the hydrodynamic drag, F_d, and lift, F_l, as well as the adhesion force, F_a, and gravity, F_g.

Fig. 2.2. Setup of the particle and substrate [18]. (a) An oblate spheroid particle attached to an infinite flat wall (substrate) at an orientation (pitch) angle of φ. The oblate spheroid is defined by an aspect ratio of $\alpha = b/a$, where b is the semi-minor axis and a is the semi-major axis. Near the wall of the substrate, the particle is subjected to a linear shear flow with a shear rate of $\dot{\gamma}_o$. The resulting forces and moments exerted on the particle are depicted in (b). F_d, F_l, F_a, F_g and F_f are the drag, lift, adhesion, gravity and friction forces, respectively. M and N denote the hydrodynamic moment exerted by the linear shear flow and the

normal force. *O* is the centre of the particle, while *P* is the point where the particle pivots from the torque. l_n and l_d are the normal and drag lever arms.

2.2 Balance of forces and torques

The four forces are accounted for using the balance of forces and torques. Consequently, there are theoretically three possible modes of detachment, which are rolling, sliding and lifting [19-21], as expressed mathematically below:

Rolling: $$M + F_l l_n > \left(F_g + F_a\right) l_n, \quad (1)$$

Sliding: $$F_d > \mu_s \left(F_g + F_a - F_l\right), \quad (2)$$

Lifting: $$F_l > F_g + F_a, \quad (3)$$

where F_d, F_l, F_a and F_g are the drag, lift, adhesion and gravity forces, respectively. M denotes the hydrodynamic moment exerted by the linear shear flow. In Eqn. (1), l_n and l_d are the normal and drag lever arms, respectively. In Eqn. (2), μ_s is the coefficient of static friction. Following Eqns. (1) - (3), detachment is initiated when any one of the disequilibria is achieved. Eqn. (1) is called torque balance.

These detachment criteria allow for the modelling of the effect from variations such as particle aspect ratio, fluid velocity, fluid salinity and fluid pH conditions on particle detachment. Incipient detachment has often been reported to occur more frequently by rolling, and less so by sliding and lifting [22-24]. Furthermore, for colloidal-sized particles with an equivalent radius of 1nm < r_e < 10 μm, lift and gravitational forces are often omitted without much detriment to accuracy [25].

Therefore, Eqn. (1), known as torque balance, is often the primary criterion used to study particle detachment. Although torque balance is conceptually simple, determining the input values for hydrodynamic drag and moment, as well as the adhesion force and lever arms, poses a significant challenge. Particularly for microparticles, direct laboratory measurements are often difficult, unreliable or even impossible. Consequently, most of the inputs to the torque balance are often evaluated theoretically or numerically, along with their inherent assumptions.

2.3 Hydrodynamic drag, lift and moment

The detaching forces and torques are exerted by the linear shear flow on the particle. The analytical formula for the drag and lift exerted on a wall-bound sphere particle has

previously been derived by O'Neill, and Leighton and Acrivos, respectively [26, 27], such that:

$$F_d = 1.7009 \times 6\pi\mu v_o r, \quad (4)$$

$$M = 0.94399 \times 4\pi\mu v_o r^2, \quad (5)$$

$$F_l = 9.22 r^4 \dot{\gamma}_o^2 \rho, \quad (6)$$

where μ is the dynamic viscosity of the fluid, v_o the particle centre velocity, r the sphere radius and ρ is the fluid density. The particle centre velocity, v_o, which is the fluid velocity at the height of the particle centre, could also be expressed in terms of the shear rate, such that $v_o = r\dot{\gamma}_o$.

For an oblate spheroid or cylinder deposited at non-zero angles, Eqs. (4)-(6) are modified using shape factors and rearranged, resulting in the following:

$$F_d = 6\pi\mu r_e^2 \dot{\gamma}_o f_d(\alpha) f_{d,\varphi}(\alpha, \varphi), \quad (7)$$

$$F_l = 9.22 r_e^4 \dot{\gamma}_o^2 \rho f_l(\alpha) f_{l,\varphi}(\alpha, \varphi), \quad (8)$$

$$M = F_d l_d f_M(\alpha) f_{M,\varphi}(\alpha, \varphi). \quad (9)$$

The shape factors f_d, f_l and f_M account for the variation due to the aspect ratio. Similarly, $f_{d,\varphi}$, $f_{l,\varphi}$ and $f_{M,\varphi}$ account for the orientation angle, if any, on the drag, lift and moment exerted on the particle, respectively.

2.4 Adhesion force

The adhesion force is the primary force that resists the detachment of a particle from a substrate. Attractive and repulsive intermolecular interactions can occur between any two surfaces. An established theory for describing these interactions is the Derjaguin-Landau-Verwey-Overbeek (DLVO) model. The DLVO model states that the interaction potential between a particle and a substrate is the simple superposition of the attractive van der Waals, U_{vdw}, and the repulsive electrical double layer, U_{edl} [28-31]. Born repulsion, U_{born}, is often added as a simplistic mechanism to allow for reversible deposition at the primary minimum [32]. Therefore, the total DLVO interaction potential, U_{DLVO}, can be expressed as:

$$U_{DLVO} = U_{vdw} + U_{edl} + U_{born.} \quad (10)$$

Consequently, the DLVO interaction force, F_{DLVO} is taken as the negative derivative of the interaction energy, U_{DLVO}, such that:

$$F_{DLVO} = -\frac{dU_{DLVO}}{dh}, \tag{11}$$

where h is the distance of separation between the centre of the particle and the substrate. According to the sign conventions for DLVO forces, negative is attraction and positive is repulsion. Having determined the DLVO interaction force through Eqn. (11), the adhesion force, F_a, is defined as the maximum pull-off force required to remove a particle from a surface.

A typical DLVO force profile is shown in Fig. 2.3 (a). The long-range van der Waals force (VDW) attracts the particle as it approaches the plane wall. There exists an equilibrium distance when the attractive VDW is balanced by the repulsive electric double layer (EDL) and Born repulsion forces, preventing further proximity. Hence, depending on the separation distance, a particle can experience varying magnitudes of the DLVO force, up to a maximum value at the primary minimum (i.e. the adhesion force). VDW and EDL are also sensitive to changes such as salinity, pH, material and temperature, which in turn varies the overall DLVO force profile. Consequently, a combination of different factors could lead to either favourable or unfavourable conditions.

2.4.1 Favourable conditions versus unfavourable conditions

Referring to Fig. 2.3 (a), favourable conditions refer to the presence of only one primary minimum, with the absence of an energy barrier, thus ‘favourable for particle deposition’. In contrast, Fig. 2.3(b) shows the DLVO force profile under unfavourable conditions, which is defined by the presence of a repulsive energy barrier (thereby ‘unfavourable for particle deposition’). The repulsive EDL force exceeds the attractive VDW force at the energy barrier. Note also the additional secondary minimum, with a much smaller magnitude.

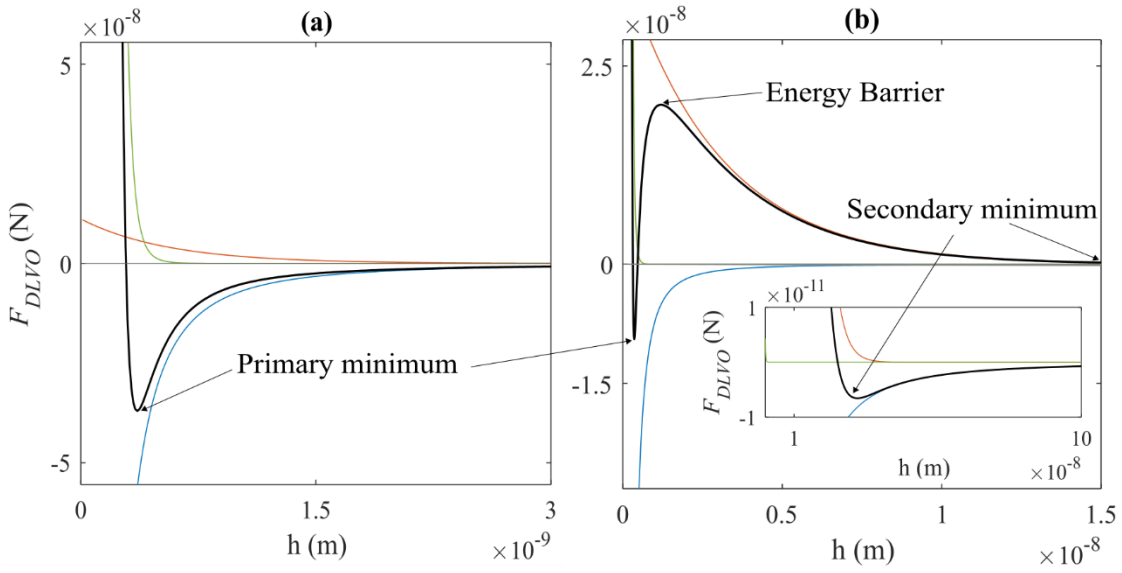

Fig. 2.3. Comparison of the DLVO force profile under (a) favourable and (b) unfavourable conditions. The total DLVO force profile (black curve) is the sum of the van der Waals (blue curve), electric double layer (red curve) and Born repulsion forces (green curve) at varying separation distances. (b) DLVO force profile under unfavourable conditions. Unfavourable conditions are defined by the presence of an energy barrier and a secondary minimum, which are otherwise absent under favourable conditions. The inset plot magnifies the secondary minimum. Note the difference in magnitude of the y-axis. Negative and positive terms correspond to attractive and repulsive forces, respectively.

2.4.2 Van der Waals and Electrical double layer

The van der Waals force arises due to temporary fluctuations in the electron density of molecules, causing an imbalance of charges [31]. The resulting attractive force is known as the London dispersion force. In addition to the London dispersion force, van der Waals forces can also include dipole-dipole interactions and hydrogen bonding [33]. The van der Waals interaction is often quantified using the Hamaker constant, determined either through the Hamaker or Lifshitz theory [31].

Separately, the electrical double layer force arises from the presence of two ion layers accumulating in an ionic solution near a charged solid surface. The first layer is a tightly bound layer of ions in the fluid to balance the charges on the solid surface, and the second diffuse layer, which is a more concentrated region of highly charged particles compared to the bulk fluid [30]. The zeta potential is the potential in the slip plane, which is often a good indication of the surface potential, required for the calculation of EDL forces [34]. A good background on interparticle forces is provided in [31].

2.4.3 Surface Element Integration (SEI)

For the case of non-spherical particles, the surface element integration (SEI) technique is used to determine the interaction energy and the adhesion force [35, 36]. Fundamentally, SEI attempts to scale the interaction energy per unit area, *E*, from that of two infinite flat plates to that experienced between an arbitrarily shaped particle and an infinite flat plate. This is expressed by Eqn. (12):

$$U = \iint E(h) \frac{\boldsymbol{n} \cdot \boldsymbol{k}}{|\boldsymbol{n} \cdot \boldsymbol{k}|} dxdy, \tag{12}$$

where *U* is the interaction energy of the arbitrarily shaped particle with the infinite plate. *E(h)* is the interaction energy per unit area between two parallel infinite plates separated at a distance, *h* [36]. In Eqn. (12), $\boldsymbol{n}$ is the unit outward normal from the surface element and $\boldsymbol{k}$ is the unit vector directed toward the positive z-axis (i.e. the axis perpendicular to the plate). The expressions for Eqn. (12) are presented in more detail for the specific cases of an oblate spheroid and a cylinder in Chapter 4 and for an oblate spheroid with non-zero orientation angle in Chapter 5.

Following the DLVO framework [28, 29, 32], the interaction energy per unit area between two parallel infinite plates, *E*, separated by a distance, *h* is given by:

$$E_{vdw} = -\frac{A_h}{12\pi h^2}, \tag{13}$$

$$E_{edl} = 32\varepsilon_o \varepsilon_r \kappa \gamma_1 \gamma_2 \left(\frac{k_B T}{ze}\right)^2 \exp(-\kappa h), \tag{14}$$

$$E_{born} = \frac{A_h \sigma^6}{360\pi h^8}, \tag{15}$$

$$E(h) = E_{vdw} + E_{edl} + E_{born}, \tag{16}$$

where A_h is the Hamaker constant using Lifshitz theory [31]. In Eqn. (14), ε_o is the permittivity of a vacuum (8.85×10-12 $C^2N^{-1}m^{-2}$), ε_r the relative permittivity of water (78.46). κ is the inverse Debye length ($\kappa = \sqrt{(e^2/\varepsilon_o \varepsilon_r k_B T) \sum z_i{}^2 n_i}$), *z* the ion valency, *n* the number concentration of the i-th ion species in the solution, *e* (1.6×10-19 C) the charge of an electron, *T* the absolute temperature and k_B is the Boltzmann constant (1.380649×10^{-23} J K^{-1}). γ_1 and γ_2 are the reduced surface potential for the particle and the

substrate glass, respectively (γ=tanh$(ze\zeta/4k_BT)$. ζ is the zeta potential and σ is the atomic collision coefficient (5Å).

2.5 Hertz contact theory

In addition to hydrodynamic and adhesion forces, the lever arm for the forces also plays a crucial role in the torque balance. Hertz contact theory describes the deformation between two solids in contact [37]. Hertz contact theory was applied in this study to calculate the radius of the contact area, l_n (i.e. the normal lever arm) in response to an applied normal force (adhesion force in this case). For a sphere on a flat infinite plane, l_n is given by:

$$l_n^3 = \frac{3F_a r_e}{4E^*} \quad , \quad \frac{1}{E^*} \equiv \frac{1-\nu_1^2}{E_{y1}} + \frac{1-\nu_2^2}{E_{y2}}, \tag{17}$$

where the effective Young's modulus, E^*, is given as a function of the Poisson's ratio, ν and the Young's modulus of elasticity, E_y. Subscripts 1 and 2 represent the particle and surface, respectively. For the case of oblate spheroids attached at non-zero orientation angles, the Hertz theory for elliptical contact is presented in Appendix C.

2.6 Summary of the simulation workflow

Referring to Fig. 2.4, the numerical modelling in this study was performed primarily through the commercial software ANSYS CFX and MATLAB. MATLAB was used for calculating the SEI adhesion forces, Hertz contact and the final coupling of the individual forces through torque or force balance. In this study, the hydrodynamic force and the adhesion force are assumed to be independent of each other.

Specific to the CFD modelling, the laminar steady state model was used. For the various oblate spheroids and cylinders, CFD determines the velocity and pressure distributions throughout the particle surfaces by the numerical solution of the Navier-Stokes equation. Integration of the pressure gradient and the shear that acts on the surface in the perpendicular and parallel directions to flow yields the lift and drag forces, respectively. Pressure gradient and shear also cause a resultant moment due to the imbalance of low velocity flow near the wall with the mean flow. By determination of the drag, lift and moment, their respective shape factors can be determined, which allows

for the application to other aspect ratios and orientation angles without requiring additional CFD simulations.

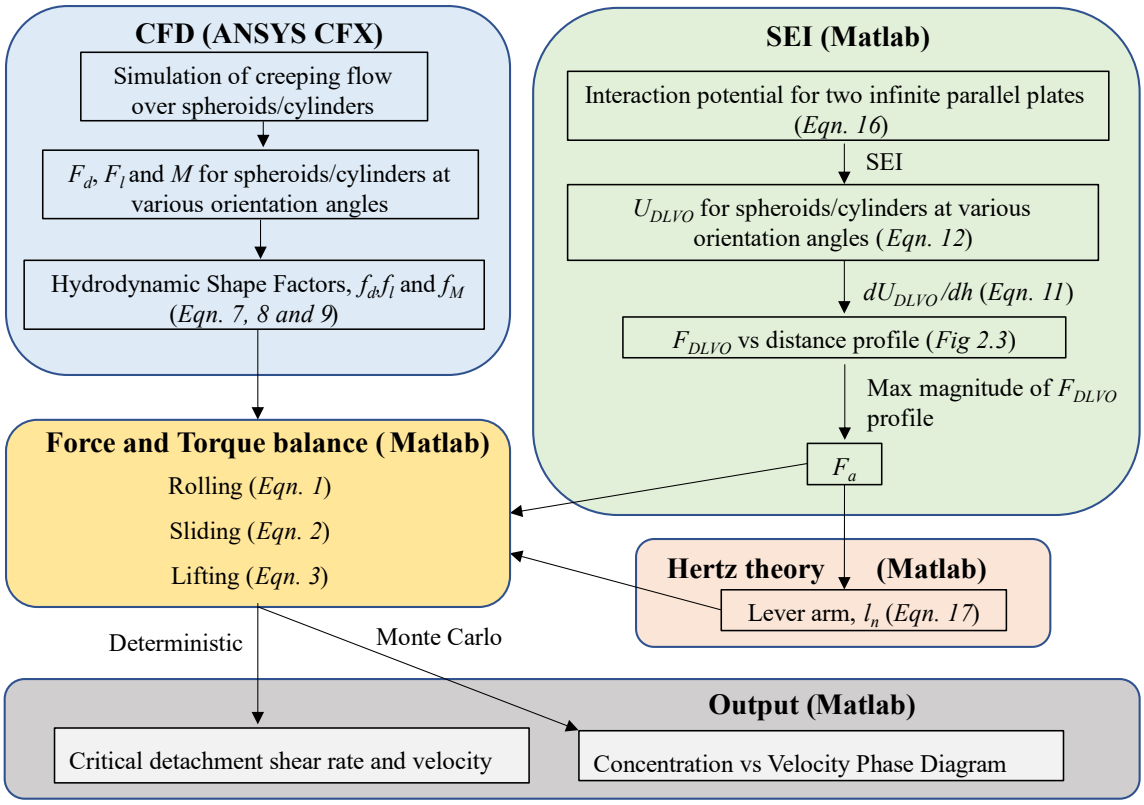

Fig. 2.4. Workflow diagram of the modelling process for particle detachment.

The empirical correlations for drag, lift and moment are inputs for the force and torque balance, which are implemented by code in MATLAB, along with the direct numerical calculations of SEI adhesion force and Hertz theory.

2.7 Direct visualisation experiments

2.7.1 Experiment materials: fluid and particles

In this study, favourable or unfavourable conditions for the experiments were achieved by altering the fluid salinity and fluid pH values. Sodium chloride was dissolved in deionised water (DI) to achieve the desired salinity, between 0.000128 M and 0.3 M NaCl. Similarly, by adding sodium hydroxide or hydrochloric acid, the pH of the solution can be altered between pH 3 and pH 11, respectively. High salinities and low pH tend to create favourable conditions and vice versa. The glass visualisation flow cell (Ibidi, Germany) has a single rectangular channel of dimensions 48.2 mm x 5 mm (width x depth). Depending on the study, the channel height used was 150 μm or 450 μm. The

particles used are hydrophilic carboxylate (latex) polystyrene microsphere particles (Polysciences Inc. USA) with radii of 1 to 5 μm, and kaolinite powder (Sigma-Aldrich, Australia) with volume equivalent sphere radii of 1 to 5 μm.

2.7.2 Polystyrene latex stretching procedure

For oblate spheroids, polystyrene spheres were stretched according to the methodology pioneered by [38] and modified by [39]. Briefly, small concentrations of the polystyrene spheres are mixed in a PVA solution and poured into a Petri dish to dry. The PVA-polystyrene film is then placed between two silicon sheets and clamped between two steel platens. Heating the film at 135° C exceeds the glass transition temperature of the polystyrene, which softens the polystyrene particles. When the temperature is achieved, compression is applied to the platens, deforming the polystyrene spheres into oblate spheroids. The silicon sheets ensure that the compression pressure is distributed evenly for equal deformation of particles in both the centre and on the edge of the platens. The compression pressure is maintained while the film is left to cool. Subsequently, the PVA-polystyrene film is dissolved with a 30% isopropanol solution to remove the PVA film. The mixing and centrifuging was repeated 10 times to minimise any remaining PVA film on the particles.

2.7.3 Visualisation rig

The visualisation methodology is based on the work of [23]. Fig. 2.5 shows the setup used to visualise the detachment of particles in the microfluidic channel. The particles, consisting of polystyrene spheres, oblate spheroids, or natural kaolinites, are injected with the carrier fluid using a syringe into the visualisation cell and left to rest for at least 2 h. After the particles have deposited on the cell bottom, the visualisation cell is placed under the optical microscope, ensuring that the cell is perfectly horizontal to prevent uneven lighting. A high precision syringe pump (Model 270, Cole-Parmer, USA) injects particle-free solutions into the cell at varying velocities ranging from 2.70×10^{-3} ml/min up to 210 ml/min. The computer displays the images from the microscope in real time. Image processing is used to analyse the laboratory images, to determine the number of attached particles, the semi-major axis (when injecting kaolinite) and the orientation angle (when injecting oblate spheroids).

The presence of air bubbles throughout the experiment poses a significant problem for the results. The introduction of air bubbles causes a strong capillary force at the air-liquid interface that removes most of the particles in the cell, thereby invalidating the results. Some precautionary steps involved a) using glass syringes instead of plastic syringes for a smooth flow, b) installing a three-way valve to prevent air bubbles when changing the syringe and c) ensuring that the tubing is always free from any air bubbles before connecting with the cell.

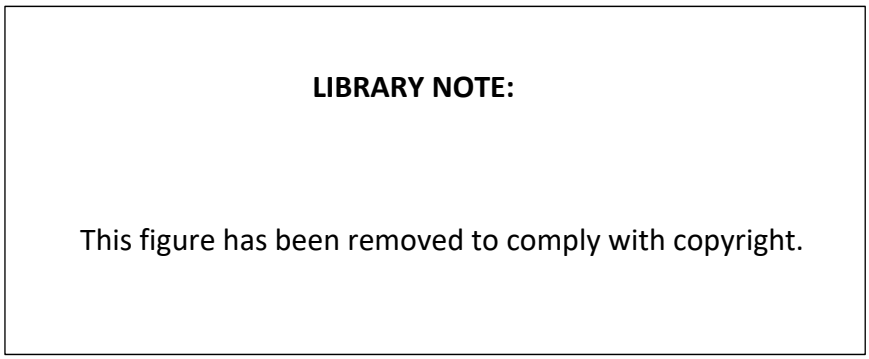

Fig. 2.5. Laboratory setup for direct visualisation of particle detachment: 1 – syringe pump, 2 – syringe, 3 – syringe pump, 4 – three-way valve, 5 – beaker, 6 – visualisation cell , 7 – optical microscope, 8 – computer [40].

2.7.4 Visualisation image processing

The raw microscope images obtained from the visualisation experiments undergo further image processing to quantify and characterise the detachment of particles. MATLAB codes were written along with the usage of the image processing toolbox. A primary step was the binarisation of the image to distinguish the particles from the background. The binarisation process requires a threshold value that is determined by trial and error and is quite subjective. Codes were written to number and outline every individual particle counted by the image processing so that it can be manually checked and validated.

This page is intentionally left blank

Chapter 3

Literature Review

3.1 Kaolinite detachment

Kaolinite is the most common clay and has diverse uses in the manufacturing of plastics, paper, rubber, pharmaceuticals and paint [41, 42]. It can also affect the transport of other particles such as pesticides, drugs, contaminants, microorganisms and fertilisers [43-47]. Kaolinite is the primary source of fines in the petroleum industry, causing fines migration, formation damage, and a significant loss of well-productivity [2, 48].

Kaolinite consists of an octahedral alumina sheet and a tetrahedral silica sheet, bound by sharing hydroxyls and oxygens between the sheets [42]. The clay mineral has broad size distributions, ranging from 0.2 μm platelets to 30 μm stacks and aggregates [49]. The aspect ratio (height/width) of the clay mineral also varies widely, with values ranging from 0.03 to 0.5, depending on factors such as the source of the clay, its structure and the measurement technique used [50-53].

Polystyrene latex spheres are used in most experimental studies on particle detachment [54, 55] because the material is well defined, uniform and spherical [56]. However, kaolinites have a more complex structure, existing not only as individual platelets but also in various stacks and aggregates [41]. In kaolinites, the pH and salinity of the solution not only affect the magnitude of the adhesion force but also change the charge distribution on clay surfaces, so structures such as ‘booklets’ or 'house of cards' can form, depending on whether kaolinite platelets are attached through edge-edge, edge-face or face-face interactions [57-59]. The shape and structure, in turn, affect their susceptibility to detachment by hydrodynamic forces [60].

In response, some works attempt to characterise the effect of pH and salinity on the structure of kaolinite clusters and detachment [58, 60]. Fixing the salinity at 0.004 M NaCl, a non-linear detachment trend of kaolinites was observed in column filtration experiments within the range of pH 3 to 8. The detachment rate peaked at pH 5, with lower rates achieved when approaching pH 3 or pH 8 [58]. More loose clusters formed at pH 5 compared to compact booklets at pH 3 or pH 8, leading to a higher detachment rate at intermediate pH [57, 58]. A separate visualisation study on the impact of salinity has shown that significant kaolinite detachment occurs in low salinity conditions [48]. The qualitative nature of the previous studies, coupled with their failure to consider the effects of hydrodynamic forces, hindered the development of mechanistic models to predict the detachment of kaolinite. Derivation of mathematical models for particle transport in porous materials is difficult due to the lack of such data [61-64].

Various studies have investigated the impact of factors such as particle size [65-68], aspect ratio [36, 69, 70], deposition angle [70, 71] and aggregate structure [58] on particle detachment. However, it remains unclear how the distribution of these parameters on kaolinite particles will affect their subsequent detachment. It is also unclear which of these parameters is most significant to predict particle detachment.

Modelling the detachment of kaolinite can be difficult due to the wide variation in their size, structure and shape. Some attempts include using a stochastic approach to model the transport behaviour of kaolinite through a column experiment, accounting for the size distribution of both sand and kaolinite [72]. In another study, a qualitative match was achieved with the torque balance model for spheres of different radii. The size variation was suggested to be the cause of the gradual detachment trend observed in the laboratory [73]. However, though variation in size can explain the gradual detachment, these studies approximated kaolinites as spheres, which cannot account for the complicated structures present in natural kaolinite.

3.2 Impact of shape on particle detachment

The transport and retention behaviour of non-spherical shapes has received recent attention, with column filtration experiments conducted for rods [74-76], barrels [77], peanut shapes [78], buckled particles and ellipsoids [79]. Non-spherical particles were shown to attach and detach differently than sphere particles. Consequently, the

assumption of particle sphericity prevents an accurate characterisation of filtration for irregular particles. However, filtration studies are not without limitations, particularly for studying particle detachment.

Filtration consists of various mechanisms that act simultaneously, including detachment, but also attachment, bridging, straining, ripening and near wall transport [76, 78, 80, 81]. For example, there have been conflicting observations in filtration studies regarding the effect of high particle aspect ratios on particle retention, with some studies showing enhancement [75, 76] and others, reduction [74, 77], depending on the dominant mechanisms at play. Despite the steady increase of work on irregular particles, the work done so far is still in a pioneering stage, when compared with the established models for spherical particles.

Studies on irregular particles with a sole focus on detachment are considerably fewer. Visualisation experiments were performed by Aramrak et al. [82], investigating the detachment of rod, barrels and oblong disks by a moving air-water interface. There is a pronounced dependence of detachment on shape, where particles with edges (barrels) have a higher tendency for detachment. However, the findings are applicable only in two-phase flows, where capillary forces are dominant.

Brambilla et al. [45] developed models for the detachment of prolate spheroids to examine the mobilisation of bacteria in turbulent wind conditions. Despite the models, it remains uncertain how the variation in the hydrodynamics and adhesion force affects subsequent detachment. Similarly, a study by Decuzzi and Ferrari [11] compared the retention of spherical and oblate spheroidal drug carriers subjected to laminar shear flows. Oblate spheroids were shown to have the highest retention (detach less readily) than spheres. However, the mechanics of ligand-receptor bonds are different from the DLVO adhesion forces considered in this thesis.

The quantitative impact of the particle shape on both the adhesion forces and the hydrodynamics is still poorly understood. Likewise, more studies are required to investigate the impact of shape on the detachment of irregular particles.

3.3 Challenges in the laboratory modelling of particle detachment

The challenge of obtaining direct laboratory measurements of the hydrodynamic and adhesion forces that act on a particle at the microscale presents a significant obstacle to the study of particle detachment [83].

In the case of adhesion forces, the current understanding of particle adhesion is based primarily on theoretical models, with a multitude of mechanisms and models proposed by various authors to explain laboratory observations. Retention of particles under unfavourable conditions is a notable example. There has yet to be any consensus on how particle retention could occur in the presence of a repulsive energy barrier. Some authors propose deposition in the secondary minimum [55, 84-86] while others suggest the deposition at the primary minima, where the energy barrier is overcome by local physical and chemical heterogeneity [87, 88]. Without direct measurements of the adhesion forces, both explanations appear justified.

There have been several attempts to complement theoretical studies with laboratory measurements, such as atomic force microscopy (AFM) [89]. The microscopy technique is used primarily to assess the microscale topography of the surface. Furthermore, the deflection of the AFM cantilever can be correlated with the adhesion force using DLVO theory [89]. Therefore, AFM could also be used to indirectly measure the adhesion force. However, the interpretation of the AFM data is not straightforward, relying on several assumptions that some authors consider speculative [88]. As an alternative, the surface force apparatus (SFA) has shown reliable measurements that are in good agreement with theory [31, 90], but is prohibitive in its application due to the complexity of the equipment and the high requirements for sample preparation.

Consequently, core scale experiments are more frequently used, where fluids of well defined properties are injected into a core and the filtrate is subsequently analysed [7, 91]. However, the black-box approach lacks detailed information on the in situ flow and capture mechanisms on the microscale. Identical results (suspended concentrations) could potentially be achieved by different variations in factors (pH, salinity and pore geometry) [87, 92].

There is a steady trend for studying particle detachment using direct visualisation methods. The method often involves a microfluidic cell with a rectangular channel placed

under a microscope, such that the flow, attachment and detachment of particles can be viewed in real time. It is used frequently in microbiology to study the detachment of microorganisms [93-95] but the use of microfluidic visualisation has since extended to non-biological particles [82, 96, 97]. Direct visualisation has been instrumental in providing validation and a new understanding of detachment.

Rolling as the most frequent mode of detachment was validated through direct visualisation studies. Direct visualisation of glass particles on rough stainless steel surfaces under turbulent air flows shows that rolling detachment occurs before sliding and lifting [24]. Further visualisation studies have analysed the impact of surface roughness and charge heterogeneity [87] and the impact of particle size [98] on detachment, as well as particle deposition under unfavourable conditions [84, 87]. However, the visualisation of non-spherical particles is still lacking, particularly for studying detachment. The lack of visualisation data hinders the validation of models and physical understanding of the detachment of irregular particles.

3.4 Detachment of particles under unfavourable conditions

The study of unfavourable conditions is significant, as it is more commonly encountered in nature compared to favourable conditions [55]. Infiltration studies, the transport, retention and detachment of particles in favourable conditions match well with theoretical predictions. However, under unfavourable conditions, the particle retention in column experiments is often significantly higher than predicted by the theory [55, 88, 99, 100]. Given the ubiquity of unfavourable conditions and the uncertainty associated, the detachment of particles under unfavourable conditions warrants further scrutiny.

According to the DLVO theory, the presence of the primary and secondary minima means that the particles could be retained in both wells [30]. The detachment of particles from the primary minimum is already well understood and characterised [55]. However, the role of the secondary minimum in particle retention is still debated. Although an adhesion force is present at the secondary minimum, the magnitude is significantly lower than that of the primary minimum. Furthermore, considering that the attraction at the secondary minimum occurs at a considerable distance (tens of nanometres compared to a few angstroms at the primary minimum), some authors question whether the particles could still be considered in contact with the substrate [101]. Therefore, it remains

uncertain whether the secondary minimum could exert a significant adhesion force for immobilisation and whether the torque balance and sliding friction models could still be used as physical contact is assumed [86, 101].

Several hypotheses have been proposed for the deposition of particles under unfavourable conditions. For one, particles could be deposited only at the secondary minimum, as the energy barrier prevents retention at the primary minimum [84]. Alternatively, particles could be deposited in both primary and secondary minima as sufficient energy is gained to overcome the energy barrier [23, 102]. Recent studies favour explanations of surface roughness and chemical heterogeneities that can completely remove the local energy barrier for deposition at the primary minimum [87, 88, 103-105]. In the case of filtration, the presence of stagnation zones behind collectors where there are no hydrodynamic forces provides an additional mechanism for deposition in the weak secondary minimum, along with bridging and straining [106].

Currently, there is yet to be a clear consensus regarding the mechanistic modelling of particle detachment from the secondary minimum.

3.5 Criteria for the initiation of rolling detachment

The torque balance model is a predominant model in the literature for predicting the rolling detachment of particles [19, 25, 107, 108]. The deformation of the particle at the contact provides the lever arm for the adhesion force to act, and this is counteracted by the detaching torque of fluid flows. Detachment is assumed to occur immediately whenever the equilibrium between the two torques is violated. Despite widespread use, torque balance is not without limitations. The model reportedly tends to overestimate the resisting torque, since the adhesion force realistically does not act over the equilibrium contact area as predicted by contact theories (Hertz, Johnson-Kendall-Roberts (JKR) or Derjaguin-Muller-Toporov (DMT)) during detachment [109].

Another alternative to the torque balance model is the energy approach to rolling friction [54]. The model relies on the empirical hysteresis loss factor, which accounts for the energy loss during elastic deformation and recovery when rolling. To the author's knowledge, the rolling friction model is rarely used to model particle detachment.

Separately, the Dominik and Tielens (DT) model was originally developed to study the detachment of space dust in astrophysics [110, 111]. In the DT model, the resistance torque originates from the asymmetric pressure distribution throughout the contact area. The resulting moment is generated from the difference in the pressure distribution between the leading edge and the trailing edge [112]. The relative merits and limitations of these models for predicting particle detachment have not yet been evaluated.

3.6 Deposition orientation angle between the particle and substrate

Owing to the irregular shape of natural particles, the deposition orientation angle between the particle and substrate is another factor that could impact detachment. Following the previous discussion in Section 3.1.1, kaolinites adopt different orientation angles depending on whether they experience edge-to-edge, face-to-face or face-to-edge interactions. In addition, recent visualisation studies have reported the presence of orientation angles when particles are deposited on the substrate [82, 113-115], contrary to the conventional understanding that particles will reorient with hydrodynamic flow to achieve equilibrium [78].

Gomez-Flores et al. [70] experimentally investigated the deposition rate of bullet-shaped silica particles depositing with six different salinities. When comparing the deposition of bullet-like particles versus spheres, the shape and deposition angle is reported to be only significant at intermediate salinities. Modelling bullet-like particles as volume equivalent spheres was apparently sufficient to predict deposition at low and high salinities. At intermediate salinities, only certain orientation angles were able to overcome the unfavourable energy barrier and be attached. However, there is a lack of direct visualisation to confirm this finding, as the deposition was inferred using mass balance. Additionally, the bullet-like particles used in the experiments were approximated as ellipsoids or cylindrical rods, which might affect the validity of their numerical findings. Finally, since the study focused on deposition, it is unclear how their findings could be applied to particle detachment.

A similar study investigated the deposition of stretched latex spheroids on two surfaces: humic acid and alginate [116]. However, because of the coated surfaces, there are presence of non-DLVO forces, which prevented a quantitative fit from the DLVO predictions. In addition, the study has also neglected the impact of hydrodynamic forces

on deposition mechanics, relying solely on the variation of the DLVO with particle orientation to explain the results.

Cooley et al. [117] produced visualisation tests on the adhesion of sphere, oblate, spheroid and rod polystyrene particles. Anisotropic oblate and rod-shaped particles were shown to have the highest retention compared to spheres. The increased localisation was due to increased marginalisation (the particle being brought near surfaces from bulk flow), which led to higher collision frequency and adhesion. Li and Ma [118] reported similar findings in their numerical studies, where the irregular shapes of the rod-shaped colloids cause a greater interception of the colloids with the substrate. However, the studies did not consider the detachment behaviour of the particles.

Although most of the authors reported the importance of shape and orientation in deposition, Shave et al. [113] showed that shape does not influence deposition due to the diffusion limit. Moreover, it was shown that the particles do not stabilise, but rather remain in the orientation angle upon collision, contrary to common assumptions in the literature. Given the apparent contradiction, there is still a lack of systematic study of the role of orientation angle in particle detachment. Many studies on particle orientation are based on theoretical considerations of the DLVO profile. Of the limited experimental studies on orientation angles, most methods used the quartz crystal microbalance (QCM) method, which is a mass balance method. The visualisation of particles attached at an angle and their consequent detachment has yet to be attempted.

Incidentally, the study of prolate and oblate spheroids under linear shear flow as they approach, attach and detach from a wall has been scrutinised in the biomedical field; the shape resembles bacteria, red blood cells and platelets. The early work of Jeffery [77] showed that an oblate spheroid in unbounded shear flow follows a periodic orbital trajectory (Jeffery orbit). Since then, numerical [78, 79] and experimental [80, 81] works have investigated the various possible trajectories undertaken by a spheroid, as a combination of interactions between flow drag and moments, wall interference, and adhesion forces. Non-spherical particles introduce periodic rotations/oscillations that cause drifting toward the substrate [117-119]. However, most studies are concerned with the trajectory as it approaches and adheres, instead of detachment. Furthermore, the attachment mechanism is different from that of DLVO, where the bonds occur only in specific orientations [82] and further strengthen with time [120].

3.7 Research gaps

Following the previous discussion of the literature, four main research gaps were identified:

i. Classical studies on particle detachment are mostly confined to ideal sphere particles. The few recent works that have accounted for non-spherical particles have only considered the impact of particle aspect ratio on adhesion forces, without considering the hydrodynamics. Furthermore, the focus has primarily been on particle transport and attachment rather than detachment. The impact of the particle aspect ratio on both the hydrodynamic and adhesion forces has yet to be systematically investigated. Attempts to quantify the combined impact of the adhesion and hydrodynamics toward the subsequent detachment are also limited.

ii. Unfavourable conditions are more commonly encountered in natural environments compared with favourable conditions. However, because of the presence of the additional repulsive energy barrier, there is currently no consensus on the understanding and modelling of the deposition and detachment behaviour of particles from the substrate. Furthermore, it is still unclear whether torque balance could qualitatively predict particle detachment under unfavourable conditions.

iii. Kaolinite, being the most ubiquitous clay, has received a significant amount of scrutiny to understand its transport in porous media. However, the work to date has generally assumed kaolinites to be perfect spheres to simplify the modelling. This is despite the numerous reports that kaolinite could adopt complex geometries that could not be captured by assuming a sphere. Furthermore, the modelling of kaolinite has mostly been deterministic and does not account for the parameter distributions present in natural particles.

iv. It was frequently assumed that particles would reorient with the hydrodynamic flow to minimise resistance and reach an equilibrium side-on attachment with the substrate. However, there are increasing reports of recent

studies suggesting a pronounced orientation angle in particle attachment even under shear flow. The literature that considered the orientation angle generally focused on the transport of the particle from the flow to the substrate and its subsequent attachment. There has yet to be any systematic study that accounts for the impact of the orientation angle on detachment, accounting for both the adhesion and the hydrodynamic forces.

3.8 Research objectives

Considering the research gaps, the following research objectives are formulated.

i. The first objective is the systematic quantification of the effect of shape and aspect ratio on the hydrodynamic and adhesion forces in the context of particle detachment. A kaolinite particle is approximated either as a cylinder or an oblate spheroid with varying aspect ratios. By holding the volume constant, the variation of drag, lift, hydrodynamic torque and adhesion force will be determined using CFD and SEI. The resultant critical velocity for detachment will be evaluated using the torque balance model.

ii. The second objective is to evaluate the effectiveness of the torque balance model in quantifying and predicting particle detachment under unfavourable conditions. The applicability of the torque balance for both engineered and natural particles will be evaluated by comparison with direct visualisation experiments. Alternatives to torque balance, such as the rolling friction model and the DT model, will also be applied, with their respective merits evaluated.

iii. The third objective is to better understand and characterise the dominating mechanisms that affect the detachment of natural kaolinite particles, accounting for the observed gradual detachment behaviour. Rather than deterministic inputs, the inputs to the torque balance model will be distributed stochastically and compared with direct visualisation observations of kaolinites under shear flow.

iv. The fourth objective is to characterise the impact of orientation angle. Similar in method to objective one, the variation in drag, lift, hydrodynamic torque and adhesion force will be evaluated numerically for different particle

orientation angles. To facilitate better characterisation, spherical latex polystyrene particles of well-defined volume and shape will be stretched into oblate spheroids. The subsequent detachment trend measured from the direct visualisation experiment can then be compared with the stochastic torque balance model. To avoid uncertainties that arise from unfavourable conditions, the study will be limited to favourable conditions.

This page is intentionally left blank

Chapter 4

Impact of shape on particle detachment in linear shear flows

Statement of Authorship

Title of Paper	Impact of shape on particle detachment in linear shear flows
Publication Status	☑ Published ☐ Accepted for Publication ☐ Submitted for Publication ☐ Unpublished and Unsubmitted work written in manuscript style
Publication Details	Ting, H.Z., Bedrikovetsky, P., Tian, Z.F. & Carageorgos, T. 2021, 'Impact of shape on particle detachment in linear shear flows', Chemical Engineering Science, vol. 241.

Principal Author

Name of Principal Author (Candidate)	Heng Zheng Ting
Contribution to the Paper	Generation and analysis of all CFD numerical data, analysis and interpretation of the lab data and wrote the manuscript.
Overall percentage (%)	80%
Certification:	This paper reports on original research I conducted during the period of my Higher Degree by Research candidature and is not subject to any obligations or contractual agreements with a th ain its inclusion in this thesis. I am the primary author of this paper.
Signature	Date: 24/02/2023

Co-Author Contributions

By signing the Statement of Authorship, each author certifies that:

i. the candidate's stated contribution to the publication is accurate (as detailed above);

ii. permission is granted for the candidate in include the publication in the thesis; and

iii. the sum of all co-author contributions is equal to 100% less the candidate's stated contribution.

Name of Co-Author	Zhao Feng Tian
Contribution to the Paper	Co-supervised the development of the work, assist in the development of the CFD model and reviewed and assessed the manuscript.
Signature	Date: 23/02/2023

Name of Co-Author	Pavel Bedrikovetsky
Contribution to the Paper	Formulated the problem, co-supervised the development of the work and reviewed and assess the manuscript
Signature	Date: 24/02/2023

Name of Co-Author	Themis Carageorgos		
Contribution to the Paper	Performed laboratory experiments		
Signature		Date	24/02/2023

Name of Co-Author			
Contribution to the Paper			
Signature		Date	

Chemical Engineering Science 241 (2021) 116658

Contents lists available at ScienceDirect

Chemical Engineering Science

journal homepage: www.elsevier.com/locate/ces

Impact of shape on particle detachment in linear shear flows

Heng Zheng Ting [a], Pavel Bedrikovetsky [b,*], Zhao Feng Tian [a], Themis Carageorgos [b]

[a] School of Mechanical Engineering, The University of Adelaide, Adelaide 5000, SA, Australia
[b] Australian School of Petroleum and Energy Resources, The University of Adelaide, Adelaide 5000, SA, Australia

HIGHLIGHTS

- Detachment of spheroids and cylinders is significantly different to spheres.
- Particle detachment is non-monotonic with particle aspect ratio.
- Oblate spheroids and cylinders detach preferably by rolling and sliding respectively.
- The detachment model was in good agreement with direct visualisation experiments.

ARTICLE INFO

Article history:
Received 28 November 2020
Received in revised form 5 February 2021
Accepted 9 April 2021
Available online 20 April 2021

Keywords:
Colloid
Suspension
Detachment
Porous Media
Shape
DLVO

ABSTRACT

Transport and detachment of colloidal particles with irregular shapes occur in geology, environmental, and water-resource engineering. We investigated the effect of shape and aspect ratio on the detachment of non-spherical microparticles attached to a plane substrate, in Couette linear shear flow, under favourable conditions. The detachment conditions were determined by the mechanical equilibrium of drag, lift, gravity and adhesion forces acting on the particle. Drag and lift were evaluated using Computational Fluid Dynamics (CFD), introducing the shape-dependent corrections into traditional formulae for spherical particles. The adhesive particle–surface force is determined by the Surface Element Integration (SEI) method, which also corrects the classical DLVO expression. The forces exerted on spheroids and cylinders can significantly differ from spheres and their detachment exhibit non-monotonic dependencies with aspect ratio. Direct visualisation experiments were performed by piecewise-constant change of flow velocity and the observed detachment were in good agreement with the mechanical-equilibrium based predictions.

1. Introduction

Detachment of colloids and nanoparticles from substrates occurs in numerous natural and technological processes. Some examples include the removal of contaminants from semiconductor surfaces (Reinhardt & Kern 2018), resuspension of dust particles in indoor environments (Zhang et al. 2008), cross-flow microfiltration (Kang et al. 2004), transport of pathogens in subsurface soil (Bradford et al. 2013), as well as the optimisation of pharmaceutical drug delivery (Cui & Sommerfeld 2015; Decuzzi & Ferrari 2006).

In the petroleum industry, understanding particle detachment is crucial, as it is a mechanism for fines generation and a necessary precursor for fines migration (Ryan & Elimelech 1996). Within a petroleum reservoir, typical sources of mobile fines are clay minerals such as kaolinite, illite and chlorite (Russell et al. 2018). These particles are typically attached on pore wall surfaces by adhesion forces, or cemented to rock surfaces through authigenic growth (Worden & Morad 2003). Numerous literature and industry reports have shown that alterations in pore conditions during hydrocarbon production, such as increased flow velocity, reduction in pH and salinity, can cause particle mobilisation (Russell et al. 2018). The fines migration after detachment can be simulated by several stochastic mathematical models (Shapiro 2007; Shapiro & Wesselingh 2008).

Four main forces act on a particle attached to a substrate: the hydrodynamic forces of drag, F_d and lift, F_L, along with the adhesion force, F_a and gravity F_g (Fig. 1). The normal forces cause a slight deformation at the particle–wall contact, yielding the normal lever arm, l_n. By using the equilibrium of forces and torques (EFT), the particle has three possible modes of detachment: rolling, sliding and lifting, as expressed in (1), (2) and (3), respectively (Hubbe 1984). $M$is the moment exerted by the drag, acting through the

* Corresponding author.
E-mail address: pavel@asp.adelaide.edu.au (P. Bedrikovetsky).

https://doi.org/10.1016/j.ces.2021.116658
0009-2509/

Nomenclature

A_h	Hamaker constant
a	Semi-major axis
b	Semi-minor axis
D	Distance of closest separation
e	Charge of an electron
E	Adhesion energy per unit area between 2 parallel infinites plates
E_Y	Young's modulus
$E_Y{}^*$	Effective Young's modulus
F_a	Adhesion force
F_d	Drag force
F_d^∞	Freestream drag force
F_g	Gravitational force
F_L	Lift force
F^s	Resistance coefficient for drag
F_T	Total adhesion force
f_d	Drag shape factor
f_d^∞	Freestream drag shape factors
f_L	Lift shape factor
f_M	Moment shape factor
g	Gravitational acceleration
H	Distance between particle centre and flat plate surface
h	Local distance of a surface element from the flat plate
$\boldsymbol{k}$	Unit vector directed toward the positive z-axis
k_B	Boltzmann constant
L	Separation distance between two parallel plates
l	Separation distance between the top and bottom plate of the laboratory flow cell
l_d	Lever arm for drag force
l_n	Lever arm for normal force
M	Moment exerted by drag
$\boldsymbol{n}$	Unit outward normal from the surface element
n_i	Number concentration of the ion species
O	Particle centre
Re_p	Particle Reynolds Number
r_e	Volume equivalent sphere radius
T	Temperature
T'	Additional couple that acts about the spheroid centre
T^s	Resistance coefficient for torque
U	Adhesion energy
V	Top wall velocity
v	Flow rate averaged velocity
v_o	Particle centre velocity
z_i	Valency of the ion species

Greek Symbols

α	Aspect ratio
β	Ratio of adhesion to drag force
$\dot{\gamma}_o$	Shear rate
ε_o	Permittivity of vacuum
ε_r	Relative permittivity of solvent
κ	Inverse Debye length
γ	Reduced surface potential
μ	Fluid dynamic viscosity
μ_s	Coefficient of static friction
ρ	Fluid density
ρ_p	Particle density
σ	Atomic collision distance
ν	Poisson ratio
ψ	Sphericity of cylinder
χ	Circularity of cylinder

Subscripts

Cyl	Cylinder
Sphd	Spheroid
vdw	Van Der Waals
edl	Electric double layer
cr	Critical
T	Total
1	Particle
2	Plane

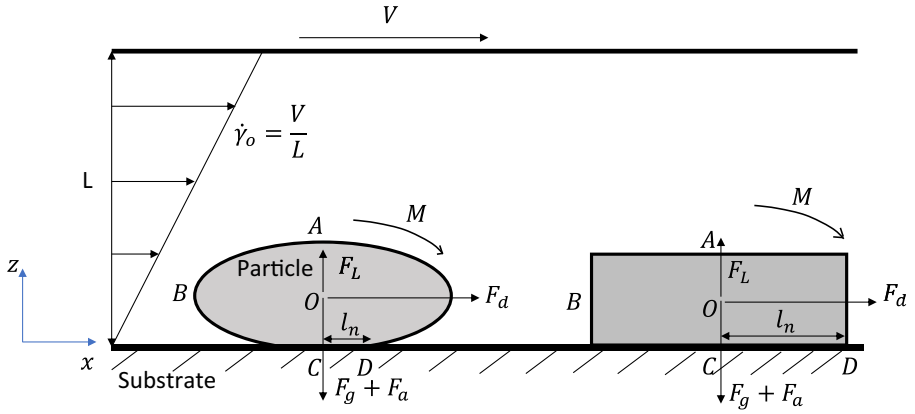

Fig 1. Torque balance for an oblate spheroid and a cylinder of aspect ratio, $\alpha = b/a$, adhered to a plane, under linear shear rate, $\dot{\gamma}_o$, from a Couette flow. The semi-major axis, a and semi-minor axis, b, are shown in the figure as OB and OA respectively. V is the top wall velocity, while L is the distance of separation between the two parallel plates. The four forces acting on the particle are drag, F_d, lift, F_L, adhesion force, F_a and gravity, F_g. M is the moment exerted by drag. The 4 forces generate 2 competing torques at pivot point D, through OC and CD, corresponding to the drag lever arm, l_d and normal lever arm, l_n respectively.

drag lever arm, l_d, while μ_s is the coefficient of static friction. Detachment is assumed to occur immediately when any one of the equilibria is disrupted.

$$\text{Rolling}: \quad M + F_L l_n > (F_g + F_a) l_n \tag{1}$$

$$\text{Sliding}: \quad F_d > \mu_s (F_g + F_a - F_L) \tag{2}$$

$$\text{Lifting}: \quad F_L > F_g + F_a \tag{3}$$

For a sphere particle attached to a wall under linear shear flows, F_d and M are given by O'Neill (1968) based on Stokes law, while F_L was derived by Leighton and Acrivos (1985). Similarly, for the adhesion force between a sphere and a plane, analytical expressions exist based on the Derjaguin-Landau-Verwey-Overbeek (DLVO) theory, which evaluates the adhesion force as the sum of van der Waals and electric double layer forces.

Though colloidal particles in natural porous media exist in irregular geometries, there are scarce literature on the impact of particle shape on their detachment behaviour. Experimental and numerical filtration studies have considered rods (Liu et al. 2010; Salerno et al. 2006; Seymour et al. 2013), barrels (Knappenberger et al. 2015), peanut shapes (Xu et al. 2008), buckled particles and ellipsoids (Torres-Díaz et al. 2019). The non-spherical particles were shown to exhibit noticeably different attachment and detachment rates compared with spherical particles. It is therefore evident that filtration models assuming particles as spheres would be insufficient to capture the actual filtration behaviour for irregular colloids.

However, filtration is a combination of various mechanisms, involving not only detachment but also attachment, as well as straining, bridging and near wall transport (Seymour et al. 2013; Vahidkhah & Bagchi 2015; Xu et al. 2008). Consequently, there were conflicting results from separate filtration studies, where high particle aspect ratios could either enhance (Salerno et al. 2006; Seymour et al. 2013) or reduce retention (Knappenberger et al. 2015; Liu et al. 2010) depending on the dominant mechanisms at play. Filtration studies are thus ineffective to study the impact of shape on solely the detachment behaviour.

Specific to detachment, Cerda (1987) modelled the DLVO interaction of kaolinite clays as plates, while Mahmood et al. (2001) consequently added half-cylinder edges to the plates to account for side-on attachment. By accounting for shape and orientation, the models were reported to be in good agreement with experiment results for kaolinite detachment in porous media formed by glass beads, under varying salinities and pH. However, the investigations considered only the impact of shape on the adhesion forces, claiming that the hydrodynamic forces of drag and lift are negligible (Cerda 1987). The validity of this omission has yet to be proven.

Similarly, Aramrak et al. (2013) considered the detachment of colloid particles of various shapes in the presence of two phases (gas and liquid), where capillary forces are dominant and are not applicable for one phase flows. Brambilla et al. (2017) presented adhesion force and aerodynamic models to study the turbulent wind resuspension of bacteria as a prolate spheroid, but remained inconclusive on how the combined effect of adhesion force and aerodynamics could impact their detachment. Decuzzi and Ferrari (2006) investigated the difference in adhesion between oblate spheroids and spherical drug carriers under laminar shear flows. It was concluded that for the same particle volume, spheres have lower adhesive strength and detach more readily than oblate spheroids. However, the adhesion force was provided by highly specific and selective ligand-receptor bonds present only in biological systems rather than the DLVO adhesion forces relevant to this study. Adhesion force was modelled using a stochastic approach rather than the conventional DLVO model. Consequently, their findings may not be applicable for the case of non-biological systems, such as the detachment of clays from petroleum systems.

The above brief analysis reveals that the mechanical equilibrium conditions for particles with complex geometry attached to a substrate in shear flows are not available. Specifically, there has yet to be any work done that systematically quantify the impact of the particle shape on both the hydrodynamic and adhesion forces towards the detachment of colloidal particles from a substrate.

Therefore, this paper aims to address this gap. The mechanical equilibrium conditions for particles with non-spherical geometries attached to a substrate in shear flows were studied. To focus on an application, the detachment of kaolinite particles from reservoir rocks was studied, where the kaolinite particles are modelled as either oblate spheroids or cylinder discs. We performed Computational Fluid Dynamics (CFD) modelling of shear flows around spheroid and cylinder particles attached to a plane. The empirical formulae for drag and lift versus aspect ratio of the bodies was subsequently derived.

Similarly, the DLVO adhesion forces for the spheroid and cylinder particles were evaluated using Surface Element Integration (SEI). The combined impact on detachment is investigated by using the equilibrium of forces and torques (EFT) criteria. The derived formulae exhibited results that differ significantly from those obtained for equivolume spherical particles. We also performed laboratory observations on the mobilisation of latex spheres in visualisation cells and applied the derived formulae for mechanical equilibrium to interpret the visual images/observations. The results of predictions closely match the experiment data. This study was constrained to favourable conditions only.

2. Theory

2.1. Geometry and flow configuration

The particles were attached to a plane and modelled as either an oblate spheroid or a cylinder, where their axis of symmetry is perpendicular to the plane, as shown in Fig. 1. OB is the semi-major axis, a and OA is the semi-minor axis, b. The size of the particle is defined by the volume equivalent sphere radius, r_e, while the shape is defined by the aspect ratio, $\alpha = b/a$. The particles were under linear Couette shear flow, perpendicular to the axis of symmetry (in the x-direction), with a shear rate of $\dot{\gamma}_o = V/L$, generated by moving the top plate at velocity, V and fixing the bottom plate. Consistent with flows in porous media, the study was constrained to Stokes flow, where $\mathrm{Re_p} \ll 1$ ($\mathrm{Re_p} = \rho\dot{\gamma}_o r_e^2/\mu$). ρ and μ are the fluid density and dynamic viscosity respectively. Particle centre velocity, v_o is given by $v_o = \dot{\gamma}_o b$, where $b = r_e\alpha^{2/3}$.

2.2. Gravitational force

The gravitational force is

$$F_g = \frac{4}{3}\pi r_e^3 g(\rho_p - \rho) \tag{4}$$

where g is the gravitational acceleration and ρ_p is the density of the particle (Bedrikovetsky et al. 2011).

2.3. Hydrodynamics

Hydrodynamic forces act to detach the particles from the substrate surface. The drag, F_d, lift, F_L, and moment, M for an oblate spheroid or cylinder are given as:

$$F_d = 6\pi\mu r_e^2\dot{\gamma}_o f_d \tag{5}$$

$$F_L = 9.22 r_e^4\dot{\gamma}_o^2\rho f_L \tag{6}$$

$$M = F_d l_d f_M \tag{7}$$

Equations (5) and (7) are based on the works of O'Neill (1968) and Equation (6) from Leighton and Acrivos (1985), for a sphere particle attached to a wall in linear shear flows. To extend the for-

mulation for non-spherical shapes, f_d, f_L and f_M are the drag, lift and moment shape factors added to account for the shape, as well as wall effects. For a sphere, $f_d = 1.7009$ and f_M = 1.37 (Hubbe 1984; O'Neill 1968), while $f_L = 1$ (Leighton & Acrivos 1985). Note that for convenience, Equation (7) was expressed in a different form to O'Neill and please refer to Hubbe (1984) for the derivation. In the Stokes regime ($Re_p \ll 1$), the shape factors are solely a function of the aspect ratio. An alternative approach to derive the approximate formulae for drag and lift is the method of asymptotic analogies in Navier-Stokes boundary layers (Polyanin & Dil'man 1990, 1994).

2.3.1. Computational Fluid Dynamics (CFD)

The hydrodynamic shape factors were determined by CFD, using the commercial software ANSYS/CFX. The simulation domain was based on the simulations by Derksen and Larsen (2011), where the length × width × height was $72r_e \times 24r_e \times 24r_e$. This domain was reported to be adequate to capture the physical behaviour of the flow, based on their domain sensitivity studies for a single sphere on wall (Derksen & Larsen 2011). The CFD model consists of a Couette flow, with the top wall moving at a constant velocity, V, to generate a linear shear flow. The mesh next to the surface of the particle was refined to accurately capture the high gradient flow near the solid boundary. The top wall was set to move at a velocity, $V = 0.05$ m/s in the x-direction to create a shear flow. Similarly, periodic boundaries were applied at both ends of the domain boundaries in the x-direction. No-slip condition was implemented for the bottom wall and the particle surface, while the two vertical sides of the domain that are parallel to the flow were assigned symmetry boundary conditions. All the flows are in the laminar regime and therefore the laminar solver was used throughout the investigation.

2.3.2. Verification

To test the accuracy of the CFD results, the shape factors calculated were compared with literature values for freestream drag. Analogous to Equation (5), the drag force for an object in unbounded flow, F_d^∞, is a function of the freestream drag shape factors, f_d^∞ as shown in Equation (8). Equation (8) is applicable for both spheroids and cylinders, with their shape factors expressed as (9) and (10), respectively. Loth (2008) presented the $f_{d,Sphd}^\infty$ for oblate spheroids based on the analytical expressions by Oberbeck (1876), given by Equation (9). Similarly, Clift et al. (1978) provided the $f_{d,Cyl}^\infty$ for cylinders in freestream by fitting experimental data, formulated as (10).

$$F_d^\infty = 6\pi\mu r_e v_0 f_d^\infty \tag{8}$$

$$f_{d,Sphd}^\infty = \frac{\frac{8}{3}\alpha^{-\frac{1}{3}}(\alpha^2-1)}{\alpha - \frac{(3-2\alpha^2)(\cos^{-1}\alpha)}{\sqrt{(1-\alpha^2)}}} \tag{9}$$

$$f_{d,Cyl}^\infty = \frac{1}{\chi\sqrt{\psi}} e^{0.576\sqrt{\psi\chi}(\chi-1)} \tag{10}$$

where ψ and χ are the sphericity and circularity of the cylinder, respectively, given by $\psi = \frac{(18\alpha^2)^{\frac{1}{3}}}{2\alpha+1}$; $\chi = \left(\frac{3}{16}\right)^{\frac{1}{3}}\alpha^{-\frac{1}{6}}\sqrt{\pi}$. Note that for linear shear flows, both Equations (9) and (10) are solely a function of aspect ratio, α. The axis of symmetry for both the oblate spheroids and cylinders is perpendicular to the direction of flow.

2.4. Adhesion force

Adhesion force, F_a between the particle and the plane wall was determined using DLVO theory, where the total adhesion energy, U_T is the sum of the van der Waals, U_{vdw} and electric double layer, U_{edl} interactions (Derjaguin & Landau 1941; Verwey & Overbeek 1948). Born repulsion was added to account for reversible deposition at the primary minimum (Ruckenstein & Prieve 1976), leading to:

$$U_T = U_{vdw} + U_{edl} + U_{born} \tag{11}$$

The total adhesion force, F_T was obtained through the derivative of the total adhesion energy, as shown by (12). The analysis was limited to favourable conditions, where there is no repulsive energy barrier arising from the electric double layer force. Hence, the value of adhesion force, F_a used for the detachment analysis (Equations (1), (2) and (3)) was taken from the primary minimum.

$$F_T = -\frac{dU_T}{dD} \tag{12}$$

To account for non-spherical shapes, the Surface Element Integration (SEI) method was used (Bhattacharjee & Elimelech 1997). Fig. 2 shows the SEI configuration for an oblate spheroid and a cylinder. As the particle approaches the plane wall, the van der Waals force continues to attract it up to an equilibrium distance, where the stronger, short-ranged repulsive electric double layer and Born repulsion forces act to prevent further proximity.

The general SEI formulation for an arbitrary particle shape is given as (Bhattacharjee & Elimelech 1997):

$$U = \iint E(h)\frac{\boldsymbol{n}.\boldsymbol{k}}{|\boldsymbol{n}.\boldsymbol{k}|}dxdy, \tag{13}$$

where U is the interaction energy of the particle with the infinite plate. $E(h)$ is defined as the interaction energy per unit area between 2 parallel infinite plates separated at a distance h. For an oblate spheroid, its surface can be described using (14),

$$z = b\sqrt{1-\frac{r^2}{a^2}}; H = D + b; h = H - z. \tag{14}$$

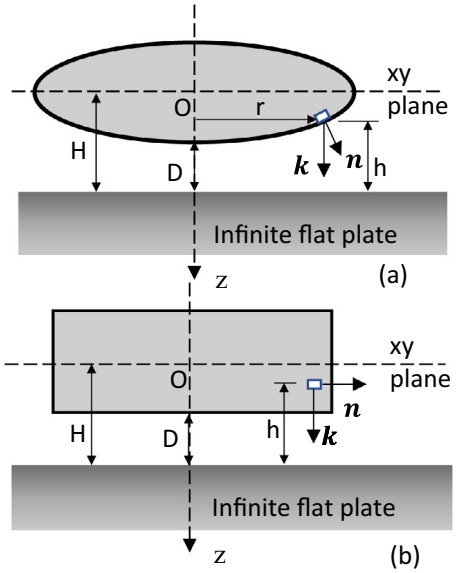

Fig 2. SEI configuration for (a) an oblate spheroid and (b) a cylinder. H is the distance between the particle centre, O from the flat plate surface, while h is the local distance of a surface element from the flat plate. D is the distance of closest approach between the particle and the plane. **n** is the unit outward normal from the surface element and **k** is the unit vector directed toward the positive z-axis. The separation distance is in the scale of nanometers, so the particle is effectively touching the wall in macroscale.

Substituting (14) into (13) gives the SEI equation (15) for determining the adhesion energy of an oblate spheroid with an infinite flat plate, U_{Sphd} in radial coordinate system as shown in Fig. 2. Equation (15) was solved numerically using MATLAB.

$$U_{Sphd} = 2\pi \int_0^a \left[E\left(H - b\sqrt{1-\frac{r^2}{a^2}}\right) - E\left(H + b\sqrt{1-\frac{r^2}{a^2}}\right)\right] rdr \quad (15)$$

Similarly, using SEI for a cylinder and an infinite flat plate, Wu et al. (2013) give the expression

$$U_{Cyl} = \pi a^2 [E(D) - E(D+2b)]. \quad (16)$$

As SEI scales the interaction between two infinite flat plates to that of any arbitrarily shaped particle with an infinite flat plate, the expressions for $E(h)$ are required for the van der Waals, electric double layer and Born repulsion forces, expressed by (17), (18) and (19), respectively (Gregory 1975; Israelachvili 2011; Mahmood et al. 2001).

$$E_{vdw} = -\frac{A_h}{12\pi h^2}, \quad (17)$$

$$E_{edl} = 32\varepsilon_o \varepsilon_r \kappa \gamma_1 \gamma_2 \left(\frac{k_B T}{ze}\right)^2 \exp(-\kappa h), \quad (18)$$

$$E_{born} = \frac{A_h \sigma^6}{360\pi h^8}, \quad (19)$$

where A_h is the Hamaker constant, ε_o the permittivity in vacuum, ε_r the relative permittivity of the solvent, k_B the Boltzmann constant, T temperature, z valency, and e is the charge of an electron. κ is the inverse Debye length given by $\kappa = \sqrt{\frac{e^2}{\varepsilon_o \varepsilon_r k_B T} \sum z_i^2 n_i}$ where z_i and n_i are the valency and number concentration of the i-th ion species present in the solution. $\gamma_j = \tanh\left(\frac{ze\zeta_j}{4k_B T}\right)$, with ζ corresponding to the zeta potential. Subscripts j = 1, 2 denote the particle and plane respectively. σ is the atomic collision constant.

Eqns. (17)-(19) assume instant dependency of the electrostatic energy on ionic strength and pH of brine in thin separation particle–substrate layer. Molecular diffusion from the bulk flow in a pore towards the attached fine can result in significant delay between the brine compositions in the separate layers and the overall fluid (Russell & Bedrikovetsky 2018). The delay equation for adhesion force substitutes an explicit energy expression in the cases where the delay effects are significant (Polyanin et al. 2018; Polyanin & Zhurov 2015).

2.7. Lever arm

Hertz contact theory was used to determine the radius of the contact deformation area for a sphere and a plane (Johnson 1985), which was used as l_n. For an oblate spheroid and a plane, Hertz theory was expressed as (20). $E_Y{}^*$ is the effective Young's modulus determined through (21).

$$l_n = \sqrt[3]{\frac{3(F_a + F_g - F_L)b}{4E_Y{}^*}}, \quad (20)$$

$$\frac{1}{E_Y{}^*} = \frac{1-\nu_1^2}{E_{Y1}} + \frac{1-\nu_2^2}{E_{Y2}}, \quad (21)$$

where ν is the Poisson's ratio and E_Y, the Young's modulus of elasticity. Subscripts 1 and 2 denote the particle and surface, respectively. In the case of a thin cylinder, the adhesion force is applied through the centre of the circle, i.e. $l_n \equiv a$ (refer Fig. 1). It was assumed that the vertical deformation of the particle is negligible, such that $l_d \equiv b$.

2.8. Poiseuille shear flow correlation

As the data from numerical modelling were in terms of the particle centre velocity, v_o, the Poiseuille flow equation was used, expressed in terms of experiment parameters, for direct comparison with laboratory flow rates (Sharma et al. 1991).

$$v_o = 6v\left(\frac{b}{l}\right)\left[1 - \left(\frac{b}{l}\right)\right], \quad (22)$$

where v was the flow rate averaged velocity used in the lab, and l was the separation distance between the top and bottom plate of the laboratory flow cell.

3. Laboratory study: flow visualisation experiment

3.1. Materials and set-up

The carrier fluid was prepared by the dissolution of sodium chloride in deionized water; salinity was 0.3 M; pH was 3. The salinity and pH were fixed for the entire experiment. The bottom of the visualisation cell was a glass coverslip previously soaked in acetone with further rinsing in ethanol and deionized water. The sizes of the flow cell were 48.2 mm × 5 mm × 0.15 mm. The Ibidi's visualisation cell was used (Ibidi 2018) with hydrophilic carboxylate microsphere particles of 3 μm radius (Polysciences 2018). The software Dot-count v1.2 (LCLN 2012) was used to quantify the number of particles attached to the solid surface from the photo images in each step of the test.

Referring to Fig. 3, the set-up for photographing and filming of the cell bottom with the attached particles consisted of the syringe pump, the visualisation cell placed under optical microscope, and PC for displaying the images from the microscope in real time. The optical microscope was equipped with Soft Imaging System's Colorview III camera and AnalySIS Life Sciences software to control the camera. In addition, the particles inside the channel can be viewed with 100x, 200x, or 500x magnification using the micro-imaging Stream Essentials software. Further details of the experiment are reported in Chequer et al. (2019) and Chequer et al. (2021).

3.2. Methodology of visualisation experiments

The electrophoretic mobilities/streaming potentials for the glass coverslip and the latex spheres, immersed in the carrier brine, have been measured using Zetasizer Nano Z (Malvern 2013). The values of zeta potentials were calculated using the Smoluchowski approximation (Israelachvili 2011).

Saturation of the cell by the attached particles had been performed by the particle suspension with concentration 300 ppm under lower velocity $2.2\text{x}10^{-5}$ m/s. 25 PV (pore volumes) were injected to achieve the initial saturation. DLVO calculations of maximum adhesion force and estimates of the drag indicate that the above-mentioned saturation conditions correspond to particle attachment to the substrate. Besides, the energy profile for the particle–substrate interaction contains primary energy minimum only, so the attachment occurs under favourable conditions.

After the initial saturation, 10 tests were performed with varying velocity, which were increased from one step to another in order to induce particle detachment. The velocity values varied from $v = 2.2 \times 10^{-5}$ m/s to 2.2 m/s in 10 incremental steps. We flushed 25 PV at each step. An average number of attached parti-

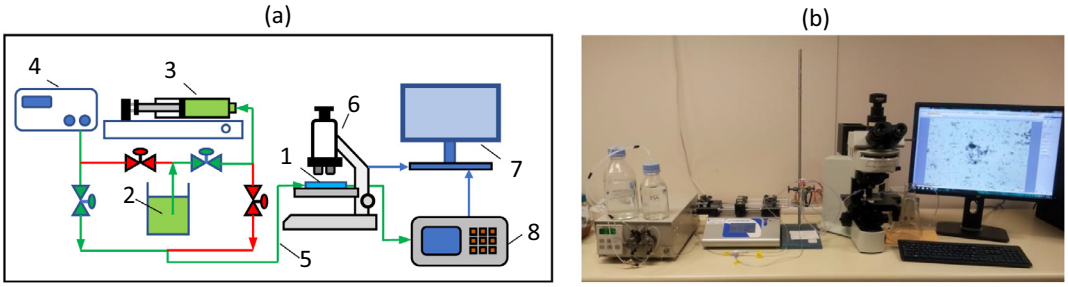

Fig 3. Laboratory setup. (a) Schematic of the setup with 1: parallel plate flowthrough cell, 2: injected solution, 3: syringe pump, 4: HPLC pump, 5: plastic tubing, 6: optical microscope, 7: display monitor, 8: particle counter. (b) Photo of the setup (Chequer et al. 2019).

cles was used to evaluate particle detachment. Videos were taken at the beginning of every change in flow velocity. Particle detachment can be visualised directly with the microscope, effectively identifying the corresponding conditions leading to the detachment, for comparison with theory.

4. Results

4.1. Hydrodynamics

4.1.1. CFD basecase validation and sensitivity

The basecase sphere-on-wall model was first verified with values from literature to test the validity of the CFD parameters by comparing the shape factors as presented in (5), (6) and (7).

From Table 1, it was shown that the effect of the CFD mesh size on the predicted forces is negligible for the medium and fine meshes. The CFD results of the fine mesh have a good agreement (deviation <0.3%) with the drag and moment shape factors from literature. Thus, the fine mesh setting was used for all the subsequent runs. The discrepancy between the simulated lift values and the values from literature (Leighton & Acrivos 1985) is up to 4%. However, it was shown in Table 3 that the magnitude of lift was consistently 3 orders of magnitude lower than drag and was therefore omitted. Also, the popular Saffman lift (Saffman 1965) formulated for shear flows in an infinite domain was inapplicable for this wall bounded case (Henry & Minier 2014), showing an underestimation of 89% when compared to the CFD lift results.

In addition, the validity of the shape factors for a sphere-on-wall was examined over a wide range of particle Reynolds number as shown in Fig. 4. The plots should converge to f_d = 1.7009, f_L=1 and f_M = 1.37 as detailed in Table 1. The shape factors were constant below Re_p < 0.1, above which, there is noticeable deviation. This agrees with the literature, reporting the validity of Stokes law to a maximum of Re_p = 0.1 (Bird et al. 2001).

Lastly, to test the validity of the CFD spheroid models, Table 2 shows the match between the CFD and the values from Hsu and Ganatos (1989) for an oblate spheroid at a small distance away from a plane wall. In Table 2, F^s and T^s are defined as

$$F_d = 6\pi\mu a H \dot{\gamma}_o F^s, \tag{23}$$

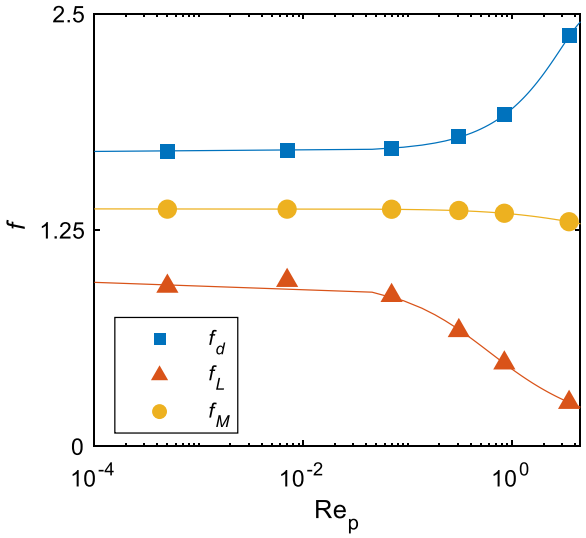

Fig 4. Sensitivity of drag, f_d, lift, f_L, and moment, f_M shape factors to different particle Reynolds number, for a sphere-on-wall subjected to different shear rates, $\dot{\gamma}_o$.

$$T' = 4\pi\mu a^3 \dot{\gamma}_o T^s, \tag{24}$$

where H is the distance between the spheroid centre and plane; F^s and T^s are the resistance coefficients for drag and torque, respectively. T' is the additional couple that acts about the spheroid centre due to wall effects that would otherwise be absent in an unbounded flow. Once again, there is close agreement between the CFD results and the results from literature, with a maximum deviation of 1.13% for the range considered.

4.1.2. Drag shape factor, f_d

CFD simulations were conducted for the spheroids and cylinders, where r_e was held constant at 3 μm, whilst changing a and b to achieve the desired aspect ratio. Table 3 shows the CFD results for the equivolume spheroid shapes with varying α.

For the drag shape factor, Fig. 5 compares the f_d for particles attached to a wall, to the freestream drag shape factors, f_d^∞.

Table 1
Impact of varying CFD basecase mesh sizes on the drag, lift and moment shape factors for a sphere-on-wall.

Mesh Size	Number of Mesh Nodes	f_d			f_L			f_M		
		CFD	O'Neill	Deviation	CFD	Leighton & Acrivos	Deviation	CFD	O'Neill	Deviation
Fine	4,136,524	1.7056	1.7009	0.28%	0.9600	1	−4.00%	1.3697	1.37	−0.02%
Medium	1,370,082	1.7061		0.31%	0.9657		−3.43%	1.3695		−0.04%
Coarse	630,852	1.7067		0.34%	1.0415		4.15%	1.3691		−0.06%

Table 2
Validation of CFD spheroid drag and torque factor with Hsu and Ganatos (1989) for a spheroid at a small distance, H/a, from a plane wall.

α	H/a	F^s	F^s_{CFD}	Deviation	T^s	T^s_{CFD}	Deviation
0.1	1.1	0.832	0.841	1.13%	0.1014	0.1020	0.50%
0.5	0.55	1.576	1.583	0.46%	0.3055	0.3064	0.28%

Table 3
CFD simulation results for an oblate spheroid-on-wall at 6 different aspect ratios under $\dot{\gamma}_o$ = 694 1/s. The drag of a spheroid comprises the pressure and friction components, with their respective magnitude and percentage contribution as shown. The calculated F_d, F_L and M were used to infer the shape factors using (5),(6) and (7). r_e = 3μm.

Geometry		Drag Components				Drag		Lift		Moment	
α	Surface Area (1×10^{-10} m^2)	Pressure (1×10^{-11} N)	Pressure (%)	Friction (1×10^{-10} N)	Friction (%)	F_d (1×10^{-10} N)	f_d	F_L (1×10^{-13} N)	f_L	M (1×10^{-16} Nm)	f_M
1	1.13	6.42	36%	1.14	64%	1.79	1.706	3.45	0.960	7.35	1.370
0.5	1.24	3.74	27%	1.00	73%	1.38	1.317	2.17	0.604	3.88	1.489
0.25	1.61	2.29	18%	1.03	82%	1.26	1.202	1.68	0.468	2.79	1.863
0.1	2.70	1.30	9%	1.29	91%	1.42	1.353	1.84	0.513	3.20	3.495
0.05	4.21	0.94	5%	1.70	95%	1.79	1.710	2.08	0.580	5.04	6.908
0.025	6.63	0.72	3%	2.40	97%	2.47	2.355	3.45	0.961	8.93	14.104

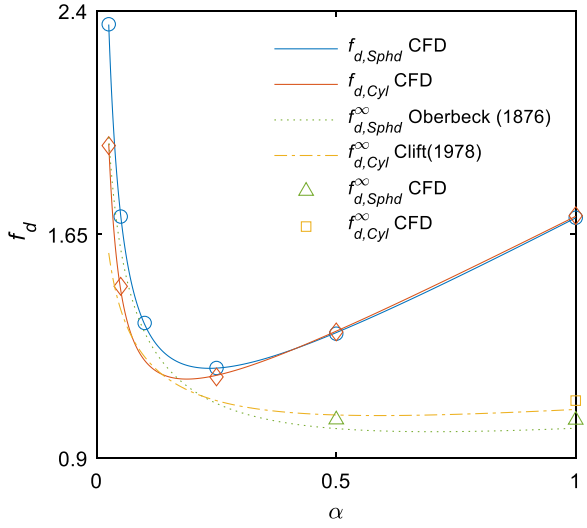

Fig 5. CFD drag shape factors, $f_{d,}$ for spheroids and cylinders of varying aspect ratios, α fixed on a plane. The CFD results were compared to freestream drag shape factors, f^∞_d by Oberbeck (1876) and Clift (1978). Solid lines are for particles touching the wall while dashed lines represent particles in freestream. Subscripts 'Sphd' and 'Cyl' denotes spheroids and cylinders, respectively. Solid lines are fitted through the CFD simulated (○ and ◇) points, between $0.025<\alpha<1$. CFD freestream drag data $f^\infty_{d,Sphd}$ CFD and $f^\infty_{d,Cyl}$ CFD was also plotted as a validation.

The main result shown is that the drag for spheroids and cylinders are non-monotonic with α. The slight non-monotonic trend (not apparent in the graph) in f^∞_d was amplified when the particles are touching a wall. For f_d at $\alpha = 1$, it initially reduces with decreasing α, followed by a rapid increase again when $\alpha < 0.24$ (spheroid) and $\alpha < 0.19$ (cylinder), eventually exceeding the f_d for a sphere. The cylinder with a higher initial f^∞_d at $\alpha = 1$ is exceeded by spheroid drag when $\alpha \to 0$. This overlapping behaviour is reproduced in the wall-bounded case. Modelling spheroids and cylinders as spheres could cause an underestimation of up to 32% and overestimation by 38% depending on the aspect ratio. If $\alpha < 0.025$, the underestimation could be even higher.

In Fig. 5, the CFD simulated $f^\infty_{d,Sphd}$ and $f^\infty_{d,Cyl}$ for α = 1 & 0.5 showed a maximum deviation of 3% when compared with theoretical freestream values from Oberbeck (1876) and Clift (1978). Overall, there were only slight variations in f_d between spheroids and cylinders when $\alpha > 0.3$. The impact of geometry on f_d only becomes significant when $\alpha < 0.3$.

The lines of best fit for $f_{d,Sphd}$ and $f_{d,Cyl}$, at $0.025 \le \alpha \le 1$ are given by (25) and (26) as

$$f_{d,Sphd} = (0.8707\alpha^2 + 0.7908\alpha + 0.05844)(\alpha + 0.008453)^{-1} \quad (25)$$

$$f_{d,Cyl} = (0.8306\alpha^2 + 0.8525\alpha + 0.03278)(\alpha + 0.00294)^{-1} \quad (26)$$

To investigate the non-monotonic drag behaviour of the particles, the $F_{d,Sphd}$ determined from CFD was categorised further into friction and pressure drag, as shown in Fig. 6. It was evidenced that the non-monotonic trend in F_d originates from the friction drag component (purple dotted lines). From Fig. 6(b), as expected, the friction drag generally increased with surface area, except for the transition between sphere to spheroid at $\alpha = 0.5$. It is speculated that for $0.5 < \alpha < 1$, though the normalised surface area decreases with increasing α (dotted purple line), the friction drag increases nevertheless, due to the increased velocity difference between the spheroid surface and the fluid.

4.1.3. Lift shape factor, f_L

As shown in Table 3, the magnitude of F_L was consistently 3 orders of magnitude lower than F_d for all ranges of α, in agreement with literature values (Chequer & Bedrikovetsky 2019). Therefore, f_L was excluded from the subsequent analysis.

4.1.4. Moment shape factor, f_M

The f_M values for spheroids and cylinders are presented in Fig. 7. Modelling the torque of spheroids and cylinders as spheres could cause an underestimation of up to 21.5% and overestimation by 63.2% depending on the aspect ratio. The lines of best fit for f_M are given as:

$$f_{M,Sphd} = (1.296\alpha^2 + 0.1509\alpha + 0.03718)(\alpha^2 + 0.0843\alpha + 0.0002284)^{-1} \quad (27)$$

$$f_{M,Cyl} = (0.05955\alpha^2 + 1.337\alpha + 0.3813)(\alpha + 0.1358)^{-1} \quad (28)$$

4.2. Adhesion force, F_a

The results presented were all for latex (r_e = 3 μm) on glass in NaCl solution, where the Hamaker constant was evaluated to be 1.46×10^{-20} J (Israelachvili 2011). Three discrete values were used for the salinity (0.1, 0.3 and 0.6 Mol NaCl) and pH (3, 7 and 9) in the

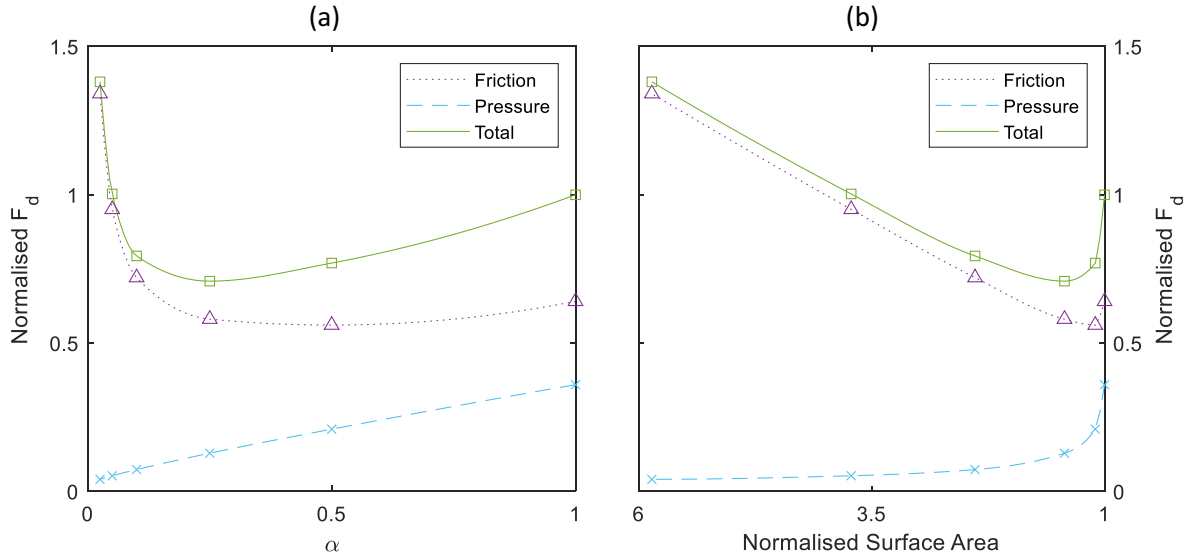

Fig 6. Breakdown of the spheroid drag force components into friction and pressure drag. The drag force was normalised against the total drag for a sphere and plotted as both a function of (a) aspect ratio and (b) spheroid surface area normalised by the surface of a volume equivalent sphere. Note the reversed axis for the normalised surface area.

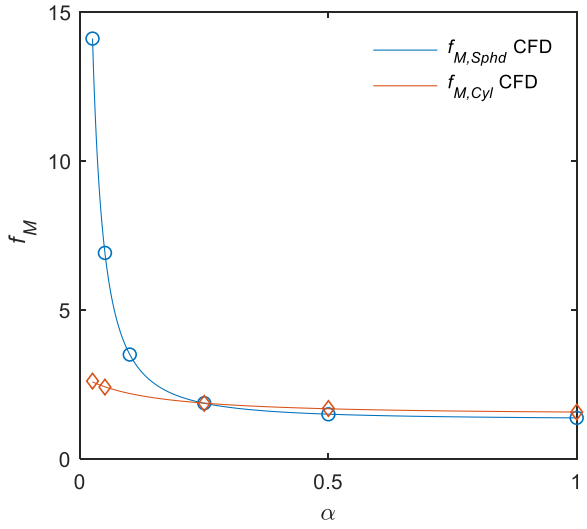

Fig 7. CFD predicted moment shape factors, $f_{M,Sphd}$ and $f_{M,Cyl}$ for spheroids and cylinders of varying aspect ratios. Solid lines are fitted through the simulated CFD points, between $0.025<\alpha<1$.

investigation. The salinity and pH were chosen such that they provide favourable conditions.

4.2.1. DLVO profile

Referring to Figure 8, there is a considerable variation in the primary minimum with changing α, ranging from $F_a = 2.9 \times 10^{-8}$ to 1.3×10^{-5} N for spheroids and $F_a = 1.1 \times 10^{-4}$ to 2.5×10^{-3} N for cylinders. For all α, the maximum adhesion force for spheroids and cylinders occurred when D = 3.67 Å and 4.29 Å, respectively. Hence, it was shown that cylinders, though separated slightly further from the collector, have consistently stronger F_a compared to spheroids, regardless of α. Decreasing α has the effect of exposing more particle surfaces closer to the plane, causing a higher attraction for both spheroids and cylinders.

4.2.2. Impact of salinity

The impact of salinity on F_a is shown in Fig. 9. Using the hydrodynamic shape factors determined from Section 4.1, the calculated F_a was normalised against F_d. From the range of salinities considered, the overlapping lines for both spheroids and cylinders suggest that F_a was independent of the change in salinity under favourable conditions. This independence can be attributed to the minimal change in zeta potentials in high salinity conditions.

4.2.3. Impact of pH

Similarly, the impact of pH is shown in Fig. 10. Unlike salinity, pH caused a modest variation in F_a values when changing from acid (pH3) to alkaline (pH 11) conditions. At 0.6 Mol, high pH causes a decrease in F_a, due to the stronger electric double layer repulsion force.

4.3. Phase diagrams

4.3.1. Modes of detachment: spheroid vs cylinder

Though there were 3 modes of detachment, the detachment by lifting is omitted since lifting is the least likely mode of detachment due to its small magnitude of around 3 orders lower than F_d.

Fig. 11 incorporates both the results for hydrodynamics and adhesion forces to determine the critical particle centre velocity for detachment, $v_{o,cr}$ for various α. The $v_{o,cr}$ was determined by solving for $\dot{\gamma}_o$ in (1) and (2). μ_s between latex and glass was taken to be 0.5 (Zoeteweij et al. 2009). The critical detachment velocity plot for cylinders was not presented as the range of $v_{o,cr}$ were in the range of 100–10000 m/s. These velocities far exceeded the validity range of Re < 0.1 for the CFD shape factors in this investigation and is also non-physical in underground porous media flows. However, the detachment velocity plot for cylinders still yielded some qualitative information.

Firstly, spheroids and cylinders are most likely to detach through rolling and sliding, respectively. This was because the lever arm for the detachment torque was much greater (i.e $l_n < l_d$) for spheroids, consequently favouring rolling detachment (refer Section 2.5). Cylinders were also more resistant to detachment in general, requiring a much higher range of $v_{o,cr}$ regardless of rolling or sliding when compared to spheroids, due to the combined impact of its higher F_a, lower F_d and M, and also $l_n > l_d$.

Secondly, it is crucial to account for the shape impact in both the hydrodynamic force and adhesion force. Sections 4.1.2 and 4.1.4 have shown that modelling spheroids and cylinders as

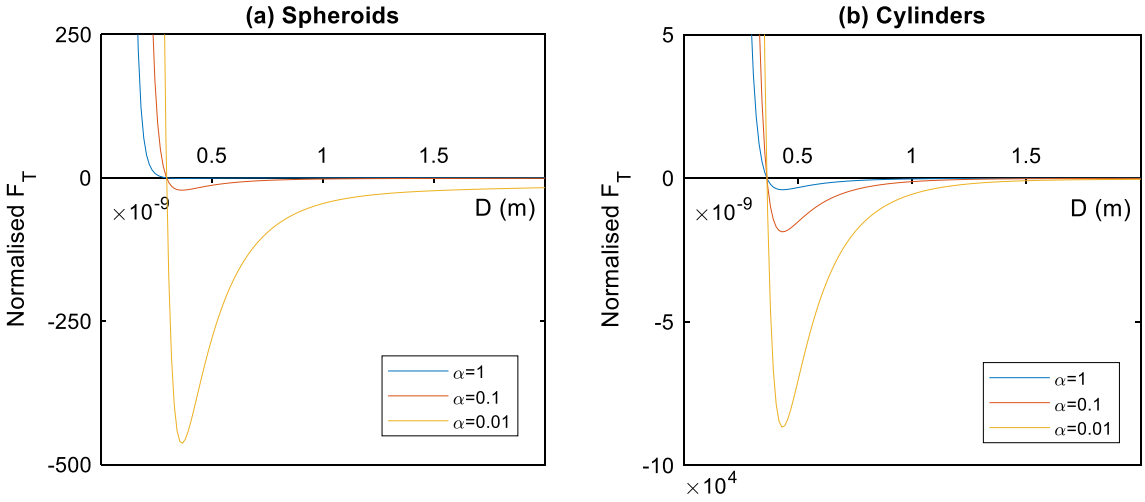

Fig 8. DLVO adhesion force profile with varying distance of closest separation, D and aspect ratios for a latex-glass system at 0.3 Mol, pH 7 and r_e = 3μm. The total adhesion force, F_T was normalised against the maximum adhesion force for a sphere. The primary minima at 3 different aspect ratios (α =1, 0.1 and 0.01) were plotted for (a) spheroids and (b) cylinders. Analysis for different aspect ratios are done by holding the volume of the particles constant while varying a and b. (Note the difference in magnitude of the F_T axis between spheroids and cylinders).

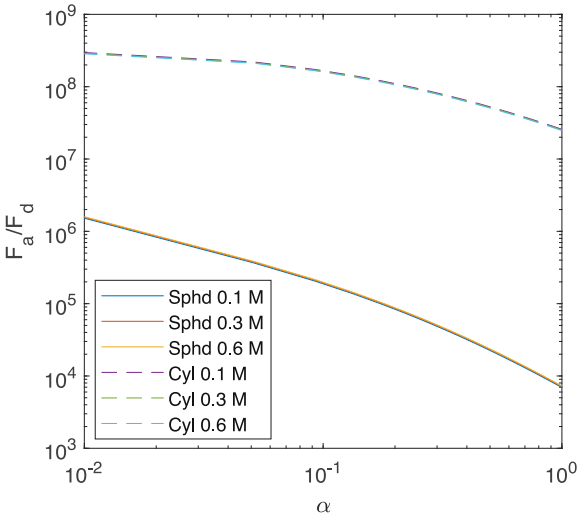

Fig 9. Impact of salinity on the normalised adhesion force, F_a/F_d of spheroid (—) and cylinder (– –) particles with varying aspect ratio. F_a has been normalised with the drag force, F_d where the $\dot{\gamma}_o$ =20 s^{-1}. The conditions were kept constant at pH 3 in a latex-glass system and r_e = 3μm. The plots at three different salinities all overlap for both spheroid and cylinders, showing no variation in F_a/F_d despite the salinity change.

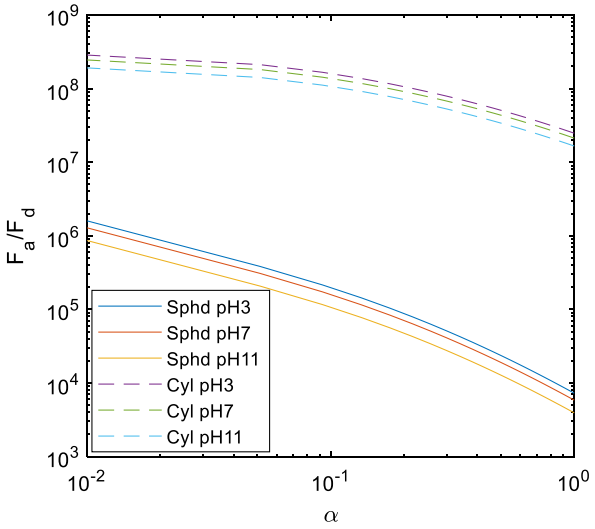

Fig 10. Impact of pH on the normalised adhesion force, F_a/F_d of spheroid (—) and cylinder (– –) particles with varying aspect ratio. F_a has been normalised with the drag force, F_d, where the $\dot{\gamma}_o$ =20 s^{-1}. The conditions were kept constant at 0.6 Mol in a latex-glass system and r_e = 3 μm.

volume equivalent spheres can both underestimate and overestimate hydrodynamic forces to significant percentages, which was manifested in the deviations of critical flow velocities for spheroids (dotted lines vs solid lines in Fig. 11). Using the uncorrected model (dotted lines), the detachment velocity was initially underestimated and consequently overestimated towards smaller aspect ratios. For rolling, the $v_{o,cr}$ is overestimated by up to an order of magnitude at $\alpha = 0.025$ for spheroids. Based on the corrected model (solid lines), the $v_{o,cr}$ for spheroids could vary up to 1733% (rolling), depending on α when compared to a sphere.

4.3.2. F_a/F_d approximation for rolling

Specific to rolling detachment in spheroids, Equations (1) and (7) could be simplified by omitting F_L and F_g due to the small size of colloids (Chequer & Bedrikovetsky 2019), leading to

$$\frac{F_a}{F_d} = \frac{f_M l_d}{l_n} \tag{29}$$

Hence, β, which is defined as F_a/F_d is proposed as a dimensionless parameter for characterising rolling detachment. Let $\beta_{cr} = F_{a,cr}/F_{d,cr}$, which is the ratio of the critical adhesion force to critical drag at incipient rolling detachment. A high β_{cr} value reflects conditions (salinity, pH and velocity) that cause particles to be easily detached by hydrodynamic torque and vice versa. Rolling detachment occurs when $\beta < \beta_{cr}$. From Fig. 9, it was shown that F_a/F_d was independent of salinity. Accordingly, Fig. 12 shows the calculated β_{cr} using CFD and SEI results, as a function of α at 3 different pH.

β_{cr} is consistently the highest at pH 11 when compared with pH 3 and pH 7. It was demonstrated in Fig. 10 that pH 11 yields the lowest F_a compared to pH 3 and pH 7. Consequently, to prevent rolling detachment in pH 11, F_d must be much lower than F_a, leading to high β_{cr}. Separately, β_{cr} is highest at $\alpha = 1$, regardless of

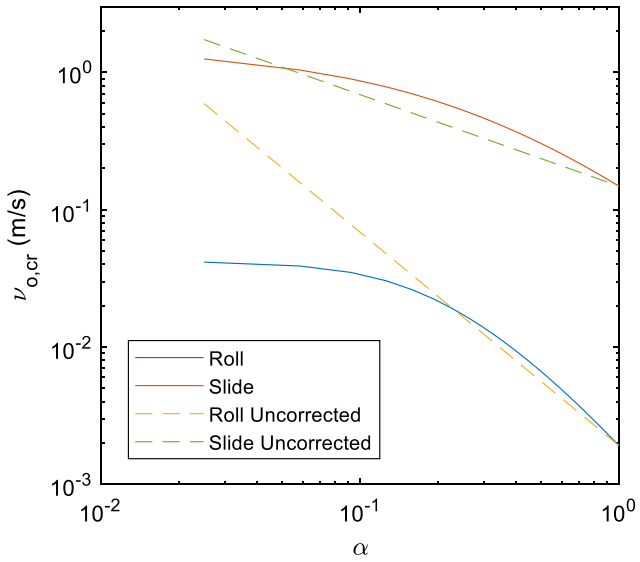

Fig 11. The impact of considering the hydrodynamic variation with varying aspect ratio for spheroids. $v_{o,cr}$ is the critical particle centre velocity required for either rolling or sliding detachment based on Expressions (1) and (2). The 'uncorrected' (– –) data is plotted by accounting for aspect ratio in the adhesion force only. As for hydrodynamics in the uncorrected case, the drag and moment for a volume equivalent sphere was used, regardless of the aspect ratio (i.e f_d = 1.7009 and f_M = 1.37 for all aspect ratios). This was for latex on glass, 0.3 M, pH 7 and $r_e = 3\mu$m.

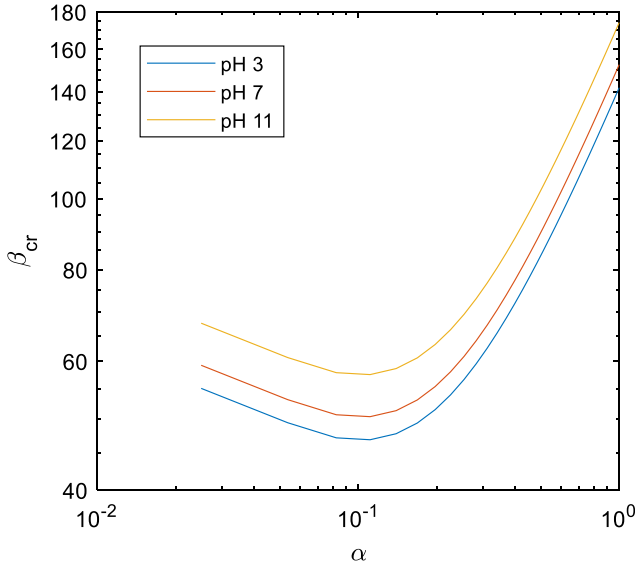

Fig 12. Critical adhesion force to drag ratio, $(\beta_{cr} = F_a/F_d)$ for the initiation of spheroid rolling detachment. Data was for latex on glass system at $r_e = 3\mu$m, 0.6 Mol NaCl in three different pH.

salinity and pH, implying that spheres are the easiest to detach by hydrodynamic torque compared to any other aspect ratios studied in the current paper. Interestingly, below $\alpha = 0.1$, the β_{cr} increases again with decreasing α. Also, though F_a changes by orders of magnitude with α (Section 4.2.1), the greater lever arm for drag (l_d) compared with l_n allows the lesser variation in F_d to be amplified with comparable effect on rolling detachment. Since F_a exhibit monotonic behaviour with α, the non-monotonic trend in β_{cr} originates from F_d.

4.4. Comparison between modelling and laboratory visualisation

Fig. 13 shows the direct visualisation for a spot on the glass slide, subjected to varying flow rate averaged velocity, v. Red circles mark particles that would disappear in the next image frame. For example, some particles from the four clusters marked in (a) are no longer apparent in frame (b). Particle detachments occurred immediately in the first velocity increment from 2.2×10^{-5} to 2.2×10^{-4} m/s, as shown in frames (a) to (b). However, it was observed that they were not strictly single sphere-on-wall detachments as modelled in Fig. 1. Rather, the premature detachments occurred quite likely by detaching from clusters, rather than the glass surface. This was further supported by the absence of detachment from particles that exist as a single particle until frame (e). Premature detachment from clusters could be explained by the adhesion force between the latex-latex particles, which are weaker compared to the latex-glass system (Chequer et al. 2019). Upon the initiation of single particle detachment, the subsequent frames all exhibit detachment at ever increasing rates. It was hence concluded that single particle detachment occurred only from frame (e) onwards. Separately, above the values of $v = 2.2 \times 10^{-1}$ m/s, almost no single particles are left, except for clustered particles which are noticeably more resistant to detachment.

The laboratory observations were compared against the proposed torque and force equilibrium model, as shown in Fig. 14, which was plotted to quantitatively predict the critical detachment velocity required for single particle detachment in the labs.

At the data point where the sphere radius was $3\mu m$, it was shown that single particle-on-wall detachment in the experiment occurred only when exceeding the theoretical rolling critical flow velocity of 0.023 m/s. In further agreement, laboratory observations by Chequer et al. (2021) reported the detachment of $5\mu m$ latex spheres when $v = 0.022$ m/s. This is expected since Fig. 14 predicts a critical detachment velocity of 0.012 m/s. Hence, the presented EFT model and the input parameters used are considerably accurate in quantitatively predicting particle detachment.

5. Discussions

The shape factors from CFD were only valid for $Re_p < 0.1$. For Fig. 11, it should be noted that the $v_{o,cr}$ values correspond to Re_p that exceeded the range of validity for the CFD shape factor results ($Re_p < 0.1$), with Re_p up to 44 for spheroids (sliding) and 5.6×10^5 for cylinders (rolling). Fig. 4 has shown that f_d and f_M increases and decreases respectively with higher Re_p. Hence, the predicted detachment trend might be invalid. For example, at $Re_p = 1$, the drag for a sphere-on-plane was underestimated by around 13% (Fig. 4). Therefore, further flow investigation in the higher Re_p regime is required, where the Stokes law is no longer valid. However, the dominant detachment mechanism for spheroids is rolling. Re_p corresponding to the spheroid rolling $v_{o,cr}$ was up to 1.45 at $\alpha = 0.025$. A CFD simulation for the spheroid at $\alpha = 0.025$ under $Re_p = 1.4$ confirmed that there were only minor deviations within ± 2% in f_d and f_M when compared to Equations (25) and (27). Therefore, the main trend for the rolling detachment presented remains valid.

It was acknowledged that the laboratory experiments were only done on spherical particles, but it served to validate the methodology and input parameters of the analysis. Furthermore, as presented in Table 2 and Fig. 5, a level of confidence in the CFD predicted hydrodynamic shape factors for the cylindrical and spheroidal particles has been obtained by validation against data from the literature. Nevertheless, the tests described in Section 3 can be repeated for non-spherical latex or clay particles to further assess the validity of the model. This would form the basis of our future work.

Also, it was very apparent that the single particles detach gradually, rather than in one go as would be predicted by the model, upon reaching the critical velocity. In fact, a vast proportion of

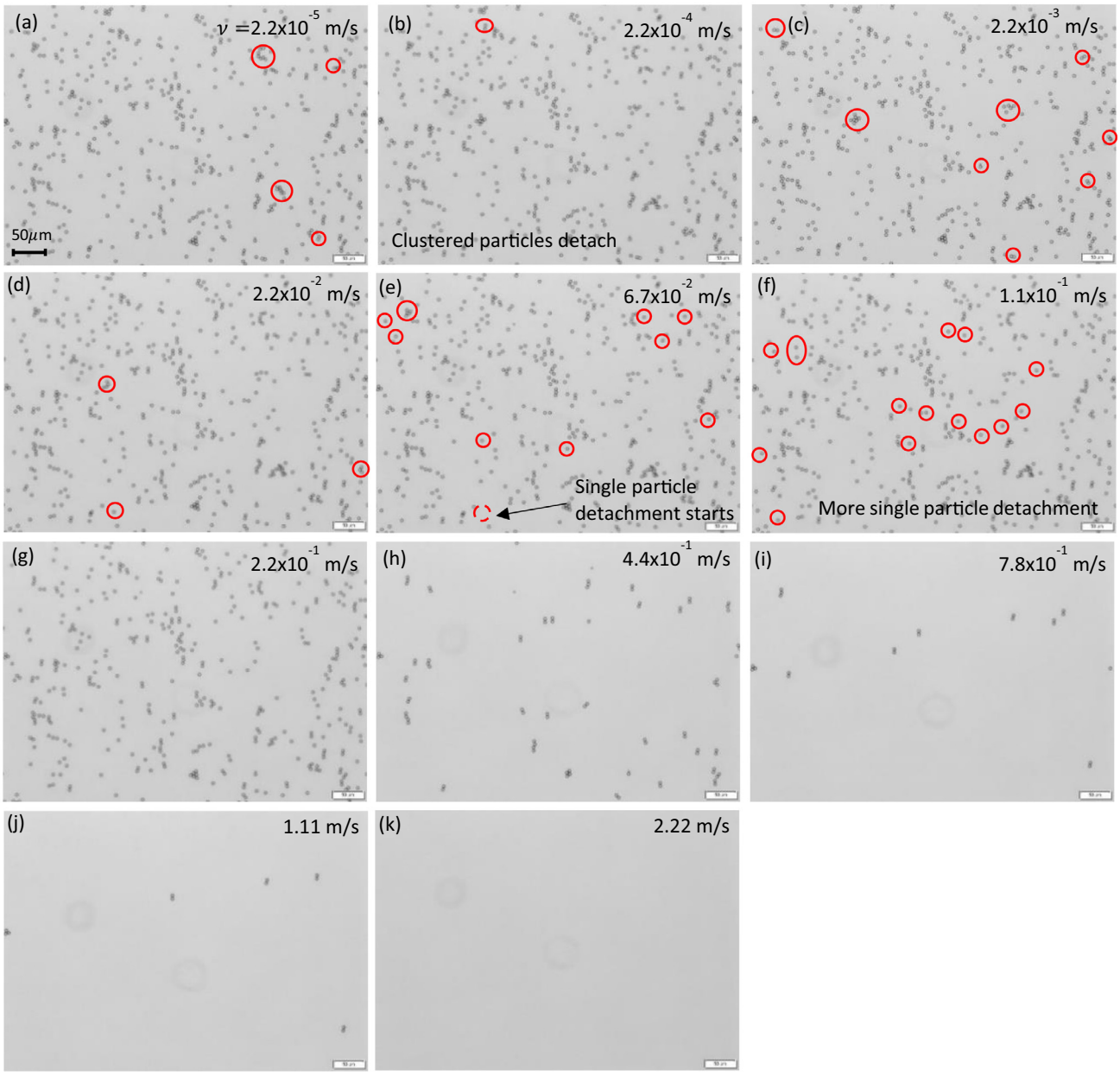

Fig 13. Lab visualisation of the detachment of r_e = 3μm latex spheres on glass system at 0.3 M of NaCl, pH 3, subjected to varying average flow velocities, v. Flow direction is from top to bottom. Photographs are taken for the same spot at increasing velocities. Red circles indicate that the particles will be detached in the next picture (i.e. the next velocity increment). Particle detachment continues at a higher rate with increasing velocity (from frames a to k) until no particles are left. Frames (g) onward are no longer marked with red circles as the detachments are very apparent. The temperature was recorded to be 25 °C on average. (For interpretation of the references to colour in this figure legend, the reader is referred to the web version of this article.)

the single particles appear to require detachment velocities higher than that predicted by theory. This was attributed to the presence of clusters (Chequer et al. 2019) as well as possible charge heterogeneity and surface roughness/asperities (Bradford & Torkzaban 2013; Chequer et al. 2021; Walz 1998). These surface heterogeneities could cause a distribution of primary minima depths (Hoek & Agarwal 2006) as well as alter the lever arms available for rolling detachment (Rasmuson et al. 2017; Shen et al. 2019).

The higher velocities used in the laboratory has exceeded $Re_p > 0.1$, even for the velocity (v = 0.067 m/s) where single particle detachment was initiated (Re_p = 0.23). This might cause a modest error. The phenomenon where the remaining clusters exist in linear line formation shows that the hydrodynamic shadowing effect is significant and can cause clusters to detach slower compared to single particles. This merits further investigation.

The β parameter used to characterise rolling detachment is only applicable when assuming a flat plate without asperities, such that for each F_a, there is a unique l_n given by Hertz theory. In the presence of asperities, a ratio of attaching torque to detaching torque (as opposed to force ratio) is needed to fully characterise rolling detachment.

In applying the model for kaolinite detachment, it is unsure whether a spheroid or cylinder could best represent the kaolinite particles in the absence of laboratory data. The choice of spheroid or cylinder could make a substantial difference in terms of the magnitude of force required for detachment and the detachment mode. However, it was certain that modelling kaolinite as a sphere could potentially overestimate or underestimate the detachment criteria, depending on the aspect ratio. It would also fail to capture the non-monotonic behaviour exhibited in the model. While the

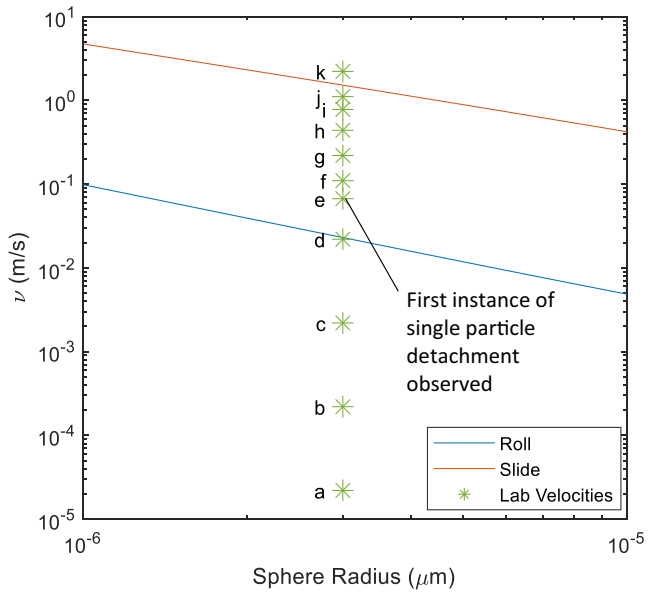

Fig 14. Critical average velocities, v, predicted by the EFT model, for the rolling and sliding detachment of latex spheres of radius 1–10 μm, from glass surface under 0.3 M and pH 3. The points a-k correspond to the average velocities used in the direct visualisation laboratory.

particle was assumed to be attached with its axis of symmetry perpendicular to plane, this is justified as kaolinite particles are most likely to attach to plane in a face-on configuration (Cerda 1987).

The sliding detachment of cylinder predicted in this model is supported by the experimental study by Onoe et al. (2005) on cylindrical silicon particles with diameters between 10 and 30 μm, and α = 0.03 to 2. Cylinder particles with low α (below a≈0.15) were shown to detach by sliding in response to the force applied by an AFM cantilever. A more complicated slide-jump behaviour was observed for high α cylinders.

The analytical expressions for drag, lift, and adhesion forces obtained in the present work can improve the modelling of fines detachment during colloidal-suspension-nano transport in porous media. The abovementioned forces are functions of velocity, salinity, pH, stress, and temperature. For each irregular-shaped particle attached to an asperous surface of a micro-heterogeneous rock, Eqs. (1–3) determine whether an attached particle detach or remain attached under those conditions. So, the attached particles concentration is a function of velocity, salinity, pH, stress, and temperature. This function is called the maximum retention function. It closes the mass balance equations in the governing system for colloidal flows in porous media. Being introduced by Bedrikovetsky et al. (2011); Bedrikovetsky et al. (2012), it is currently used for particle detachment modelling in geothermal reservoirs (Cheng & Milsch 2020; Kanimozhi et al. 2021), fines migration in oilfields (Arab & Pourafshary 2013; Muneer et al. 2020), aquifer contamination (Bianco et al. 2016; Tosco et al. 2014), low-salinity waterflooding (Dang et al. 2016; Yuan & Moghanloo 2018; Yuan et al. 2016), CO_2 geo-sequestration (Othman et al. 2018) and in subterranean reservoirs (Leij et al. 2015; Li et al. 2020).

The simple hydrodynamic shape factors presented in this paper are not only limited to kaolinite clays but may also be readily applicable for the modelling of other clays such as illite and chlorite, silica silts, bacteria, dust, contaminants and engineered nanoparticles.

For two phase flows, the capillary forces which are not accounted for in detachment criteria (1)–(3) could dominate over the adhesion and hydrodynamic forces (Aramrak et al. 2013). Therefore, capillary forces need to be considered in modelling particle detachment from solid substrates by the interfacial menisci surface (Shapiro 2016, 2018).

7. Conclusion

The impact of aspect ratio (0.025<α < 1) towards the detachment behaviour of oblate spheroids and cylinders was studied under linear shear flows (Re_p < 0.1). CFD modelling of drag, lift and moment, SEI calculations of DLVO forces and laboratory visualisation study allowed the following conclusions to be drawn:

- There can be a significant difference between the detachment of spherical particles compared with spheroids and cylinders when aspect ratio $\ll$1. Consequently, equivalent sphere models are inadequate to capture the detachment behaviour of non-spherical particles with small aspect ratios. Modelling non-spherical particles as spheres could potentially lead to an overestimation of the detachment $v_{o,cr}$ by an order of magnitude for spheroids.
- Particle detachment is non-monotonic with particle aspect ratio. The decrease in aspect ratio generally leads to an increased retention of colloids on a surface but reduces again at very low α. The non-monotonic behaviour arises from the friction component of drag.
- Oblate spheroids and cylinders are most likely to detach by rolling and sliding respectively.
- $\beta_{cr} = \frac{F_{a,cr}}{F_{d,cr}}$ was proposed as a dimensionless parameter to characterise rolling detachment, which occurs when $\beta < \beta_{cr}$. The β parameter was determined using CFD and SEI in this investigation.
- The detachment model has been validated with reasonable accuracy against data from direct visualisation experiments of latex sphere detachment from glass under favourable conditions of 0.3 M of NaCl and pH 3.

Data availability

The data that support the findings of this study are available from the corresponding author upon reasonable request.

CRediT authorship contribution statement

Heng Zheng Ting: Software, Formal analysis, Writing - original draft, Writing - review & editing. **Pavel Bedrikovetsky:** Conceptualization, Methodology, Supervision. **Zhao Feng Tian:** Conceptualization, Methodology, Supervision. **Themis Carageorgos:** Methodology, Investigation, Resources.

Declaration of Competing Interest

The authors declare that they have no known competing financial interests or personal relationships that could have appeared to influence the work reported in this paper.

Acknowledgements

This work was supported with supercomputing resources provided by the Phoenix HPC service at the University of Adelaide. HZ Ting thanks the Adelaide Graduate Research Scholarship for financial support.

References

Arab, D., Pourafshary, P., 2013. Nanoparticles-assisted surface charge modification of the porous medium to treat colloidal particles migration induced by low salinity water flooding. Colloids and Surfaces A: Physicochemical and Engineering Aspects 436, 803–814.

Aramrak, S., Flury, M., Harsh, J.B., Zollars, R.L., Davis, H.P., 2013. Does colloid shape affect detachment of colloids by a moving air-water interface?. Langmuir 29 (19), 5770–5780.

Bedrikovetsky, P., Siqueira, F.D., Furtado, C.A., Souza, A.L.S., 2011. Modified Particle Detachment Model for Colloidal Transport in Porous Media. Transport in Porous Media 86 (2), 353–383.

Bedrikovetsky, P., Zeinijahromi, A., Siqueira, F.D., Furtado, C.A., Souza, A.L.S., 2012. Particle Detachment Under Velocity Alternation During Suspension Transport in Porous Media. Transport in Porous Media 91 (1), 173–197.

Bhattacharjee, S., Elimelech, M., 1997. Surface Element Integration: A Novel Technique for Evaluation of DLVO Interaction between a Particle and a Flat Plate. Journal of Colloid and Interface Science 193, 273–285.

Bianco, C., Tosco, T., Sethi, R., 2016. A 3-dimensional micro- and nanoparticle transport and filtration model (MNM3D) applied to the migration of carbon-based nanomaterials in porous media. J Contam Hydrol 193 (Oct), 10–20.

Bird, R.B., Stewart, W.E., Lightfoot, E.N., 2001. Transport Phenomena. John Wiley & Sons, New York.

Bradford, S.A., Morales, V.L., Zhang, W., Harvey, R.W., Packman, A.I., Mohanram, A., Welty, C., 2013. Transport and Fate of Microbial Pathogens in Agricultural Settings. Critical Reviews in Environmental Science and Technology 43 (8), 775–893.

Bradford, S.A., Torkzaban, S., 2013. Colloid interaction energies for physically and chemically heterogeneous porous media. Langmuir 29 (11), 3668–3676.

Brambilla, S., Speckart, S., Brown, M.J., 2017. Adhesion and aerodynamic forces for the resuspension of non-spherical particles in outdoor environments. Journal of Aerosol Science 112, 52–67.

Cerda, M., 1987. Mobilization of Kaolinite Fines in Porous Media. Colloids and Surfaces 27 (1–3), 219–241.

Cheng, C., Milsch, H., 2020. 'Permeability Variations in Illite-Bearing Sandstone: Effects of Temperature and NaCl Fluid Salinity', *Journal of Geophysical Research: Solid*. Earth 125, no. 9.

Chequer, L., Bedrikovetsky, P., 2019. Suspension-colloidal flow accompanied by detachment of oversaturated and undersaturated fines in porous media. Chemical Engineering Science 198, 16–32.

Chequer, L., Bedrikovetsky, P., Carageorgos, T., Badalyan, A., Gitis, V., 2019. Mobilization of Attached Clustered Colloids in Porous Media. Water Resources Research 55 (7), 5696–5714.

Chequer, L., Carageorgos, T., Naby, M., Hussaini, M., Lee, W., Bedrikovetsky, P., 2021. Colloidal detachment from solid surfaces: Phase diagrams to determine the detachment regime. Chemical Engineering Science 229.

Clift, R., Grace, J.R., Weber, M.E., 1978. Bubbles, drops and particles. Academic Press, New York.

Cui, Y., Sommerfeld, M., 2015. Forces on micron-sized particles randomly distributed on the surface of larger particles and possibility of detachment. International Journal of Multiphase Flow 72, 39–52.

Dang, C., Nghiem, L., Nguyen, N., Chen, Z., Nguyen, Q., 2016. Mechanistic modeling of low salinity water flooding. Journal of Petroleum Science and Engineering 146, 191–209.

Decuzzi, P., Ferrari, M., 2006. The adhesive strength of non-spherical particles mediated by specific interactions. Biomaterials vol. 27, no. 30 (Oct), 5307–5314.

Derjaguin, B., Landau, L., 1941. Theory of the Stability of Strongly Charged Lyophobic Sols and of the Adhesion of Strongly Charged Particles in Solutions of Electrolytes. J Acta Physicochim 14 (6), 633–662.

Derksen, J.J., Larsen, R.A., 2011. Drag and lift forces on random assemblies of wall-attached spheres in low-Reynolds-number shear flow. Journal of Fluid Mechanics 673, 548–573.

Gregory, J., 1975. Interaction of unequal double layers at constant charge. Journal of Colloid and Interface Science 51 (1), 44–51.

Henry, C., Minier, J.-P., 2014. Progress in particle resuspension from rough surfaces by turbulent flows. Progress in Energy and Combustion Science 45, 1–53.

Hoek, EM & Agarwal, GK 2006, 'Extended DLVO interactions between spherical particles and rough surfaces', J Colloid Interface Sci, vol. 298, no. 1, Jun 1, pp. 50-58.

Hsu, R., Ganatos, P., 1989. The motion of a rigid body in viscous fluid bounded by a plane wall. Journal of Fluid Mechanics 207, 29–72.

Hubbe, M., 1984. Theory of Detachment of Colloidal Particles from Flat Surfaces Exposed to Flow. Colloids and Surfaces 12, 151–178.

Ibidi 2018, Instructions: sticky-Slide I Luer, Ibidi, Germany, viewed 12/6/2020, <https://ibidi.com/sticky-slides/63-sticky-slide-i-luer.html>.

Israelachvili, J.N., 2011. Intermolecular and Surface Forces. Elsevier Inc., Amsterdam.

Johnson, K.L., 1985. Contact mechanics. Cambridge University Press.

Kang, S., Subramani, A., Hoek, E., Deshusses, M., Matsumoto, M., 2004. Direct observation of biofouling in cross-flow microfiltration: mechanisms of deposition and release. Journal of Membrane Science 244 (1–2), 151–165.

Kanimozhi, B., Rajkumar, P., Kumar, R.S., Mahalingam, S., Thamizhmani, V., Selvakumar, A., Ravikumar, S., Kesavakumar, R., Pranesh, V., 2021. Kaolinite fines colloidal-suspension transport in high temperature porous subsurface aqueous environment: Implications to the geothermal sandstone and hot sedimentary aquifer reservoirs permeability. Geothermics 89.

Knappenberger, T., Aramrak, S., Flury, M., 2015. Transport of barrel and spherical shaped colloids in unsaturated porous media. J Contam Hydrol 180 (Sep), ,. 69–79.

LCLN 2012, Image Analysis: Dot Count, MIT, Massachusetts, viewed 22/5/2020, <http://reuter.mit.edu/software/dotcount/>.

Leighton, D., Acrivos, A., 1985. The lift on a small sphere touching a plane in the presence of a simple shear flow. Journal of Applied Mathematics and Physics 36, 174–178.

Leij, F.J., Bradford, S.A., Wang, Y., Sciortino, A., 2015. Langmuirian Blocking of Irreversible Colloid Retention: Analytical Solution, Moments, and Setback Distance. J Environ Qual 44 (5), 1473–1482.

Li, T., Shen, C., Wu, S., Jin, C., Bradford, S.A., 2020. Synergies of surface roughness and hydration on colloid detachment in saturated porous media: Column and atomic force microscopy studies. Water Res 183, 116068.

Liu, Q., Lazouskaya, V., He, Q., Jin, Y., 2010. Effect of particle shape on colloid retention and release in saturated porous media. J Environ Qual 39 (2), 500–508.

Loth, E., 2008. Drag of non-spherical solid particles of regular and irregular shape. Powder Technology 182 (3), 342–353.

Mahmood, T., Amirtharajah, A., Sturm, T., Dennett, K., 2001. A micromechanics approach for attachment and detachment of asymmetric colloidal particles. Colloids and Surfaces 177 (2–3), 99–110.

Malvern 2013, Zetasizer Nano Series User Manual, Malvern Instruments Ltd., UK, viewed 13/3/2020, <https://www.malvernpanalytical.com/en/learn/knowledge-center/user-manuals/MAN0485EN>.

Muneer, R., Hashmet, M.R., Pourafshary, P., 2020. 'Fine Migration Control in Sandstones: Surface Force Analysis and Application of DLVO Theory', *ACS*. Omega 5 (49), 31624–31639.

O'Neill, M.E., 1968. A sphere in contact with a plane wall in a slow linear shear flow. Chemical Engineering Science 23 (11), 1293–1298.

Oberbeck, A., 1876. Ueber stationäre Flüssigkeitsbewegungen mit Berücksichtigung der inneren Reibung. Journal für die reine und angewandte Mathematik 81, 62–80.

Onoe, H., Gel, M., Hoshino, K., Matsumoto, K., Shimoyama, I., 2005. Direct Measurement of the Binding Force between Microfabricated Particles and a Planar Surface in Aqueous Solution by Force-Sensing Piezoresistive Cantilevers. Langmuir 21 (24), 11251–11261.

Othman, F., Yu, M., Kamali, F., Hussain, F., 2018. Fines migration during supercritical CO2 injection in sandstone. Journal of Natural Gas Science and Engineering 56, 344–357.

Polyanin, A.D., Dil'man, V.V., 1990. The method of asymptotic analogies in the mass and heat transfer theory and chemical engineering science. International Journal of Heat and Mass Transfer 33 (6), 1057–1072.

Polyanin, A.D., Dil'man, V.V., 1994. Methods of modeling equations and analogies in chemical engineering. CRC Press, Boca Raton, Fl.

Polyanin, A.D., Sorokin, V.G., Vyazmin, A.V., 2018. Reaction-Diffusion Models with Delay: Some Properties, Equations, Problems, and Solutions. Theoretical Foundations of Chemical Engineering 52 (3), 334–348.

Polyanin, A.D., Zhurov, A.I., 2015. The generating equations method: Constructing exact solutions to delay reaction–diffusion systems and other non-linear coupled delay PDEs. International Journal of Non-Linear Mechanics 71, 104–115.

Technical Data Sheet 1002, Polysciences, Inc., Pennsylvania, viewed 5/3/2020, <https://www.polysciences.com/default/polybead-carboxylate-microspheres-300956m>.

Rasmuson, A, Pazmino, E, Assemi, S & Johnson, WP 2017, 'Contribution of Nano- to Microscale Roughness to Heterogeneity: Closing the Gap between Unfavorable and Favorable Colloid Attachment Conditions', Environ Sci Technol, vol. 51, no. 4, Feb 21, pp. 2151-2160.

Reinhardt, K., Kern, W., 2018. Handbook of Silicon Wafer Cleaning Technology. Elsevier Inc., United Kingdom.

Ruckenstein, E., Prieve, D.C., 1976. Adsorption and Desorption of Particles and Their Chromatographic Separation. American Institute of Chemical Engineers 22 (2), 276–283.

Russell, T., Bedrikovetsky, P., 2018. Colloidal-suspension flows with delayed fines detachment: Analytical model & laboratory study. Chemical Engineering Science 190, 98–109.

Russell, T, Chequer, L, Borazjani, S, You, Z, Zeinijahromi, A & Bedrikovetsky, P 2018, 'Formation Damage by Fines Migration', in Formation Damage During Improved Oil Recovery, pp. 69-175.

Ryan, J.N., Elimelech, M., 1996. Colloid mobilization and transport in groundwater. Physicochemical and Engineering Aspects, vol, Colloids and Surfaces A, p. 107.

Saffman, P.G., 1965. The lift on a small sphere in a slow shear flow. Journal of Fluid Mechanics 22 (2), 385–400.

Salerno, B., Flamm, M., Logan, B., Velegol, D., 2006. Transport of Rodlike Colloids through Packed Beds. Environmental Science & Technology 40 (20), 6336–6340.

Seymour, MB, Chen, G, Su, C & Li, Y 2013, 'Transport and retention of colloids in porous media: does shape really matter?', Environ Sci Technol, vol. 47, no. 15, Aug 6, pp. 8391-8398.

Shapiro, A., 2007. Elliptic equation for random walks. Application to transport in microporous media. Physica A: Statistical Mechanics and its Applications 375 (1), 81–96.

Shapiro, A., 2016. Mechanics of the Separating Surface for a Two-Phase Co-current Flow in a Porous Medium. Transport in Porous Media 112 (2), 489–517.

Shapiro, A., 2018. A Three-Dimensional Model of Two-Phase Flows in a Porous Medium Accounting for Motion of the Liquid-Liquid Interface. Transport in Porous Media 122 (3), 713–744.

Shapiro, A., Wesselingh, J.A., 2008. Gas transport in tight porous media. Chemical Engineering Journal 142 (1), 14–22.
Sharma, M., Chamoun, H., Sarma, D., Schechter, R., 1991. Factors Controlling the Hydrodynamic Detachment of Particles from Surfaces. Journal of Colloid and Interface Science 149 (1), 121–134.
Shen, C., Jin, Y., Zhuang, J., Li, T., Xing, B., 2019. Role and importance of surface heterogeneities in transport of particles in saturated porous media. Critical Reviews in Environmental Science and Technology 50 (3), 244–329.
Torres-Díaz, I., Jerri, H.A., Benczédi, D., Bevan, M.A., 2019. Shape Dependent Colloidal Deposition and Detachment. Advanced Theory and Simulations 2, no. 9.
Tosco, T., Gastone, F., Sethi, R., 2014. Guar gum solutions for improved delivery of iron particles in porous media (part 2): iron transport tests and modeling in radial geometry. J Contam Hydrol 166 (Oct), 34–51.
Vahidkhah, K & Bagchi, P 2015, 'Microparticle shape effects on margination, near-wall dynamics and adhesion in a three-dimensional simulation of red blood cell suspension', Soft Matter, vol. 11, no. 11, Mar 21, pp. 2097-2109.
Verwey, E.J.W., Overbeek, J.T.G., 1948. Theory of the stability of lyophobic colloids. Elsevier, Amsterdam.
Walz, J., 1998. The effect of surface heterogeneities on colloidal forces. Advances in Colloid and Interface Science 74 (1–3), 119–168.
Worden, RH & Morad, S (eds) 2003, Clay Mineral Cements in Sandstones, Special Publication No. 34 of the International Association of Sedimentologists, Blackwell Publishing, USA.
Wu, L, Gao, B, Tian, Y, Munoz-Carpena, R & Zigler, KJ 2013, 'DLVO interactions of carbon nanotubes with isotropic planar surfaces', Langmuir, vol. 29, no. 12, Mar 26, pp. 3976-3988.
Xu, S., Qian, L., Saiers, J., 2008. Straining of nonspherical colloids in saturated porous media. Environmental Science & Technology 42 (3), 771–778.
Yuan, B., Moghanloo, R.G., 2018. Nanofluid pre-treatment, an effective strategy to improve the performance of low-salinity waterflooding. Journal of Petroleum Science and Engineering 165, 978–991.
Yuan, B., Moghanloo, R.G., Zheng, D., 2016. Analytical evaluation of nanoparticle application to mitigate fines migration in porous media. Society of Petroleum Engineers 21 (6), 2317–2332.
Zhang, X., Ahmadi, G., Qian, J., Ferro, A., 2008. Particle Detachment, Resuspension and Transport Due to Human Walking in Indoor Environments. Journal of Adhesion Science and Technology 22 (5–6), 591–621.
Zoeteweij, M.L., van der Donck, J.C.J., Versluis, R., 2009. Particle Removal in Linear Shear Flow: Model Prediction and Experimental Validation. Journal of Adhesion Science and Technology 23 (6), 899–911.

This page is intentionally left blank

Chapter 5

Detachment of irregular-shape particles under unfavourable conditions: visualisation and modelling

Statement of Authorship

Title of Paper	Detachment of irregular-shape particles under unfavourable conditions: visualisation and modelling
Publication Status	☐ Published ☐ Accepted for Publication ☑ Submitted for Publication ☐ Unpublished and Unsubmitted w ork w ritten in manuscript style
Publication Details	Ting, H.Z., Tian, Z.F. & Bedrikovetsky, P. 2023, 'Detachment of irregular-shape particles under unfavourable conditions: visualisation and modelling'.

Principal Author

Name of Principal Author (Candidate)	Heng Zheng Ting
Contribution to the Paper	Generation and analysis of all numerical data, analysis and interpretation of the lab data and wrote the manuscript
Overall percentage (%)	85%
Certification:	This paper reports on original research I conducted during the period of my Higher Degree by Research candidature and is not subject to any obligations or contractual agreements with a th ion in this thesis. I am the primary author of this paper.
Signature	Date 24/02/2023

Co-Author Contributions

By signing the Statement of Authorship, each author certifies that:

i. the candidate's stated contribution to the publication is accurate (as detailed above);

ii. permission is granted for the candidate in include the publication in the thesis; and

iii. the sum of all co-author contributions is equal to 100% less the candidate's stated contribution.

Name of Co-Author	Zhao Feng Tian
Contribution to the Paper	Co-supervised the development of the work, and reviewed and assessed the manuscript.
Signature	Date 23/02/2023

Name of Co-Author	Pavel Bedrikovetsky
Contribution to the Paper	Formulation of the problem, co-supervised the development of the work, and reviewed and assessed the manuscript
Signature	Date 24/02/2023

Please cut and paste additional co-author p

Detachment of irregular-shape particles under unfavourable conditions: visualisation and modelling

Heng Zheng Ting [a], Zhao Feng Tian [a], Pavel Bedrikovetsky [b]

[a] *School of Mechanical Engineering, The University of Adelaide, Adelaide 5000, SA, Australia*

[b] *Australian School of Petroleum and Energy Resources, The University of Adelaide, Adelaide 5000, SA, Australia*

Keywords: Colloid; Detachment; Unfavourable conditions; Secondary energy minimum; Particle shape; DLVO

Abstract

Particle detachment in unfavourable conditions is ubiquitous in many fields of chemical and environmental contexts. This work investigates the effects of particle shape and aspect ratio on mechanical-equilibrium detachment conditions from solid surfaces under unfavourable attachment conditions. We use Surface Element Integration (SEI), Hertz theory for elastic particle-substrate deformation, and Computational Fluid Dynamics (CFD), to calculate the adhesion force, its lever arm, and the hydrodynamic force, respectively. It was found that the change in aspect ratio does not remove the energy barrier between two energy minima. Direct laboratory visualisation of latex and kaolinite particle detachment is also conducted in unfavourable conditions. A two-stage detachment process with plateau under intermediate velocity range is observed. The two-stage detachment is attributed to detachment of the fines attached in primary and secondary energy minima. The laboratory visualisation data are highly matched for latex and qualitatively - for kaolinite particles.

Nomenclature

a	Semi-major axis
b	Semi-minor axis
D	Distance of closest separation
E	Young's Modulus
E^*	Effective Young's modulus
F_a	Adhesion force
F_{a1}	Adhesion force from the primary minimum
F_{a2}	Adhesion force from the secondary minimum
F_d	Drag force
F_g	Gravitational force
F_l	Lift force
F_T	Total interaction force
f_d	Drag shape factor
f_M	Moment shape factor
g	Gravitational acceleration
k_B	Boltzmann constant
l_d	Lever arm for drag force
l_n	Lever arm for normal force
M	Moment exerted by drag
O	Particle centre
p	Pressure
Re_p	Particle Reynolds number
r_e	Volume equivalent sphere radius
T	Temperature
$\boldsymbol{u}$	Fluid velocity
U_T	Interaction potential energy
v	Flow rate averaged velocity
v_o	Particle centre velocity

Greek Symbols

α	Aspect ratio
β	Hysteresis loss factor
$\dot{\gamma}_o$	Shear rate
κ	Inverse Debye length
μ	Fluid dynamic viscosity
μ_s	Coefficient of static friction
σ	Interatomic spacing distance
ρ	Fluid density
ρ_p	Particle density
ν	Poisson ratio
ξ_{cr}	Critical rolling displacement

Subscripts

Sphd	Spheroid
Cyl	Cylinder
cr	Critical

1. Introduction

Particle detachment during colloidal-suspension transport in porous media occurs in numerous technologies and natural processes, including several areas of chemical, petroleum, pharmaceutical, and environmental engineering, geology, and hydrology.

Adhesion force, F_T, acts between the particle-substrate and particle-particle pairs. Based on the well-established Derjaguin-Landau-Verwey-Overbeek (DLVO) theory, the adhesion force is modelled as the sum of the attractive van der Waals force (VDW) and the generally repulsive electric double layer force (EDL) (Derjaguin & Landau 1941; Verwey & Overbeek 1948). Born repulsion was added to allow for reversible deposition in the primary minimum (Ruckenstein & Prieve 1976). The experimental validation of DLVO for particle detachment has been provided in numerous works in colloidal science (Burdick et al. 2001; Sharma et al. 1992).

Depending on the magnitude of these individual forces, favourable and unfavourable conditions can exist. The former refers to the presence of only one primary minimum, in the absence of an energy barrier. The latter is defined by the presence of a repulsive energy barrier and a secondary minimum. The repulsive EDL force exceeds the attractive VDW force at the energy barrier. In the existence of both the primary and secondary minima, particle deposition and consequent detachment could theoretically occur from both minima (Israelachvili 2011).

The natural fine particles encountered in subterranean reservoirs, rivers, and in nanotechnology, exhibit wide variety of non-spherical shapes (Appelo and Postma 2004; Farrell et al. 2021; Li et al. 2023). The reservoir clays that produce migrating fines in sandstone rocks are kaolinites, which form the leaflets consisting of thin platelets, finger-line illites, and shell-shaped chlorites. Quartz, silica, and sand debris usually have the form of irregular polyhedrons. Those particles can be approximated by either oblate spheroids or cylinders. Depending on Young's modulus and Poisson ratio of particles and rocks, the particle attachment can be realised through relatively large or small contact areas, which corresponds to cylinders or oblate spheroids, respectively. The contact area size can highly affect drag and lift, exerting particles in the creeping flows.

In modelling the detachment of fine particles in porous media, the mechanical equilibrium conditions for the detachment of oblate spheroids and cylinders along with the effects of aspect ratio have previously been investigated (Ting et al. 2021). However, the findings in this work are applicable for favourable attachment conditions alone. Besides, the models have only been

matched with the experiments using the engineered latex particles; the model-coefficient tuning using natural reservoir clays are unavailable.

While particle attachment and detachment in favourable conditions are well understood, there remains much uncertainty for unfavourable conditions. In particular, the role of the secondary minimum and the energy barrier towards particle retention and detachment has not been explored in depth, compared to the primary minimum. For example, column filtration experiments under unfavourable conditions have frequently reported higher retention rates than predicted by theory (Molnar et al. 2015).

One of the challenges in characterising particle detachment in unfavourable conditions lies in reliably measuring the adhesion forces acting on a particle in microscale (Huang et al. 2010; Stempniewicz et al. 2018). Advancement in microscopy has facilitated attempts at evaluating the secondary minimum. For example, studies using Total Internal Reflection Microscopy (TIRM) have provided evidence that particles could be retained in the secondary minimum. Particles such as carbon black (Albery et al. 1990), polystyrene latex (Flicker et al. 1993; Prieve et al. 1990) and bacteria (van der Westen et al. 2018) were retained further away from the surface during unfavourable conditions compared to favourable conditions. This extra distance matched the secondary minimum of the theoretical DLVO plot. However, the conventional approach of Atomic Force Microscopy (AFM) commonly used to measure the adhesion force seems to be unable to measure the adhesion from the secondary minimum due to its small magnitude (Shen et al. 2019).

Even if particles could be retained in the secondary minimum, it was debated whether the secondary minimum is strong enough to cause immobilisation and can be modelled with torque balance and sliding friction which assumed physical contact (Johnson et al. 2009; Torkzaban et al. 2009). The stable deposition of particles attributed to the secondary minimum often required the presence of stagnation points (no hydrodynamic force) or straining to fully immobilise a particle (Tong & Johnson 2006a). Further uncertainty is introduced by the presence of surface and charge heterogeneities (Shen et al. 2019).

Several mechanisms for particle deposition in unfavourable conditions have been proposed. This included the accumulation of particles in the secondary minima, where primary minimum attachment is not possible due to a strong energy barrier (Kuznar & Elimelech 2007). Alternatively, some authors reasoned that there is attachment in the primary minima because the energy barrier was overcome by local asperities and chemical heterogeneity (Ziskind 2006,

Duffadar et al. 2009; Johnson et al. 2010; Pazmino et al. 2014; Rasmuson et al. 2017; Shen et al. 2019). Another possibility is that the particles were immobilised in both the primary and secondary minima due to the adhesion force alone (Bradford & Torkzaban 2015; Chequer et al. 2021).

Presently, there appears to be no widely accepted model to mechanically predict detachment from the secondary minimum. The question of whether physical contact (and hence the applicability of contact theories) is achieved in secondary minimum also deserves further scrutiny.

Direct visualisation tests have been invaluable in understanding particle detachment behaviour in the pore scale (VanNess et al. 2019). The methodology effectively removes the stagnation point and straining mechanisms present in conventional column filtration experiments. In the absence of packed beads, particle attachment and detachment could then be solely attributed to adhesion forces. A frequently executed visualisation method is the radial stagnation flow system. Latex (Tong & Johnson 2006b) and bacteria (Liu et al. 2009) were observed to translate along the slide radially and occasionally remain on the edge. Yet there seems to be few attempts in quantitatively characterising the detachment behaviour in unfavourable conditions based on the adhesion and hydrodynamic forces.

The literature concerning the modelling of particle detachment in porous media has mostly utilised torque balance as the detachment criteria (Bradford et al. 2013; Sharma et al. 1992; VanNess et al. 2019). A particle is assumed to detach from the substrate once the detachment torque exceeds the maximum attachment torque. However, there were also other alternatives to torque balance. For example, Bergendahl and Grasso (2000) used an energy approach for rolling friction, rather than torque balance. Some authors also cautioned that torque balance tends to overestimate resisting torque; the pull-off adhesive force does not strictly act over the equilibrium contact area predicted by either Hertz, Johnson-Kendall-Roberts (JKR) or Derjaguin-Muller-Toporov (DMT) (Sümer & Sitti 2008). In other disciplines such as astrophysics, the detachment of dust particles are modelled using the Dominik and Tielens (DT) model (Dominik & Tielens 1995). The DT model proposed that the resistance to rolling detachment arises from the lag between the centre of the particle and the contact area, leading to an asymmetric pressure distribution that produces opposing torque. The fact that the virtually similar phenomenon of particle detachment is characterised with different models across different disciplines warrants further study.

The energy barrier can reportedly be removed by changing salinity and pH, charge and surface heterogeneity (Rasmuson et al. 2017). Recently, through the Surface Element Integration (SEI) method as well as experimental studies, it has been shown that prolate spheroids and rods with different orientation angles would affect the DLVO profile (Gomez-Flores et al. 2020; Gomez-Flores et al. 2019). Certain orientation angle of deposition were shown to reduce the energy barrier significantly such that deposition is possible. However, studies have only been limited to the interaction energies with no considerations on adhesion force and hydrodynamics, which are required for force and torque balance considerations.

Hydrodynamic forces are major forces that cause particle detachment. The asymptotic expressions for drag at the presence of solid surface are obtained by the boundary-layer methods (O'Neill 1968; Polyanin & Dil'man 1994; Polyanin et al. 2001a). CFD is used to determine the drag for irregular shape particles. It is recognised that the drag forces are dependent on the flow regime. Previous work suggested that the detachment of flat oblate spheroids and cylinders required detachment velocities exceeding the Stokes flow regime on which the drag equations were based (Ting et al. 2021). It remained uncertain whether the shape factors reported were still valid for particle Reynolds number exceeding the Stokes regime.

In general, detachment modelling of irregular shape particles attached in the secondary energy minimum and its validation by the visualisation tests is not available.

This paper addresses the abovementioned gaps. In addressing the limitations of the previous study (Ting et al. 2021), the simulations were extended to include unfavourable attachment conditions. We also carried out the laboratory visualisation tests using kaolinite clay particles with irregular shapes. For mathematical modelling, the shape of kaolinite is approximated to be either a short cylinder or an oblate spheroid. Consequently, the work utilised Surface Element Integration (SEI) to evaluate the adhesion forces for oblate spheroids and cylinders with varying aspect ratios. Computational Fluid Dynamics (CFD) was used to model the drag and moment for spheroids beyond the Stokes regime. The comparative study of the matching accuracy for direct visualisation experiments by the torque balance model with two rolling friction models have been carried out.

2. Theory

The brief presentation of theoretical fundamentals of particle detachment, used in further mathematical modelling, includes introduction of the main forces and their lever arms (section 2.1), definition of the shape factors capturing the irregular particle geometry (section 2.2), Navier-Stokes equations and their numerical CFD solution (section 2.3), DLVO expressions for electrostatic interactions (section 2.4), and the mechanical equilibrium conditions for particle mobilisation at different regimes (section 2.5). Explanation of the alternative mechanical equilibrium models (sections 2.6 and 2.7) highlights the model used in the present work; the models will be compared in section 4 under the lab conditions.

2.1. Geometry and flow configuration

To account for the detachment of non-spherical particles from surfaces, the particles are modelled as either an oblate spheroid or cylinder, attached with the axis of rotation perpendicular to the surface (refer to Figure 1). The size and shape of the particle are defined by the volume equivalent sphere radius, r_e and aspect ratio, α respectively. Here, $\alpha = b/a$, where a is the semi-major axis and b is the semi-minor axis of the particle. A linear Couette shear flow, defined by the shear rate, $\dot{\gamma}_o$, exerts the hydrodynamic forces required to detach the particles. The flow is characterised by the particle Reynolds number, $Re_p = \rho \dot{\gamma} r_e^2 / \mu$, where ρ is the fluid density and μ is the dynamic viscosity.

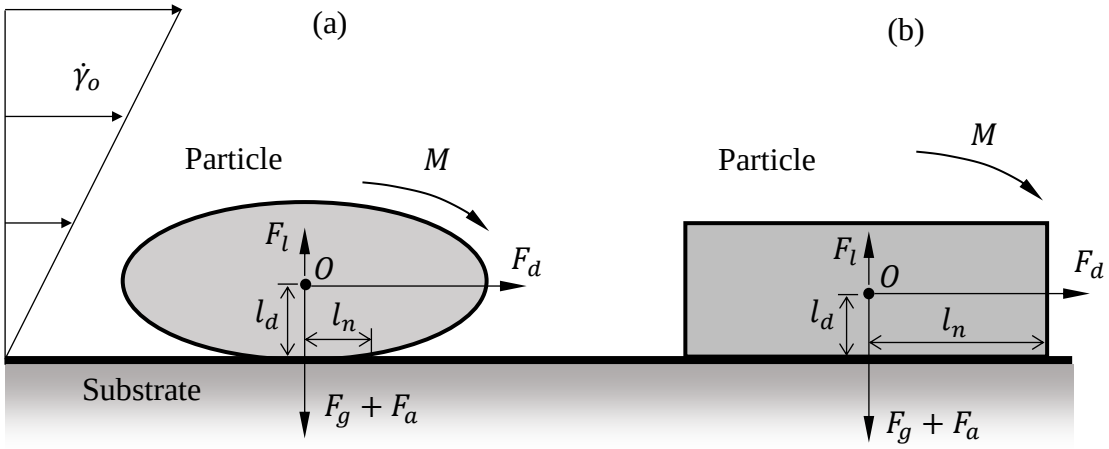

Figure 1: Mechanical equilibrium of fines particle on the solid substrate: a) oblate spheroid; b) cylindrical particle.

2.2. Hydrodynamics

The shear flow exerts the hydrodynamic forces of drag and moment, expressed as:

Drag: $$F_d = 6\pi\mu r_e^2 \dot{\gamma}_o f_d \quad (1)$$

Moment: $$M = F_d l_d f_M \quad (2)$$

The drag force, F_d and moment, M are both a function of shape factors which accounts for the different aspect ratios of the spheroids and cylinders. f_d and f_M are the drag and moment shape factors (Eqns. S1-S4 in Supplementary Materials). The shape factors are solely a function of the aspect ratio when $Re_p < 0.1$, but also becomes increasingly dependent on Re_p beyond Stokes flow. Lift force was excluded in this investigation as it was previously shown to be consistently three orders of magnitude less than drag (Ting et al. 2021).

2.3. CFD Modelling

The detailed parameters for the CFD model have been reported previously (Ting et al. 2021). Briefly, the simulation was setup with a top and bottom plate, parallel to each other. A single particle is attached to the bottom wall, which is fixed. The top wall is assigned a constant velocity which introduces a linear shear flow. The length × width × height of the simulation domain are $72r_e \times 24r_e \times 24r_e$. In investigating the applicability of the previous shape factors for $Re_p > 0.1$, identical CFD models were run but with increased top wall velocities. The maximum number of iterations was increased to ensure that the solutions converged before the termination of a run. The laminar solver of the commercial software ANSYS/CFX 2019 R2 was used, which solves numerically the following governing 3D system of viscous incompressible flow - Navier-Stokes equations for laminar flows. The system consists of continuity and momentum conservation equations:

$$\nabla \cdot \boldsymbol{u} = 0 \quad (3)$$

$$\boldsymbol{u} \cdot \nabla \boldsymbol{u} = -\frac{1}{\rho}\nabla p + \nu \nabla^2 \boldsymbol{u} \quad (4)$$

Here, $\boldsymbol{u}$ is the fluid velocity, p is the pressure and ν is the kinematic viscosity. We consider steady state flow, so the accumulation term in the right-hand side of Eq. (4) is dropped. The no-slip boundary conditions are set at the surfaces of the particle and substrate, which are assumed to be non-deformable.

The previous work (Ting et al. 2021) presents the results of the grid-independent test and the validation of the accuracy of the numerical schema of CFD software ANSYS. The results presented further in Section 4 have been obtained by using the same CFD setting and mesh.

2.4. Theory of DLVO

The electrostatic interaction between the particle and the plane is modelled using the DLVO theory. The total interaction energy, U_T is the sum of the van der Waals, electric double layer and Born repulsion:

$$U_T = U_{vdw} + U_{edl} + U_{born}. \tag{5}$$

The interaction force, F_T is the negative derivative of the interaction energy:

$$F_T = -\frac{dU_T}{dD}. \tag{6}$$

For the case of unfavourable conditions, there exist two minima in the interaction force curve. The magnitude of the forces at the primary and secondary minima are referred to as the primary, F_{a1} and secondary, F_{a2} adhesion forces, respectively. D is the distance of closest approach between the particle and the plane.

The numerical Surface Element Integration (SEI) method was used to scale the non-spherical interaction of the spheroid and cylinder with the plane (Bhattacharjee & Elimelech 1997). The analytical expressions for electrostatic force in DLVO theory can be obtained only for the cases of simple geometry (Israelachvili 2011) . The formulae for calculating each component of the interaction energy and SEI are provided in the supplementary material (Eqns. S5-S9).

2.5. Equilibrium of forces and torques

The impact of the hydrodynamic and adhesion forces on detachment are quantified using the equilibrium of forces and torque model. The particle could detach either by rolling, sliding or lifting, such that:

Rolling: $$M + F_l l_n > \left(F_g + F_a\right) l_n, \tag{7}$$

Sliding: $$F_d > \mu_s \left(F_g + F_a\right), \tag{8}$$

Lifting: $$F_l > F_g + F_a. \tag{9}$$

F_g is the gravitational force given by:

$$F_g = \frac{4}{3}\pi r_e^3 g(\rho_p - \rho). \tag{10}$$

In Expression (6), μ_s is the coefficient of static friction, while in Eqn (8), g is the gravitational acceleration and ρ_p the density of the particle. Assuming that the particles in the secondary minimum are in contact with the surface and can be treated in the same manner as the primary minimum, F_a in Expressions (7) - (9) could be F_{a1} or F_{a2} (as discussed in Section 2.4).

Detachment is assumed to occur immediately whenever any of the equilibria is disrupted. Detachment by lifting is omitted in the present study due to negligible lift forces compared to drag and adhesion forces.

For rolling detachment, the normal lever arm, l_n was determined using Hertz theory. The normal lever arm for an oblate spheroid with an infinite half-plane was equated to the radius of deformation:

$$l_n = \sqrt[3]{\frac{3(F_a + F_g)b}{4E^*}}, \tag{11}$$

$$\frac{1}{E^*} = \frac{1-\nu_1^2}{E_1} + \frac{1-\nu_2^2}{E_2}, \tag{12}$$

E^* is the effective Young's modulus, given by E and ν, which are the Young's modulus and Poisson's ratio respectively. The subscripts 1 and 2 represent the particle and surface, respectively. For cylinders, $l_n = a$. For both cylinders and spheroids, $l_d = b$.

2.6. Rolling friction

As an alternative to torque balance (5), Bergendahl and Grasso (2000) modelled the rolling detachment of particle using rolling friction, μ_R based on the work of Johnson (1985). Ignoring the lift force, the detachment criteria become as follows:

$$M \geq M_r, \tag{13}$$

where M_r is the moment that needs to be exceeded to start irreversible rolling.

The resisting torque, M_r is defined as:

$$M_r = \mu_R(F_a + F_g)r_e, \tag{14}$$

μ_R is the coefficient of rolling friction. For a sphere on a flat surface, μ_R is given as (Johnson 1985):

$$\mu_R = \frac{3}{16}\frac{\beta l_n}{r_e}, \tag{15}$$

where β is the empirical hysteresis loss factor, arising from the energy dissipation from elastic deformation and recovery during rolling. β can be interpreted as the fraction of the maximum elastic strain energy that was lost and could therefore have a maximum value of 1.

Therefore, as an alternative to torque balance, Expression (14) is derived from Eqns. (11), (12) and (13):

$$M \geq \frac{3}{16}\beta\left(F_a + F_g\right)l_n. \tag{16}$$

It is similar to torque balance, which involves the adhesion force and a lever arm, except with the coefficient $3\beta/16$.

2.7. Dominik and Tielens (DT) model

Alternatively, Dominik and Tielens (1995) modelled rolling friction by:

$$M = 4\left(F_a + F_g\right)\left(\frac{l_n}{a_o}\right)^{\frac{3}{2}}\xi_{crit}; \quad d_o < \xi_{crit} < l_n. \tag{17}$$

The equation was derived based on the Johnson-Kendall-Robertson (JKR) theory, where, ξ_{crit} is the critical rolling displacement. d_o is the equilibrium separation distance, l_n and a_0 are the contact area in the presence and absence of an external load, respectively. The $(l_n/a_0)^{3/2}$ term is weak and is often omitted for low loads (Dominik & Tielens 1997).

Different combinations of mechanical equilibrium models, presented in this section, are applied to complex flow geometries, pore and particles forms (Bradford et al. 2013; Valenzeula et al. 2018, 2019; Aracena et al. 2020).

3. Laboratory Methodology

Two sets of visualisation experiments were executed. Experiment 1 with latex particles and experiment 2 with kaolinite. The experiments were both conducted in deionised water (DI) at pH 11 to obtain a strongly unfavourable condition for deposition.

The detailed laboratory methodology and schematic of the setup for the latex and kaolinite visualisation have been detailed in previous publications (Ting et al. 2021; Yang et al. 2020). Here, a summary of the steps is detailed.

3.1. Materials and experimental setup

Polystyrene latex particles of r_e = 5 μm (Polysciences) and kaolinite particles of 0.5 μm < r_e < 3 μm (Fluka Analytical Pty. Germany) were used. The kaolinite size distributions were determined by passing the dilute kaolinite suspension in DI water through a Zetasizer Nano Z particle counter (Malvern Analyticals).

The DI water and particles are injected at 300 ppm concentration under a low velocity of 2.2×10^{-5} m/s for 1.5 PV and allowed to deposit in the glass microfluidic channel (Ibidi, Martinsried, Germany). After the initial saturation, the cell was flushed with 25 PV of DI water at each step, with increasing velocity. Flow averaged velocities, v were increased in steps, ranging from 0 up to 4.4 m/s. For each experiment, 5 different locations on the slide were monitored and photographed at each step, using an optical microscope.

3.2. Particle counting

The number of particles remaining after each velocity increment is counted using the MATLAB Image Processing Toolbox. The microscope images were first binarised by specifying a threshold through trial and error until a suitable threshold was achieved, which separates the particles from the background.

Specific to kaolinite, to reduce noise due to irregular shapes, a particle range of r_e <1.5 μm was used to filter out 'artificial particles' arising from the binarising process. The cut-off value corresponds to the minimum size resolution of the optical microscope. For cases where only a few particles (< 10) are seen to detach visually, the particles were directly subtracted without using the code. The percentage of kaolinite particles detached were taken as the average of five different locations on the glass slide.

4. Results

4.1. DLVO profile variations with the particle shape

Figure 2 shows that the magnitude of F_{a1} is significantly larger than F_{a2}. While there is considerable variation in the primary minimum with changing α, the impact of α to the secondary minima is less pronounced. In all α, cylinder shapes have consistently higher F_{a1} and F_{a2} compared to spheroids. Decreasing α has the effect of exposing more particle surfaces

closer to the plane, causing a higher attraction.

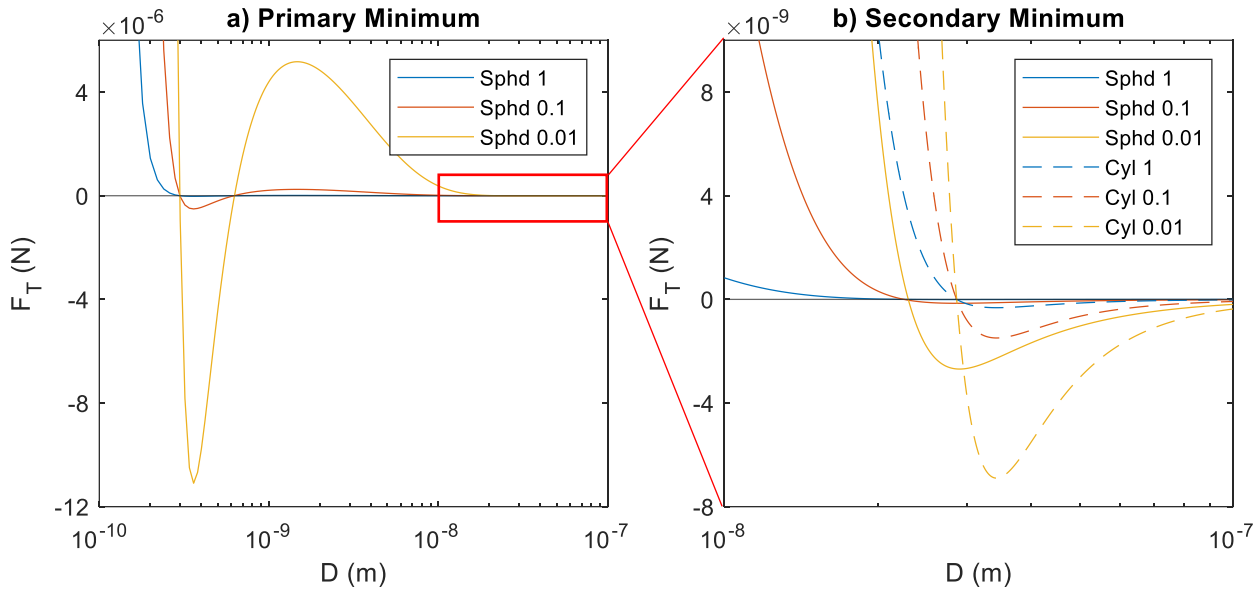

Figure 2: The variation of the DLVO force - F_T profile - versus closest separation distance, D. The curves are plotted for a latex-glass system at 0.01 M NaCl, pH 7 and r_e = 3μm. (a) The primary minima and force barriers of spheroids at 3 different aspect ratios. (b) The secondary minima of spheroids (—) and cylinders (---) at 3 different aspect ratios. Note the difference in magnitude of the primary minima compared to the secondary in the y-axis. The analyses for different aspect ratios are done by keeping the volume of the particles constant while varying the semi-major and semi-minor axis (a and b).

Within the range considered ($0.01 \leqslant \alpha \leqslant 1$), for latex and glass, the change in aspect ratios does not remove the force barrier. In fact, reducing the aspect ratio simultaneously increases the magnitude of both the attractive VDW and the repulsive EDL forces. Consequently, this causes: 1) the deepening of the primary minimum and secondary minimum; 2) the increase in force and energy barrier. This trend holds true even up to the extreme $\alpha = 1\times10^{-5}$ for both cylinders and spheroids. These are under conditions of $7 \leqslant$ pH $\leqslant 11$ and 0.000128 M NaCl $\leqslant$ salinity $\leqslant$ 0.1 M NaCl.

Consequently, flat particles (small α) are seemingly more likely to be trapped in the secondary minimum compared to spherical particles due to the strong energy barrier and deeper secondary energy well. However, if flat particles can penetrate the energy barrier, they could be more firmly attached in the primary minimum compared to the sphere particles.

4.2. Hydrodynamic shape factors at high Re_p

Referring to Figure 3, for spheroids with high α (i.e. α = 1 and 0.5), f_d rises rapidly when Re_p > 1. Conversely, f_d value of spheroids with reduced α are shown to be less dependent on Re_p. The substantial deviation in α = 1 and 0.5 is attributed to the presence of wake and recirculation at high Re_p, which are otherwise absent in laminar creeping flow.

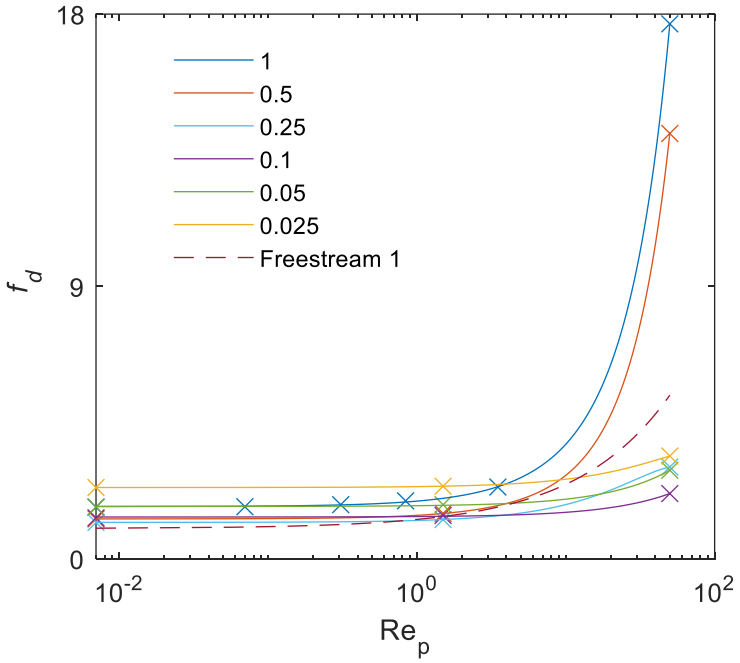

Figure 3: Variation of spheroid drag shape factors, f_d with Rep up to 50. Solid lines were plotted for spheroids of 6 different aspect ratios = 1, 0.5, 0.25, 0.1, 0.05 and 0.025. For comparison, the dashed line indicates the drag shape factor for a sphere in freestream, as obtained from Schiller and Naumann (1935), valid up to Re=800.

The presence of wake and flow recirculation reduces the pressure of fluid in the wake region, therefore increasing the drag on the particle. On the other hand, the flatter and hence more streamlined objects (α < 0.5) cause less disturbance to the flow (refer to Figure S1 for the flow pattern around spheroids). The flow separation behind the particle is thereby delayed, leading to reduced drag on the particle. It is hence less impacted by the higher Re_p flow.

This deviation of the drag from the Stokes law can be further analysed through the distribution of the pressure and friction drag as detailed in Table 1. The contribution of form versus friction drag varies significantly with Re_p for a sphere and minimally for a α = 0.025 spheroid. Friction drag which was the dominant drag component for sphere when Re_p = 0.007 was overtaken by form drag at Re_p = 50.

Separately, the impact of Re_p on the moment shape factor, f_M is less compared to f_d (Table 1 and Figure S2). The maximum deviation in f_M was calculated to be 25.4% for α = 0.5 in the range $0.007 \leqslant Re_p \leqslant 1$.

Table 1: Breakdown of spheroid drag components for the highest and lowest α (α = 1 and 0.025).

		Drag Components				Drag		Moment	
α	**Re_p**	**Form (N)**	**Form (%)**	**Friction (N)**	**Friction (%)**	**F_d (N)**	**f_d**	**M (Nm)**	**f_M**
1	0.007	6.4E-11	36%	1.1E-10	64%	1.8E-10	1.706	7.3E-16	1.370
	3.5	5.1E-08	41%	7.3E-08	59%	1.2E-07	2.371	4.8E-13	1.297
	50	8.4E-06	64%	4.8E-06	36%	1.3E-05	17.677	4.3E-11	1.080
0.025	0.007	7.2E-12	3%	2.4E-10	97%	2.5E-10	2.470	8.9E-16	14.104
	1.5	1.7E-09	3%	5.2E-08	97%	5.4E-08	2.411	1.9E-13	13.869
	50	1.1E-07	5%	2.1E-06	95%	2.2E-06	2.968	8.0E-12	14.091

4.3. Critical velocity for non-spherical detachment

Referring to Figure 4, the critical detachment velocity with aspect ratio exhibited non-monotonic behaviour as was reported previously. The critical velocity required to detach particles from the secondary minimum is several orders of magnitude lower for both spheroids and cylinders.

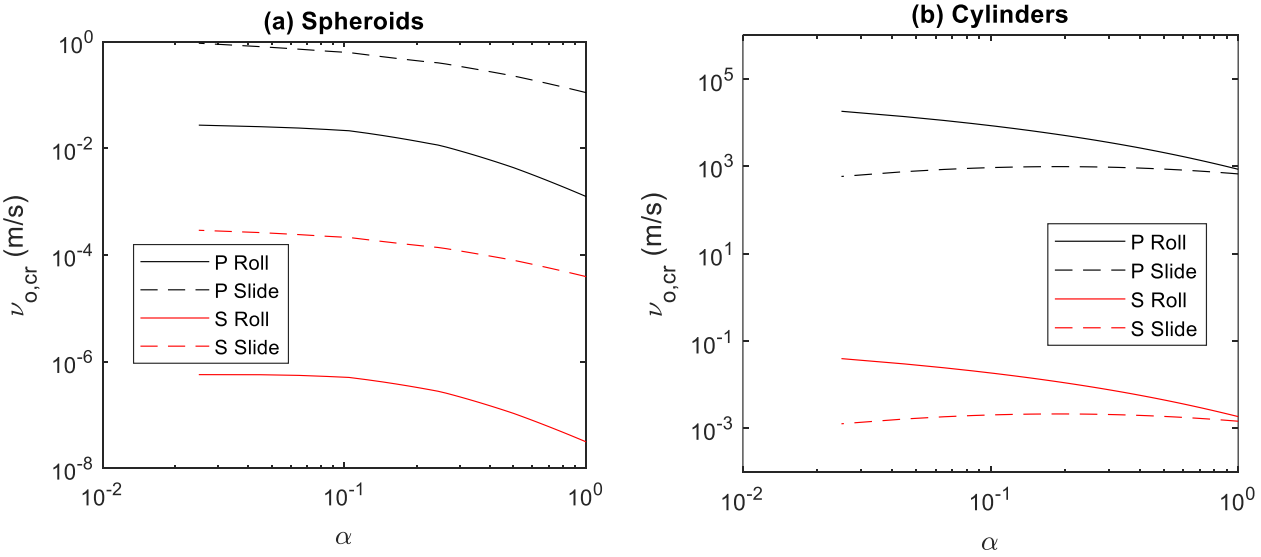

Figure 4: The impact of aspect ratio on the critical detachment velocity for (a) spheroids and (b) cylinders. $\nu_{o,cr}$ is the critical particle centre velocity required for detachment. This was for

latex on glass, under 0.01 M salinity, pH 7 and r_e = 3 μm. 'P' and 'S' denotes detachment from the primary and secondary minimum respectively.

Accounting for the deviation in f_d and f_M when $Re_p > 0.1$ yields minimal change in the critical detachment velocity trend for the spheroids (see Figure S3). High Re_p were only achieved by low aspect ratios (which requires higher detachment velocity compared to spheres). However, changing Re_p has minimal impact on the drag for low α shapes. Therefore, the shape factors proposed (Eqns. S1-S4) for Stokes flow is still appropriate even for moderately high Re_p (< 50) conditions.

Previous investigation of cylinders under favourable conditions suggest that it is not possible for the cylinders to detach from the primary minimum under typical porous media flow (Ting et al. 2021). However, by considering unfavourable conditions, Figure 4(b) shows that if cylinders were to detach at all, they are most likely to detach from the secondary minimum by sliding. For the lack of experimental data, μ_s between latex and glass in water was assumed to be 0.5 in this case. By assuming contact in secondary minimum and modelling using torque balance and sliding friction, a considerable velocity is still required for detachment from the secondary minimum. In fact, the magnitude of the detachment velocities for cylinders from the secondary minimum is comparable to those for spheres/spheroids in the primary minimum.

The considerable critical velocity required is in contrast to Johnson et al. (2009), who suggested that a slight initiation of flow is sufficient to detach particles from the secondary minimum. It was reasoned that the particles in the secondary minimum are not in contact and would not experience the resistance torque and friction found in the primary minimum. This stresses the importance of evaluating the applicability of torque balance and friction model for the secondary minimum, which will be discussed in the following section.

4.4. Direct visualisation of particle detachment under unfavourable conditions

In this section, we present the results of the two direct visualisation tests with their mathematical modelling. Some of the experiment data for the latex particles have previously been published (Chequer et al. 2021). Here, we attempt to re-interpret the data in the context of unfavourable detachment, focusing on the direct visualisation images and the period of no detachment (i.e. the transition stage).

4.4.1. Experiment 1: Changing velocity only

Experiment 1 examines the detachment of particles in response to incremental velocities. The DLVO profile for the laboratory conditions is plotted in Figure S4 (Supplementary Materials). The direct observations in Figure 5 show a distinct two-stage detachment process, with the first stage occurring after the initiation of flow from U = 0 to 2.2×10 $^{-5}$ m/s. This was followed by a transition stage of no detachment despite increasing velocities in frames (*a)* to (*c)*. Detachment of particles resumed from frames *(d)* to *(e)* and continued until frame *(i)*.

The other four observation points from different parts of the slide in the same salinity, pH and velocity conditions show the same detachment upon initiation of flow from *(o)* to *(a)*, followed by a stage of no detachment despite incremental flow velocities. However, 3 sets of the 5 observations started the second stage of detachment from *(c)* onward, rather than *(d)*, as shown in Figure 5. Thus, the second stage of detachment was considered to start from velocities ranging between U=0.0022 m/s and 0.022 m/s.

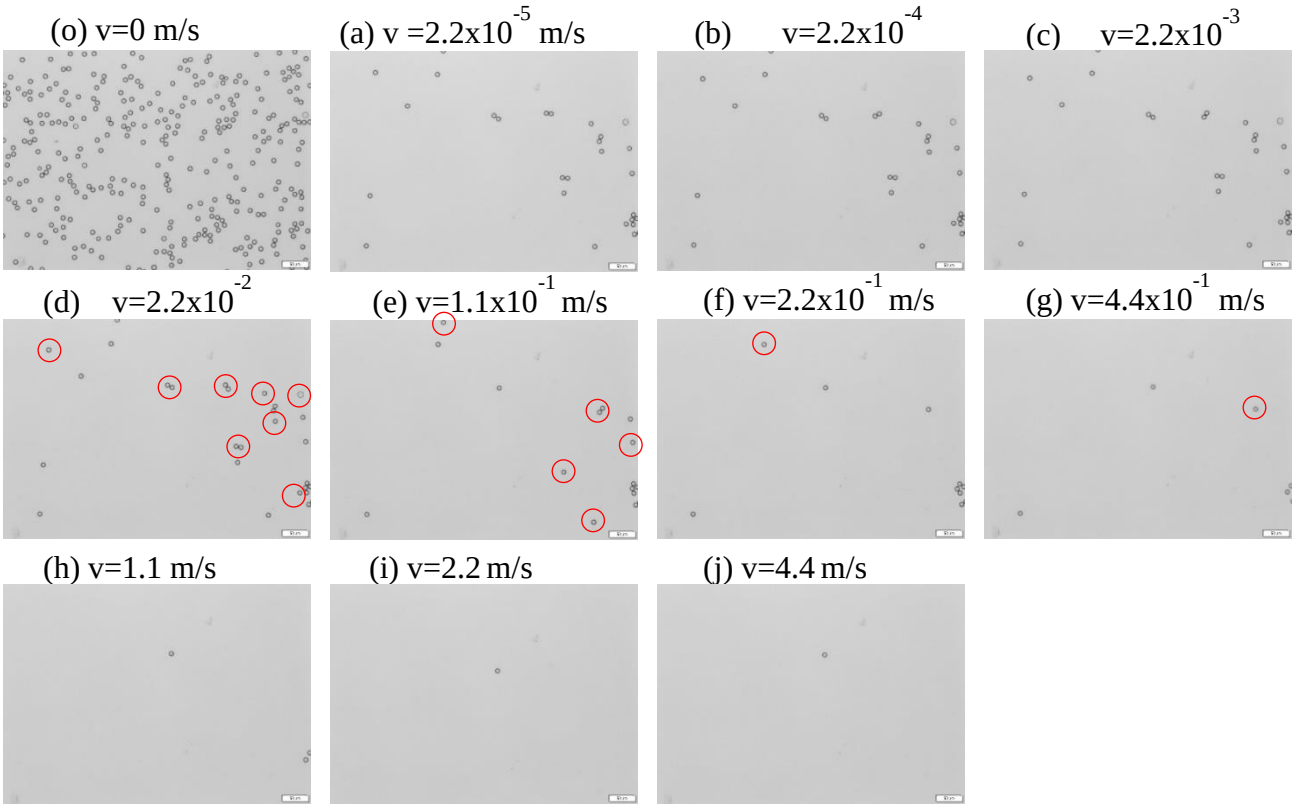

Figure 5: Lab visualisation of detachment for r_e = 5µm sphere latex on glass system at DI (0.000128 M), pH11, subjected to varying average flow velocities, v. Photographs are taken for the same spot at increasing velocities. The flow direction in the images is from the top to

bottom. Red circles highlight the particles that will be detached in the following image (i.e., the next velocity increment).

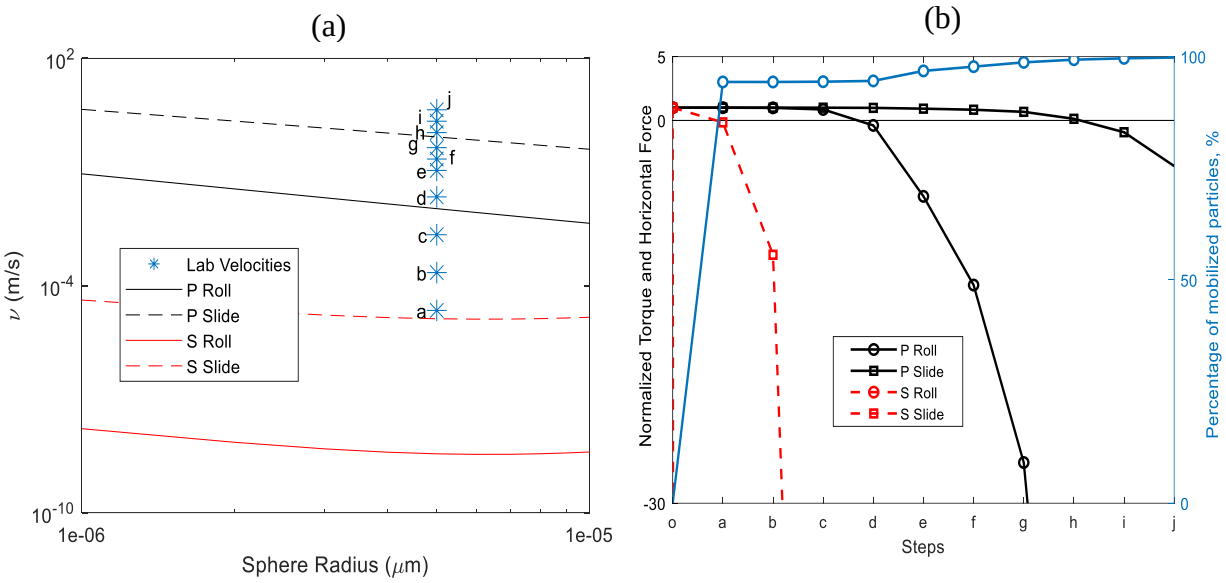

Figure 6: Phase diagrams for the detachment of latex spheres in Experiment 1. (a) Plot of critical average velocities, v for the rolling and sliding modes of detachment for latex spheres of various radii from glass surface under 0.000128 M and pH11. 'P' and 'S' denote the primary and secondary minima and are plotted using F_{a1} and F_{a2}, respectively. Detachment velocities for the latex spheres observed in the lab are plotted on the graph as points (a) → (j). (b) Normalised torque and horizontal force for each visualisation steps with the observed detachment rate plotted in blue on the right axis (Chequer et al. 2021). Theoretically, detachment should be initiated when either the normalized torque or horizontal force values fall below zero.

Figure 6(a) shows the phase diagram for the detachment of latex spheres in DI and pH 11, with velocities used in Experiment 1. Based on the adhesion force obtained from the DLVO primary and secondary minima, the required detachment velocity, v was plotted against different sphere radius for both rolling and sliding. The initial first stage of detachment (*o* to *a)* corresponds to detachment from the secondary minima, either by rolling or sliding.

In examining the instant detachment of particles from the secondary minimum upon initiation of flow (*o* to *a*), there are two possible interpretations: particles are either in contact (Bradford et al. 2013) or not in contact (Johnson et al. 2010). When contact is assumed, the torque balance and sliding friction criteria is used. Major detachment is observed from *o* to a

which is expected because it is well above the critical detachment velocity for the detachment of particles in secondary minimum (Figure 6a and 6b).

Alternatively, it could be interpreted that the particles in secondary minimum are incapable of being immobilised (not in contact with glass) and are immediately detached upon initiation of flow, as observed in Figure 5 (*o* to *a*). Consequently, our tests remain inconclusive on the ability of the secondary minimum to immobilise particles.

However, in both cases, it was proposed that all the particles that detached at the start of the flow were originally in the secondary minimum. Consequently, there was no particle detachment in *b* and *c* because the remaining particles were in the primary minimum and had not obtained sufficient velocities for particle detachment until *d* (region above the black solid line in Figure 6a).

The gradual detachment of particles from the primary minimum was attributed to the asperities and chemical heterogeneity of the surface, which alter the lever arm and adhesion force. The percentage of particles trapped in the primary and secondary minima are approximately 6% and 94%, respectively.

4.4.2. Experiment 2: Kaolinite detachment

Experiment 1 was repeated but with kaolinite particles. The velocity increments for *o* to *j* are given in Table S1. Referring to Figure 7, two-step detachment was also present for kaolinite particles, However, the two-step process was not as pronounced as latex particles.

Although there was virtually no detachment in the latex particles during the transition (*a* to *d* in Figure 5), some translation, detachment, and even reattachment was directly observed for kaolinites (Figure S5). Thus, though on average, Figure 7 shows seemingly no detachment from *c* to *g*, comparison of images before and after each velocity increment shows obvious kaolinite detachment in each image frame from *o* to *j*. Therefore, there was not a defined threshold that could be directly observed, where kaolinite detachment was initiated and terminated.

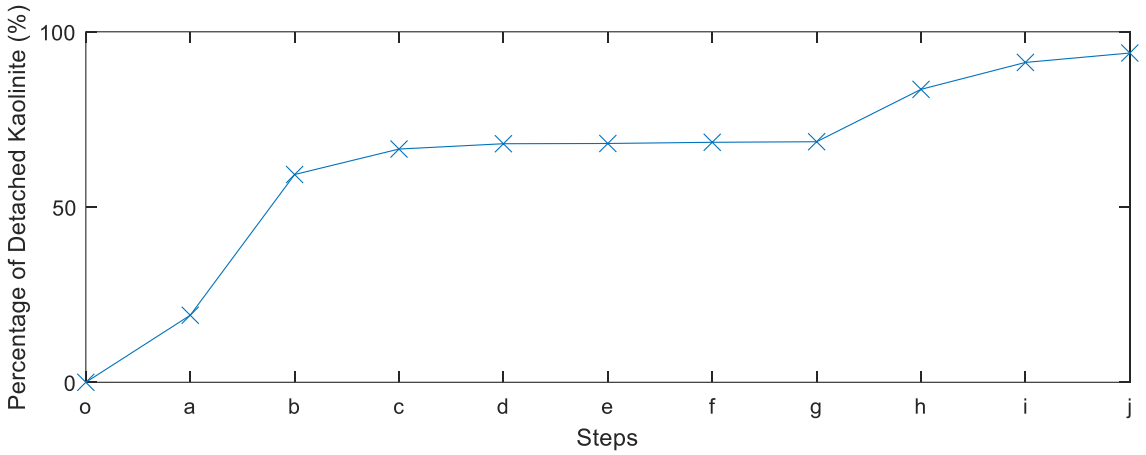

Figure 7: The percentage of initial kaolinite particles that were detached with increasing velocity steps as observed from the direct visualisation experiment. The test was performed for kaolinite and glass under DI water and pH 11.

Unlike the latex particles with controlled radius and aspect ratio, kaolinites possess a wide distribution of radii and aspect ratios, which introduced more uncertainties in the modelling. Also, it was challenging to discretise and count the kaolinite particles as they tend to form clusters. Consequently, we did not attempt to quantitatively match the kaolinite detachment observed with the equilibrium of force and torque model. In fact, for a thorough consideration of the variations in size and aspect ratio, it seems that a stochastic approach rather than a deterministic model is required. This forms the basis for our future work.

4.5. Torque Balance Alternatives

This section compares the effectiveness of using the rolling friction model and DT model as alternatives to torque balance for predicting rolling detachment. In order to reduce the uncertainty associated with the secondary minimum and the energy barrier, the models were compared based on the lab data done in favourable conditions from our previous publication (Ting et al. 2021), rather than the lab data in the current paper. The lab data was based on direct visualisation experiments for polystyrene latex on glass in 0.3 M NaCl and pH 3. Referring to Figure 8, to match the observed lab observations, the critical average velocity predicted should be between Steps (*d)* and (*e)*.

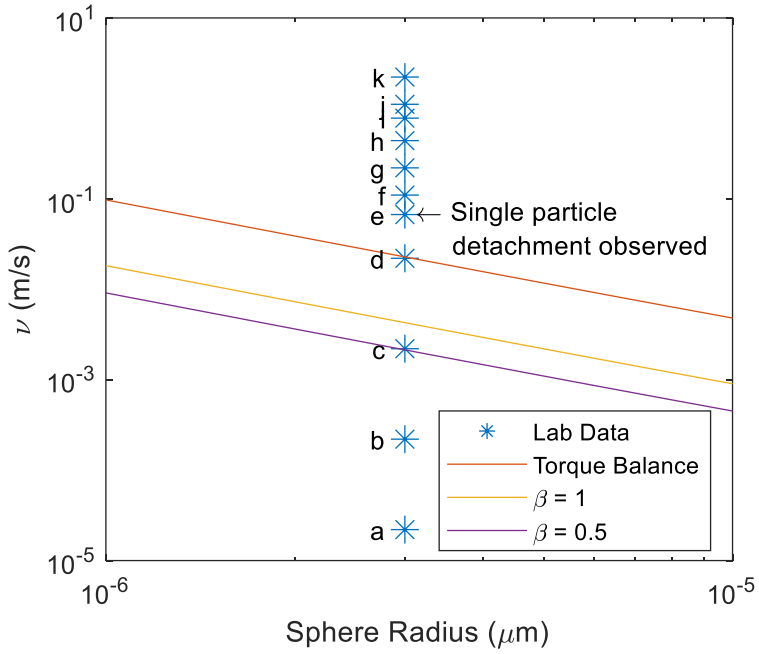

Figure 8: Critical average velocities, v, predicted by torque balance vs rolling friction. This was plotted for the rolling detachment of latex spheres of radius 1-10μm, from glass surface under 0.3 M and pH 3. The points a-k corresponds to the average velocities used in the direct visualisation laboratory with 3 μm radius. The red line is plotted using the torque balance model, while the yellow and purple lines are plotted by letting β = 1 and 0.5 in Expression. (16).

By definition, the empirical hysteresis loss factor in Expression (16) cannot be > 1. Consequently, the maximum resisting torque when β = 1 is only 19% (3/16) of the prediction of the torque balance. Consequently, the critical detachment velocity (yellow line in Figure 8) predicted by rolling friction is significantly lower than the torque balance and also the lab detachment velocity, even when β is the theoretical maximum of 1. At β < 1, the critical detachment velocity would be even lower. For example, the purple line corresponding to β = 0.5. In this case, rolling friction tends to underestimate the required v when compared to the lab observations.

The empirical data for β in literature is scarce and limited to few materials. Bergendahl and Grasso (2000) reported $\beta = 1.77 \times 10^{-3}$ for polystyrene. However, this should be treated with caution, as it seems during the derivation, the authors erroneously used the formula for a cylinder on a flat plate when deriving μ_R rather than using Eqn. (15).

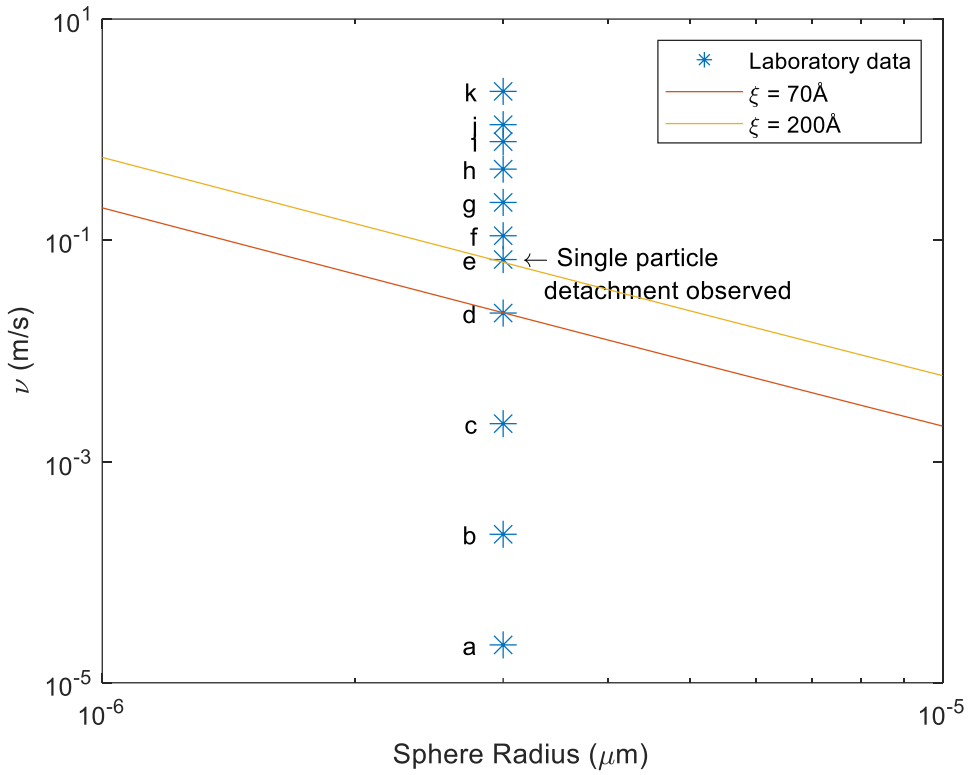

Figure 9: Critical average velocities, v, predicted by the Dominik and Tielens model Eqn. (17), for the rolling detachment of latex spheres of radius 1-10μm, from glass surface under 0.3 M and pH 3. The points a-k corresponds to the average velocities used in the direct visualisation laboratory.

As for the DT model as shown in Figure 9, $70\ \text{Å} < \xi_{cr} < 200\ \text{Å}$ matches the laboratory detachment data. The fitted ξ_{cr} values are within the range given by Dominik and Tielens (1995), where $2\text{Å} \leq \xi_{cr} \leq 64.3$ nm ($d_o \leq \xi_{cr} \leq a$) for this case.

To conclude, the rolling detachment models considered are all a function of adhesion force and some empirical parameter, i.e., l_n, β or ξ_{cr}. The rolling friction model tends to underestimate the required critical detachment velocity when compared to the favourable lab data. On the other hand, torque balance and the DT model provided good quantitative match with our data.

All 3 approaches do not seem to impact the current understanding of particle detachment. However, in the case where no better data is available for β and ξ_{cr}, torque balance seems to be the more useful criteria for predicting particle detachment.

5. Discussions

In discussing the applicability of torque balance in the secondary minimum, it is instructive to define contact. A common definition for contact is "the onset of repulsion between atoms" (Cheng & Robbins 2010). Contact can therefore be considered to occur when the distance of closest separation between the particle and the substrate is less than the interatomic spacing distance (typically $\sigma \approx 2$Å) (Israelachvili 2011). Noting that the deposition at the secondary minimum is at least D > 20Å (Figure S4), it does question the validity of applying the theories of contact mechanics which assume physical contact. Namely, Hertz theory to calculate the lever arm for torque balance, as well as the static coefficient of friction for sliding detachment in the secondary minimum. Our observations for secondary detachment were still in agreement with the torque balance models. This was because the flow rate used was not low enough to check if a critical velocity is required.

The alternative approach of Johnson et al. (2009) would mean that secondary minimum immobilisation is only present in stagnation zones. The absence of porous media in our direct visualisation experiments virtually excluded any form of stagnation zones. In support of Johnson et al. (2009), this absence of stagnation zones meant a significant amount of particles were immediately removed upon initiation of flow.

The current study examines the detachment of irregular kaolinites by assuming the particle as an oblate spheroid. However, the parameters r_e and α of the kaolinites are widely distributed and uncertain. Future work would benefit from the flow visualisation of synthetic spheroidal or cylindrical particles to validate the theoretical claims presented in this work. That way, the volume and aspect ratio could be further constrained and measured.

For the first time, naturally occurring particles (kaolinite) have been shown to exhibit a two-stage detachment process, although this requires further experiments to verify. Previous works on kaolinite detachment done on column experiments do not report any two-step detachment behaviour (Won et al. 2021). We speculate that the probabilistic distribution of the coefficients in the mechanical equilibrium equations (5-7) masks off the two-stage detachment behaviour.

The investigation of the hydrodynamic and DLVO behaviour for irregular shapes is not just useful for the understanding of particle detachment, but also in other fields such as particle stability, sedimentation, fluid rheology and filtration (Gupta et al. 2011; Knappenberger et al. 2015; Tang et al. 2014; Xu et al. 2018). For example, in sedimentation, the irregular shape of particles under unfavourable condition is also relevant as the presence of a secondary minimum

could potentially affect the size, and the flocculation behaviour of particles (Liu et al. 2022; Seher et al. 2020). However, in this work, we concentrate on the detachment conditions only, without subsequent particle transport considerations. The detachment criteria, obtained in this work, can be implemented in the particle-wall collision/attachment/detachment model for DEM-DNS modelling (Kieckhefen et al. 2020; Sakai 2016, 2020).

The effects of particle orientation are important on the forces exerted on particles, particularly for particles with non-sphere shapes (Gomez-Flores et al. 2020). In the current study, the particles are parallel to the flow direction (pitch angle is equal to zero) and the angle is equal to zero as well. The effects of various orientation angles and angles of attack on the forces and detachment will be the topic of the next study.

Here, we would like to caution that the two-stage behaviour for kaolinite was only a preliminary finding and requires further study to be verified. The use of synthetic spheroidal particles would make particle counting more distinctive and controlled. Besides the mathematical model should account for reattachment of mobilised particles. However, enrichment of governing equations to account for reattachment, and how setup could be improved is a topic of future work.

The mechanical equilibrium model (7,8) can be applied to fines detachment in reservoir rocks by accounting for surface roughness and attachment of irregular-shape clay fines in inter-grain fissures and crevices. Using Lattice-Boltzmann modelling along with Surface Element Integration, the three-point contact model by Ziskind et al. 1995, 1997 can extend shape factors for drag, lift, and DLVO forces (Cui and Sommerfeld 2018, 2022, Sommerfeld et al. 2019).

Generalisation of the current paper to fines detachment in porous media completely changes the experimental procedures and the mathematical model. The visualisation images (Fig. 5) are unfeasible, while the breakthrough particle concentrations can be measured with high accuracy.

The microscale expressions for forces and torques, obtained by CFD and SEI methods, can be used in upper-scale models for nano-colloidal-suspension transport in porous media (Fountouli & Chrysikopoulos 2020; Ma et al. 2021; Shapiro & Yuan 2012; Johnson 2020). The lower-scale expressions for the attachment-detachment rates close mass and momentum balance equations at the core scale (Bedrikovetsky 2013; Iliev et al. 2015; Ariane et al. 2018; Deshpande et al. 2020; Ciu and Sommerfeld 2015, 2022). At the upper scale, the torque balance given by Eq. (7) is expressed as maximum retention concentration versus velocity, Fig. 7 (Bedrikovetsky et al. 2011). The derivation of effective transport equations can be performed

using different upscaling techniques: random-walk models (Shapiro 2007), exact averaging in population-balance models (Bedrikovetsky 2008; Bedrikovetsky et al. 2019), continuous upscaling (Shapiro 2021, 2022), or numerical 3D network modelling (Bhuvankar et al. 2022; Cihan et al. 2022). In large-scale approximation, where dissipative and non-equilibrium fluxes are neglected if compared with the advective fluxes, the exact solutions are derived by non-linear modifications of method of characteristics using Riemann invariants (Polyanin & Zaitsev 2003; Polyanin et al. 2001b). The dissipative and non-equilibrium effects can be accounted for in analytical solutions by matching the asymptotic expansions (Polyanin & Dil'man 1994; Polyanin et al. 2001a).

6. Conclusions

CFD modelling of hydrodynamic force, SEI calculations of adhesion forces and direct visualisation experiments for unfavourable conditions allow drawing the following conclusions:

- Change in aspect ratio of spheroids and cylinders ($0.01 < \alpha < 1$) does not remove energy barrier for latex-glass interaction.
- The hydrodynamic shape factors previously proposed for Stokes flow is appropriate even for moderately high Re_p (< 50) conditions.
- Torque balance model is more effective in predicting particle detachment compared to the alternative rolling friction and DT model.
- Direct visualisation in unfavourable conditions matches the torque balance theory.
- The laboratory observations matched with the mathematical model for two-stage detachment suggest that secondary minimum retention is present in both latex spheres and kaolinite particles. For the first time, it was shown that natural particles (kaolinites) can exhibit a two-stage detachment process.

7. Data Availability

The data that support the findings of this study are available from the corresponding author upon reasonable request.

8. Declaration of Interests

The authors declare that they have no known competing financial interests or personal relationships that could have appeared to influence the work reported in this paper.

9. Acknowledgements

This work was supported with supercomputing resources provided by the Phoenix HPC service at the University of Adelaide. HZ Ting thanks the Adelaide Graduate Research Scholarship for financial support. The authors are deeply grateful to Eng. Yutong Yang (The University of Adelaide) for providing the laboratory data for kaolinite detachment, and to Dr. Themis Carageorgos (The University of Adelaide) for editing the text.

10. References

Albery, W, Fredlein, R, O'Shea, G & Smith, A 1990, 'Colloidal deposition under conditions of controlled potential', *Faraday Discussions of the Chemical Society*, vol. 90, pp. 223-234.

Appelo, C. A. J., & Postma, D. (2004). Geochemistry, groundwater and pollution. CRC press.

Aracena, K.D.L.Á.V., Uñac, R.O., Ippolito, I. and Vidales, A.M., 2020. Movement initiation of millimeter particles on a rotating rough surface: The role of adhesion. Particuology, 53, pp.92-99.

Ariane, M., Sommerfeld, M., & Alexiadis, A. (2018). Wall collision and drug-carrierdetachment in dry powder inhalers: Using DEM to devise a sub-scale modelfor CFD calculations. Powder Technology, 334, 65–75.

Bedrikovetsky, P 2008, 'Upscaling of stochastic micro model for suspension transport in porous media', *Transport in Porous Media*, vol. 75, no. 3, pp. 335-369.

Bedrikovetsky, P., 2013. Mathematical theory of oil and gas recovery: with applications to ex-USSR oil and gas fields (Vol. 4). Springer Science & Business Media.

Bedrikovetsky, P, Osipov, Y, Kuzmina, L & Malgaresi, G 2019, 'Exact upscaling for transport of size-distributed colloids', *Water Resources Research*, vol. 55, pp. 1011-1039.

Bedrikovetsky, P, Siqueira, FD, Furtado, CA & Souza, ALS 2011, 'Modified Particle Detachment Model for Colloidal Transport in Porous Media', *Transport in Porous Media*, vol. 86, no. 2, pp. 353-383.

Bergendahl, J & Grasso, D 2000, 'Prediction of colloid detachment in a model porous media: hydrodynamics', *Chemical Engineering Science*, vol. 55.

Bhattacharjee, S & Elimelech, M 1997, 'Surface Element Integration: A Novel Technique for Evaluation of DLVO Interaction between a Particle and a Flat Plate', *Journal of Colloid and Interface Science*, vol. 193, pp. 273-285.

Bhuvankar, P, Cihan, A & Birkholzer, J 2022, 'Pore-scale CFD simulations of clay mobilization in natural porous media due to freash water injection', *Chemical Engineering Science*, vol. 247.

Bradford, SA & Torkzaban, S 2015, 'Determining Parameters and Mechanisms of Colloid Retention and Release in Porous Media', *Langmuir*, vol. 31, no. 44, Nov 10, pp. 12096-12105.

Bradford, SA, Torkzaban, S & Shapiro, A 2013, 'A theoretical analysis of colloid attachment and straining in chemically heterogeneous porous media', *Langmuir*, vol. 29, no. 23, Jun 11, pp. 6944-6952.

Burdick, GM, Berman, NS & Beaudoin, SP 2001, 'Describing hydrodynamic particle removal from surfaces using the particle Reynolds number', *Journal of Nanoparticle Research*, vol. 3, pp. 455-467.

Cheng, S & Robbins, MO 2010, 'Defining Contact at the Atomic Scale', *Tribology Letters*, vol. 39, no. 3, pp. 329-348.

Chequer, L, Carageorgos, T, Naby, M, Hussaini, M, Lee, W & Bedrikovetsky, P 2021, 'Colloidal detachment from solid surfaces: Phase diagrams to determine the detachment regime', *Chemical Engineering Science*, vol. 229.

Cihan, A, Petrusak, R, Bhuvankar, P, Alumbaugh, D, Trautz, R & Birkholzer, J 2022, 'Permeability Decline by Clay Fines Migration around a Low-salinity Fluid Injection Well', *Groundwater*, vol. 60, no. 1, pp. 87-98.

Cui, Y., & Sommerfeld, M. (2018). Application of Lattice–Boltzmann method foranalysing detachment of micron-sized particles from carrier particles inturbulent flows. Flow Turbulence and Combustion, 100, 271–297.

Cui, Y. and Sommerfeld, M., 2022. Lattice–Boltzmann simulations for analysing the detachment of micron-sized spherical particles from surfaces with large-scale roughness structures. Particuology, 61, pp.47-59.

Deshpande, R., Antonyuk, S. and Iliev, O., 2020. DEM-CFD study of the filter cake formation process due to non-spherical particles. Particuology, 53, pp.48-57.

Dominik, C & Tielens, AGGM 1995, 'Resistance to rolling in the adhesive contact of two elastic spheres', *Philosophical Magazine A*, vol. 72, no. 3, pp. 783-803.

Dominik, C & Tielens, AGGM 1997, 'The Physics of Dust Coagulation and the Structure of Dust Aggregates in Space', *The Astrophysical Journal*, vol. 480, no. 2, pp. 647-673.

Duffadar, R, Kalasin, S, Davis, JM & Santore, MM 2009, 'The impact of nanoscale chemical features on micron-scale adhesion: crossover from heterogeneity-dominated to mean-field behavior', *J Colloid Interface Sci*, vol. 337, no. 2, Sep 15, pp. 396-407.

Farrell, N.J.C., Debenham, N., Wilson, L., Wilson, M.J., Healy, D., King, R.C., Holford, S.P. and Taylor, C.W., 2021. The effect of authigenic clays on fault zone permeability. Journal of Geophysical Research: Solid Earth, 126(10), p.e2021JB022615.

Flicker, S, Tipa, J & Bike, S 1993, 'Quantifying Double-Layer Repulsion between a Colloidal Sphere and a Glass Plate using Total Internal Reflection Microscopy', *Journal of Colloid and Interface Science*, vol. 158, pp. 317-325.

Fountouli, TV & Chrysikopoulos, CV 2020, 'Effect of Clay Colloid Particles on Formaldehyde Transport in Unsaturated Porous Media', *Water*, vol. 12, no. 12.

Gomez-Flores, A, Bradford, SA, Hwang, G, Choi, S, Tong, M & Kim, H 2020, 'Shape and orientation of bare silica particles influence their deposition under intermediate ionic strength: A study with QCM–D and DLVO theory', *Colloids and Surfaces A: Physicochemical and Engineering Aspects*, vol. 599.

Gomez-Flores, A, Bradford, SA, Wu, L & Kim, H 2019, 'Interaction energies for hollow and solid cylinders: Role of aspect ratio and particle orientation', *Colloids and Surfaces A: Physicochemical and Engineering Aspects*, vol. 580.

Gupta, V, Hampton, MA, Stokes, JR, Nguyen, AV & Miller, JD 2011, 'Particle interactions in kaolinite suspensions and corresponding aggregate structures', *J Colloid Interface Sci*, vol. 359, no. 1, Jul 1, pp. 95-103.

Huang, Q., Mesbah-Nejad, A., Tadayyon, S.M., Norton, P., Zhang, H. and Zhu, J., 2010. Measurement of inter-particle forces by an interfacial force microscope. Particuology, 8(5), pp.400-406.

Iliev, O., Kirsch, R., Lakdawala, Z., Rief, S., & Steiner, K. (2015). Modeling andSimlation of Filtration Processes. In Currents in Industrial Mathematics. pp.163–228. Springer.

Israelachvili, JN 2011, *Intermolecular and Surface Forces*, 3rd edn, Elsevier Inc., Amsterdam.

Johnson, KL 1985, *Contact mechanics*, Cambridge University Press.

Johnson, WP, Li, X, Tong, M & Ma, H 2009, 'Comment on "Transport and fate of bacteria in porous media: Coupled effects of chemical conditions and pore space geometry" by Saeed Torkzaban et al', *Water Resources Research*, vol. 45, no. 9.

Johnson, WP, Pazmino, E & Ma, H 2010, 'Direct observations of colloid retention in granular media in the presence of energy barriers, and implications for inferred mechanisms from indirect observations', *Water Res*, vol. 44, no. 4, Feb, pp. 1158-1169.

Johnson, W. P. (2020). Quantitative linking of nanoscale interactions to continuum-scale nanoparticle and microplastic transport in environmental granular media. Environmental Science & Technology, 54(13), 8032-8042.

Kieckhefen, P, Pietsch, S, Dosta, M & Heinrich, S 2020, 'Possibilities and Limits of Computational Fluid Dynamics-Discrete Element Method Simulations in Process Engineering: A Review of Recent Advancements and Future Trends', *Annu Rev Chem Biomol Eng*, vol. 11, Jun 7, pp. 397-422.

Knappenberger, T, Aramrak, S & Flury, M 2015, 'Transport of barrel and spherical shaped colloids in unsaturated porous media', *J Contam Hydrol*, vol. 180, Sep, pp. 69-79.

Kuznar, ZA & Elimelech, M 2007, 'Direct microscopic observation of particle deposition in porous media: Role of the secondary energy minimum', *Colloids and Surfaces A: Physicochemical and Engineering Aspects*, vol. 294, no. 1-3, pp. 156-162.

Li, L., Zeng, Y. and Liu, G., 2022. Metal-based nanoparticles for cardiovascular disease diagnosis and therapy. Particuology.

Liu, L, Meng, S, Li, C & Li, Y 2022, 'Revisiting the Theory of Coagulation of Colloidal Dispersions: An Improved Expression for the Stability Ratio', *Langmuir*, vol. 38, no. 3, Jan 25, pp. 1131-1140.

Liu, YY, Janjaroen, D, Kuhlenschmidt, MS, Kuhlenschmidt, TB & Nguyen, TH 2009, 'Deposition of Cryptosporidium parWum Oocysts on Natural Organic Matter Surfaces: Microscopic Evidence for Secondary Minimum Deposition in a Radial Stagnation Point Flow Cell', *Langmuir*, vol. 25, no. 3, pp. 1594-1605.

Ma, H, Li, Y, Shen, C, Chrysikopoulos, CV & Kim, H 2021, 'Advances in Pollutant Transport in Critical Zone Environments', *Frontiers in Water*, vol. 3.

Molnar, IL, Johnson, WP, Gerhard, JI, Willson, CS & O'Carroll, DM 2015, 'Predicting colloid transport through saturated porous media: A critical review', *Water Resources Research*, vol. 51, no. 9, pp. 6804-6845.

O'Neill, M. E. (1968). A sphere in contact with a plane wall in a slow linear shearflow. Chemical Engineering Science, 23, 1293–1298.

Pazmino, E, Trauscht, J & Johnson, WP 2014, 'Release of colloids from primary minimum contact under unfavorable conditions by perturbations in ionic strength and flow rate', *Environ Sci Technol*, vol. 48, no. 16, Aug 19, pp. 9227-9235.

Polyanin, AD & Dil'man, VV 1994, Methods of modeling equations and analogies in chemical engineering, CRC Press, Boca Raton, Fl.

Polyanin, AD, Kutepov, AM, Kazenin, DA & Vyazmin, AV 2001a, *Hydrodynamics, mass and heat transfer in chemical engineering*, vol. 14, CRC Press, London.

Polyanin, AD & Zaitsev, VF 2003, Handbook of Nonlinear Partial Differential Equations: Exact Solutions, Methods and Problems, Chapman and Hall/CRC, New York.

Polyanin, AD, Zaitsev, VF & Moussiaux, A 2001b, *Handbook of first-order partial differential equations*, CRC Press, London.

Prieve, DC, Bike, S & Frej, NA 1990, 'Brownian Motion of a Single Microscopic Sphere in a Colloidal Force Field', *Faraday Discussions of the Chemical Society*, vol. 90, pp. 209-222.

Rasmuson, A, Pazmino, E, Assemi, S & Johnson, WP 2017, 'Contribution of Nano- to Microscale Roughness to Heterogeneity: Closing the Gap between Unfavorable and Favorable Colloid Attachment Conditions', *Environ Sci Technol*, vol. 51, no. 4, Feb 21, pp. 2151-2160.

Sakai, M 2016, 'How Should the Discrete Element Method Be Applied in Industrial Systems?: A Review', *KONA Powder and Particle Journal*, vol. 33, no. 0, pp. 169-178.

Sakai, M., Mori, Y., Sun, X. and Takabatake, K., 2020. Recent progress on mesh-free particle methods for simulations of multi-phase flows: A review. KONA Powder and Particle Journal, 37, pp.132-144.

Schiller, L & Naumann, AZ 1935, 'A Drag Coefficient Correlation', *Ver Deut Ing*, vol. 77, pp. 318-320.

Seher, H, Geckeis, H, Fanghänel, T & Schäfer, T 2020, 'Bentonite Nanoparticle Stability and the Effect of Fulvic Acids: Experiments and Modelling', *Colloids and Interfaces*, vol. 4, no. 2.

Shapiro, A 2007, 'Elliptic equation for random walks. Application to transport in microporous media', *Physica A: Statistical Mechanics and its Applications*, vol. 375, no. 1, pp. 81-96.

Shapiro, AA 2021, 'Continuous upscaling and averaging', *Chemical Engineering Science*, vol. 234, pp. 1-13.

Shapiro, AA 2022, 'Continuous upscaling of the 3D diffusion equation in a heterogenous medium', *Chemical Engineering Science*, vol. 248.

Shapiro, AA & Yuan, H 2012, 'Application of stochastic approaches to modelling suspension flow in porous media', in A Skogseid & V Fasano (eds), *Statistical Mechanics and Random Walks: Principles, Processes and Applications*, Nova Science Publishers.

Sharma, M, Chamoun, H, Sarma, D & Schechter, R 1992, 'Factors Controlling the Hydrodynamic Detachment of Particles from Surfaces', *Journal of Colloid and Interface Science*, vol. 149, no. 1, pp. 121-134.

Shen, C, Jin, Y, Zhuang, J, Li, T & Xing, B 2019, 'Role and importance of surface heterogeneities in transport of particles in saturated porous media', *Critical Reviews in Environmental Science and Technology*, vol. 50, no. 3, pp. 244-329.

Sommerfeld, M., Cui, Y., & Schmalfuss, S. (2019). Potential and constraints for theapplication of CFD combined with Lagrangian particle tracking to dry powderinhalers. European Journal of Pharmaceutical Sciences, 128, 299–324.

Tang, FH, Alonso-Marroquin, F & Maggi, F 2014, 'Stochastic collision and aggregation analysis of kaolinite in water through experiments and the spheropolygon theory', *Water Research*, vol. 53, Apr 15, pp. 180-190.

Ting, HZ, Bedrikovetsky, P, Tian, ZF & Carageorgos, T 2021, 'Impact of shape on particle detachment in linear shear flows', *Chemical Engineering Science*, vol. 241.

Tong, M & Johnson, WP 2006a, 'Excess Colloid Retention in Porous Media as a Function of Colloid Size, Fluid Velocity, and Grain Angularity', *Environmental Science & Technology*, vol. 40, pp. 7725-7731.

Tong, M & Johnson, WP 2006b, 'Observed and Simulated Fluid Drag effects on Colloid Deposition in the Presence of an Energy Barrier in an Impinging Jet System', *Environ Sci Technol*, vol. 40, pp. 5015-5021.

Torkzaban, S, Walker, SL & Bradford, SA 2009, 'Reply to comment by William P. Johnson et al. on "Transport and fate of bacteria in porous media: Coupled effects of chemical conditions and pore space geometry"', *Water Resources Research*, vol. 45, no. 9.

Valenzuela Aracena, K. A., Benito, J. G., Oger, L., Ippolito, I., U˜nac, R. O., & Vidales, A.M. (2018). Frequency–amplitude behavior in the incipient movement of grainsunder vibration. Particuology, 40, 1–9.

Valenzuela Aracena, K. A., Oger, L., U˜nac, R. O., & Vidales, A. M. (2019). Resuspen-sion due to vertical oscillations: Experiments and numerical modeling. GranularMatter, 21, 51.

van der Westen, R, Sjollema, J, Molenaar, R, Sharma, PK, van der Mei, HC & Busscher, HJ 2018, 'Floating and Tether-Coupled Adhesion of Bacteria to Hydrophobic and Hydrophilic Surfaces', *Langmuir*, vol. 34, no. 17, May 1, pp. 4937-4944.

VanNess, K, Rasmuson, A, Ron, CA & Johnson, WP 2019, 'A Unified Force and Torque Balance for Colloid Transport: Predicting Attachment and Mobilization under Favorable and Unfavorable Conditions', *Langmuir*, vol. 35, no. 27, Jul 9, pp. 9061-9070.

Xu, A, Shi, L & Zhao, TS 2018, 'Thermal effects on the sedimentation behavior of elliptical particles', *International Journal of Heat and Mass Transfer*, vol. 126, pp. 753-764.

Ziskind, G., M. Fichman, and C. Gutfinger. 1995. Resuspension of particulates from surfaces to turbulent flows—review and analysis. J. Aerosol Sci. 26 (4):613–644. doi:10.1016/0021-8502(94)00139-P.

Ziskind, G., M. Fichman, and C. Gutfinger. 1997. Adhesion moment model for estimating particle detachment from a surface. J. Aerosol Sci. 28 (4):623–634. doi:10.1016/S0021-8502(96)00460-0.

Ziskind, G. 2006. Particle resuspension from surfaces: Revisited and re-evaluated. Rev. Chem. Eng. 22 (1–2): 1–123. doi:10.1515/REVCE.2006.22.1-2.1.

Yang, Y, Dang-Le, B, Kutty, G, Mbeveri, S, Carageorgos, T, Badalyan, A & Bedrikovetsky, P 2020, 'Kaolinite Detachment from Silica Substrate - Laboratory and Theoretical Study', *International Journal of Water and Wastewater Treatment*, vol. 6, no. 3.

This page is intentionally left blank

Chapter 6

Image interpretation for kaolinite detachment from solid substrate: Type curves, stochastic model

Statement of Authorship

Title of Paper	Image interpretation for kaolinite detachment from solid substrate: Type curves, stochastic model
Publication Status	☑ Published ☐ Accepted for Publication ☐ Submitted for Publication ☐ Unpublished and Unsubmitted work written in manuscript style
Publication Details	Ting, HZ, Yang, Y, Tian, ZF, Carageorgos, T & Bedrikovetsky, P 2022, 'Image interpretation for kaolinite detachment from solid substrate: Type curves, stochastic model', Colloids and Surfaces A: Physicochemical and Engineering Aspects, vol. 650.

Principal Author

Name of Principal Author (Candidate)	Heng Zheng Ting
Contribution to the Paper	Generation and analysis of numerical data, image processing and interpretation of experiment data, validation of analysis code and wrote manuscript.
Overall percentage (%)	50%
Certification:	This paper reports on original research I conducted during the period of my Higher Degree by Research candidature and is not subject to any obligations or contractual agreements with a third party [redacted] on in this thesis. I am the primary author of this paper.
Signature	[redacted] Date 24/02/2023

Co-Author Contributions

By signing the Statement of Authorship, each author certifies that:

i. the candidate's stated contribution to the publication is accurate (as detailed above);

ii. permission is granted for the candidate in include the publication in the thesis; and

iii. the sum of all co-author contributions is equal to 100% less the candidate's stated contribution.

Name of Co-Author	Yutong Yang
Contribution to the Paper	Ran visualisation experiments for kaolinite, wrote numerical codes for Monte Carlo and fitting the laboratory results, assessed and reviewed the manuscript.
Signature	[redacted] Date 24/02/2023

Name of Co-Author	Zhao Feng Tian
Contribution to the Paper	Co-supervised the development of the work, reviewed and assessed the manuscript.
Signature	[redacted] Date 24/02/2023

Name of Co-Author	Themis Carageorgos
Contribution to the Paper	Co-supervised the development of the work, reviewed and assessed the manuscript.
Signature	Date 24/02/2023

Name of Co-Author	Pavel Bedrikovetsky
Contribution to the Paper	Formulated the problem, co-supervised the development of the work, reviewed and assessed the manuscript.
Signature	Date 24/02/2023

Colloids and Surfaces A: Physicochemical and Engineering Aspects 650 (2022) 129451

Contents lists available at ScienceDirect

Colloids and Surfaces A: Physicochemical and Engineering Aspects

journal homepage: www.elsevier.com/locate/colsurfa

Image interpretation for kaolinite detachment from solid substrate: Type curves, stochastic model

Heng Zheng Ting [a], Yutong Yang [b], Zhao Feng Tian [a], Themis Carageorgos [b], Pavel Bedrikovetsky [b,*]

[a] School of Mechanical Engineering, The University of Adelaide, Adelaide 5000, SA, Australia
[b] Australian School of Petroleum and Energy Resources, The University of Adelaide, Adelaide 5000, SA, Australia

HIGHLIGHTS

- Gradual particle detachment is explained by probabilistic distributions of properties.
- The properties are semi-major axis, aspect ratio, lever arm ratio and zeta potentials.
- Type curve "retained concentration vs velocity" monotonically decreases.
- The type curve has a plateau in the case of unfavourable attachment.
- The model allows calculating particle concentrations in both energy minima.

GRAPHICAL ABSTRACT

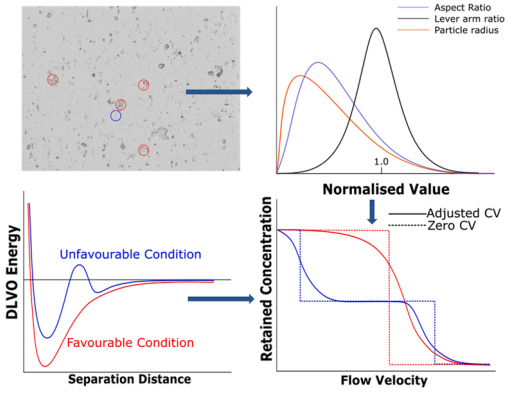

ARTICLE INFO

Keywords:
Kaolinite particles
Direct visualisation
DLVO Theory
Colloidal mobilisation
Stochastic modelling, Irregular shaped particles

ABSTRACT

Kaolinite clays are the most widespread natural fines attached to the rock surface; they can be mobilised by the flow with further migration in porous spaces, straining in thin pore throats and causing significant decline in the rock permeability. We conducted mathematical and laboratory studies of kaolinite detachment from solid substrates in visualisation cells. The mechanical equilibrium of the attached particles in the creeping flow was described by the torque balance. For uniform particles and substrates, this model presents fines detachment using only two rates that correspond to particles in primary and secondary energy minima, i.e., the attached concentration versus velocity is a piecewise-constant function. To observe this maximum retention function, we saturated a single-channel micromodel visualisation cell with a transparent top with kaolinite particles; it was then subjected to a flow with a piecewise-constant increasing rate. Images of the remaining attached fines were filmed after each rate increase. All the tests exhibit gradual fines detachment. To explain the phenomenon, we assumed a probabilistic distribution of the properties of the particles and the substrate. For two-parametric probability distribution functions, it adds the standard deviations to the list of model parameters. The continuous fines detachment versus velocity was highly matched by the torque balance equation with probabilistically distributed coefficients. The match allowed restoring probabilistic distributions of the selected model parameters

* Corresponding author.
E-mail address: pavel@asp.adelaide.edu.au (P. Bedrikovetsky).

https://doi.org/10.1016/j.colsurfa.2022.129451
Received 6 April 2022; Received in revised form 6 June 2022; Accepted 9 June 2022
Available online 13 June 2022

from the measured maximum retention function. The sensitivity of the detachment rate to properties follows a decreasing order: semi-major axis, aspect ratio, lever arm ratio, and zeta potential. This work fundamentally advances lab-based mathematical modelling of colloidal detachment from solid surfaces by developing stochastic torque-balance equation, where standard deviations of the model coefficients are tuning / matching parameters along with their mean values. This approach allows determining the probabilistic distributions of the model coefficients from the image processing, and also calculating the attached concentration variation within six standard deviations of each parameter, permitting placing the model parameters in the order of their effect on particle detachment.

Nomenclature

a	semi-major axis of oblate spheroid.
A	cross sectional area of the visualisation cell.
b	semi-minor axis of oblate spheroid.
D	distance of closest separation.
F_a	adhesion force.
F_d	drag force.
F_l	lift force.
F_g	gravitational force.
F_{DLVO}	DLVO force.
f_d	drag shape factor.
f_l	lift shape factor.
f_M	moment shape factor.
k_B	Boltzmann constant.
l_r	lever arm ratio (l_d/l_n).
l_d	lever arm for drag force.
l_n	lever arm for normal force.
L	height of the visualisation cell.
M	moment exerted by drag.
Q	volumetric flow rate.
Re_p	particle Reynolds Number.
r_e	volume equivalent sphere radius.
T	absolute temperature.
U	interaction potential energy.
v	area-averaged velocity.
v_{cr}	critical detachment velocity.
W	channel width.
$\overline{x}$	mean.

Greek Symbols

α	aspect ratio (b/a).
$\dot{\gamma}_o$	shear rate.
μ	fluid dynamic viscosity.
μ_s	static coefficient of friction.
ρ	density.
σ	standard deviation.
ζ	zeta potential.

Subscripts

vdw	Van Der Waals.
edl	Electrical double layer.
cr	Critical.
k	Kaolinite.
g	Glass.

1. Introduction

Kaolinite is one of the most prevalent clay minerals on the earth's crust. The clay mineral has useful applications in various manufacturing fields such as paper, plastics, pharmaceuticals, rubber and paint [1,2]. In many cases, the presence of kaolinite either enhances or retards the transport of other colloidal particles such as contaminants, microorganisms, pesticides, fertilisers, and drugs [3–7]. Pertaining to the petroleum industry, kaolinite is the main source of fines, leading to fines migration and formation damage, and thereby causing major well-productivity loss [8,9]. However, fines migration decelerates injected water in oilfields and results in enhanced oil recovery for chemical and low-salinity flooding [10–15]. Therefore, it is important to understand and characterise the detachment of kaolinites from surfaces. Fines attachment and detachment in porous and fractured media and their modelling is currently a hot research topic [7,16–18].

Kaolinite is a 1:1 layer clay that comprises one tetrahedral silica sheet and one octahedral alumina sheet, bonded by sharing oxygens and hydroxyls between the sheets [2]. Kaolinites have broad size distributions, ranging from 0.2 μm platelets, up to 50 μm for stacks and aggregates [19]. Similarly, the clay mineral also exists in a wide range of aspect ratios (height/width), from 0.03 to 0.5, depending on the clay source, structure and measurement methodology [20–23].

Most experimental studies on particle detachment use polystyrene latex spheres as the material for particles [24,25], which are uniform, spherical and well-defined [26]. However, unlike latex, kaolinite exists not just as a regular platelet, but also as stacks and aggregates [1]. In fact, the geometry of the kaolinite particles/aggregates can be complicated. Depending on the pH and salinity of the solution, it is frequently reported that individual kaolinite platelets can form aggregates through association at the kaolinite edge-edge (E-E), edge-face (E-F), face-face (F-F) or a combination of the three [27–29].

Noting the great diversity in the size, structure, and shape of kaolinites, it follows that modelling their detachment can be challenging. Some works approximate kaolinites as spheres of varying radii. For example, Won and Burns [30] modelled the transport of kaolinite through a sand filter by using a stochastic approach to account for the size distribution of the sand and spherical kaolinite particles. Random sampling of measured kaolinite and sand sizes allows modelling the upper and low breakthrough curves. It was found that the experimental breakthrough curve lays between the upper and low breakthrough curves. Similarly, Yang et al. [31] used a torque balance model for spheres and found a good match with the gradual detachment of kaolinite particles observed in direct visualisation experiments.

The advantage of visualisation tests with image filming if compared with coreflooding is that the attached concentration can be determined from the images, while breakthrough concentrations are too low to be measured. Visualisation tests with image analysis but without mathematical modelling have been performed in [9,32,33].

The important parameters affecting fines detachment are particle size [34–37], aspect ratio [38–40], deposition angle [40,41] and aggregate structure [28]. However, the effects of probabilistic distribution of those parameters on the clay fines detachment has not been investigated. In addition, there has yet to be a systematic study to rank the relative importance of the described parameters in terms of particle detachment.

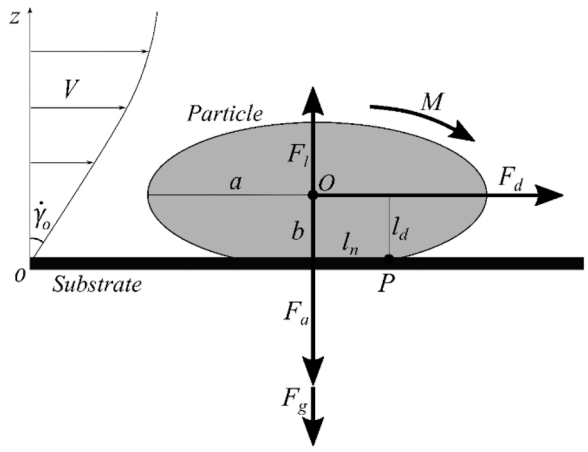

Fig. 1. Forces and moments acting on an oblate spheroid particle attached to a wall under shear flow.

Some works account for the impact of salinity and pH on the structure of the kaolinite aggregates and their consequent detachment [28,42,43]. In column filtration experiments at 0.004 M NaCl, the detachment of kaolinite was shown to be nonmonotonic with changes in pH (3 <pH<8) [28]. Starting from pH 3, the detachment rate of kaolinite peaked at pH 5, before being reduced to the lowest rate at pH 8. Song and Kovscek [9] also directly visualised significant detachment of kaolinite in response to low salinity flushing and consequent plugging of pore throats. However, the studies were qualitative and neither considered the impact of hydrodynamic forces, nor offered any mechanistic models to predict the detachment criteria. Absence of these data significantly restrains the mathematical modelling of colloid-suspension transport in porous media [44–47].

Several authors account for the probabilistic distributions of colloid and substrate parameters in the mathematical modelling and explained gradual fines detachment by probabilistic distributions of parameters. Burdick et al. [48] performed the visualisation test and measured distributions of particle and asperity sizes. The detachment has been calculated using torque balance. The quantitative agreement with lab data was observed. No experimental data matching by the model was performed. The model considered favourable attachment only.

Goldasteh et al. [49] and Nasr et al. [50] performed visualisation tests on glass beads detachment from plane substrate under turbulent wind flow. Surface roughness and particle size distributions were measured. The attaching adhesion force was calculated using Van Der Waals expression, so the attachment was favourable only. The torque balance model was used to model fines detachment. Only mean values of parameters of surface roughness and particle size have been tuned for an optimal matching.

Visualisation tests with latex particle detachment from glass substrate have been performed by Chequer et al. [51]. The paper introduces phase diagrams that determine areas in the velocity-salinity space where rolling, sliding, and lifting of detaching fines occur. The mathematical model assumes stochastic distribution of surface roughness in torque-balance equation, yielding close agreement with experimental image-based data. The tests have been performed using engineered spherical latex particles only.

Finally, the list of model parameters in mechanical-equilibrium equations lacks shape factor for irregular form particles, the stochastic torque-balance equation was applied for favourable conditions only, and standard deviations of the model parameters have not been tuned for the optimal experimental data matching by the stochastic model.

The present paper fills these gaps. We developed a stochastic torque balance that allows for the variation in kaolinite aspect ratio and lever arm ratio, and accounts for unfavourable attachment. For normal and log-normal parameter distributions, standard deviations are added to the list of tuning parameters. This allows determining the model parameter distributions from the image processing and permits the parametric study to determine the primary physical factors that influence the detachment of kaolinite from surfaces, counting the variations within six standard deviations. It was found that the intermediate plateau in the curve "attached concentration vs velocity" indicates two mechanisms for particle attachment-detachment; the height of the plateau determines the fractions of the particles attached in primary and secondary minima. The numerical model was then fitted to direct visualisation of kaolinite detachment for both favourable and unfavourable conditions, resulting in high match.

2. Formulation of the problem

2.1. Physics of particle detachment in a shear flow

The kaolinite particle/aggregate is modelled as an oblate spheroid attached to a fixed infinite plane (Fig. 1). Hele-Shaw flow occurs between two parallel planes [52,53]. Near-wall flow is approximated by linear shear flow with a shear rate of $\dot{\gamma}_o$. The size and shape of the particle is quantified using the volume equivalent sphere radius, r_e and the aspect ratio, α, respectively. Here, the aspect ratio, $\alpha = b/a$; where a is the semi-major axis and b is the semi-minor axis of the spheroid.

2.2. Force and torque balance

As shown in Fig. 1, four main forces of drag, F_d, lift, F_l, gravity, F_g and adhesion, F_a act on the particle [39,48,54]. The equilibrium of forces and torques of the four forces was used to predict the detachment of kaolinite. It was assumed that detachment occurs when any one of the inequalities is achieved, yielding either rolling, sliding or lifting [55–57], such that:

$$\text{Rolling}: M + F_l l_n > \left(F_g + F_a\right) l_n, \tag{1}$$

$$\text{Sliding}: F_d > \mu_s\left(F_g + F_a - F_l\right), \tag{2}$$

$$\text{Lifting}: F_l > F_g + F_a, \tag{3}$$

where M is the moment exerted by the drag force, l_n is the normal lever arm and μ_s is the static coefficient of friction. Here, only the rolling mode of detachment was considered, as it was previously shown to be the most dominant mode of spheroid detachment [38]. The gravitational force, F_g, is calculated as:

$$F_g = \frac{4}{3}\pi r_e^3(\rho_k - \rho). \tag{4}$$

ρ_k and ρ are the density of kaolinite (2650 kg/m^3) and water (997 kg/m^3) respectively [58].

2.3. Hydrodynamic forces

The hydrodynamic forces of drag and lift, exerted on the attached particle against the attaching adhesion and gravitational forces, trigger the kaolinite detachment. For spheroids, the drag, F_d, the lift, F_l, and the moment of drag, M, are expressed as in [38,59,60]:

$$F_d = 6\pi\mu r_e^2 \dot{\gamma}_o f_d, \tag{5}$$

$$F_l = 9.22 r_e^4 \dot{\gamma}_o^2 \rho f_l, \tag{6}$$

$$M = F_d l_d f_M. \tag{7}$$

Here, μ is the dynamic viscosity of water and l_d is the lever arm for drag. The factors f_d, f_l and f_M are the drag, lift and moment shape factors, respectively. These shape factors account for the presence of the wall and for the shape of the particle. Indeed, the absence of the wall (when f_d

= 1) yields the Stokes formula for a spherical particle [52,53]. Computational Fluid Dynamics (CFD) model assumes non-deformable particle and substrate. No-slip boundary conditions are set at the liquid-particle and liquid-substrate surfaces for Navier-Stokes equation. Numerical solution of the 3D flow problem allows calculating the total drag F_d and moment M via an integral of normal component of the pressure drop and tangent shear stress over the particle-liquid surface. The volume equivalent sphere radius, r_e is calculated from the formula for the volume of oblate spheroid:

$$r_e = \left(a^2 b\right)^{\frac{1}{3}} \tag{8}$$

The shear, $\dot{\gamma}_o$ on the substrate is calculated from the quadratic velocity distribution for Hele-Shaw flow between the parallel planes [52,53]:

$$\dot{\gamma}_o = \frac{6Q}{WL^2} \tag{9}$$

Here, Q is the volumetric flow rate, L is the distance between the parallel planes, W is the width of the cell, and v is the velocity:

$$Q = vWL \tag{10}$$

Finally, the factors f_d and f_M are calculated as the proportionality coefficients in Eqs. (5) and (7). The dependence of the shape factor on the aspect ratio of the oblate spheroid has previously been evaluated as [38]:

$$f_{d,Sphd} = \left(0.8707\alpha^2 + 0.7908\alpha + 0.05844\right)\left(\alpha + 0.008453\right)^{-1}, \tag{11}$$

$$f_{M,Sphd} = \left(1.296\alpha^2 + 0.1509\alpha + 0.03718\right)\left(\alpha^2 + 0.0843\alpha + 0.0002284\right)^{-1}, \tag{12}$$

Eqs.(11) and (12) are valid for $0.025 < \alpha < 1$ and $Re_p < 1$ ($Re_p = \rho\dot{\gamma}_o r_e^2/\mu$). For low Reynolds numbers typical for the Tests 1–4 ($Re_p <$ 0.014) of the current work, lift and gravity are negligible compared with drag and is dropped from Eq. (1) further in the text.

2.4. Adhesion force

The adhesion force provides the main attachment force that resists detachment. It was modelled using the Derjaguin-Landau-Verwey-Overbeek (DLVO) theory, where the interaction potential energy, U, between the kaolinite and the substrate is the summation of the van der Waals and electric double layer [61,62]. The Born repulsion force [63] was included to allow for reversible deposition in the primary minimum such that:

$$U = U_{vdw} + U_{edl} + U_{born} \tag{13}$$

$$F_{DLVO} = -\frac{dU}{dD} \tag{14}$$

The DLVO force, F_{DLVO}, is equal to the minus energy gradient. D is the closest separation distance between the particle and the plate surface. The conventional formulae for energy potentials in Eq. (13) are given by Eqs. (S2-S4) following the works [64,65].

The adhesion force, F_a is defined as the maximum attaching DLVO force [64]. The adhesion force is calculated from the conditions of maximum for F_{DLVO} (D), i.e. for D-value where second derivative of energy, U is equal zero, and third derivative is positive. For unfavourable conditions (where an energy barrier is present), another adhesion force could also be obtained for the secondary minimum [66].

As we approximated kaolinite particles as an oblate spheroid, the surface element integration (SEI) method [65] was used to determine the interaction potential of oblate spheroids of various aspect ratios with an infinite flat plate. Further details of the SEI method and the calculations of the van der Waals, electric double layer and Born force are provided in the Supplementary Materials (Eqs. (S1)-(S4)).

2.5. Mechanical equilibrium of attached fines with stochastic coefficients

To account for the variability of natural kaolinite, stochastic inputs were used for the torque balance Eq. (1). We accounted for the variation in kaolinite size and shape through the semi-major axis and the aspect ratio (a and α, respectively). Semi-major axis, a was chosen instead of r_e because the semi-major axis could be measured directly by the image software in the flow visualisation experiment under the microscope (Section S3, Fig. S2). To account for asperities that could affect the effective lever arm, the lever arm ratio, l_r ($=l_d/l_n$) for the torque balance was also varied as a parameter [51]. Finally, the variation in the surface charge of the kaolinite particle was considered using a distribution of zeta potentials, ζ, for kaolinite and glass.

The aspect ratio, α and the semi-major axis of the oblate spheroid, a are distributed log-normally; the mean and standard deviation are available from the literature [21] and our laboratory measurements. We assume normal distributions for the lever arm ratio and zeta potential due to the lack of better data. The correlations between those four parameters are neglected.

It was previously shown that the lift and gravitational forces are negligible for particle detachment as they are consistently several orders of magnitude lower than drag [38]. By excluding lift and gravity and rearranging the torque balance in Eq. (1) accounting for Eqs. (8)–(10), the critical velocity for kaolinite detachment, v_{cr} is given as:

$$v_{cr} = \frac{F_a L}{36\pi\mu r_e^2 l_r f_m f_d} \tag{15}$$

2.6. Sensitivity study

The sensitivity of the model to each individual parameter was evaluated by keeping the four other parameters unchanged while allocating only the parameter of interest as a distribution. The resulting output range in the detachment velocity indicates the significance of the parameter. Only data generated within a 95% confidence interval of the input distribution was considered to avoid outliers.

2.7. Optimisation fit

Running a Monte Carlo simulation of Eq. (15) generated a cumulative probability distribution curve for the detachment velocities with retained kaolinite concentration. The curve was fitted by optimisation to the direct visualisation experiment data using the genetic algorithm, (*ga*) function in the MATLAB Optimisation Toolbox (R2021b). The *ga* function optimises and calculates the mean and standard deviation for the input parameters (α, a and l_r), so that it minimises the velocity difference, Δv_{cr} between each simulated point with the observed detachment velocity from the visualisation experiments.

3. Laboratory study

Direct visualisation studies were conducted to compare the detachment of kaolinites with the torque balance model. Here, the details of the experiments are presented.

3.1. Materials: fluids and solids

A single-channel micromodel visualisation cell (Ibidi, Germany) with transparent top (plastic) and bottom (borosilicate glass coverslip) planes was used for the visualisation experiments. The cells used had a height, L of 450 μm, width, W of 5 mm, and length of 49.2 mm. The cells were hollow, i.e., no grains to model a pore structure were used. The cover slip surface was cleaned by consecutive soakings in acetone, ethanol, and MilliQ water. The surfaces were then dried at room temperature for 48 h.

To quantify the attached particle concentration, we used the Image

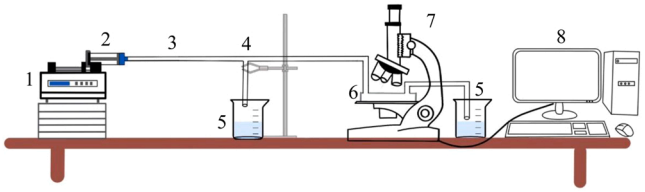

Fig. 2. Laboratory setup for visualisation of kaolinite detachment. Schematic: 1 – syringe pump, 2 - glass syringe, 3 - pipe flow, 4 - three-way valve, 5 - beakers, 6 – visualisation cell, 7 - optical microscope, 8 - desktop computer.

Processing Toolbox in MATLAB. The retained concentration of kaolinite after each flow increment was determined based on the microscope image taken in each consecutive step. The kaolinite particles were discretised from the background through image binarisation by specifying a threshold. To filter out noise during the binarising process, we specified a cut-off limit of $a < 1.5$ μm (Fig. S2 of the Supplementary Material presents an example of the image binarisation). This limiting value was based on the minimum resolution of the optical microscope. As there are five different slide locations sampled for each velocity increment, the retained concentration of kaolinite was averaged over the five data sets. Similar method to evaluate concentrations of attached particles from images have been developed in works [67–69].

The kaolinite particles used in the experiments are supplied by Sigma-Aldrich; the particle size varied from 2 to 10 μm. The injected solutions were prepared to the desired salinity by adding sodium chloride to deaerated deionised (DI) water. A Mettler Toledo conductivity meter was used to measure the conductivity of the solutions. Similarly, hydrochloric acid (HCl) and sodium hydroxide (NaOH) were added to control the pH values. The pH values were evaluated by a Mettler Toledo pH meter. Prior to injection into the visualisation cell, the saline solution with the suspended kaolinite particles was placed in an ultrasonic bath to minimise gravity sedimentation.

3.2. Zeta potential measurements

The Malvern Zetasizer Nano Z (UK) was used to measure the zeta potentials, ζ of the kaolinite suspensions with different salinity and pH values. The suspensions were diluted to the required concentration and injected into a conductive Zetasizer glass cell and five consecutive measurements of the zeta potentials of the kaolinite particles were performed. Measurements were repeated after 48 h to ensure measurement accuracy.

The zeta potential for the borosilicate glass of the Ibidi cell was determined based on the crushed and ground glass of the cell bottom using the same Malvern Zetasizer. The composition of the matter is: 73 wt% of SiO_2, 10% B_2O_3, 7% Na_2O, 7% Al_2O_3 and 3% of CaO. The measured zeta potential values for kaolinite and glass are presented in Section S4 of the Supplementary Material.

3.3. Laboratory setup

Fig. 2 illustrates the laboratory setup for the flow visualisation experiment. The pumping system comprised a Monojet 180 ml syringe fixed on a Cole Parmer dual syringe pump, which delivers the required flow rates at the admissible accuracy. The syringe outlet is connected to a three-way valve through plastic tubing. This valve enables the injection of fluids without the presence of air bubbles that can cause disturbances to the test. The cell is fixed on an Olympus BX51 optical microscope deck. The microscope has a camera on the top, equipped with Soft Imaging System's Colorview III camera and AnalySIS Life Sciences' software to control the camera. The microscope is connected to a computer: the software allows photograph images to be taken in real time. STREAMLINE software (Olympus) takes images for 5 chosen 'spots' along the length of the cell. More detailed description of the laboratory setup is available from Chequer et al. [51].

Table 1
Details of the pH, salinity and concentration used for the kaolinite visualisation experiments.

Test	1	2	3	4
Salinity (M NaCl)	0.3		0.01	0.000128 (DI)
pH	3		11	11
Kaolinite concentration (ppm)	300	150	300	300

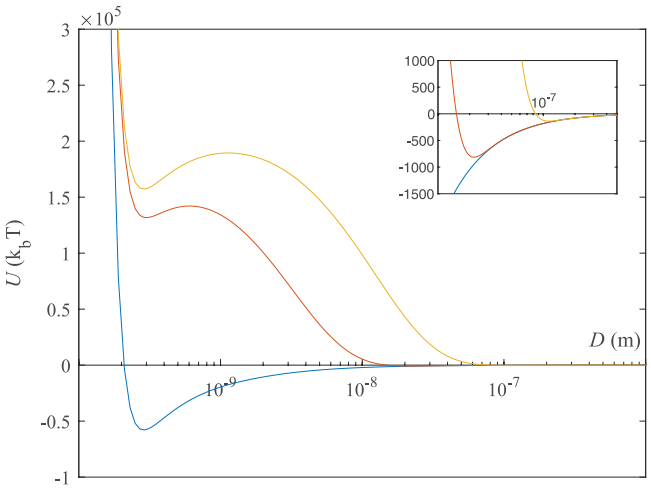

Fig. 3. DLVO energy profiles for Tests 1, 2, 3 and 4. The kaolinite particles have $r_e = 5$ μm, $\alpha = 0.2$ attached to glass. The blue line is for Tests 1 and 2 (0.3 M, pH 3); the red line for Test 3 (0.01 M, pH 11) and the yellow for Test 4 (DI, pH 11). The inset graph is a magnified portion to show the secondary minimum where D > 10 nm.

3.4. Experimental procedure/methodology

Four sets of visualisation experiments were conducted under varying salinity and pH conditions, as specified in Table 1. Tests 1 and 2 were undertaken with identical pH and salinities, only varying the initial kaolinite saturation concentration. Referring to Fig. 3, the pH and salinity conditions for Tests 1 and 2 correspond to favourable conditions. Tests 3 and 4 were under unfavourable conditions.

The kaolinite suspension with concentrations of either 150 ppm or 300 ppm was injected via a 5 ml syringe into the cell to saturate the substrate. The plastic tubing was flushed several times with solution to remove any foreign particles and air bubbles. The salinity and pH of the solution are kept constant throughout the experiment. The cell was left to rest for at least two hours to allow for a complete saturation of the cell bottom by the kaolinite particles, before connecting the tubing for further particle-free fluid injections.

Afterwards, we injected the particle-free solutions with piecewise-constant increasing rates until image stabilisation is achieved. In other words, the next flow rate is only applied after no further particle detachment is observed with the previous flow. The flow rates, Q applied in the tests vary from 0.0027 ml/min to 135 ml/min. This corresponds to velocities, v, of 2×10^{-5} m/s to 1 m/s. The exact velocities are detailed in Tables S1 and S2 of the Supplementary Material. The stabilisation time between each step ranges from 5 s to 10 h; the lowest flow rates required the maximum stabilisation time and vice versa.

4. Results

4.1. DLVO energy and force profiles

The DLVO energy and force profiles for kaolinite and glass [40,41,

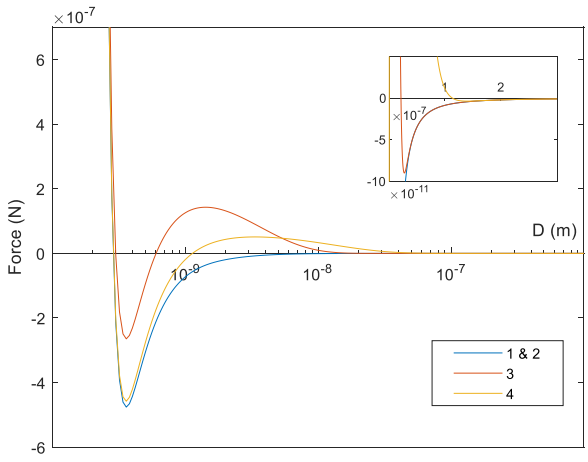

Fig. 4. DLVO force profiles for Test 1, 2, 3 and 4. The kaolinite particles are of $r_e = 5$ μm, $\alpha = 0.2$ attached to glass. The blue line is for Tests 1 and 2 (0.3 M, pH 3), the red lines for Test 3 (0.01 M, pH 11) and the yellow for Test 4 (DI, pH 11). The inset graph is a magnified portion to show the secondary minimum where D > 10 nm.

70] are shown in Fig. 3. The experiments conducted span both the favourable (Tests 1 and 2) and unfavourable regions for attachment (Tests 3 and 4). Here T is the absolute temperature and k_B is the Boltzmann constant.

According to Fig. 3, there should theoretically be one location of attachment at the primary minima for the favourable conditions. As for the unfavourable conditions, there are theoretically two possible points of attachment, corresponding to the primary and secondary minima.

The DLVO force profiles in Fig. 4 depict the variation of DLVO forces with varying distance [37,70,71]. The magnitude of the minima is taken as the adhesion force. The adhesion force at the primary minima for Test 1 and Test 4 seems to be of similar magnitude.

4.2. Favourable attachment

Focusing first on favourable conditions, a set of images from the direct visualisation for kaolinite is presented in Fig. 5. The red circles mark the locations of fines detachment. The pairs of red circles in the couples of sequential images show a particle present in a previous circle and its disappearance in the following circle. Each of the five red circles in image 0 of Fig. 5 contains one particle, while the particles disappear in the same circles in image 1.

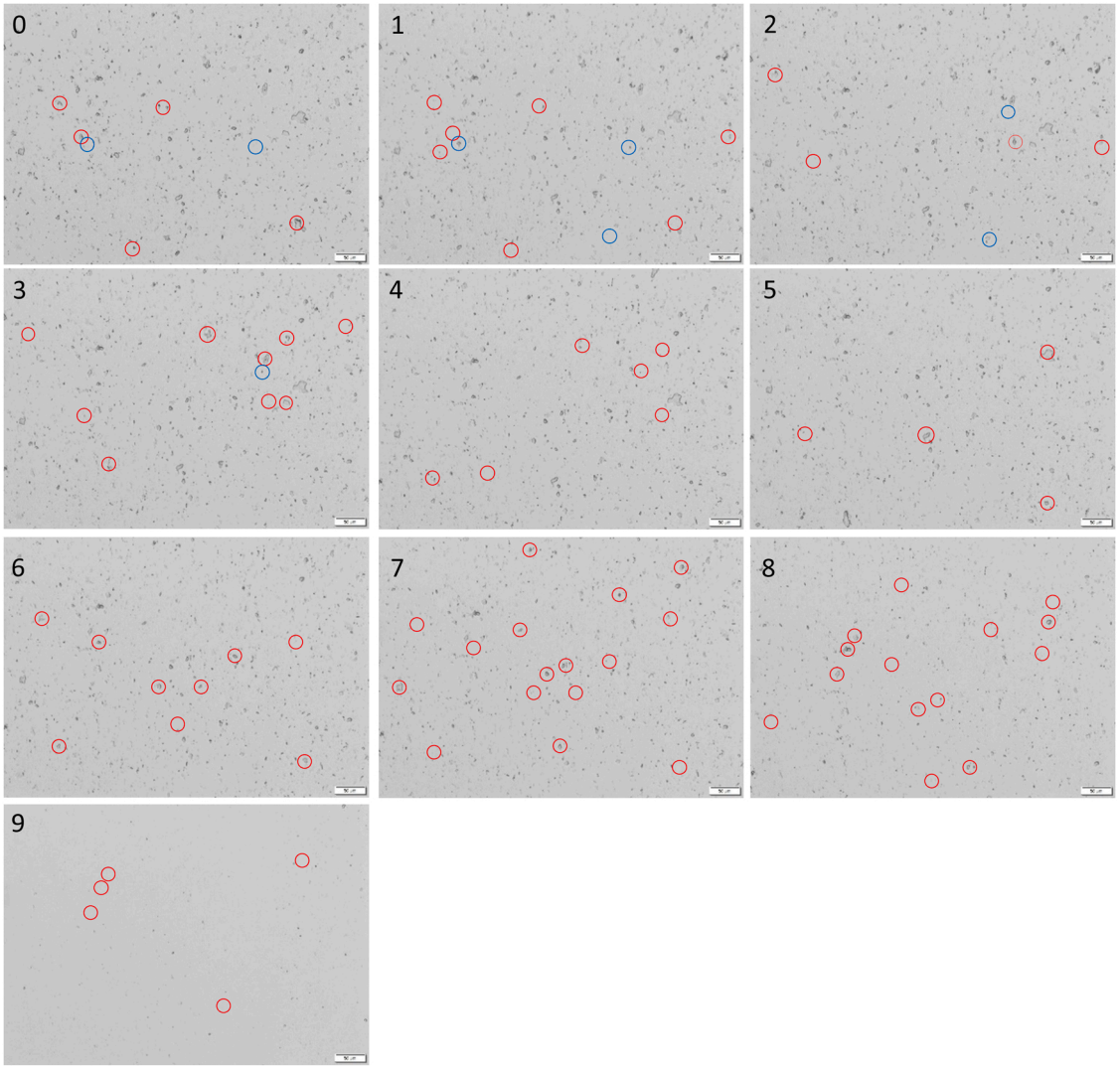

Fig. 5. Images of Test 1 with velocity increments over 9 steps (0.3 M, pH 3, 300 ppm kaolinite particles). The flow direction is from top to bottom of the images. The red and blue circles highlight kaolinite particles that will either detach or reattach respectively in the next image corresponding to the velocity increment. The circles do not mark all the detachments and reattachments but only highlight obvious examples.

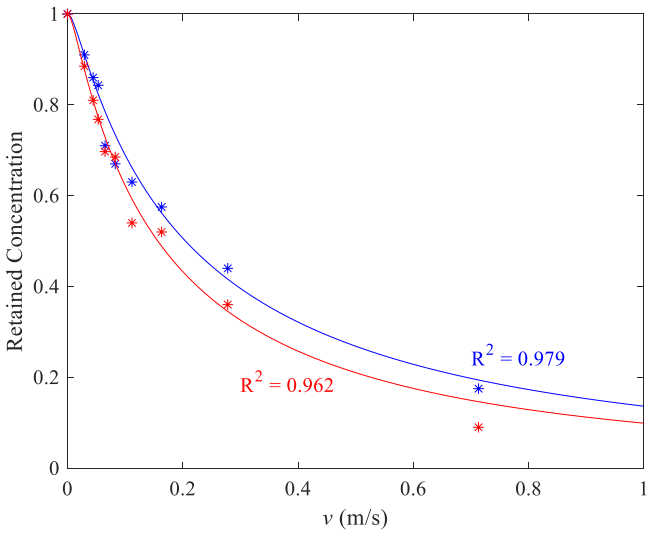

Fig. 6. Plot of retained kaolinite concentration versus averaged flow velocity. The solid lines are fitted over the experiment data plotted as (*). The blue and red curves represent Tests 1 and 2 respectively.

Similarly, the locations of fines reattachment are marked by blue circles. The pairs of blue circles in the couples of sequential images show a particle absent in a previous circle and its appearance in the subsequent circle. Two blue circles in image 0 of Fig. 5 are empty, while particles appear in the same circles in image 1, which indicates particle reattachment at those locations.

The visualisation allows many details to be observed that would otherwise not be possible through core flooding experiments. Both detachment and reattachment are observed in the images. Detachment occurs throughout every image frame, while reattachment occurred only in the earlier stages where the flow velocity was low.

The mathematical modelling in Fig. 6 shows close matching of the retained concentration points counted from the direct visualisation experiment and fitted with the optimisation code. The respective R^2 shows a good fit between the simulations with both sets of the laboratory data.

4.3. Unfavourable attachment

Fig. 7 shows the images obtained from the flow visualisation laboratory for kaolinites under the unfavourable condition of DI and pH 11. Unlike favourable conditions where there is detachment throughout, a transition stage of little to no detachment was observed between frames 4 and 5: a seemingly two-stage detachment phenomenon. Another set of the visualisation data for test 3 is provided in Fig S3 of the Supplementary Material.

Fig. 8 shows the matching of the stochastic torque balance model with the two sets of experiments completed under unfavourable conditions. Referring first to the laboratory results, the two-stage detachment is observed in both sets of experiments. If the detachments were attributed to the primary and secondary minima respectively, the percentage of primary deposition was 80% in Test 3 and 32% in Test 4.

The solid lines in Fig. 8 show the curve fitted with the torque balance model. Test 3 exhibits a better fit than Test 4. In Test 4, the observed detachment was significantly less than that predicted by the torque balance at low velocities, particularly for steps 0–1 (detachment from the secondary minimum). Noting that steps 0–1 of Test 4 also had the most significant amount of reattachment compared to the other 3 tests, we suggest that the deviation is due to reattachment.

Finally, the dashed lines in Fig. 8 indicate the effect of reducing the standard deviation of the input parameters by 1/3. Reducing the standard deviation to zero reproduces the step curve predicted by deterministic models. The converse of broadening the uncertainty was not so successful, as some of the input parameters would then be of negative values.

4.4. Sensitivity analysis

In modelling the detachment of kaolinites, we attempted to identify the most significant parameters that will affect the goodness of the fit.

The PDFs (probability distribution functions) for α, a, l_r and ζ are detailed in Table 2. The data for α was adapted from the literature, which uses a Scanning Electron Microscopy (SEM) to measure the side-on (height to width) aspect ratio of kaolinite particles [21]. The probability distribution for a was determined from the direct visualisation experiment using image processing (Section S3 of Supplementary Material). For the lever arm ratio, the probability distribution was not given in the reference [72]. Assuming normal distribution, the median between the upper (307) and lower limit (84) of the experiment data was taken as the mean; the difference between the median and upper and lower limits was divided by three to obtain the standard deviation. Finally, for ζ, the measured values were taken as the mean while the standard deviation was taken as the error margin provided by the manufacturer of $\pm$ 10%.

Using the input probability distributions as listed in Table 2, Fig. 9 shows the sensitivity of the critical detachment velocity, v_{cr} toward the five input parameters. The parameters ranked in order of decreasing importance are the a, α and l_r, ζ_k and ζ_g. For a, α and l_r, the greatest impact was observed in the favourable condition (0.3 M and pH 3) compared to the unfavourable conditions.

4.5. Verification of the curve fitting

The optimisation code determines the mean, $\bar{x}$ and the standard deviation, σ for the inputs that could reproduce the detachment curve obtained from the flow visualisation laboratory. As ζ was shown to have negligible impact on the detachment velocity in the sensitivity study, it was excluded from the curve fitting. So, six parameters – mean values for semi-major axis a, aspect ratio α, lever arm ratio l_r, and their standard deviations – were used for the lab data matching by the model. The details of the three probability distributions, obtained by the deviation-minimisation matching, are listed in Table 3.

The calculated mean and standard deviation for the curve fitting allow for verification with literature values to assess the validity of the fit. When comparing the fitted values with the values from the literature in Table 2, the parameters were all within the typical values from experimental and theoretical calculations. Besides, we measured semi-major axis for kaolinite particles used in the tests (Section S3, Fig. S2). The results of direct measurements (line three in Table 2) and tuning (columns four and five in Table 3) exhibit high agreement, which also validates the proposed torque balance model with stochastic coefficients.

5. Discussions

Test and model limitations Quantifying the detachment of kaolinite particles from the direct visualisation laboratory presented some challenges. It was difficult to differentiate the images as either individual particles or clusters. In some cases, individual clusters were shown to spread after being flushed, as the particles in the clusters were scattered. In other words, the experiments consist not only of detachments of individual kaolinite particles from the glass surface, but also detachments within the clusters themselves, which are not accounted for in the model.

Similarly, some reattachment was observed in the earlier stages (steps 0–4) of low velocity flow. The reattachment would affect the percentage of retained particles, which was not considered in the stochastic torque balance model. To assess the validity of omitting

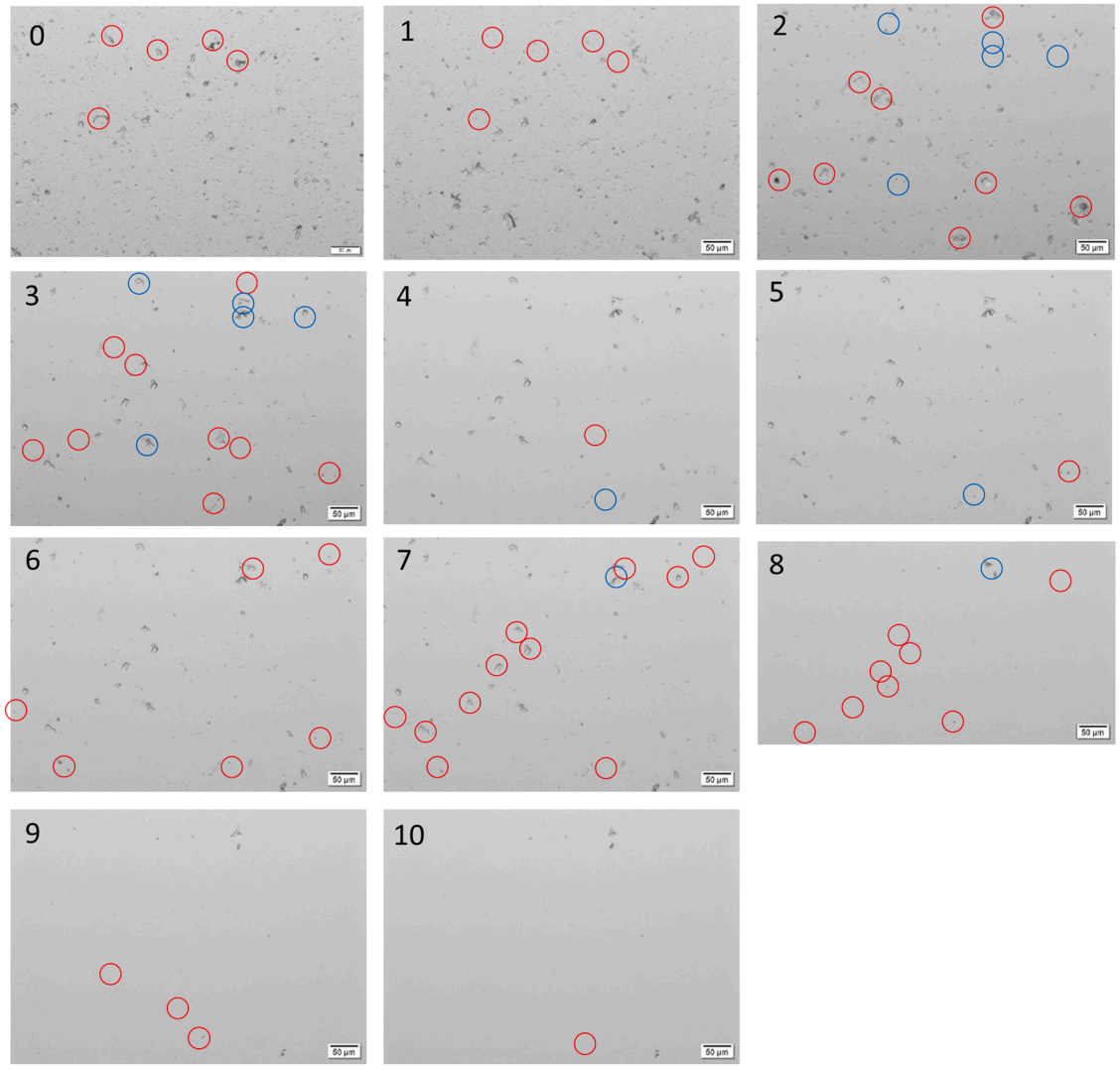

Fig. 7. Images of test 4 with velocity increments over 10 steps (DI, pH 11, 300 ppm kaolinite particles). The red and blue circles highlight kaolinite particles that will either detach or reattach respectively in the next frame/velocity increment. The circles do not mark all detachments and reattachments but only highlight obvious examples. Frame 8 was truncated as the picture was taken slightly off the reference point during the visualisation.

reattachment, we approximated the ratio of reattached to detached particles by observing 1/16 of the microscope image and manually counted the number of reattached kaolinite particles. The ratio of reattachment to detachment was estimated to be between 1:5 and 1:50. Although reattachment is beyond the scope of this article, investigating reattachment is a basis for future study.

The fitting of Test 4 was not as robust as the other three tests. The authors propose that this is because the most reattachment occurred in Test 4. Although a better R^2 value could be achieved for Test 4, the fitted input parameters for a deviated too much from the measured values of the flow visualisation experiment.

Although surface heterogeneity has been recognised as an important factor that influences particle attachment and detachment [25,73,74], we did not measure it in this work. However, there is some evidence that the surface charge heterogeneity is not a dominant factor in our study. High pH compensated surface charge heterogeneity [75], so a higher coefficient of determination would be expected in Tests 3 and 4, where pH11 was applied, than in Tests 1 and 2 with pH3. However, R^2 is equally high in all four tests, indicating that under the conditions of our lab study, surface charge heterogeneity is not a dominant factor. However, surface roughness could have played a role in gradual detachment of fines.

The order of importance of the input parameters determined from the sensitivity study is specific for the chosen probability distributions in this study. It is cautioned that changes in any of the input distributions might change the order of importance. This relates particularly to the aspect ratio and the lever arm ratio that were not measured directly but obtained from the literature.

Tuning standard deviations of the model parameters along with their mean values in mechanical equilibrium equations can be applied in numerous colloidal-transport areas: two-phase flows, where capillary force detaches the attached fines; single-phase flows with a variety of surface and colloidal properties (surface roughness, chemical heterogeneity, etc.); flows in porous media.

Forms and orientations of attached kaolinite Kaolinite particles are complex. They can exist as plates, stacks, aggregates of stacks, and assemblies of aggregates [1]. The literature has shown how the orientation and deposition structure changes with pH values [28,40,41]. However, the microscope used for this investigation could not observe the structures because of the limited resolution.

Our main assumption is that all this complicated structure can be approximated as a single spheroidal particle deposited on a smooth plane substrate with semi-minor axis perpendicular to the substrate. However, it could be possible that the spheroid is attached in other

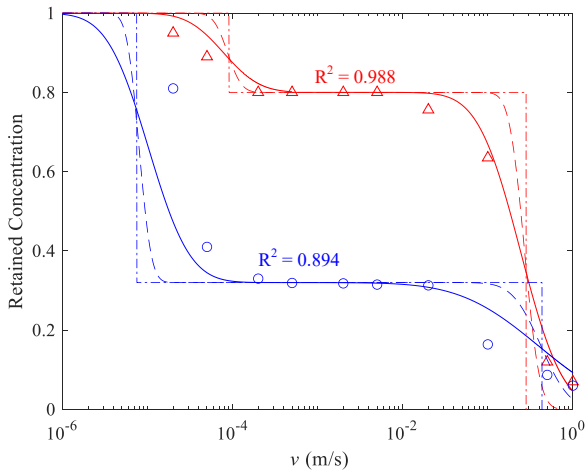

Fig. 8. Matching of the detachment of kaolinite observed from Tests 3 and 4 with the stochastic torque balance model. The points 'o' and 'Δ' are the laboratory data, while red and blue corresponds to Test 3 and 4 respectively. The dashed (–) and dash dotted (-·-) curves were plotted by reducing the standard deviation by 1/3 of the initial value and to zero, respectively. The goodness of fit is given by the R^2 value.

Table 2
Mean and standard deviations for the input parameters obtained from measurements or from the literature.

Parameter	Distribution	$\bar{x}$	σ	Source
α	Lognormal	-1.942	0.683	Veghte and Freedman [21]
a	Lognormal	-13.00	0.55	Microscope image measurements (Fig. S2.)
l_r	Normal	195.5	37.2	Kalantariasl and Bedrikovetsky[72]
ζ_g and ζ_k	Normal	Measured value	±10%	Zetasizer measurements and user manual

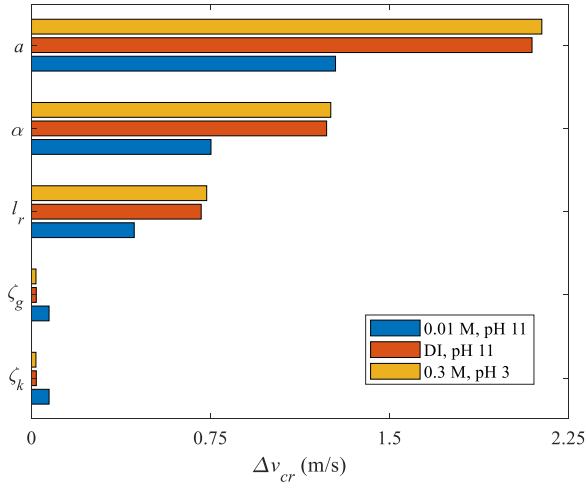

Fig. 9. Sensitivity analysis based on the distribution of input parameters. The analysis considers three combinations of pH and salinity conditions as shown in the legend, corresponding to Tests 1, 2, 3 and 4.

configurations, for example, when the semi-minor axis is parallel to the substrate surface. Yet, under the action of small flux perturbations, to minimise the hydrodynamic resistance, with high probability the particle moves to another position, where the semi-minor axis is perpendicular to the substrate surface. This claim is supported by SEM images

Table 3
The mean and standard deviation of the input parameters determined from optimisation fitting.

Test	α		a (μm)		l_r	
	Lognormal		Lognormal		Normal	
	$\bar{x}$	σ	$\bar{x}$	σ	$\bar{x}$	σ
1	-1.45	0.878	-12.05	0.848	152.2	44.24
2	-1.45	0.867	-12.17	0.923	214.5	62.66
3	-1.65	0.812	-12.50	0.321	160.0	20.46
4	-1.44	0.869	-12.10	1.000	90.1	49.14

[21,23]. Different orientations of the spheroid particles attached to asperous surfaces is the topic of forthcoming work, where the orientation angle could be used as an additional fitting parameter.

Let us discuss which form of kaolinite fines – spheroidal or rectangular / cylindrical – is more realistic for flow conditions of the current study. The previous work [38] used the expressions for drag and adhesion forces for cylinder particles without any gap between the smooth surfaces of the particle and the substrate. For typical sizes and materials used in this paper, cylinder particles could still be detached, but the critical velocities that provide the detachment, are significantly higher than those applied in our tests. This is explained by no-flow between the cylindrical particles and plane smooth substrates. In addition, the adhesion force that resists the detachment of the cylinder was three orders of magnitude higher than that of oblate spheroids. Therefore, the geometric model for the cylindrical particles was abandoned.

Papers [51,73] highlight high effects of substrate asperities on the mechanical equilibrium of the attached particles in creep flows. The flow through the contact area between irregular rectangular-form particles and asperous substrates does exist. It may explain the kaolinite detachment in our low-velocity tests. Indeed, the spheroid particles provide flow through the contact area. Therefore, we chose spheroid geometry for modelling. Paper [21] measured the size of kaolinite in the vertical projection, which we took as *2a*, and at the height at the side projection, which we assumed to be equal to *2b*.

Porous media applications For porous and fractured media, the curve "retained concentration vs velocity" is a fundamental material function for the system 'rock-colloid" and is called the maximum retention function [54]. In this work, we determine the maximum retention function directly by visualisation measurements of stabilised values for retained concentrations that correspond to applied velocities. In porous media, the retained concentration can be measured by X-ray CT (computational tomography) scanning that provides the in-situ retained concentrations along the core. Alternative method is suspension concentration measurements at the core effluent.

The maximum retention function is the mathematical model for clay fines detachment and closes the system of governing equations of colloidal-suspension-nano transport in porous media [8,10,12]. The proposed approach of mechanical equilibrium with stochastic coefficients can be applied for two-phase flows, where the particles are detached by capillary force, and for varying surface properties reflecting surface roughness, chemical micro heterogeneity, and multiple particle capture mechanisms [76,77]. The obtained curves (Figs. 6, 8) can be recalculated for bundles of parallel size-distributed capillary and can be used in microscale models for particulate flows [4,46,78]. The derivation of upper-scale effective transport equations can be performed using different upscaling techniques: random-walk models [79], exact averaging in population-balance models [80,81], or continuous upscaling [82,83]. In large-scale approximation, where dissipative and non-equilibrium fluxes are neglected if compared with the advective fluxes, the exact solutions are derived by non-linear modifications of method of characteristics using Riemann invariants [84,85]. The dissipative and non-equilibrium effects can be accounted for in analytical solutions by matching the asymptotic expansions [44,45].

6. Conclusions

Based on the stochastic torque balance model for particle detachment, direct visualisation of kaolinite flow and detachment in transparent cell, and the optimal fitting of the random model parameters, we draw the following conclusions.

The gradual detachment of kaolinite with incremental velocity in the direct visualisation experiment can be reproduced by the probabilistic distribution of the kaolinite aspect ratio, semi-major axis, lever arm ratio, and zeta potentials in the torque balance equations. The model and experiments matched well in both favourable and unfavourable conditions.

Matching the visualisation data – attached particle concentration versus velocity – by the torque balance model with stochastic coefficients using standard deviations as tuning parameters allows restoring the probabilistic model parameter distributions.

Tuning standard deviations of the model parameters allows calculating the attached concentrations within six standard deviations. The factors affecting fines detachment in order of decreasing their significance are the semi-major axis, aspect ratio, lever arm ratio, and zeta potentials.

Two-stage kaolinite detachment under unfavourable conditions was observed through direct visualisation. The observations suggest that kaolinites are attached in both the primary and secondary minima. These visualisations, along with the modelling data, allow for the determination of the percentage of particles attached in the secondary and primary minima.

Two-stage kaolinite detachment corresponds to plateau in the curve "retained concentration vs velocity" and indicates the existence of secondary energy minimum. In the ideal case of uniform particles and substrate, where the coefficients of variation of all parameters are zero, the curve consists of three constant values, where the plateau corresponds to intermediate constant. At large values of the standard deviations of model coefficients, the plateau disappears.

High match between the experimental data and the mechanical equilibrium model with stochastic coefficients has been observed. Besides, the particle semi-major axis and its standard deviation as obtained from the direct measurements and the model matching highly agrees, which validates the proposed stochastic torque-balance model.

CRediT authorship contribution statement

Heng Zheng Ting: Formal analysis, Validation, Writing – original draft, Writing – review & editing. **Yutong Yang:** Formal analysis, Investigation, Software, Writing – review & editing. **Zhao Feng Tian:** Conceptualisation, Supervision, Methodology. **Themis Carageorgos:** Conceptualisation, Methodology, Resources. **Pavel Bedrikovetsky:** Conceptualisation, Supervision, Methodology.

Declaration of Competing Interest

The authors declare that they have no known competing financial interests or personal relationships that could have appeared to influence the work reported in this paper.

Data availability

Data will be made available on request.

Acknowledgement

This work was supported with the supercomputing resources provided by the Phoenix HPC service at the University of Adelaide.

Appendix A. Stochastic mechanical equilibrium model

Due to micro-heterogeneity of the system colloid-surface, the properties – model parameters – in Eq. (1) are random variables. Let x be a vector of random parameters in Eq. (1).

$$\bar{x} = (x_1, x_2, \ldots x_n) \tag{A1}$$

In this paper we consider five model parameters, n = 5:

$$\bar{x} = \left(a, \alpha, l_r, \varsigma_k, \varsigma_g\right), \quad n = 5 \tag{A2}$$

Probabilistic distribution of parameters is given by a density function $f(x)$. Eq. (1) contains velocity v as an independent variable in expressions for drag and lift, so it allows expressing v as a function of vector x - $v = v_{cr}(x)$ – which is a minimum velocity that mobilises attached particle with the properties expressed by the parameters x. The domain Ω_v that corresponds to the set of parameter values for the particles that are mobilised by the flow with velocity v

$$\Omega_v = \{\bar{x} \in R^n : \ v_{cr}(\bar{x}) < v\} \tag{A3}$$

defines the remaining particle concentration

$$\sigma_{cr}(v) = \sigma_0 \iiint_{\Omega_v} f(\bar{x}) dx_1 dx_2 \ldots dx_n \tag{A4}$$

In our case, the remaining particle concentration vs velocity is accumulated distribution function. One plateau indicates two attachment-detachment mechanisms – fines accumulation in primary and secondary energy minima. In a general case of colloidal transport in porous media, n-1 plateaus indicate n capture mechanisms (bridging, straining, size exclusion, etc., [76,77]).

In this work, the five model parameters are assumed to be independent, so the the probabilistic distribution $f(x)$ is a product of five individual PDFs $f_i(x_i)$, i = 1,2…5. Integral (A4) can be calculated by the method of Monte-Carlo. We consider biparametric probability distribution functions, that are defined by medium values and standard deviations

$$f(\bar{x}) = f_1(x_1, \bar{x}_1, \sigma_1) \bullet f_2(x_2, \bar{x}_2, \sigma_2) \ldots \bullet f_n(x_n, \bar{x}_n, \sigma_n) \tag{A5}$$

The matching procedure of mathematical model, given by Eqs. (1) and (A4), comprises the tuning of medium values and standard deviations using non-linear least square method

$$\min_{\bar{x}_1,\sigma_1,\bar{x}_2,\sigma_2\ldots\bar{x}_n,\sigma_n} \int_0^{v_{\max}} \left(\frac{\sigma_{cr}(v,\bar{x}_1,\sigma_1,\bar{x}_2,\sigma_2\ldots\bar{x}_n,\sigma_n) - \sigma_{\exp}(v)}{\sigma_{cr}(v,\bar{x}_1,\sigma_1,\bar{x}_2,\sigma_2\ldots\bar{x}_n,\sigma_n)} \right)^2 dv \tag{A6}$$

In porous media and under the conditions of the current tests, lift and gravity are negligible if compared with drag and electrostatic force [69,72]. Substitution of Eq. (7) into Eq. (1) will make the resulting equation equivalent to Eq. (2) by

$$\frac{l_n}{l_d f_M} = \mu_s \tag{A7}$$

Therefore, in this work we use Eq. (1) as a mechanical equilibrium condition; its breaching causes mobilisation of the attached particles.

Appendix B. Supporting information

Supplementary data associated with this article can be found in the online version at doi:10.1016/j.colsurfa.2022.129451.

References

[1] F. Bergaya, G. Lagaly, Handbook of Clay Science. 2nd ed., Elsevier,, Amsterdam, 2013, pp. 1–19.
[2] H.H. Murray, Applied Clay Mineralogy - Occurrences, Processing and Application of Kaolins, Bentonites, Palygorskite-Sepiolite, and Common Clays, Elsevier,, Boston, 2006, pp. 1–6.
[3] T. Sen, K.C. Khilar, Review on subsurface colloids and colloid-associated contaminant transport in saturated porous media, Adv. Colloid Interface Sci. 119 (2–3) (2006) 71–96.
[4] T.V. Fountouli, C.V. Chrysikopoulos, Effect of Clay Colloid Particles on Formaldehyde Transport in Unsaturated Porous Media, Water 12 (2020) 12.
[5] M.E. Awad, A. Lopez-Galindo, M. Setti, M.M. El-Rahmany, C.V. Iborra, Kaolinite in pharmaceutics and biomedicine, Int J. Pharm. 533 (1) (2017) 34–48.
[6] G.L. Li, C.H. Zhou, S. Fiore, W.H. Yu, Interactions between microorganisms and clay minerals: New insights and broader applications, Appl. Clay Sci. 177 (2019) 91–113.
[7] V.I. Syngouna, C.V. Chrysikopoulos, Cotransport of clay colloids and viruses in water saturated porous media, Colloids Surf. A: Physicochem. Eng. Asp. 416 (2013) 56–65.
[8] T. Russell, L. Chequer, S. Borazjani, Z. You, A. Zeinijahromi, P. Bedrikovetsky, Formation Damage by Fines Migration, Form. Damage Improv. Oil Recovery 69–175 (2018).
[9] W. Song, A.R. Kovscek, Direct visualization of pore-scale fines migration and formation damage during low-salinity waterflooding, J. Nat. Gas. Sci. Eng. 34 (2016) 1276–1283.
[10] A. Zeinijahromi, T.K. Nguyen, P. Bedrikovetsky, Mathematical Model for Fines-Migration Assisted Waterflooding With Induced Formation Damage, SPE J. 18 (3) (2013) 518–533.
[11] F. Hussain, A. Zeinijahromi, P. Bedrikovetsky, A. Badalyan, T. Carageorgos, Y. Cinar, An experimental study of improved oil recovery through fines-assisted waterflooding, J. Pet. Sci. Eng. 109 (2013) 187–197.
[12] A. Zeinijahromi, P. Lemon, P. Bedrikovetsky, Effects of induced fines migration on water cut during waterflooding, J. Pet. Sci. Eng. 78 (3–4) (2011) 609–617.
[13] S. Iglauer, Y. Wu, P. Shuler, Y. Tang, W.A. Goddard, Alkyl polyglycoside surfactant–alcohol cosolvent formulations for improved oil recovery, Colloids Surf. A: Physicochem. Eng. Asp. 339 (1–3) (2009) 48–59.
[14] Y. Huang, C. Dai, Z. Chen, M. Cao, Q. Liu, Z. Chu, et al., Probing the mechanism of in situ oil droplet swelling during low salinity water flooding, Colloids Surf. A: Physicochem. Eng. Asp. (2022) 636.
[15] X. Li, W. Huang, F. Yu, R. He, T. Geng, X. Li, et al., Study on the construction of anionic-cationic surfactant binary mixed system and its wettability alteration performance in tight reservoirs, Colloids Surf. A: Physicochem. Eng. Asp. (2022) 633.
[16] L. Zheng, L. Wang, S.C. James, C.V. Chrysikopoulos, Colloid transport through a variable-aperture fracture under unfavorable attachment conditions: Characterization with a continuous time random walk model, Colloids Surf. A: Physicochem. Eng. Asp. (2022) 644.
[17] T. Wang, S.I. Andersen, A. Shapiro, Coalescence of oil droplets in microchannels under brine flow, Colloids Surf. A: Physicochem. Eng. Asp. (2020) 598.
[18] C.V. Chrysikopoulos, A. Abdel-Salam, Modeling colloid transport and deposition in saturated fractures, Colloids Surf. A: Physicochem. Eng. Asp. 121 (1997) 189–202.
[19] H.H. Murray, Overview-clay mineral applications, Appl. Clay Sci. 5 (1991) 379–395.
[20] R. Beckett, D. Murphy, S. Tadjiki, D.J. Chittleborough, J.C. Giddings, Determination of thickness, aspect ratio and size distributions for platey particles using sedimentation field-flow fractionation and electron microscopy, Colloids Surf. A: Physicochem. Eng. Asp. 120 (1–3) (1997) 17–26.
[21] D.P. Veghte, M.A. Freedman, Facile method for determining the aspect ratios of mineral dust aerosol by electron microscopy, Aerosol Sci. Technol. 48 (7) (2014) 715–724.
[22] H. Cheng, Z. Zhang, Q. Liu, J. Leung, A new method for determining platy particle aspect ratio: A kaolinite case study, Appl. Clay Sci. 97–98 (2014) 125–131.
[23] M.S. Żbik, N.A. Raftery, R.S.C. Smart, R.L. Frost, Kaolinite platelet orientation for XRD and AFM applications, Appl. Clay Sci. 50 (3) (2010) 299–304.
[24] J. Bergendahl, D. Grasso, Mechanistic basis for particle detachment from granular media, Environ. Sci. Technol. 37 (10) (2003) 2317–2322.
[25] I.L. Molnar, W.P. Johnson, J.I. Gerhard, C.S. Willson, D.M. O'Carroll, Predicting colloid transport through saturated porous media: A critical review, Water Resour. Res. 51 (9) (2015) 6804–6845.
[26] M. Elimelech, C. O'Melia, Effect of electrolyte type on the electrophoretic mobility of polystyrene latex colloids, Colloids Surf. 44 (1990) 165–178.
[27] A.M. Palomino, J.C. Santamarina, Fabric Map for Kaolinite: Effects of pH and Ionic Concentration on Behaviour, Clays Clay Miner. 53 (3) (2005) 211–223.
[28] T. Mahmood, A. Amirtharajah, T. Sturm, K. Dennett, A micromechanics approach for attachment and detachment of asymmetric colloidal particles, Colloids Surf. 177 (2–3) (2001) 99–110.
[29] M.S. Zbik, R.S. Smart, G.E. Morris, Kaolinite flocculation structure, J. Colloid Interface Sci. 328 (1) (2008) 73–80.
[30] J. Won, S.E. Burns, Stochastic modeling of kaolinite transport through a sand filter, Can. Geotech. J. 56 (11) (2019) 1573–1583.
[31] Y. Yang, B. Dang-Le, G. Kutty, S. Mbeveri, T. Carageorgos, A. Badalyan, et al., Kaolinite Detachment from Silica Substrate - Laboratory and Theoretical Study, Int. J. Water Wastewater Treat. 6 (2020) 3.
[32] Z.A. Kuznar, M. Elimelech, Direct microscopic observation of particle deposition in porous media: Role of the secondary energy minimum, Colloids Surf. A: Physicochem. Eng. Asp. 294 (1–3) (2007) 156–162.
[33] W.P. Johnson, E. Pazmino, H. Ma, Direct observations of colloid retention in granular media in the presence of energy barriers, and implications for inferred mechanisms from indirect observations, Water Res 44 (4) (2010) 1158–1169.
[34] C.V. Chrysikopoulos, V.E. Katzourakis, Colloid particle size-dependent dispersivity, Water Resour. Res. 51 (6) (2015) 4668–4683.
[35] Z. You, A. Badalyan, Y. Yang, P. Bedrikovetsky, M. Hand, Fines migration in geothermal reservoirs: Laboratory and mathematical modelling, Geothermics 77 (2019) 344–367.
[36] Z. You, Y. Yang, A. Badalyan, P. Bedrikovetsky, M. Hand, Mathematical modelling of fines migration in geothermal reservoirs, Geothermics 59 (2016) 123–133.
[37] S.C. James, C.V. Chrysikopoulos, Analytical solutions for monodisperse and polydisperse colloid transport in uniform fractures, Colloids Surf. A: Physicochem. Eng. Asp. 226 (1–3) (2003) 101–118.
[38] H.Z. Ting, P. Bedrikovetsky, Z.F. Tian, T. Carageorgos, Impact of shape on particle detachment in linear shear flows, Chem. Eng. Sci. (2021) 241.
[39] J. Won, T. Kim, M. Kang, Y. Choe, H. Choi, Kaolinite and illite colloid transport in saturated porous media, Colloids Surf. A: Physicochem. Eng. Asp. (2021) 626.
[40] A. Gomez-Flores, S.A. Bradford, G. Hwang, S. Choi, M. Tong, H. Kim, Shape and orientation of bare silica particles influence their deposition under intermediate ionic strength: A study with QCM–D and DLVO theory, Colloids Surf. A: Physicochem. Eng. Asp. (2020) 599.
[41] A. Gomez-Flores, S.A. Bradford, L. Wu, H. Kim, Interaction energies for hollow and solid cylinders: Role of aspect ratio and particle orientation, Colloids Surf. A: Physicochem. Eng. Asp. (2019) 580.
[42] M. Cerda, Mobilization of Kaolinite Fines in Porous Media. Colloids and Surfaces 27 (1–3) (1987) 219–241.
[43] J. Won, H. Choo, S.E. Burns, Impact of Solution Chemistry on Deposition and Breakthrough Behaviors of Kaolinite in Silica Sand, J. Geotech. Geoenviron. Eng. 146 (2020) 1.
[44] A.D. Polyanin, A.M. Kutepov, D.A. Kazenin, A.V. Vyazmin, Hydrodynamics, mass and heat transfer in chemical engineering, CRC Press,, London, 2001.
[45] A.D. Polyanin, V.V. Dil'man, Methods of Modeling Equations and Analogies in Chemical Engineering, CRC Press,, Boca Raton, Fl, 1994.
[46] A.A. Shapiro, H. Yuan, Application of stochastic approaches to modelling suspension flow in porous media, in: A. Skogseid, V. Fasano (Eds.), Statistical Mechanics and Random Walks: Principles, Processes and Applications, Nova Science Publishers, 2012.
[47] Y. Ding, X. Meng, D. Yang, Numerical simulation of polydisperse dense particles transport in a random-orientated fracture with spatially variable apertures, Colloids Surf. A: Physicochem. Eng. Asp. (2021) 610.
[48] G.M. Burdick, N.S. Berman, S.P. Beaudoin, Hydrodynamic particle removal from surfaces, Thin Solid Films 488 (1–2) (2005) 116–123.

[49] I. Goldasteh, G. Ahmadi, A.R. Ferro, Monte Carlo simulation of micron size spherical particle removal and resuspension from substrate under fluid flows, J. Aerosol Sci. 66 (2013) 62–71.
[50] B. Nasr, G. Ahmadi, A.R. Ferro, S. Dhaniyala, Overview of mechanistic particle resuspension models: comparison with compilation of experimental data, J. Adhes. Sci. Technol. 33 (24) (2019) 2631–2660.
[51] L. Chequer, T. Carageorgos, M. Naby, M. Hussaini, W. Lee, P. Bedrikovetsky, Colloidal detachment from solid surfaces: Phase diagrams to determine the detachment regime, Chem. Eng. Sci. (2021) 229.
[52] R.B. Bird, W.E. Stewart, E.N. Lightfoot. Transport Phenomena, 2nd ed..,, John Wiley & Sons,, New York, 2001.
[53] L. Landau, E. Lifshitz, Fluid Mechanics (Course on Theoretical Physics, vol. 6). 2nd ed., Pergamon Press,, Oxford, 1987.
[54] P. Bedrikovetsky, F.D. Siqueira, C.A. Furtado, A.L.S. Souza, Modified Particle Detachment Model for Colloidal Transport in Porous Media, Transp. Porous Media 86 (2) (2011) 353–383.
[55] M. Hubbe, Theory of detachment of colloidal particles from flat surfaces exposed to flow, Colloids Surf. 12 (1984) 151–178.
[56] C. Henry, J.-P. Minier, Progress in particle resuspension from rough surfaces by turbulent flows, Prog. Energy Combust. Sci. 45 (2014) 1–53.
[57] J. Sun, R. Ran, S. Muftu, A.Z. Gu, K.-T. Wan, The mechanistic aspects of microbial transport in porous media, Colloids Surf. A: Physicochem. Eng. Asp. (2020) 603.
[58] W.M. Haynes (Ed.), CRC Handbook of Chemistry and Physics. 95 ed., CRC Press LLC, Oakville, 2014.
[59] M.E. O'Neill, A sphere in contact with a plane wall in a slow linear shear flow, Chem. Eng. Sci. 23 (11) (1968) 1293–1298.
[60] D. Leighton, A. Acrivos, The lift on a small sphere touching a plane in the presence of a simple shear flow, J. Appl. Math. Phys. 36 (1985) 174–178.
[61] B. Derjaguin, L. Landau, Theory of the Stability of Strongly Charged Lyophobic Sols and of the Adhesion of Strongly Charged Particles in Solutions of Electrolytes, J. Acta Physicochim 14 (6) (1941) 633–662.
[62] E.J.W. Verwey, J.T.G. Overbeek, Theory of the stability of lyophobic colloids, Elsevier,, Amsterdam, 1948.
[63] E. Ruckenstein, D.C. Prieve, Adsorption and Desorption of Particles and Their Chromatographic Separation, Am. Inst. Chem. Eng. 22 (2) (1976) 276–283.
[64] J.N. Israelachvili, Intermolecular and Surface Forces. 3rd ed., Elsevier Inc,, Amsterdam, 2011.
[65] S. Bhattacharjee, M. Elimelech, Surface Element Integration: A Novel Technique for Evaluation of DLVO Interaction between a Particle and a Flat Plate, J. Colloid Interface Sci. 193 (1997) 273–285.
[66] S.A. Bradford, S. Torkzaban, A. Wiegmann, Pore-Scale Simulations to Determine the Applied Hydrodynamic Torque and Colloid Immobilization, Vadose Zone J. 10 (2011) 1.
[67] S. Aramrak, M. Flury, J.B. Harsh, R.L. Zollars, H.P. Davis, Does colloid shape affect detachment of colloids by a moving air-water interface? Langmuir 29 (19) (2013) 5770–5780.
[68] V. Lazouskaya, L.P. Wang, D. Or, G. Wang, J.L. Caplan, Y. Jin, Colloid mobilization by fluid displacement fronts in channels, J. Colloid Interface Sci. 406 (2013) 44–50.
[69] P. Sharma, M. Flury, J. Zhou, Detachment of colloids from a solid surface by a moving air-water interface, J. Colloid Interface Sci. 326 (1) (2008) 143–150.
[70] J.F. Carstens, J. Bachmann, I. Neuweiler, A new approach to determine the relative importance of DLVO and non-DLVO colloid retention mechanisms in porous media, Colloids Surf. A: Physicochem. Eng. Asp. 560 (2019) 330–335.
[71] A.K. Kottsova, M. Mirzaie Yegane, A.A. Tchistiakov, P.L.J. Zitha, Effect of electrostatic interaction on the retention and remobilization of colloidal particles in porous media, Colloids Surf. A: Physicochem. Eng. Asp. (2021) 617.
[72] A. Kalantariasl, P. Bedrikovetsky, Stabilization of External Filter Cake by Colloidal Forces in a "Well–Reservoir" System, Ind. Eng. Chem. Res. 53 (2) (2013) 930–944.
[73] C. Shen, Y. Jin, J. Zhuang, T. Li, B. Xing, Role and importance of surface heterogeneities in transport of particles in saturated porous media, Crit. Rev. Environ. Sci. Technol. 50 (3) (2019) 244–329.
[74] S.A. Bradford, S. Torkzaban, Colloid interaction energies for physically and chemically heterogeneous porous media, Langmuir 29 (11) (2013) 3668–3676.
[75] N. Tufenkji, M. Elimelech, Breakdown of Colloid Filtration Theory: Role of the Secondary Energy Minimum and Surface Charge Heterogeneities, Langmuir 21 (3) (2005) 841–852.
[76] R. Guedes, F. Al-Abduwani, P. Bedrikovetsky, P. Currie, Deep-bed filtration under multiple particle-capture mechanisms, Soc. Pet. Eng. 14 (3) (2009) 477–487.
[77] R. Farajzadeh, P. Bedrikovetsky, M. Lotfollahi, L.W. Lake, Simultaneous sorption and mechanical entrapment during polymer flow through porous media, Water Resour. Res. 52 (3) (2016) 2279–2298.
[78] H. Ma, Y. Li, C. Shen, C.V. Chrysikopoulos, H. Kim, Advances in pollutant transport in critical zone environments, Front. Water (2021) 3.
[79] A.A. Shapiro, Elliptic equation for random walks. Application to transport in microporous media, Phys. A: Stat. Mech. its Appl. 375 (1) (2007) 81–96.
[80] P. Bedrikovetsky, Upscaling of stochastic micro model for suspension transport in porous media, Transp. Porous Media 75 (3) (2008) 335–369.
[81] P. Bedrikovetsky, Y. Osipov, L. Kuzmina, G. Malgaresi, Exact upscaling for transport of size-distributed colloids, Water Resour. Res. 55 (2019) 1011–1039.
[82] A.A. Shapiro, Continuous upscaling and averaging, Chem. Eng. Sci. 234 (2021) 1–13.
[83] A.A. Shapiro, Continuous upscaling of the 3D diffusion equation in a heterogenous medium, Chem. Eng. Sci. (2022) 248.
[84] A.D. Polyanin, V.F. Zaitsev, Handbook of Nonlinear Partial Differential Equations: Exact Solutions, Methods Probl. N. Y.: Chapman Hall. /CRC (2003).
[85] A.D. Polyanin, V.F. Zaitsev, A. Moussiaux, Handbook of First-order Partial Differential Equations, CRC Press,, London, 2001.

This page is intentionally left blank

Chapter 7

Detachment of inclined spheroidal particles from flat substrates

Statement of Authorship

Title of Paper	Detachment of inclined spheroidal particles from flat substrates
Publication Status	☐ Published ☐ Accepted for Publication ☑ Submitted for Publication ☐ Unpublished and Unsubmitted work written in manuscript style
Publication Details	Ting, H.Z., Yang, Y., Tian, Z.F., Carageorgos, T. and Bedrikovetsky, P. 2023 'Detachment of inclined spheroidal particles from flat substrates',

Principal Author

Name of Principal Author (Candidate)	Heng Zheng Ting		
Contribution to the Paper	Formulated the problem, planned numerical approach, generation and analysis of numerical data, manufacturing of stretched polystyrene particles, performed visualisation experiments, wrote manuscript.		
Overall percentage (%)	70%		
Certification:	This paper reports on original research I conducted during the period of my Higher Degree by Research candidature and is not subject to any obligations or contractual agreements with a thir[illegible] its inclusion in this thesis. I am the primary author of this paper.		
Signature		Date	24/02/2023

Co-Author Contributions

By signing the Statement of Authorship, each author certifies that:

i. the candidate's stated contribution to the publication is accurate (as detailed above);

ii. permission is granted for the candidate in include the publication in the thesis; and

iii. the sum of all co-author contributions is equal to 100% less the candidate's stated contribution.

Name of Co-Author	Yutong Yang		
Contribution to the Paper	Performed visualisation experiments, developed Monte Carlo code, reviewed and assessed the manuscript		
Signature		Date	24/02/2023

Name of Co-Author	Zhao Feng Tian		
Contribution to the Paper	Co-supervised the development of the work, reviewed and assessed the manuscript		
Signature		Date	23/02/2023

Name of Co-Author	Themis Carageorgos
Contribution to the Paper	Co-supervised the laboratory investigations, reviewed and assessed the manuscript
Signature	Date 24/02/2023

Name of Co-Author	Pavel Bedrikovetsky
Contribution to the Paper	Co-supervised the development of the work, reviewed and assessed the manuscript
Signature	Date 24/02/2023

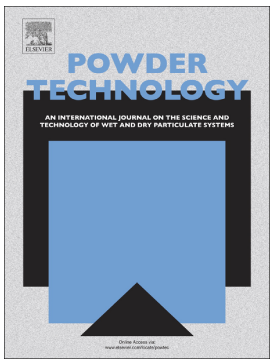

Detachment of inclined spheroidal particles from flat substrates

Heng Zheng Ting, Yutong Yang, Zhao Feng Tian, Themis Carageorgos, Pavel Bedrikovetsky

PII: S0032-5910(23)00538-7

DOI: https://doi.org/10.1016/j.powtec.2023.118754

Reference: PTEC 118754

To appear in: *Powder Technology*

Received date: 13 March 2023

Revised date: 15 June 2023

Accepted date: 21 June 2023

Please cite this article as: H.Z. Ting, Y. Yang, Z.F. Tian, et al., Detachment of inclined spheroidal particles from flat substrates, *Powder Technology* (2023), https://doi.org/10.1016/j.powtec.2023.118754

Detachment of inclined spheroidal particles from flat substrates

Heng Zheng Ting [a], Yutong Yang [b], Zhao Feng Tian [a], Themis Carageorgos [b], Pavel Bedrikovetsky [b]

[a] *School of Electrical and Mechanical Engineering, The University of Adelaide, Adelaide 5000, SA, Australia*

[b] *Australian School of Petroleum and Energy Resources, The University of Adelaide, Adelaide 5000, SA, Australia*

Keywords: detachment; colloid; DLVO; visualisation; modelling; adhesion force

Abstract:

The detachment of fine particles attached to a solid substrate or rock surface significantly affects colloidal transport in porous media. The work is devoted to quantifying the detachment conditions for inclined oblate spheroids subjected to creeping viscous flow. A numerical and a laboratory study were conducted to systematically evaluate the impact of the orientation (pitch) angle toward the hydrodynamic moment, adhesive DLVO force, contact area, and critical detachment velocity. The methodology developed to produce stretched latex polystyrene particles reduces the geometric uncertainty of nonspherical fines. The geometry of the produced oblate spheroids is fully determined by the semi-major and semi-minor axes. For inclined attached particles, an explicit formula has been derived for the detaching velocity, where the detaching drag torque exceeds the attaching adhesion torque. The probabilistic distribution of the model parameters for the detachment velocity of the inclined particles attached to the plane substrate provides upscaling for fines detachment from the particle to porous media scale.

Nomenclature

a	Semi-major axis of a spheroid, L [m]
b	Semi-minor axis of a spheroid, L [m]
D	Distance of closest separation, L [m]
E	Interaction energy potential per unit area of two parallel plates, MT^{-2} [J m^{-2}]
F_a	Adhesion force, MLT^{-2} [N]
F_d	Drag force, MLT^{-2} [N]
F_f	Friction force, MLT^{-2} [N]
F_g	Gravity force, MLT^{-2} [N]
F_l	Lift force, MLT^{-2} [N]
f_a	Normalised adhesion force

f_d	Shape factor for drag force
f_M	Shape factor for moment
$f_{M,\varphi}$	Shape factor for moment due to the non-zero orientation angle
H	Distance between particle centre and substrate, L [m]
h	Local distance for surface element, L [m]
$\widehat{\boldsymbol{k}}$	Unit vector along the positive Z-axis of the space-fixed coordinates
l_d	Lever arm for drag force, L [m]
l_n	Lever arm for normal force, L [m]
L	Height of the visualisation cell, L [m]
M	Hydrodynamic moment, ML^2T^{-2} [N m]
N	Normal force, MLT^{-2} [N]
$\boldsymbol{n}$	Outward normal unit vector in body-fixed coordinates
$\widehat{\boldsymbol{n}}$	Outward normal unit vector in space-fixed coordinates
r_e	Volume equivalent sphere radius, L [m]
U	Interaction energy between particle and infinite flat plate, ML^2T^{-2} [J]
v	Area-averaged velocity, LT^{-1} [m s^{-1}]
v_{cr}	Critical detachment velocity, LT^{-1} [m s^{-1}]

Greek Letters

α	Aspect ratio (b/a)
σ	Normalised attached particle concentration
$\dot{\gamma}_o$	Shear rate, T^{-1}, [s^{-1}]
μ	Dynamic viscosity, ML^2T^{-1}, [Pa s]
φ	Orientation angle, [degree]

1 Introduction

The detachment of particles from surfaces is relevant to various research and industrial applications, such as the removal of dust and pollutants [1-5], pharmaceutical drug delivery [6-8], bacteria movement in aquifers [9] and kaolinite fines production in petroleum reservoirs [10-13]. Indeed, studies from various disciplines have attempted to model and characterise the phenomenon of particle detachment. However, compared with studies on spheres, the modelling of the detachment of nonspherical particles is only relatively recent in the literature [4, 14, 15], even though most particles in these applications are not spherical.

The nonspherical shape of natural particles can lead to different detachment behaviours, depending on the deposition orientation (pitch) angle between the particle and the substrate, which is otherwise absent in spherical particles. For example, in the case of kaolinites, the minerals could adopt edge-to-edge, face-to-edge or face-to-face attachments, each with different orientation angles and different detachment rates [16, 17]. Furthermore, there is an emerging trend in the literature reporting the presence of orientation angles when particles are deposited in visualisation experiments [18-21]. The presence of the orientation angle is

contrary to the assumption that particles will reorient with the hydrodynamic flow to achieve more energetically favourable orientations [22].

Several laboratory and simulation studies have been performed on the transport and retention of nonspherical particles on the walls of the substrate. Early studies are predominantly column experiments [23-26], which, with the myriad of mechanisms involved in filtration [11, 27, 28], often hinder the understanding of the impact of particle shape on particle detachment [29]. Since then, recent studies have been conducted for simple cases of linear shear flows on flat substrates without porous media, through QCM-D [30, 31], impinging jets [19], microfluidic channels [20, 32, 33], aerodynamic flow cells [34] and simulations [35].

The nonspherical shape of the particles impacts the particle deposition on the surfaces. Rotation of nonspherical particles with flow may cause a greater tendency for particles to drift toward walls, increasing collision [32, 35, 36] as well as overcoming energy barriers under unfavourable conditions [30]. However, even without the complex interplay arising from porous media, the rate of retention of nonspherical particles in a channel flow compared with spheres could either be enhanced [32, 35], reduced [31, 37] or remain unchanged [20]. Given the apparent contradiction, there is still a lack of systematic studies of the role of the orientation angle and the aspect ratio of particles in particle detachment.

Furthermore, the bulk of the studies on nonspherical particles are focused on deposition; it remains uncertain how the findings would apply to particle detachment. Although there are a few direct visualisation experiments on nonspherical particles [19, 20, 32], the studies have focused on the initial transport and deposition on the substrate without investigating the consequent detachment behaviours. Furthermore, though particle attachment and detachment are an interplay of hydrodynamic and adhesion forces [38, 39], studies often focus solely on the variation of hydrodynamic forces [36, 40, 41], or adhesion forces [30, 31, 42], to explain the results. To the authors' knowledge, there has yet to be any systematic attempt to characterise the impact of the orientation angle and the aspect ratio of particles on both the hydrodynamic and adhesion forces in terms of the subsequent detachment behaviour of nonspherical particles.

This paper aims to fill that gap by performing direct visualisation experiments on stretched polystyrene oblate spheroid particles with controlled sizes and aspect ratios. Visualisation enables the particle orientation angle and detachment rates to be determined, then subsequently

compared with a stochastic torque balance model for particle detachment. Computational fluid dynamics (CFD) and surface element integration (SEI) were used to systematically quantify the effect of varying the orientation angle, φ and the spheroid aspect ratio, α on the hydrodynamic moment, the adhesion force and the contact area in terms of the resultant detachment behaviours. The introduction of the orientation angle into the formulae for shape factors for the drag, its moment and for adhesion forces enables quantification of the hydrodynamic and electrostatic fluid-particle-substrate interactions.

2 Laboratory Methodology

Direct visualisation experiments were conducted to observe the difference in detachment between spheres and oblate spheroids with a stepwise increase in the fluid velocity. The laboratory visualisations consist of four sets of experiments using four particle samples: S1, S2, S3 and S4. S1 and S3 are oblate spheroids and spheres, respectively, with a volume equivalent radius, r_e of 1.55 µm. Similarly, S2 and S4 are oblate spheroids and spheres with r_e = 2.965 µm, respectively. The raw materials for the samples are polystyrene latex spheres (Polysciences, USA). To obtain oblate spheroid samples (S1 and S2), the purchased sphere particles undergo further stretching and processing, as detailed below.

2.1 Preparation of the stretched latex sample (S1 and S2)

The latex stretching procedure was based on the work of Ahn et al. [43]. Briefly, 2 g of PVA crystals were mixed with 20 ml of preheated distilled water at 85°C. The mixture was stirred for at least 6 h. Then 0.365 ml of glycerol and 0.1 % (w/v) of r_e =1.5 or 3 µm of polystyrene latex particles were added to the PVA mixture. The PVA mixture was poured into a 10 cm diameter Petri dish, ensuring that the surface was level. The mixture was left to dry for 24 h. The PVA film was removed with a spatula and cut into four quarters. A quarter of the PVA film was placed between two 3 mm thick silicone rubber sheets (Industrial Gaskets, Australia) and two steel platens (see Fig. S1 in the supplementary materials for a picture of the equipment). The PVA-silicon-platen assembly was mounted on a bearing puller and was tightened enough to ensure that the assembly did not slide.

The bearing puller assembly was placed in an oven and heated at 135°C for 1.5 h. The assembly was taken out of the oven and a wrench was used to tighten the bearing puller as tightly as possible while the assembly was still hot. The bearing puller was placed back in the

oven again for another 1 h at 135°C. The oven was turned off and the assembly was left to cool. The film was removed from the platens and dissolved in a 30% water-isopropanol mixture at 65°C for 1 h. The latex particles were centrifuged and the supernatant was carefully removed using a syringe. A fresh solution of 30% isopropanol mixture was added to the sediment and the sample was centrifuged and decanted for another ten times. Finally, the samples were left to dry under a fume chamber.

2.2 Preparation of the control spheres (S3 and S4)

The sphere samples were used as a control and base case to compare with the manufactured spheroids. Taking into account the potential alterations in particle properties due to the stretching procedure [30], the spheres also underwent the same PVA embedment and heating procedure as described in Section 2.1, but without the tightening and compression process of the bearing puller.

2.3 Materials and setup

Details of the setup and procedure of the direct visualisation experiment have been reported in detail in previous publications [22, 29]. Briefly, the carrier fluid was prepared by dissolving sodium chloride in deionised (DI) water to achieve a salinity of 0.3 M NaCl. Hydrochloric acid was added until the solution reached pH 3. The combined salinity and pH provided a favourable condition for attachment. The dried samples of either S1, S2, S3 or S4 were then mixed with the carrier fluid and injected into the microfluidic cell (Ibidi, Germany) until the cell was fully saturated. The microfluidic cell has a rectangular channel with a height, width, and length of 450 µm, 5 mm and 48.2 mm, respectively. The cell was then connected to a syringe pump, but left to rest for at least two hours to allow the polystyrene particles to attach to the bottom of the cell.

The concentration of the suspension was difficult to determine since, during the decanting of the supernatant, some of the initial particles were lost. The concentration of the suspension was done by trial and error, such that it was diluted to have at least 50 particles per image frame when viewed in the visualisation cell, but was not concentrated enough to form clusters.

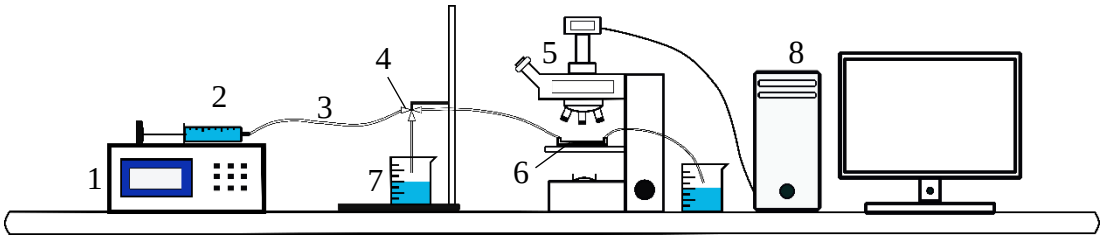

Fig. 1. Diagram of the flow visualisation setup. 1: syringe pump, 2: glass syringe, 3: tubing, 4: three-way valve, 5: optical microscope, 6: microfluidic cell, 7: beaker, 8: computer and monitor display.

Fig. 1 shows the setup of the visualisation experiment. After the sample particles were deposited in the cell, the syringe pump introduced the flow of particle-free solutions (0.3 M NaCl, pH 3) at stepwise increasing flow rates ranging from 0.001 ml/min up to 210 ml/min. The exact flow rates and velocity increments are detailed in Table S2. The particle-free solution flowed through the tubing, past the three-way valve, and into the microfluidic cell inlet. The flow was then discharged from the cell outlet into a beaker. The three-way valve has been installed to prevent the entry of air bubbles when the syringe is refilled.

Microscope images were taken from seven different spots along the visualisation cell for each velocity increment. The optical microscope (BX51 TRF, Olympus, Australia) was equipped with Soft Imaging System's Colorview III camera and AnalySIS Life Sciences software. The images were then processed to determine the concentration of particles in each velocity step and the initial orientation angle of deposition. The number of detached particles was calculated by comparing the concentration of the attached particles at each velocity increment.

2.4 Characterisation of S1 and S2

Table 1 summarises the stochastic distributions for the volume equivalent sphere radius, r_e, the semi-major axis, a, and the deposition orientation angle, φ of the oblate spheroids S1 and S2. A normal distribution was assumed, characterised by the mean and standard deviation (S.D.).

Table 1: Distribution of the properties of the manufactured oblate spheroidal particles.

Parameters	S1		S2		Source
	Mean	**S.D.**	**Mean**	**S.D.**	
r_e (μm)	1.55	0.031	2.965	0.148	Manufacturer data sheet
a (μm)	1.90	0.161	4.53	0.3233	SEM imaging
φ (degree)	41.9	12.01	36.9	14.94	Direct visualisation

The average aspect ratios of samples S1 and S2 are α = 0.54 and 0.28, respectively ($\alpha = (r_e/a)^3$). For spheres S3 and S4, the samples have identical r_e distributions as S1 and S2, respectively. However, due to the spherical geometry, the parameters a and φ are irrelevant for the sphere samples.

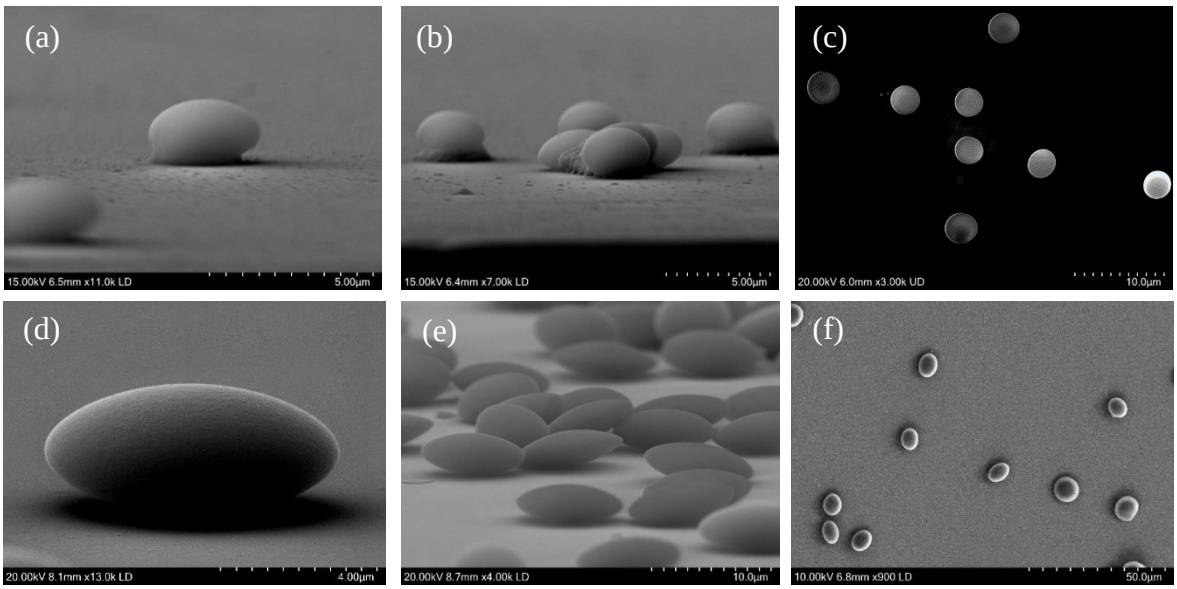

Fig. 2. SEM images for S1 (first row) and S2 (second row). The first and second columns show the 3D geometry of the oblate spheroid particles taken from a side view. The third column is the plane-view image.

Fig. 2 shows the SEM images for S1 and S2 taken at several different spots of the sample. Side and plane images were taken using a field emission scanning electron microscope (FE-SEM) (Hitachi SU7000) to visualise the 3D geometry and to measure the semi-major axis of the particle, respectively. The plane-view SEM images were further processed using the MATLAB Image Processing Toolbox (R2021b). The semi-major axis, a, was determined using the property 'MajorAxisLength' divided by two. Fig. S3 in the supplementary materials shows the fitted normal distribution curves for the calculated semi-major axis.

Similarly, the deposition orientation angle, φ of the particle is obtained by processing the direct visualisation images taken from the optical microscope when the flow velocity is zero (initial saturated condition). Further details of the procedures are given in Sections S2 and S3 of the supplementary materials.

2.5 Zeta potential measurements.

The reader is referred to the previous work [22] for more details of the zeta potential measurements. Zeta potential measurements were performed for a) the original sphere particles as provided by the supplier, b) the sphere particles that have undergone additional procedures as specified in Section 2.2 and c) the stretched latex particles (from Section 2.1). Details of the zeta potential values are provided in Table S1 of the supplementary materials.

3 Laboratory results

3.1 Direct visualisation of oblate spheroids

The images obtained from the direct visualisation of the S2 sample particles are presented in Fig. 3. The S2 sample particles were used in the main study, as they are larger than the S1 sample particles and therefore easier to visualise. A set of visualisations for the S1 sample particles is also presented in the supplementary materials (Fig. S4). From step 0 to step 3 (v = 0 to 2×10^{-4} m/s), there was no change in the attached particles in Fig. 3. Between steps 4 and 5 there was a slight reorientation of two particles, as highlighted by the blue circles. However, only two of the seven other visualisation spots of S2 exhibited reorientation between steps 4 and 5. Therefore, the reorientation is regarded as an anomaly.

Neither reorientation nor particle detachment was observed with a further increase in the velocity between step 5 up to step 9. The increase in velocity during step 10 (v = 0.5 m/s) initiated both reorientation and detachment of the oblate spheroids. In other words, some particles were observed to lie flat (reorient) or disappear (detach) from the image frame. At higher velocities from step 10 onwards, more particles were detached than reoriented. This trend was observed in all the additional six observation spots for S2.

Fig. 4 shows the comparison between the initial deposition image (v = 0 m/s) and the image when detachment and reorientation were initiated (v = 0.5 m/s). The image processing code traces the outline of the visualised spheroids and calculates the orientation angle based on

the projected semi-major and semi-minor axis. Depending on the orientation angle, the colour of the outline changes between red for particles approaching an end-on attachment, green for particles approaching a side-on configuration and blue for particles orientated intermediately.

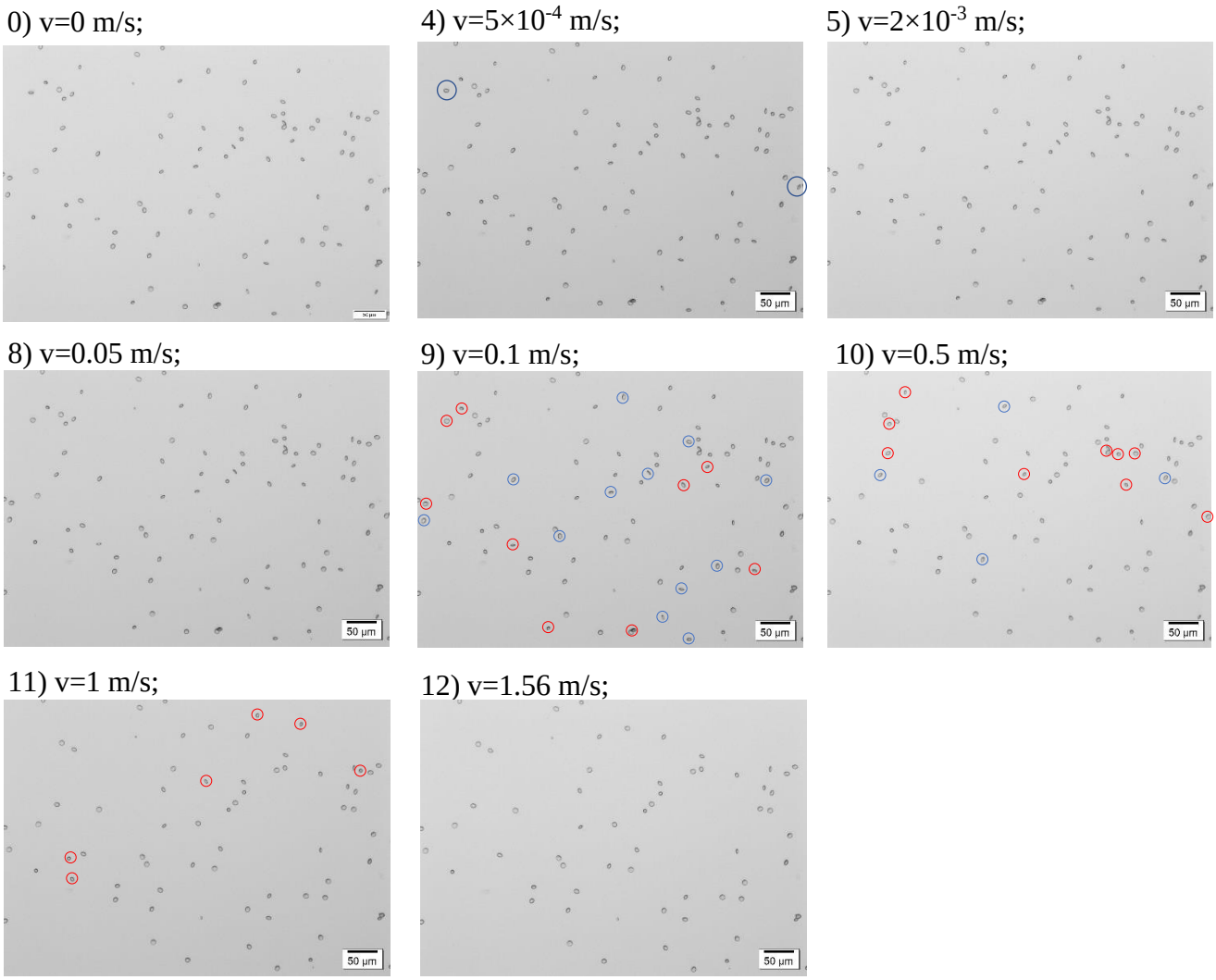

Fig. 3. Direct visualisation of the oblate spheroid particle, S2 (r_e = 2.965 µm) with incremental stepwise flow velocity. Blue circles indicate that reorientation will occur in the next image (the velocity increment). Similarly, the red circles highlight all the particles that will detach in the next frame. The flow direction is from the top to the bottom of each image. Images from steps 1-3 and steps 6-7 were omitted because no changes were observed.

Between the two image frames, some of the initially red particles become blue particles as a result of reorientation. Likewise, some of the blue particles become green particles. Another portion of the particles (dashed red circles) is completely detached. Whether it was by reorientation or detachment, all of these changes occur among the blue and red particles, which are deposited at an angle. The green particles with minimal φ appear to be stable and unchanged.

Stretched latex particles were shown to attach to the glass substrate at various φ, averaging at 37° and 41° for S1 and S2, respectively.

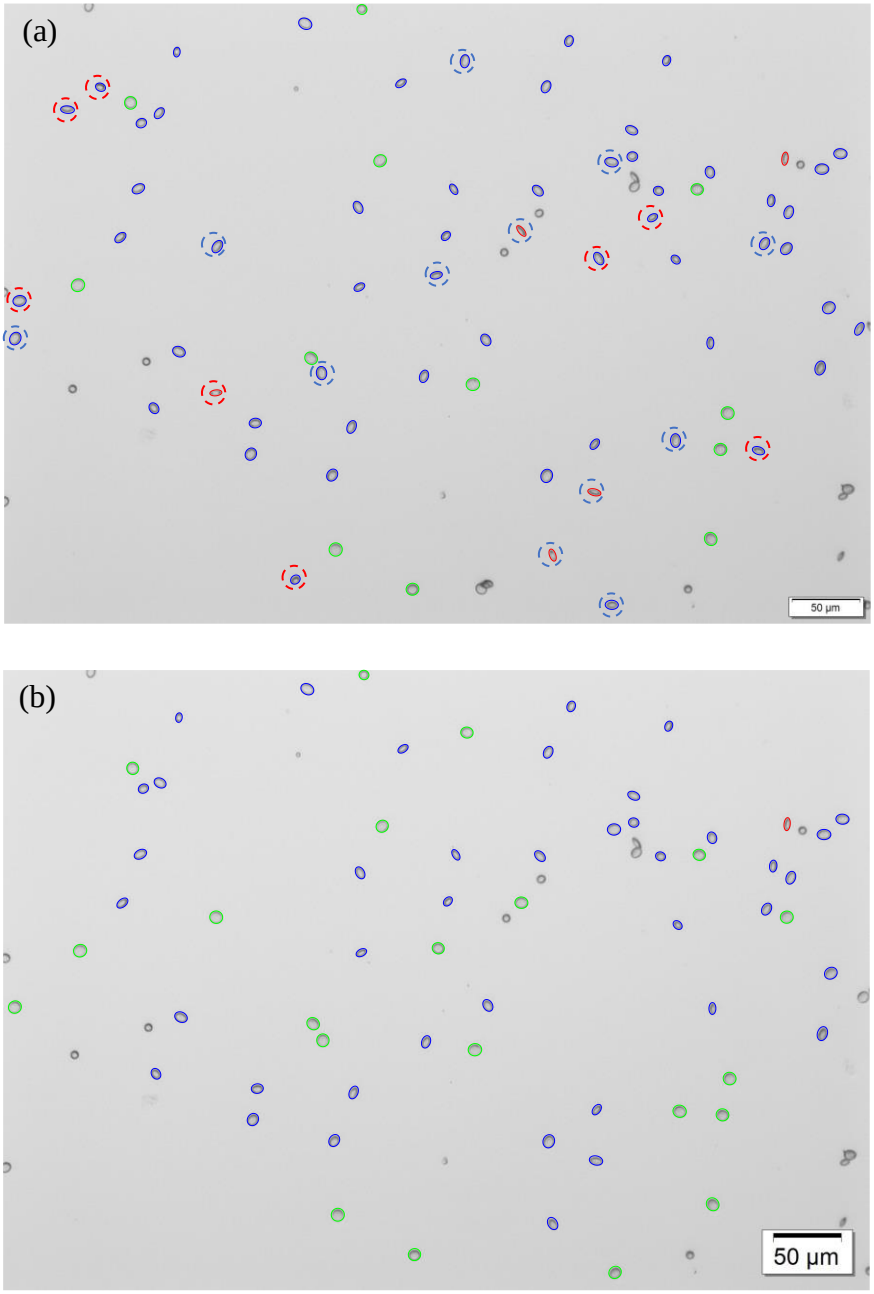

Fig. 4. Visualisation of the S2 sample showing the initial particle orientation angle with subsequent reorientation and detachment. (a) Initial deposition angle when v = 0 (step 0). (b) Reorientation and detachment of oblate spheroids when v = 0.5 m/s (step 10). The colour of the solid particle outlines indicates the orientation angle: green (0° ⩽ φ <30°), blue (30° ⩽ φ <60°) and red (60° ⩽ φ⩽90°). Particles that have not been encircled are excluded from analysis, either due to incomplete particles at the edge of the photograph, contaminant particles/spheres or clustering. As with the convention in Fig. 3, the dashed red and dashed blue circles in (a) highlight particles that will either detach or reorient in the next image frame (b), respectively.

3.2 Detachment rate of spheres versus oblate spheroids

Fig. 5 plots the concentration of attached particles normalised by the initial particle concentration at step 0 as a function of the area-averaged velocity based on the visualisation experiments. In fluid mechanics in porous media, this dependency is called the maximum retention function (MRF), which is the phenomenological function of transport equations [12, 44]. For all four samples, detachment was initiated when the velocity was increased to 0.5 m/s at step 10. No detachments were observed below v=0.5 m/s, except for some contaminant particles, which were excluded from the particle count. Note that the reorientation that occurred together with detachment, as discussed in the previous section, is not reflected in the detachment curves such as the ones in Fig. 5, because the reorientation cannot be identified by counting the number of attached particles.

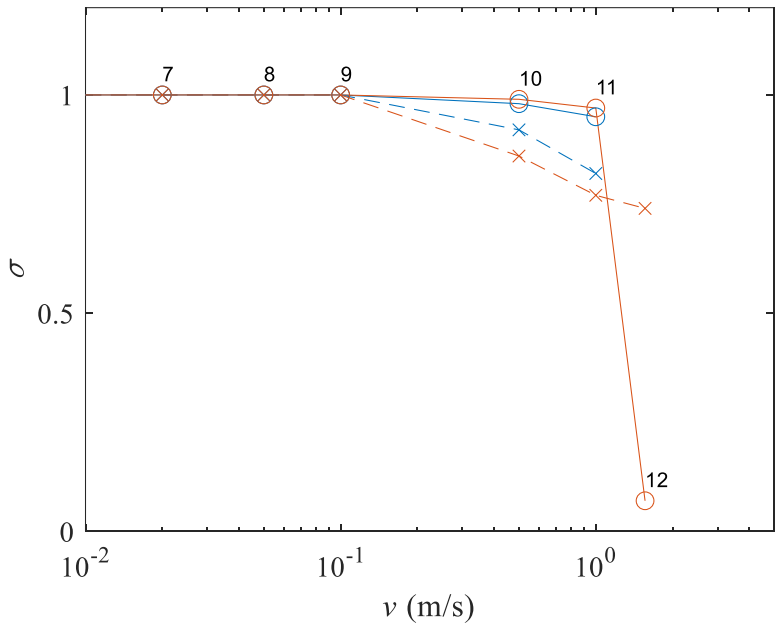

Fig. 5. Rate of particle detachment calculated from the laboratory visualisation of polystyrene (PS) spheres and spheroids. σ and v denote the normalised attached particle concentrations and the area-averaged flow velocity. The blue and red lines are plotted for the particles where r_e = 1.55 μm and 3 μm, respectively. Solid lines with 'o' markers are for spherical particles, while dashed lines with 'x' markers are for spheroidal particles. The numbers labelled beside the 'o' markers correspond to the step number. The graph has been truncated to show data from step 7 onwards alone, as there are no changes in the previous steps.

Although the oblate spheroids (S1 and S2) and the spheres (S3 and S4) initiate detachment at the same velocity threshold (v = 0.5 m/s), they detach at different rates. In general, spheroids of both sizes are shown to detach at a faster rate than spheres initially. However, at the highest velocities, it was apparent that the spheres (S4) detached much more than the spheroids (S2) of equal r_e. Among the spheroids, S2, which has a larger volume and a lower α, is shown to detach faster than S1, as expected. However, when comparing the spheres, S3 had a slightly higher detachment rate than S4. Considering the difference in σ of 1.3% between S3 and S4, we interpreted this as negligible.

4 Mathematical modelling

To further understand the observations made in the direct visualisation experiments, we conducted numerical modelling on the detachment of oblate spheroids with different orientation angles.

4.1 Theory and setup of the problem

Fig. 6a shows the formulation of the problem, where an oblate spheroid with an arbitrary aspect ratio, α, is attached to the substrate at an arbitrary orientation angle, φ. The orientation angle is defined as the angle between the semi-minor axis, b, and the vertical. It is assumed that the substrate is flat and the particle is subjected to a linear shear flow, with a shear rate of $\dot{\gamma}_o$. The free body diagram (Fig. 6b) shows all the forces and moments considered in the analysis. The contact between the particle and the substrate leads to deformation on the particle surface with a contact area with the substrate. Taking the moment around the point P, the contact radius forms the lever arm for the adhesion force.

Although there are theoretically three modes of detachment, rolling, sliding and lifting [45], this study focuses on the rolling mode of detachment, as it has been shown to be the dominant mechanism for the detachment of spheres [4, 39] and oblate spheroids [29]. Furthermore, the gravitational force and the lift force are also omitted from this study, as they are negligible compared with the magnitude of the adhesion force [29, 46]. The magnitudes of the lift and gravitational forces in this study are presented in S11 and S12 of the supplementary materials to further justify the omission. Briefly, the drag force is between one to three orders of magnitude higher than the lift (depending on the orientation angle) and consistently four orders of magnitude higher than the gravitational/buoyancy force.

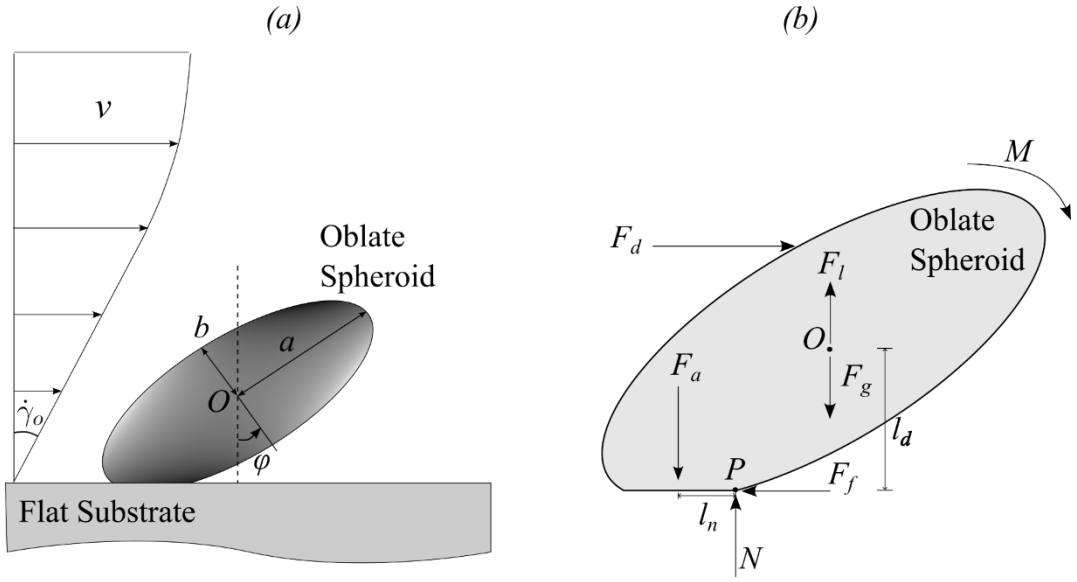

Fig. 6. Configuration of the particle and substrate. (a) An oblate spheroid particle attached to an infinite flat wall (substrate) at an orientation (pitch) angle of φ. The oblate spheroid is defined by an aspect ratio of $\alpha = b/a$, where b is the semi-minor axis and a is the semi-major axis. Near the substrate wall, the particle is subjected to a linear shear flow with a shear rate of $\dot{\gamma}_o$. The resultant forces and moments exerted on the particle are depicted in (b). F_d, F_l, F_a, F_g, and F_f are the drag, lift, adhesion, gravity and friction forces, respectively. N and M denote the normal force and the hydrodynamic moment exerted by the linear shear flow. O is the centre of the particle, while P is the point where the particle pivots from the torque. l_n and l_d are the normal and drag lever arms.

Lastly, it was assumed that rolling detachment occurs immediately whenever the detaching hydrodynamic torque exceeds the attaching torque such that:

$$M > F_a l_n . \tag{1}$$

4.1.1 Hydrodynamics and shape factors

Consider the drag, F_d, and its moment, M, exerted on a sphere located on the plane substrate by the creeping flow parallel to the substrate, the steady-state solution of the linear Stokes equation for non-inertial flow allows for explicit formulae [45, 47]:

$$F_d = 1.7009 \times 6\pi\mu r_e{}^2\dot{\gamma}_o, \;\; M = 1.37 F_d l_d, \tag{2}$$

where, μ (8.899×10^{-4} Pa.s) and r_e are the dynamic viscosity and the volume equivalent sphere radius, respectively. $\dot{\gamma}_o$ is the shear rate on the substate calculated from the Hele-Shaw velocity profile near the substrate.

F_d in Eqn. (2) allows for one dimensionless group alone. Therefore, the introduction of another dimensionless group for the aspect ratio, α of the spheroidal particle in Eqn. (2), yields

an aspect-ratio-dependent drag shape factor $f_d(\alpha)$ [48]. The same corresponds to M in Eqn. (2), so the moment shape factor $f_M(\alpha)$ also depends on the aspect ratio alone:

$$F_d = 6\pi\mu r_e^2 \dot{\gamma}_o f_d(\alpha),\ M = F_d l_d f_M(\alpha). \tag{3}$$

For spheroidal particles, the drag and its moment are calculated by using CFD. The numerical solution of the Navier-Stokes equations calculates the velocity and pressure distributions near the spheroid surface, allowing calculations of the pressure gradient and shear on the surface. The total of the integrals of pressure gradient and shear over the surface is equal to the drag, F_d, yielding the aspect-ratio-dependent drag shape factor from first Eq. (3). The total of the integrals of the moments for the pressure gradient and for the shear over the surface is equal to the overall moment M exerting from the viscous fluid on the spheroidal particle, yielding the aspect-ratio-dependent moment shape factor f_M from second Eq. (3). Expression $F_d l_d$ is an approximate estimate for the moment, so the shape factors for the drag and moment are different and calculated by CFD independently.

Further introduction of the orientation angle, φ as an independent variable yields aspect ratio- and angle dependencies for both shape factors of two independent variables. This reflects the functional dependency of three independent dimensionless groups [48]. However, after separating $f_M(\alpha)$ of the function of two variables $f_M(\alpha,\varphi)$, the expressions (3) become:

$$F_d = 6\pi\mu r_e^2 \dot{\gamma}_o f_d(\alpha,\varphi),\ M = 6\pi\mu r_e^2 \dot{\gamma}_o f_d(\alpha,0) l_d f_M(\alpha) f_{M,\varphi}(\alpha,\varphi). \tag{4}$$

The separation is justified in section 4.2.1 by the simple features of the function $f_M(\alpha,\varphi)$.

Let us discuss the physical significance of the shape factors. In Eqns. (3) and (4), three shape factors: f_d, f_M and $f_{M,\varphi}$, are introduced. Firstly, f_d accounts for the deviation from the drag of a sphere because of the presence of the aspect ratio in spheroids. Secondly, f_M accounts for the fact that the resultant drag force does not act directly through the geometric centre of the particle, but slightly above, due to the higher velocity on top of the particle than near the substrate. For example, in the case of spheres, the drag acts at $1.37r_e$. The justification and derivation of f_d and f_M have previously been presented, with their origins from the Stokes law [29]. In this work, an additional shape factor, $f_{M,\varphi}$ is introduced to account for the change in M of a spheroid when $\varphi \neq 0°$. The shape factors, f_d, f_M and $f_{M,\varphi,}$ are determined using CFD, which will be detailed in the next section.

4.1.2 CFD modelling

The commercial software ANSYS/CFX (2021 R2) was used. Details and validation of the CFD model have previously been presented [29]. Briefly, a simulation domain of $72r_e \times 24r_e \times 24r_e$ (length × width × height) was created. In the simulation, a Couette flow with linear shear was implemented by allocating a constant velocity of 0.05 m/s to the top wall, while the bottom wall and the particle surface have a non-slip wall boundary condition. Symmetry boundary conditions were used for the two vertical walls parallel to the flow. Periodic boundaries were assigned for both ends of the flow domain. For particle Reynolds numbers below 0.1, the basecase model has a deviation of 0.28%, 4% and 0.02% respectively, when comparing the drag, moment and lift values with analytical sphere formulae. A grid independence test showed that the mesh size was sufficiently refined [29]. We simulated fluid flows around oblate spheroids with three aspect ratios of α = 0.25, 0.5 and 0.75 and orientation angles where $0° \leqslant \varphi \leqslant 90°$. For each simulation, a single oblate spheroid with a particular α and φ was added to the domain to determine the moment, *M*, exerted by the shear flow. Subsequently, $f_{M,\varphi}$ can be determined by substituting the calculated *M* from CFD into Eqn. (4).

4.1.3 Adhesion force and SEI modelling

The introduction of φ also affects the adhesion force. The surface element integration method (SEI) [49] is used to calculate the variation of F_a as a function of φ. The relevant coordinates and geometric setup are shown in Fig. 7.

To calculate the adhesion force of an arbitrarily orientated oblate spheroid along the *Y*-*Z* plane, the surface element integration (SEI) for the interaction energy is expressed as [49]:

$$U(D) = \int_0^{2\pi} \int_0^{\pi} \hat{\mathbf{n}} \cdot \hat{\mathbf{k}} E(H - Z) r^2 \sin\theta d\theta d\phi \,, \tag{5}$$

where *U* is the interaction potential between the infinite flat plate and the oblate spheroid. In Eqn. (5), $\hat{\boldsymbol{n}}$ is the outer unit normal vector on the surface element defined in space-fixed coordinates and $\hat{\boldsymbol{k}}$ is the unit along the positive *Z*-axis of the space-fixed coordinates. *E* is the interaction potential per unit area between a pair of infinite flat plates separated at a distance *h (= H-Z)*. The equations for calculating *E*, $\hat{\boldsymbol{n}} \cdot \hat{\boldsymbol{k}}$ and *r*, are given in Section S5 of the supplementary materials. More details and derivations are also given in the original work [49]. The interaction force is the negative derivative of Eqn. (5), and F_a is taken as the magnitude of

the primary minimum in the DLVO force curve [9, 15, 50]. The double integral in Eqn. (5) was solved numerically using MATLAB. The SEI code has been validated with the original work of Bhattacharjee et al. [49], as detailed in Fig. S5 in the supplementary materials.

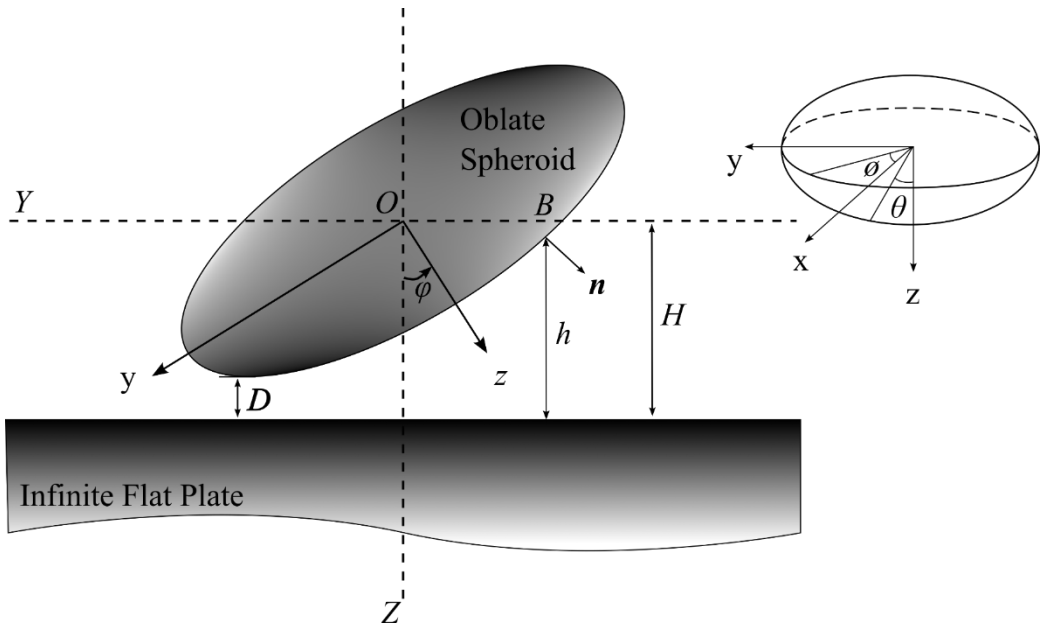

Fig. 7. Geometric configuration of an oblate spheroid orientated at an angle, φ, interacting with an infinite flat plate for surface element integration (SEI) calculations. The body-fixed *x*-*y*-*z* coordinates and the spaced-fixed coordinates *X*-*Y*-*Z* both have the same origin, *O*, at the centre of the spheroid. The inset diagram shows the oblate spheroid defined by the body-fixed Cartesian coordinate *x*-*y*-*z*, as well as the spherical coordinate system of *r*, θ and ϕ. The positive axes of *x* and *X* are both pointed out of the page (towards the reader). A rotation about the *X*-axis in an anticlockwise direction causes a coordinate transform of *y*-*z* while *x* remains the same. *D* is the distance of closest separation, while *H* is the distance between the particle centre and the infinite flat plate. For any point *B* on the surface of the spheroid, there is a corresponding local distance, *h*, and a local unit normal vector, ***n***. Note that ***n*** is defined in body-fixed coordinates.

The adhesion force for inclined spheroids is normalised with respect to the adhesion force of volume equivalent spheres. The corresponding adhesion factor is a function of two independent variables: the orientation angle and the aspect ratio $f_a=f_a(\alpha,\varphi)$.

4.1.4 Hertz contact theory for the determination of l_n

In addition to the adhesion force, it is necessary to determine the lever arm for the adhesion force. Hertz contact theory is used to evaluate the geometry of the contact area between the oblate spheroid and the substrate. The relevant equations are presented in Section S7 of the supplementary materials.

Briefly, the principal radii of curvature of the oblate spheroid are first determined at the point of contact. For a side-on configuration (φ = 0°), the contact area is circular and the

calculation of the contact area is straightforward once the principal radius of curvature at the contact is determined. When $\varphi \neq 0°$, the contact area is elliptical, and the equations for the semi-major and semi-minor radii of the contact area have to be evaluated numerically. MATLAB was used to solve the equations. Ultimately, as shown in Fig. 6, l_n is equal to the radius of the circular contact area when $\varphi = 0°$. For other orientation angles, l_n is equal to the semi-minor radius, b_c of the elliptical contact area.

4.1.5 Monte Carlo simulation of the critical detachment velocity

Lastly, for a direct comparison of the model with the laboratory observations, rearrangement of Eqns. (1)-(4) yields the equation that correlates the geometry and orientation angle of the particles with the critical detachment velocity, v_{cr}, such that:

$$v_{cr} = \frac{F_a L l_n}{36\pi\mu {r_e}^2 l_d f_{M,\varphi} f_M f_d(\alpha, 0)}. \quad (6)$$

Note that for Hele-Shaw flows occurring in the rectangular microfluidic channel, $\dot{\gamma}_o = 6v/L$ [51], where v is the area averaged velocity (flow rate divided by the cross sectional area) and L is the height of the visualisation chamber (450 µm). The derivations for Eqn. (6) are presented in more detail in [22].

For uniform particles and substrates, Eq. (6) defines the critical detachment velocity: no detachment occurs at any lower velocity, and the overall detachment occurs at the critical velocity. This stepwise detachment contradicts the experimentally observed gradual detachment during a continuous or piecewise constant velocity increase [52]. We explain the gradual detachment by probabilistic distributions of parameters in Eqn. (6) and use the Monte Carlo method to determine the probability distribution function for the critical velocity.

The distribution in particle geometry and orientation resulted in a distribution of critical detachment velocities. Based on the measured parameters, as detailed in Table 1, a series of Monte Carlo simulations based on Eqn. (6) were performed for particles S1, S2, S3 and S4. Depending on the samples, 500 spheres or oblate spheroids were randomly generated according to the probabilistic distributions evaluated in Section 2.4. For S3 and S4, only r_e was distributed: for S1 and S2, the simulation accounts for the distribution in r_e, a and φ. The cumulative distribution function of the percentage of particles detached against the area-averaged velocity was plotted and compared with the experimental data.

4.2 Numerical Results

4.2.1 Hydrodynamics

The variation of M with various orientation angles is presented in Fig. 8. Consider the form of the curve $f_{M,\varphi}$ from Eqn. (4), following the sign conventions for φ in relation to the substrate and the direction of shear flow, as presented in Fig. 6a. The curve $f_{M,\varphi}$ versus φ is not exactly symmetrical with respect to the axes φ=90°, but the maximum deviation from the symmetrical curve in the angle interval [90°, 180°] is equal to 0.23%, which is negligible.

The minor deviation arises from the lift force (refer to Section S11 of the supplementary materials) which changes direction so that when $\varphi < 90°$ (tilting away from the oncoming flow), the lift force pushes the particle towards the substrate, and upwards, when $\varphi > 90°$ (tilting towards the oncoming flow). Tables S3-S5 in the supplementary materials show that the drag, F_d vs φ, is also symmetrical with respect to the axes φ=90°. The symmetrical behaviour of the drag and the change in the direction of the lift force agree with the simulation results of prolate spheroids at various orientation angles reported in [53].

For practical purposes, the symmetry of the curve is convenient, as for a given φ, hence no distinctions have to be made between the oblate spheroid tilting upstream or downstream. Note, however, that though the orientation away or towards the upstream does not affect the torque balance, it could potentially affect the subsequent fate of the particle. For example, particles oriented away from upstream are potentially more likely to reorient to a lower orientation angle upon the disruption of the torque balance, rather than detach into the mainstream flow.

As shown in Fig. 8, the lower the α, the greater is the variation in $f_{M,\varphi}$ and M with φ. The hydrodynamic moment peaks at $\varphi = 90°$ (end-on configuration) in all cases, with a maximum deviation of up to 8.5 times when compared with a spheroid lying flat.

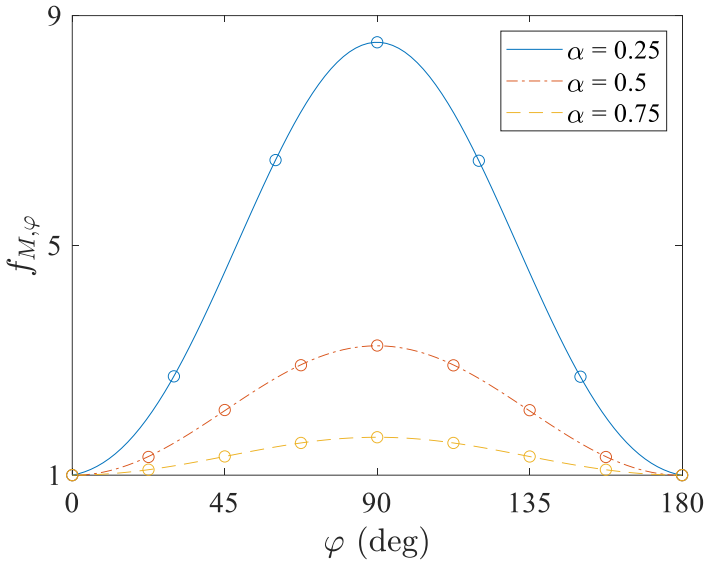

Fig. 8. Variation of the hydrodynamic moment, M exerted on spheroids of constant volume (r_e = 3 μm) with different orientation angles at three aspect ratios. The coefficient $f_{M,\varphi}$ is the hydrodynamic moment, M normalised by the moment for a spheroid of the same α at φ = 0 (side on configuration). The line is fitted to the 'o' symbols which are evaluated using CFD.

To quantify the variation, the line of best fit for the variation of $f_{M,\varphi}$ with the orientation angle is given by:

$$f_{M,\varphi} = a_1 sin\left(a_2\varphi + a_3\right) + b_1 sin\left(b_2\varphi - b_3\right), \tag{7}$$

where the coefficients are dependent on the values of α and φ, as detailed in Table 2.

Table 2: Coefficients to determine $f_{M,\varphi}$ for three α. The values were calculated for φ in degrees.

α	a1	a2	a3	b1	b2	b3
0.25	6.408	0.74427	23.0616	2.128	2.49867	225.230
0.5	2.126	0.03384	86.8604	-1.126	2.00478	89.668
0.75	1.384	0.26196	66.4631	0.2757	2.13942	-102.502

4.2.2 Adhesion force

Fig. 9 shows the variation of the normalised adhesion force with φ. Except for spheres, the maximum adhesion force occurs when φ = 0° and decreases to a minimum at φ = 90°. Similar to M, the largest variation in f_a with respect to φ occurs for the spheroid with the lowest α. Except for spheres, the steepest variation in F_a occurs between 0°<φ<30°. Lastly, there is a reversal of trends; at φ = 0°, the maximum F_a occurs for the lowest α, but at φ = 90°, the maximum F_a occurs in the highest α, i.e. the spheres.

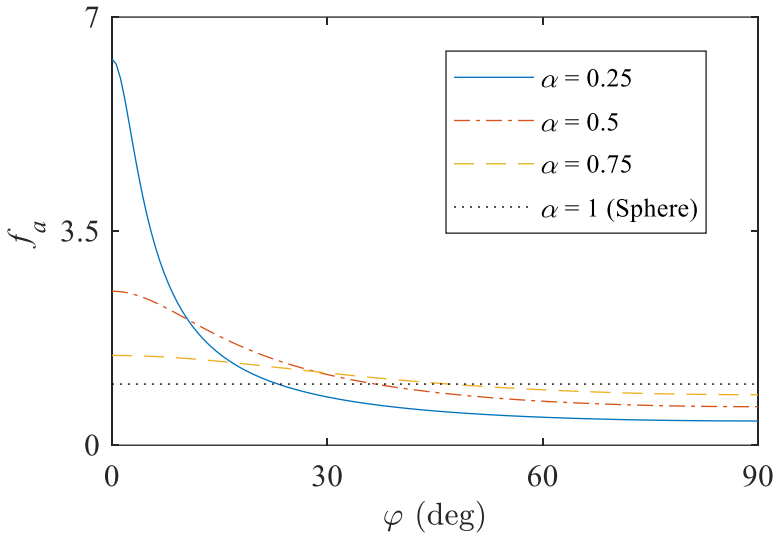

Fig. 9. Variation in the adhesion force of a spheroid (r_e = 3 μm) with changing orientation angle and aspect ratio. f_a is the normalised adhesion force of a spheroid at an arbitrary angle to the adhesion force of a volume equivalent sphere (radius = 3 μm). The distance of the spheroid centre, H, is varied to ensure that the distance of the closest separation, *D*, remains the same.

4.2.3 Critical detachment velocity

Finally, the combined impacts of α and φ on the hydrodynamics, adhesion force and normal lever arm are evaluated by investigating their effects on the critical detachment velocities of the spheroids, as shown in Fig. 10.

Referring to Fig. 10(b), the impact of the orientation angle towards the particle detachment is more prominent in highly skewed (low α) particles. As the aspect ratio approaches 1 (sphere), the detachment of the particles becomes independent of the orientation angle, as expected. The critical detachment velocity decreases with increasing orientation angle for all the spheroids. For the case of α = 0.25, the critical detachment velocity of oblate spheroids can vary by three orders of magnitude with the orientation angle (4.6 m/s at φ = 0° and 2×10^{-3} m/s at φ = 90°).

The detachment trend is reversed as the particle orientation changes from 0° to 90°. In other words, at 0°, particles with aspect ratios of 0.75 are the easiest to detach, while at 90°, particles with α = 0.25 are the easiest to detach. At around φ = 30° to 40° (intermediate angles), the critical detachment velocity for spheroids is similar to that of spheres, regardless of α.

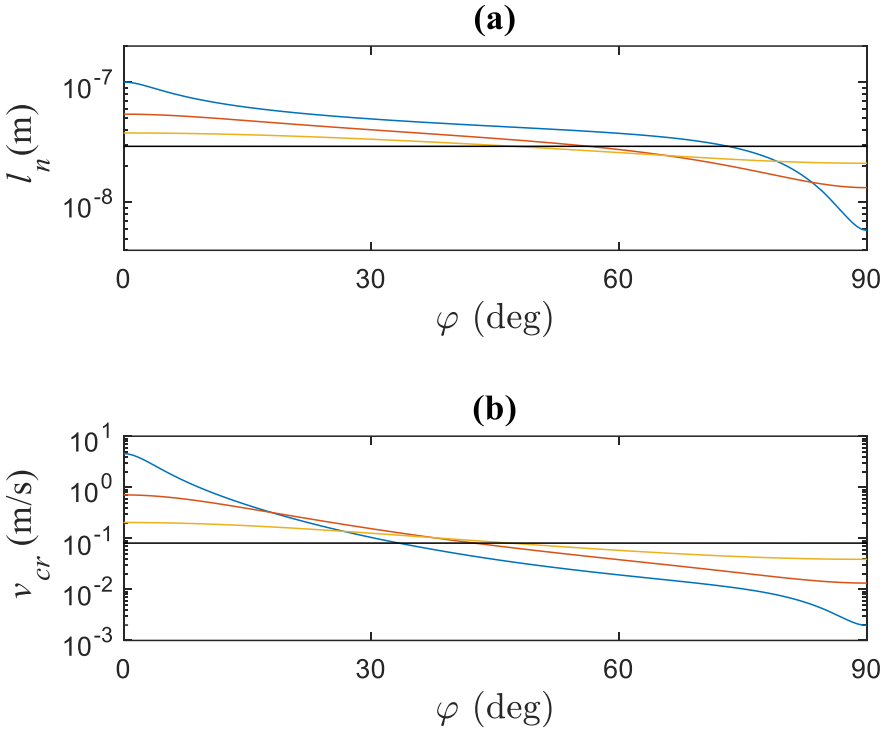

Fig. 10. Variation of the (a) normal lever arm and (b) critical detachment velocity with orientation angle for oblate spheroids and a sphere. Blue, red and yellow colours represent α = 0.25, 0.5 and 0.75, respectively. The black line represents a perfect sphere. The volumes of the particles were kept constant at r_e= 3 μm.

4.3 Comparison of laboratory data with the stochastic torque balance model

Lastly, the detachment of particles from the visualisation experiment is compared with the numerical model, as shown in Fig. 11. Focusing first on the numerical modelling (solid curves), the detachment curve of spheroids is more spread than for spheres; the sphere curve approaches a stepwise detachment trend. In both spheres and spheroids, particles with larger r_e require a lower v_{cr}.

By comparing the numerical results in Fig. 11(a) and (b), an interesting result was obtained. For a given r_e,, spheroids initiate detachment earlier than spheres; yet as the velocity continues to increase, spheroids also resist detachment better than spheres at higher velocities. For an oblate spheroid of constant r_e and α, the initial detachment at low velocities is attributed to the spheroids that are deposited at a high φ ($\approx$90°), with their low critical detachment velocity being as presented in Fig. 10(b). As the flow velocity continues to increase, spheroids with intermediate φ begin to detach at similar critical detachment velocities to spheres. Toward higher velocities, only spheroids with low φ (approaching 0°) remain on the substrate as they require high velocity to detach. The high v_{cr} when φ approaches 0° arises from the combined

effect of reduced hydrodynamic moments (Fig. 8), increased adhesion forces (Fig. 9) and increased normal lever arms for adhesion (Fig. 10a).

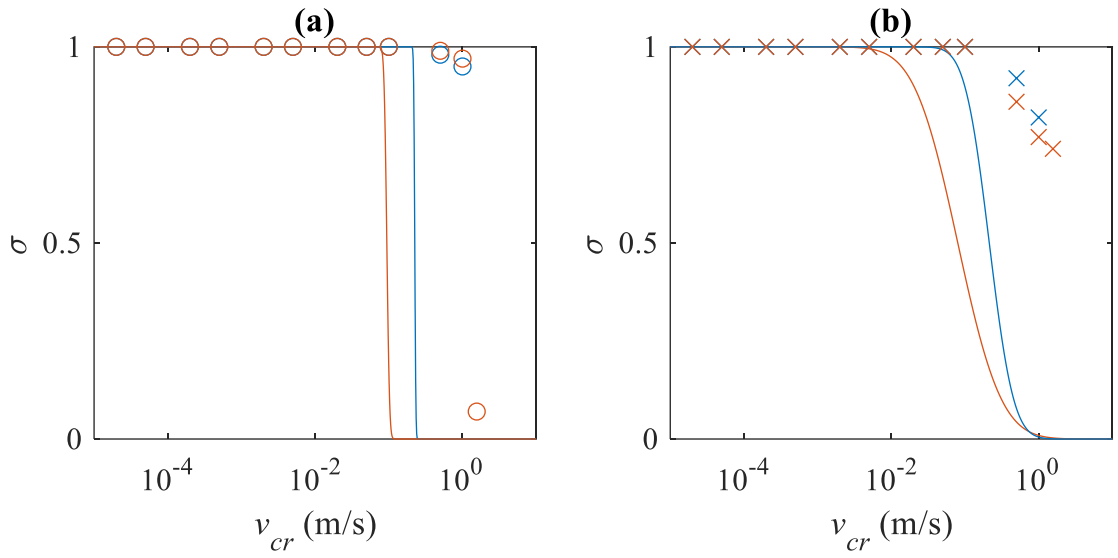

Fig. 11. Plot of normalised attached particle concentrations versus the critical detachment velocity for (a) spheres and (b) spheroids. Blue and red represent the data set for r_e = 1.5 µm and 3 µm, respectively. The solid curves are plotted using the stochastic torque balance model, while the 'o' and 'x' points are obtained from visualisation experiments of spheres and spheroids, respectively. In (a), the solid curves are plotted for the spheres by the distribution in r_e (spheres do not have φ and α). In (b), the calculated v_{cr} was plotted, allowing for the distribution in r_e, φ and α for the spheroids.

In comparison with the visualisation data, the steep detachment of spheres versus the gradual detachment of spheroids in the numerical modelling matches the observations in the experiment qualitatively. The visualised higher detachment rate of the larger S2 spheroid sample compared with the smaller S1 spheroid is also reflected in the numerical model.

However, the numerical model consistently underestimates the required detachment velocity. Furthermore, the different threshold velocities for the initiation of detachment are absent in the visualisation. In other words, although the model predicts that detachment is initiated with lower velocities for the spheroids than the spheres, the visualisation shows the initiation of detachment occurring at v_{cr} = 0.5 m/s for all four data sets.

5 Discussion

Let us discuss the limitations of the visualisation studies. The whole detachment curve (where σ approaches zero) could not be observed, as higher flow velocities could not be achieved due to the limitation of the syringe pump. The experiment could be repeated with a microfluidic cell of a shorter height, thus increasing the flow velocity for the same flow rate.

However, qualitatively, the visualisations have shown that a) the spheroid particles are deposited at an angle, b) reorientation occurs in the same order of magnitude as detachment (not less), c) detachment occurs more often than reorientation at higher velocities, d) particles deposited with an orientation angle (red and blue particles in Fig. 4) are more likely to reorient or detach than particles at $\varphi \approx 0°$ and e) spheroids can be retained at higher velocities, when spheres would have detached.

A significant deviation is observed between the predicted and observed detachment, for both the spheroids and the spheres. Therefore, it can be deduced that the deviation in the curves may not be primarily from the shape factors (the sphere modelling did not use any shape factors). Firstly, the underestimation of the critical detachment velocity is potentially due to the underestimation of the adhesion torque, which comprises the adhesion force and the contact area. Both parameters are interrelated: the adhesion force increases the contact area and the contact area increases the adhesion force. This requires an iterative solution by trial and error [39]. Yet, due to computational limitations, the model for DLVO attraction used in this work assumes a single touching spheroid-substrate point. The contact area that degenerates into a touching point corresponds to infinite Young's modulus. The lower the Young's modulus, the larger the contact area, and the higher the electrostatic attraction. The actual attachment torque for the polystyrene particles might be larger than calculated. This potentially explains the underestimation of the detachment velocity by the current mathematical model, when compared with the laboratory data (Fig. 11).

Secondly, from a torque balance perspective, both reorientation and detachment could occur when the equilibrium between the detaching hydrodynamic torque and the attaching adhesion torque is disrupted, i.e. the detaching hydrodynamic torque becomes larger than the attaching adhesion torque (no distinction is made in the model). The possibility of both scenarios presents an explanation as to why reorientation occurs at the same velocity threshold as detachment. However, in the current modelling, it is assumed that all particles will detach (not reorient) whenever the detaching hydrodynamic torque becomes larger than the attaching adhesion torque, which provides another possible explanation for the overestimation of the detachment rate by the model. Distinguishing between reorientation and detachment will require dynamic modelling methods, which are grounds for future work [14].

Thirdly, another potential source of experimental errors could be the presence of PVA residue that affects the surface charge of the particle, as has been reported in numerous works

[19, 21, 23, 30]. In attempts to quantify the change in surface charges, we conducted zeta potential measurements, but the low yield of the manufacturing process makes it challenging to obtain reliable zeta potential measurements using the dilute samples (see Section S9 of the supplementary materials). The zeta potential of the PVA-processed particles was consistently reduced when compared with stock particles from the manufacturer. The particles were also assumed to deform uniformly into an oblate spheroid. Additionally, given the sensitivity of the detachment to the orientation angle, the determination of the orientation angle from the image processing is prone to errors in processing and fitting of the distributions. The image processing is highly sensitive to the binarisation threshold, which has to be determined by trial and error [22]. Indications of the physical factors explaining the deviations between the laboratory and the modelling data from the abovementioned list of reasons would require additional investigations.

Lastly, the presence of surface roughness in the visualisation slides could also alter the detachment behaviour, leading to deviations from the predicted detachment velocities. The presence of surface roughness has been reported to a) increase the lever arm for adhesion, b) reduce the lever arm for drag [54], c) increase/decrease the adhesion force, depending on the scale and morphology of the roughness [55] and d) increase drag [53].

The size of the particles considered in this study coincides with particles such as platelets (α = 0.25, r_e = 1.5 µm) [56] and kaolinites (0.03 <α< 0.5; 0.2 <r_e<50 µm) [22], which are frequently studied in the literature. Given that the orientation angle can result in deviations of up to three orders of magnitude in the detachment velocity, it is justified that the orientation angle requires further study and application in future modelling works. However, for shapes other than spheres and oblate spheroids, the dominant detachment mechanism may not be rolling. Sliding and lifting detachment would also need to be considered for other shapes [57, 58].

Numerous works have proposed correlations to quantify the impact of nonspherical shapes on the drag [59-61] but are limited when used in the context of resuspension where the presence of a wall affects the hydrodynamic forces [62, 63]. Similar studies have quantified the impact of orientation angles (roll/yaw angles) in wall-bound prolate spheroids [64] and sphere chains [57, 65] on the hydrodynamic forces. In agreement with our studies, the hydrodynamics forces are increased when the orientation angle approaches 90°. Nonetheless,

by implementing torque balance, a mechanistic model to quantify the variation in hydrodynamics towards the detachment rate is proposed in this paper.

Previous work [29] suggests that the detachment rate generally reduces with decreasing aspect ratios (for $0.25 \leqslant \alpha \leqslant 1$) in oblate spheroids. However, the current study shows that the trend is only true for small orientation angles. For higher orientation angles ($\varphi > 45°$), the trend is reversed: the detachment increases with the decreasing aspect ratio. Indeed, this reversal of trends is a potential explanation for the seemingly contradictory results of the literature where nonspherical particles could either increase or decrease retention. The model in this study suggests that the oblate spheroids could either be easier or harder to detach, compared with spheres, depending on the orientation angle adopted (as discussed in Section 4.3). It would be interesting in future work to run the visualisation experiments mixing spheres and oblate spheroid particles of various aspect ratios and orientation angles to test the hypothesis.

The important extension of the current paper is fines detachment in porous media. This development changes the experimental procedures and the mathematical model. For reservoir cores, which are not transparent, it is impossible to visualise images like those presented in Fig. 3 and Fig. 4. Even for transparent columns obtained by compacting glass spheres, the detachment conditions on the spheres are significantly more complex than those on the plane substrates. However, the breakthrough particle concentrations can be measured with high accuracy during flow in porous media, which enables verification of the particle detachment model [66, 67].

In the present work, the microscale expressions for forces and torques in Eqns. (3-4) are obtained by using CFD and SEI methods. These expressions must be extended for use in upper-scale models for nano-colloidal-suspension transport in porous media [50, 66-68]. However, Eqns. (1)-(4) and (6) must also be significantly modified to account for rock surface roughness. One way around this would be to use the three-point contact model of [69-71]. Using Lattice-Boltzmann (LB), CFD, and Discrete Element Method (DEM) modelling can extend shape factors for drag, lift, and DLVO forces [4, 5, 7, 72]. The particle-scale expressions for the attachment-detachment rates, obtained by LB, CFD, and DEM modelling, close the governing system of mass balance equations at the core scale, providing the model for colloidal-suspension transport in porous media [8, 73, 74].

The torque balance given by Eqns. (1)-(4) is expressed as the maximum retention concentration MRF versus velocity, (Fig. 11) [12, 44], at the upper scale. Upscaling of the transport equations could be done using exact averaging in population balance models [75, 76], random walk models [77], continuous upscaling [78, 79], or numerical 3D network modelling [80]. Furthermore, exact solutions can be obtained by non-linear modifications of methods of characteristics using Riemann invariants [81, 82] for approximate cases where advective fluxes are dominant and dissipative/non-equilibrium fluxes are negligible. Otherwise, the dissipative and non-equilibrium effects can be included by matching the asymptotic expansions [83, 84] in the mathematical formulation.

For uniform spheres, MRF is stepwise. For spheres with distributed size, velocity changes at some interval from the beginning of the detachment to its completion. Fig. 11 shows that for inclined spheroidal particles, this velocity interval is significantly larger. This is explained by mutual distributions of spheroid semi-major axes and orientation angles.

6 Conclusions

Laboratory visualisation of particle detachment from solid surfaces and torque balance modelling allow us to draw the following conclusions:

Integrating the methodology of transparent cell saturation by the colloidal fines, the imaging technique, and fine spheroid production with the geometric projection formulae allows for a direct comparison between the detachments of spherical and oblate spheroidal particles under different orientation angles.

The developed mechanistic model for particle detachment quantifies the impact of the orientation angle and aspect ratio on the adhesion force, hydrodynamic moment and contact area.

An increase in the orientation angle from 0 ° to 90 ° yields a decrease in the detachment velocity. In the interval of the orientation angle from 0 ° to some intermediate values, the higher the aspect ratio, the lower the detachment velocity is. In the interval from the intermediate angle to 90°, the dependency is opposite.

Production of ‘ideal’ latex spheroids avoids uncertainty in the modelling of the detachment of nonspherical particles (compared with previous studies of kaolinite fines). The

velocity interval from the detachment beginning to its completion for inclined spheroidal particles is significantly wider than that for spheres.

The stochastic model underestimates the critical detachment velocity, but qualitatively matches the trends of the dependency of the aspect ratio, orientation angle and particle size, as observed in the visualisation experiments.

Detachment velocities for the particles with orientation angles φ and -φ are equal for cases where the lift forces are negligible.

CRediT authorship contribution statement

Heng Zheng Ting: Methodology, Investigation, Formal analysis, Validation, Writing-original draft. **Yutong Yang**: Investigation, Formal analysis, Validation. **Zhao Feng Tian**: Supervision, Conceptualisation, Methodology. **Themis Carageorgos**: Conceptualisation, Methodology, Resources. **Pavel Bedrikovetsky**: Conceptualisation, Methodology, Supervision.

Declaration of Competing Interests

The authors declare that they have no known competing financial interests or personal relationships that could have appeared to influence the work reported in this paper.

Acknowledgements

This work was supported with the supercomputing resources provided by the Phoenix HPC service at the University of Adelaide. The authors acknowledge the instruments and expertise of Microscopy Australia at Adelaide Microscopy, The University of Adelaide, enabled by NCRIS, university, and state government support.

Appendix A Supplementary Data

Supplementary data to this article can be found online.

References

1. Boor BE, Siegel JA, Novoselac A. Monolayer and Multilayer Particle Deposits on Hard Surfaces: Literature Review and Implications for Particle Resuspension in the Indoor Environment. Aerosol Science and Technology. 2013;47(8):831-47.

2. Kok JF, Parteli EJ, Michaels TI, Karam DB. The physics of wind-blown sand and dust. Reports on Progress in Physics. 2012;75(10):106901.

3. Bai B, Rao D, Chang T, Guo Z. A nonlinear attachment-detachment model with adsorption hysteresis for suspension-colloidal transport in porous media. Journal of Hydrology. 2019;578.

4. Schulz D, Woschny N, Schmidt E, Kruggel-Emden H. Modelling of the detachment of adhesive dust particles during bulk solid particle impact to enhance dust detachment functions. Powder Technology. 2022;400.

5. Schulz D, Reinecke SR, Woschny N, Schmidt E, Kruggel-Emden H. Development and evaluation of force balance based functions for dust detachment from bulk particles stressed by fluid flow. Powder Technology. 2023;417.

6. Di J, Gao X, Du Y, Zhang H, Gao J, Zheng A. Size, shape, charge and "stealthy" surface: Carrier properties affect the drug circulation time in vivo. Asian Journal of Pharmaceutical Sciences. 2021;16(4):444-58.

7. Cui Y, Sommerfeld M. Forces on micron-sized particles randomly distributed on the surface of larger particles and possibility of detachment. International Journal of Multiphase Flow. 2015;72:39-52.

8. Ariane M, Sommerfeld M, Alexiadis A. Wall collision and drug-carrier detachment in dry powder inhalers: Using DEM to devise a sub-scale model for CFD calculations. Powder Technology. 2018;334:65-75.

9. Bradford SA, Morales VL, Zhang W, Harvey RW, Packman AI, Mohanram A, et al. Transport and Fate of Microbial Pathogens in Agricultural Settings. Critical Reviews in Environmental Science and Technology. 2013;43(8):775-893.

10. Russell T, Chequer L, Borazjani S, You Z, Zeinijahromi A, Bedrikovetsky P. Formation Damage by Fines Migration. Formation Damage During Improved Oil Recovery2018. p. 69-175.

11. Bai B, Nie Q, Wu H, Hou J. The attachment-detachment mechanism of ionic/nanoscale/microscale substances on quartz sand in water. Powder Technology. 2021;394:1158-68.

12. Bedrikovetsky P, Siqueira FD, Furtado CA, Souza ALS. Modified Particle Detachment Model for Colloidal Transport in Porous Media. Transport in Porous Media. 2011;86(2):353-83.

13. Bai B, Bai F, Nie Q, Jia X. A high-strength red mud–fly ash geopolymer and the implications of curing temperature. Powder Technology. 2023;416.

14. Henry C, Minier J-P, Brambilla S. Particle resuspension: Challenges and perspectives for future models. Physics Reports. 2023;1007:1-98.

15. Lee H, Kang S, Kim SC, Pui DYH. Modeling transport of colloidal particles through polydisperse fibrous membrane filters under unfavorable chemical and physical conditions. Powder Technology. 2019;355:7-17.

16. Palomino AM, Santamarina JC. Fabric Map for Kaolinite: Effects of pH and Ionic Concentration on Behaviour. Clays and Clay Minerals. 2005;53(3):211-23.

17. Mahmood T, Amirtharajah A, Sturm T, Dennett K. A micromechanics approach for attachment and detachment of asymmetric colloidal particles. Colloids and Surfaces. 2001;177(2-3):99-110.

18. Xu Z, Niu WA, Rivera SL, Tuominen MT, Siegrist MS, Santore MM. Surface Chemistry Guides the Orientations of Adhering E. coli Cells Captured from Flow. Langmuir. 2021;37(25):7720-9.

19. Ma H, Bolster C, Johnson WP, Li K, Pazmino E, Camacho KM, et al. Coupled influences of particle shape, surface property and flow hydrodynamics on rod-shaped colloid transport in porous media. J Colloid Interface Sci. 2020;577:471-80.

20. Shave MK, Balciunaite A, Xu Z, Santore MM. Rapid Electrostatic Capture of Rod-Shaped Particles on Planar Surfaces: Standing up to Shear. Langmuir. 2019;35(40):13070-7.

21. Aramrak S, Flury M, Harsh JB, Zollars RL, Davis HP. Does colloid shape affect detachment of colloids by a moving air-water interface? Langmuir. 2013;29(19):5770-80.

22. Ting HZ, Yang Y, Tian ZF, Carageorgos T, Bedrikovetsky P. Image interpretation for kaolinite detachment from solid substrate: Type curves, stochastic model. Colloids and Surfaces A: Physicochemical and Engineering Aspects. 2022;650.

23. Seymour MB, Chen G, Su C, Li Y. Transport and retention of colloids in porous media: does shape really matter? Environ Sci Technol. 2013;47(15):8391-8.

24. Liu Q, Lazouskaya V, He Q, Jin Y. Effect of particle shape on colloid retention and release in saturated porous media. J Environ Qual. 2010;39(2):500-8.

25. Salerno B, Flamm M, Logan B, Velegol D. Transport of Rodlike Colloids through Packed Beds. Environmental Science & Technology. 2006;40(20):6336-40.

26. Knappenberger T, Aramrak S, Flury M. Transport of barrel and spherical shaped colloids in unsaturated porous media. J Contam Hydrol. 2015;180:69-79.

27. Lin D, Hu L, Bradford SA, Zhang X, Lo IMC. Pore-network modeling of colloid transport and retention considering surface deposition, hydrodynamic bridging, and straining. Journal of Hydrology. 2021;603.

28. Bai B, Xu T, Nie Q, Li P. Temperature-driven migration of heavy metal Pb2+ along with moisture movement in unsaturated soils. International Journal of Heat and Mass Transfer. 2020;153.

29. Ting HZ, Bedrikovetsky P, Tian ZF, Carageorgos T. Impact of shape on particle detachment in linear shear flows. Chemical Engineering Science. 2021;241.

30. Gomez-Flores A, Bradford SA, Hwang G, Choi S, Tong M, Kim H. Shape and orientation of bare silica particles influence their deposition under intermediate ionic strength: A study with QCM–D and DLVO theory. Colloids and Surfaces A: Physicochemical and Engineering Aspects. 2020;599.

31. McNew CP, Kananizadeh N, Li Y, LeBoeuf EJ. The attachment of colloidal particles to environmentally relevant surfaces and the effect of particle shape. Chemosphere. 2017;168:65-79.

32. Cooley M, Sarode A, Hoore M, Fedosov DA, Mitragotri S, Sen Gupta A. Influence of particle size and shape on their margination and wall-adhesion: implications in drug delivery vehicle design across nano-to-micro scale. Nanoscale. 2018;10(32):15350-64.

33. Mody NA, Lomakin O, Doggett TA, Diacovo TG, King MR. Mechanics of transient platelet adhesion to von Willebrand factor under flow. Biophysical Journal. 2005;88(2):1432-43.

34. Kottapalli K, Novosselov IV. Experimental study of aerodynamic resuspension of RDX residue. Aerosol Science and Technology. 2019;53(5):549-61.

35. Li K, Ma H. High Fluid Velocity and Narrow Channels Enhance the Influences of Particle Shape on Colloid Retention in Saturated Groundwater Systems Under Favorable Deposition Conditions. Frontiers in Water. 2021;3.

36. Mody NA, King MR. Three-dimensional simulations of a platelet-shaped spheroid near a wall in shear wall. Physics of Fluids. 2005;17(11).

37. Stoll M, Huber FM, Schill E, Schäfer T. Parallel-plate fracture transport experiments of nanoparticulate illite in the ultra-trace concentration range investigated by Laser-Induced Breakdown Detection (LIBD). Colloids and Surfaces A: Physicochemical and Engineering Aspects. 2017;529:222-30.

38. Bergendahl J, Grasso D. Mechanistic Basis for Particle Detachment from Granular Media. Environmental Science & Technology. 2003;37(10):2317-22.

39. Sharma M, Chamoun H, Sarma D, Schechter R. Factors Controlling the Hydrodynamic Detachment of Particles from Surfaces. Journal of Colloid and Interface Science. 1992;149(1):121-34.

40. Pozrikidis C. Orbiting motion of a freely suspended spheroid near a plane wall. Journal of Fluid Mechanics. 2005;541(-1).

41. Kaya T, Koser H. Characterization of hydrodynamic surface interactions of Escherichia coli cell bodies in shear flow. Physical Review Letters. 2009;103(13):138103.

42. Gomez-Flores A, Bradford SA, Wu L, Kim H. Interaction energies for hollow and solid cylinders: Role of aspect ratio and particle orientation. Colloids and Surfaces A: Physicochemical and Engineering Aspects. 2019;580.

43. Ahn SJ, Ahn KH, Lee SJ. Film squeezing process for generating oblate spheroidal particles with high yield and uniform sizes. Colloid and Polymer Science. 2016;294(5):859-67.

44. Bedrikovetsky P, Zeinijahromi A, Siqueira FD, Furtado CA, Souza ALS. Particle Detachment Under Velocity Alternation During Suspension Transport in Porous Media. Transport in Porous Media. 2012;91(1):173-97.

45. Hubbe M. Theory of Detachment of Colloidal Particles from Flat Surfaces Exposed to Flow. Colloids and Surfaces. 1984;12:151-78.

46. Ferrari MA, Lugarini A, Franco AT. On the settling of spherical particles in power-law fluid at moderate Reynolds number. Powder Technology. 2022;405.

47. O'Neill ME. A sphere in contact with a plane wall in a slow linear shear flow. Chemical Engineering Science. 1968;23(11):1293-8.

48. Barenblatt GI. Scaling: Cambridge University Press; 2003.

49. Bhattacharjee S, Chen J, Elimelech M. DLVO interaction energy between spheroidal particles and a flat surface. Colloids and Surfaces A: Physicochemical and Engineering Aspects. 2000;165:143-56.

50. Ma H, Li Y, Shen C, Chrysikopoulos CV, Kim H. Advances in Pollutant Transport in Critical Zone Environments. Frontiers in Water. 2021;3.

51. Bird RB, Stewart WE, Lightfoot EN. Transport Phenomena. 2nd ed. New York: John Wiley & Sons; 2001.

52. Goldasteh I, Ahmadi G, Ferro AR. Monte Carlo simulation of micron size spherical particle removal and resuspension from substrate under fluid flows. Journal of Aerosol Science. 2013;66:62-71.

53. Bhagat AM, Goswami PS. Effect of rough wall on drag, lift, and torque on an ellipsoidal particle in a linear shear flow. Physics of Fluids. 2022;34(8).

54. Burdick GM, Berman NS, Beaudoin SP. Hydrodynamic particle removal from surfaces. Thin Solid Films. 2005;488(1-2):116-23.

55. Shen C, Jin Y, Zhuang J, Li T, Xing B. Role and importance of surface heterogeneities in transport of particles in saturated porous media. Critical Reviews in Environmental Science and Technology. 2019;50(3):244-329.

56. Pozrikidis C. Flipping of an adherent blood platelet over a substrate. Journal of Fluid Mechanics. 2006;568.

57. Villagran Olivares MC, Benito JG, Unac RO, Vidales AM. Kinetic Monte Carlo method applied to micrometric particle detachment mechanisms by aerodynamic forces. J Phys Condens Matter. 2021;34(7).

58. Brambilla S, Speckart S, Brown MJ. Adhesion and aerodynamic forces for the resuspension of non-spherical particles in outdoor environments. Journal of Aerosol Science. 2017;112:52-67.

59. Loth E. Drag of non-spherical solid particles of regular and irregular shape. Powder Technology. 2008;182(3):342-53.

60. Dioguardi F, Mele D. A new shape dependent drag correlation formula for non-spherical rough particles. Experiments and results. Powder Technology. 2015;277:222-30.

61. Tran-Cong S, Gay M, Michaelides EE. Drag coefficients of irregularly shaped particles. Powder Technology. 2004;139(1):21-32.

62. Hsu R, Ganatos P. The motion of a rigid body in viscous fluid bounded by a plane wall. Journal of Fluid Mechanics. 1989;207:29-72.

63. Goldman AJ, Cox RG, Brenner H. Slow viscous motion of a sphere parallel to a plane wall-I Motion though a quiescent fluid. Chemical Engineering Science. 1967;22:637-51.

64. Fillingham P, Vaddi RS, Bruning A, Israel G, Novosselov IV. Drag, lift, and torque on a prolate spheroid resting on a smooth surface in a linear shear flow. Powder Technology. 2021;377:958-65.

65. Ekiel-Jezewska ML, Sadlej K, Wajnryb E. Friction of rodlike particles adsorbed to a planar surface in shear flow. J Chem Phys. 2008;129(4):041104.

66. Fountouli TV, Chrysikopoulos CV. Effect of Clay Colloid Particles on Formaldehyde Transport in Unsaturated Porous Media. Water. 2020;12(12).

67. Shapiro AA, Yuan H. Application of stochastic approaches to modelling suspension flow in porous media. In: Skogseid A, Fasano V, editors. Statistical Mechanics and Random Walks: Principles, Processes and Applications: Nova Science Publishers; 2012.

68. Johnson WP. Quantitative Linking of Nanoscale Interactions to Continuum-Scale Nanoparticle and Microplastic Transport in Environmental Granular Media. Environ Sci Technol. 2020;54(13):8032-42.

69. Ziskind G, Fichman M, Gutfinger C. Resuspension of particulates from surfaces to turbulent flows—review and analysis. Journal of Aerosol Science. 1995;26(4).

70. Ziskind G, Fichman M, Gutfinger C. Adhesion moment model for estimating particle detachment from a surface. Journal of Aerosol Science. 1997;28(4).

71. Ziskind G. Particle resuspension from surfaces: Revisited and re-evaluated. Reviews in Chemical Engineering. 2006;22(1-2).

72. Cui Y, Sommerfeld M. Lattice–Boltzmann simulations for analysing the detachment of micron-sized spherical particles from surfaces with large-scale roughness structures. Particuology. 2022;61:47-59.

73. Bedrikovetsky P. Mathematical theory of oil and gas recovery: with applications to ex-USSR oil and gas fields: Springer Science & Business Media; 2013.

74. Iliev O, Kirsch R, Lakdawala Z, Rief S, Steiner K. Modeling and Simulation of Filtration Processes. Currents in Industrial Mathematics: Springer; 2015. p. 163-238.

75. Bedrikovetsky P. Upscaling of stochastic micro model for suspension transport in porous media. Transport in Porous Media. 2008;75(3):335-69.

76. Bedrikovetsky P, Osipov Y, Kuzmina L, Malgaresi G. Exact upscaling for transport of size-distributed colloids. Water Resources Research. 2019;55:1011-39.

77. Shapiro AA. Elliptic equation for random walks. Application to transport in microporous media. Physica A: Statistical Mechanics and its Applications. 2007;375(1):81-96.

78. Shapiro AA. Continuous upscaling and averaging. Chemical Engineering Science. 2021;234:1-13.

79. Shapiro AA. Continuous upscaling of the 3D diffusion equation in a heterogenous medium. Chemical Engineering Science. 2022;248.

80. Cihan A, Petrusak R, Bhuvankar P, Alumbaugh D, Trautz R, Birkholzer JT. Permeability Decline by Clay Fines Migration around a Low-Salinity Fluid Injection Well. Groundwater. 2022;60(1):87-98.

81. Polyanin AD, Zaitsev VF. Handbook of Nonlinear Partial Differential Equations: Exact Solutions, Methods and Problems. New York: Chapman and Hall/CRC; 2003.

82. Polyanin AD, Zaitsev VF, Moussiaux A. Handbook of first-order partial differential equations. London: CRC Press; 2001.

83. Polyanin AD, Dil'man VV. Methods of modeling equations and analogies in chemical engineering. Boca Raton, Fl.: CRC Press; 1994.

84. Polyanin AD, Kutepov AM, Kazenin DA, Vyazmin AV. Hydrodynamics, mass and heat transfer in chemical engineering. London: CRC Press; 2001.

This page is intentionally left blank

Chapter 8

Conclusions and Future Work

The detachment of particles is pertinent to many fields of science, such as pharmaceutical, biological, manufacturing, environmental and chemical science. In these various applications, the particle geometries involved usually deviate from a perfect sphere. Yet, despite the prevalence of these non-spherical geometries, studies on how these shape deviations affect detachment have only been found very recently in the literature.

In addition, the study of particle detachment is necessarily multidisciplinary, drawing on knowledge from fields such as interparticle interactions, fluid mechanics and contact mechanics. Studies often focus on a particular field, while neglecting or oversimplifying others. On the other hand, some investigations attempt to scrutinise all parameters, particularly through numerical simulations. Although useful in determining the overall detachment behaviour, the investigation still lacks a systematic understanding of each parameter. Furthermore, in understanding the detachment of particles, there is a lack of direct visualisation experiments with which to compare the theory.

This study has utilised CFD and SEI to systematically characterise the variation in the hydrodynamic and adhesion forces in response to varying particle geometries, flow conditions and particle-substrate configurations. The detachment of particles was predominantly quantified using the torque balance for rolling detachment, although the possibilities for sliding and lifting detachment were also considered. The numerical investigations are complemented by direct visualisation experiments of particle detachment in microfluidic cells. The particles ranged from spheres, oblate spheroids and kaolinite of varying properties subjected to either favourable or unfavourable conditions.

The comparison of the numerical and experiment findings has resulted in a few key findings summarised below.

8.1 Conclusions

In addressing the recent trends presented in the literature, this work has endeavoured to systematically understand some major topics of interest in particle detachment. The gaps and objectives of this thesis are addressed through the four journal articles. The new understandings and key findings are summarised as follows:

8.1.1 Modelling irregular particles as volume-equivalent spheres is insufficient to capture the variation in detachment arising from the aspect ratio.

Objective 1 of the study was to quantify the impact of shape and aspect ratio towards adhesion and hydrodynamic force with respect to particle detachment. Using kaolinite as a specific application, the particle was approximated as a cylinder or an oblate spheroid of various aspect ratios ($0.025 < \alpha < 1$). The impact of shape and aspect ratio has been investigated by evaluating the variations in hydrodynamic drag, lift and moment, as well as adhesion force, with varying aspect ratios. For the case of the hydrodynamic drag and moment, there is a non-monotonic dependence with aspect ratio, where the drag and moment decrease to a minimum before increasing again. Depending on the magnitude of the adhesion force, the non-monotonicity from the hydrodynamic torque could extend towards the overall detachment behaviour.

Of the three possible modes of the detachment of rolling, sliding and lifting, cylinders detach preferably by sliding, while oblate spheroids by rolling. Detachment by lifting was the least likely to occur due to the negligible lift force when compared to the adhesion force. Overall, numerical modelling shows that the non-unity aspect ratio could cause a considerable deviation from the critical detachment velocity, with up to an order of magnitude difference for an oblate spheroid at $\alpha = 0.025$ compared to spheres.

8.1.2 The two-stage detachment behaviour corresponds to detachment from the primary and secondary minima.

In relation to Objective 2, the detachment of oblate spheroids was investigated under unfavourable conditions. Based on the theoretical DLVO curve, where the presence of an additional barrier introduces a secondary minimum, direct visualisation studies have

shown a two-stage detachment for both latex and kaolinite particles. The observation matches the model, which suggests detachment first from the weaker secondary minima, followed by detachment from the primary minimum. The variation in aspect ratio does not remove the repulsive energy barrier.

When comparing the torque balance model to the alternative Greenwood rolling friction model and the Dominik and Tielens (DT) model, the torque balance model, despite its tendency to overestimate the attachment torque, still appears to be the most practical. The two other models are based on empirical parameters, which prevents predictions from being made without laboratory measurements.

8.1.3 The gradual detachment behaviour of the particles observed in the experiments can be explained by parameter distributions of the particle properties.

In addressing objective 3, the visualisation focuses on natural kaolinite particles under favourable and unfavourable conditions. Stochastic modelling accounting for the distribution in the kaolinite aspect ratio, semi-major axis, lever arm ratio and zeta potentials matches the observed gradual detachment trend of kaolinite particles from the laboratory studies. Sensitivity studies revealed that the zeta potentials, lever arm ratio, aspect ratio and semi-major axis affect the detachment of kaolinite in increasing significance.

8.1.4 Particles are often deposited at an orientation angle, and the angled deposition increases the likelihood of detachment.

Objective 4 pertains to the characterisation of the impact of orientation angle towards the subsequent detachment of particles. The synthesis of stretched oblate particles from polystyrene spheres allowed the impact of the aspect ratio and orientation angle to be isolated for study, while other parameters were kept constant. Consistent with recent studies reported in the literature, the spheroids were observed to be deposited at an orientation angle, averaging around 40° in our case. Direct visualisation studies of spheres versus oblate spheroids show that the latter detach earlier at lower velocities, but also resist detachment at higher velocities. In other words, spheroids were visualised to have a more spread detachment curve with velocity because they have additional variations in the aspect ratio and orientation angle. Adding to Section 8.1.1, allowing

only for the size variation in the sphere model is inadequate to capture the visualised spheroid detachment curve.

Increasing the orientation angle has the effect of increasing the detachment rate, although the effect of the orientation angle is most prominent in highly skewed particles (low α) particles. Furthermore, the orientation angle reverses the impact of the aspect ratio on detachment. That is, in side-on configurations (orientation angle, $\varphi = 0°$), the particle with the smallest aspect ratio has the highest retention, but in end-on configurations ($\varphi = 90°$), the particle with the highest aspect ratio (spheres in this case) has the highest retention.

8.1.5 When characterising the detachment of particles, it is important to evaluate the variation in both the hydrodynamics and the adhesion force.

As the study of particle detachment is interdisciplinary, works often focus on either the hydrodynamics or the adhesion force to study the detachment of particles. However, in variations such as aspect ratio, size, shape and orientation angle, both the hydrodynamics and adhesion forces are impacted. Although the adhesion force is often one or two orders of magnitude higher than the drag, the torque balance is a function of both the force magnitude and the lever arm. The adhesion force, although greater in magnitude, has a smaller lever arm arising from the contact area between the particle and the substrate.

8.2 Future work

8.2.1 Understanding and characterising the detachment of clusters

Clustering has been shown to occur consistently among particles in nature. Here, clustering refers to the assemblage of primary particles loosely bonded by the interparticle adhesion force. Clustering has the effect of reducing detachment, since clustered particles provide a ‘shadowing’ effect in which the drag is reduced by the particle ahead of the clusters [97, 121]. Furthermore, clustering effectively increases the lever arm for the adhesion torque [122]. The different geometries adopted by the clusters could also have a greater impact than the geometries of each particle. Yet, due to the various geometries clusters could take, studying and characterising clustering is still in the infancy of the literature. Most studies have very specific applications that may not be readily transferable to other fields [58, 123, 124]. Preliminary studies can be done by

examining the clustering of spheres in regular patterns, as well as the visualisation studies of peanut-shaped particles as the most basic cases of particle clusters.

8.2.2 Visualisation experiment for unfavourable conditions

The investigation presented in Chapter 5 remains inconclusive due to the limits of the laboratory equipment which could not produce flows below the critical detachment threshold for secondary minima. In particular, the investigation of the orientation angle in Chapter 7 could be extended to unfavourable conditions to study the interaction between the energy barrier and the deposition of oblate spheroid particles.

8.2.3 Extend the work to two-phase flows.

Particularly in the petroleum field, two-phase flows occur frequently, for example, oil-water, gas-water or oil-gas phases. For the liquid and gas phases, the magnitude of capillary forces could far exceed the adhesion force, so that the adhesion force becomes somewhat negligible [33, 82]. Therefore, it is useful to study the impact of irregular shapes on capillary force and to compare how the new findings would affect the overall detachment torque, where the adhesion and hydrodynamics considered in this study are potentially negligible. Visualisation studies with the stretched particles could be repeated first by saturation with liquid, and then by flushing with water or vice versa.

8.2.4 Role of surface roughness

The assumption of perfectly smooth surfaces is very unrealistic for most real-world applications. The last decade has seen a rapid rise in investigations in attempts to understand the role of surface roughness in particle detachment [88, 125]. However, the random nature of surface roughness is a major obstacle to a unified modelling approach. Despite difficulties, there is consensus in the literature that asperities can significantly impact detachment, although, depending on the geometry and magnitude of the roughness, they could retard or enhance detachment [88, 103, 126, 127]. Future work can measure and image surface roughness present on the visualisation glass slides to determine the topography of the substrate. Imaging could help determine the importance of considering asperities and which existing models in the literature are the most applicable.

This page is intentionally left blank

References

1. Ryan JN, Elimelech M 1996, 'Colloid mobilization and transport in groundwater', *Colloids and Surfaces A: Physicochemical and Engineering Aspects*, vol. 107, pp. 1-56.

2. Russell T, Chequer L, Borazjani S, You Z, Zeinijahromi A, Bedrikovetsky P 2018, 'Formation Damage by Fines Migration', in *Formation Damage During Improved Oil Recovery*, pp. 69-175.

3. Byrne M. Formation Damage - Any Time, Any Place, Any Where [PowerPoint Slides]. Society of Petroleum Engineers; 2010 [Available from: https://www.spe.org/dl/docs/2010/MichaelByrne.pdf.

4. Chequer L, Bagheri M, Zeinijahromi A, Bedrikovetsky P 2018, 'Injectivity formation damage due to fines migration', *The APPEA Journal*, vol. 58, no. 2, pp. 700-4.

5. Zeinijahromi A, Lemon P, Bedrikovetsky P 2011, 'Effects of induced fines migration on water cut during waterflooding', *Journal of Petroleum Science and Engineering*, vol. 78, no. 3-4, pp. 609-17.

6. Yuan B, Moghanloo RG 2018, 'Nanofluid pre-treatment, an effective strategy to improve the performance of low-salinity waterflooding', *Journal of Petroleum Science and Engineering*, vol. 165, pp. 978-91.

7. Zeinijahromi A, Nguyen TK, Bedrikovetsky P 2013, 'Mathematical Model for Fines-Migration Assisted Waterflooding With Induced Formation Damage', *SPE Journal*, vol. 18, no. 3, pp. 518-33.

8. Zhai W, Bai L, Zhou R, Fan X, Kang G, Liu Y, Zhou K 2021, 'Recent Progress on Wear-Resistant Materials: Designs, Properties, and Applications', *Advanced Science*, vol. 8, no. 11, Jun, pp. 1-29.

9. Heckenthaler T, Sadhujan S, Morgenstern Y, Natarajan P, Bashouti M, Kaufman Y 2019, 'Self-Cleaning Mechanism: Why Nanotexture and Hydrophobicity Matter', *Langmuir*, vol. 35, no. 48, pp. 15526-34.

10. Peleka EN, Gallios GP, Matis KA 2017, 'A perspective on flotation: a review', *Journal of Chemical Technology & Biotechnology*, vol. 93, no. 3, pp. 615-23.

11. Decuzzi P, Ferrari M 2006, 'The adhesive strength of non-spherical particles mediated by specific interactions', *Biomaterials*, vol. 27, no. 30, Oct, pp. 5307-14.

12. Cui Y, Sommerfeld M 2015, 'Forces on micron-sized particles randomly distributed on the surface of larger particles and possibility of detachment', *International Journal of Multiphase Flow*, vol. 72, pp. 39-52.

13. Henry C, Minier J-P, Brambilla S 2023, 'Particle resuspension: Challenges and perspectives for future models', *Physics Reports*, vol. 1007, pp. 1-98.

14. Wilson MJ, Wilson L, Patey I 2018, 'The influence of individual clay minerals on formation damage of reservoir sandstones: a critical review with some new insights', *Clay Minerals*, vol. 49, no. 2, pp. 147-64.

15. Russell T, Pham D, Neishaboor MT, Badalyan A, Behr A, Genolet L, Kowollik P, Zeinijahromi A, Bedrikovetsky P 2017, 'Effects of kaolinite in rocks on fines migration', *Journal of Natural Gas Science and Engineering*, vol. 45, pp. 243-55.

16. FrackOptima 2017, *Fluid flow in porous media and Carter's equation*, viewed 5/1/2023 2023, <http://www.frackoptima.com/userguide/theory/fluidflow-porousmedium-carter.html#f2>.

17. Civan F 2015, *Reservoir Formation Damage: Fundamentals, Modeling, Assessment and Mitigation*, 3rd edn, Gulf Professional Publishing, Oxford, UK.

18. Ting HZ, Yang Y, Tian ZF, Carageorgos T, Bedrikovetsky P 2023, 'Detachment of inclined spheroidal particles from flat substrates', *Powder Technology*.

19. Bradford SA, Torkzaban S, Shapiro A 2013, 'A theoretical analysis of colloid attachment and straining in chemically heterogeneous porous media', *Langmuir*, vol. 29, no. 23, Jun 11, pp. 6944-52.

20. Tsai CJ, Pui D, Liu YH 1991, 'Particle Detachment from Disk Surfaces of Computer Disk Drives', *Journal of Aerosol Science*, vol. 22, no. 6, pp. 737-46.

21. Hubbe M 1984, 'Theory of Detachment of Colloidal Particles from Flat Surfaces Exposed to Flow', *Colloids and Surfaces*, vol. 12, pp. 151-78.

22. Bergendahl J, Grasso D 2000, 'Prediction of colloid detachment in a model porous media: hydrodynamics', *Chemical Engineering Science*, vol. 55.

23. Chequer L, Carageorgos T, Naby M, Hussaini M, Lee W, Bedrikovetsky P 2021, 'Colloidal detachment from solid surfaces: Phase diagrams to determine the detachment regime', *Chemical Engineering Science*, vol. 229.

24. Jiang Y, Matsusaka S, Masuda H, Qian Y 2008, 'Characterizing the effect of substrate surface roughness on particle–wall interaction with the airflow method', *Powder Technology*, vol. 186, no. 3, pp. 199-205.

25. Sharma M, Chamoun H, Sarma D, Schechter R 1992, 'Factors Controlling the Hydrodynamic Detachment of Particles from Surfaces', *Journal of Colloid and Interface Science*, vol. 149, no. 1, pp. 121-34.

26. O'Neill ME 1968, 'A sphere in contact with a plane wall in a slow linear shear flow', *Chemical Engineering Science*, vol. 23, no. 11, pp. 1293-8.

27. Leighton D, Acrivos A 1985, 'The lift on a small sphere touching a plane in the presence of a simple shear flow', *Journal of Applied Mathematics and Physics*, vol. 36, pp. 174-8.

28. Derjaguin B, Landau L 1941, 'Theory of the Stability of Strongly Charged Lyophobic Sols and of the Adhesion of Strongly Charged Particles in Solutions of Electrolytes', *J Acta Physicochim*, vol. 14, no. 6, pp. 633-62.

29. Verwey EJW, Overbeek JTG 1948, *Theory of the stability of lyophobic colloids*, Elsevier, Amsterdam.

30. Elimelech M, Gregory J, Jia X, Williams RA 1995, *Particle Deposition and Aggregation*, 1st edn, Butterworth-Heinemann, Boston.

31. Israelachvili JN 2011, *Intermolecular and Surface Forces*, 3rd edn, Elsevier Inc., Amsterdam.

32. Ruckenstein E, Prieve DC 1976, 'Adsorption and Desorption of Particles and Their Chromatographic Separation', *American Institute of Chemical Engineers*, vol. 22, no. 2, pp. 276-83.

33. van Oss C 2008, *The Properties of Water and their Role in Colloidal and Biological Systems*, Interface Science and Technology, 1st edn, vol. 16, Academic Press, Netherlands.

34. Bhattacharjee S 2016, 'DLS and zeta potential - What they are and what they are not?', *Journal of Controlled Release*, vol. 235, Aug 10, pp. 337-51.

35. Bhattacharjee S, Elimelech M 1997, 'Surface Element Integration: A Novel Technique for Evaluation of DLVO Interaction between a Particle and a Flat Plate', *Journal of Colloid and Interface Science*, vol. 193, pp. 273-85.

36. Ting HZ, Bedrikovetsky P, Tian ZF, Carageorgos T 2021, 'Impact of shape on particle detachment in linear shear flows', *Chemical Engineering Science*, vol. 241, pp. 1-14.

37. Barber JR 2018, *Contact Mechanics*, Solid Mechanics and Its Applications, Springer, Switzerland.

38. Champion J, Katare Y, Mitragotri S 2007, 'Making polymeric micro- and nanoparticles of complex shapes', *PNAS*, vol. 104, no. 29, pp. 11901-4.

39. Ahn SJ, Ahn KH, Lee SJ 2016, 'Film squeezing process for generating oblate spheroidal particles with high yield and uniform sizes', *Colloid and Polymer Science*, vol. 294, no. 5, pp. 859-67.

40. Ting HZ, Yang Y, Tian ZF, Carageorgos T, Bedrikovetsky P 2022, 'Image interpretation for kaolinite detachment from solid substrate: Type curves, stochastic model', *Colloids and Surfaces A: Physicochemical and Engineering Aspects*, vol. 650, pp. 1-12.

41. Bergaya F, Lagaly G 2013, 'General Introduction: Clays, Clay Minerals, and Clay Science', in *Handbook of Clay Science*, 2nd edn, vol. 5, Elsevier, Amsterdam, pp. 1-19.

42. Murray HH 2006, *Applied Clay Mineralogy - Occurrences, Processing and Application of Kaolins, Bentonites, Palygorskite-Sepiolite, and Common Clays*, Developments in Clay Science, 1st edn, vol. 2, Elsevier, Boston.

43. Sen T, Khilar KC 2006, 'Review on subsurface colloids and colloid-associated contaminant transport in saturated porous media', *Adv Colloid Interface Sci*, vol. 119, no. 2-3, Feb 28, pp. 71-96.

44. Fountouli TV, Chrysikopoulos CV 2020, 'Effect of Clay Colloid Particles on Formaldehyde Transport in Unsaturated Porous Media', *Water*, vol. 12, no. 12, pp. 3541-57.

45. Awad ME, Lopez-Galindo A, Setti M, El-Rahmany MM, Iborra CV 2017, 'Kaolinite in pharmaceutics and biomedicine', *Int J Pharm*, vol. 533, no. 1, Nov 25, pp. 34-48.

46. Li GL, Zhou CH, Fiore S, Yu WH 2019, 'Interactions between microorganisms and clay minerals: New insights and broader applications', *Applied Clay Science*, vol. 177, pp. 91-113.

47. Syngouna VI, Chrysikopoulos CV 2013, 'Cotransport of clay colloids and viruses in water saturated porous media', *Colloids and Surfaces A: Physicochemical and Engineering Aspects*, vol. 416, pp. 56-65.

48. Song W, Kovscek AR 2016, 'Direct visualization of pore-scale fines migration and formation damage during low-salinity waterflooding', *Journal of Natural Gas Science and Engineering*, vol. 34, pp. 1276-83.

49. Murray HH 1991, 'Overview-clay mineral applications', *Applied Clay Science*, vol. 5, pp. 379-95.

50. Beckett R, Murphy D, Tadjiki S, Chittleborough DJ, Giddings JC 1997, 'Determination of thickness, aspect ratio and size distributions for platey particles using sedimentation field-flow fractionation and electron microscopy', *Colloids and Surfaces A: Physicochemical and Engineering Aspects*, vol. 120, no. 1-3, pp. 17-26.

51. Veghte DP, Freedman MA 2014, 'Facile Method for Determining the Aspect Ratios of Mineral Dust Aerosol by Electron Microscopy', *Aerosol Science and Technology*, vol. 48, no. 7, pp. 715-24.

52. Cheng H, Zhang Z, Liu Q, Leung J 2014, 'A new method for determining platy particle aspect ratio: A kaolinite case study', *Applied Clay Science*, vol. 97-98, pp. 125-31.

53. Żbik MS, Raftery NA, Smart RSC, Frost RL 2010, 'Kaolinite platelet orientation for XRD and AFM applications', *Applied Clay Science*, vol. 50, no. 3, pp. 299-304.

54. Bergendahl J, Grasso D 2003, 'Mechanistic Basis for Particle Detachment from Granular Media', *Environmental Science & Technology*, vol. 37, no. 10, pp. 2317-22.

55. Molnar IL, Johnson WP, Gerhard JI, Willson CS, O'Carroll DM 2015, 'Predicting colloid transport through saturated porous media: A critical review', *Water Resources Research*, vol. 51, no. 9, pp. 6804-45.

56. Elimelech M, O'Melia C 1990, 'Effect of electrolyte type on the electrophoretic mobility of polystyrene latex colloids', *Colloids and Surfaces*, vol. 44, pp. 165-78.

57. Palomino AM, Santamarina JC 2005, 'Fabric Map for Kaolinite: Effects of pH and Ionic Concentration on Behaviour', *Clays and Clay Minerals*, vol. 53, no. 3, pp. 211-23.

58. Mahmood T, Amirtharajah A, Sturm T, Dennett K 2001, 'A micromechanics approach for attachment and detachment of asymmetric colloidal particles', *Colloids and Surfaces*, vol. 177, no. 2-3, pp. 99-110.

59. Zbik MS, Smart RS, Morris GE 2008, 'Kaolinite flocculation structure', *J Colloid Interface Sci*, vol. 328, no. 1, Dec 1, pp. 73-80.

60. Cerda M 1987, 'Mobilization of Kaolinite Fines in Porous Media', *Colloids and Surfaces*, vol. 27, no. 1-3, pp. 219-41.

61. Polyanin AD, Kutepov AM, Kazenin DA, Vyazmin AV 2001, *Hydrodynamics, mass and heat transfer in chemical engineering*, vol. 14, CRC Press, London.

62. Polyanin AD, Dil'man VV 1994, *Methods of modeling equations and analogies in chemical engineering*, CRC Press, Boca Raton, Fl.

63. Shapiro AA, Yuan H 2012, 'Application of stochastic approaches to modelling suspension flow in porous media', in Skogseid A, Fasano V (eds), *Statistical Mechanics and Random Walks: Principles, Processes and Applications*, Nova Science Publishers.

64. Ding Y, Meng X, Yang D 2021, 'Numerical simulation of polydisperse dense particles transport in a random-orientated fracture with spatially variable apertures', *Colloids and Surfaces A: Physicochemical and Engineering Aspects*, vol. 610.

65. Chrysikopoulos CV, Katzourakis VE 2015, 'Colloid particle size-dependent dispersivity', *Water Resources Research*, vol. 51, no. 6, pp. 4668-83.

66. You Z, Badalyan A, Yang Y, Bedrikovetsky P, Hand M 2019, 'Fines migration in geothermal reservoirs: Laboratory and mathematical modelling', *Geothermics*, vol. 77, pp. 344-67.

67. You Z, Yang Y, Badalyan A, Bedrikovetsky P, Hand M 2016, 'Mathematical modelling of fines migration in geothermal reservoirs', *Geothermics*, vol. 59, pp. 123-33.

68. James SC, Chrysikopoulos CV 2003, 'Analytical solutions for monodisperse and polydisperse colloid transport in uniform fractures', *Colloids and Surfaces A: Physicochemical and Engineering Aspects*, vol. 226, no. 1-3, pp. 101-18.

69. Won J, Kim T, Kang M, Choe Y, Choi H 2021, 'Kaolinite and illite colloid transport in saturated porous media', *Colloids and Surfaces A: Physicochemical and Engineering Aspects*, vol. 626.

70. Gomez-Flores A, Bradford SA, Hwang G, Choi S, Tong M, Kim H 2020, 'Shape and orientation of bare silica particles influence their deposition under intermediate ionic strength: A study with QCM–D and DLVO theory', *Colloids and Surfaces A: Physicochemical and Engineering Aspects*, vol. 599.

71. Gomez-Flores A, Bradford SA, Wu L, Kim H 2019, 'Interaction energies for hollow and solid cylinders: Role of aspect ratio and particle orientation', *Colloids and Surfaces A: Physicochemical and Engineering Aspects*, vol. 580.

72. Won J, Burns SE 2019, 'Stochastic modeling of kaolinite transport through a sand filter', *Canadian Geotechnical Journal*, vol. 56, no. 11, pp. 1573-83.

73. Yang Y, Dang-Le B, Kutty G, Mbeveri S, Carageorgos T, Badalyan A, Bedrikovetsky P 2020, 'Kaolinite Detachment from Silica Substrate - Laboratory and Theoretical Study', *International Journal of Water and Wastewater Treatment*, vol. 6, no. 3, pp. 1-7.

74. Liu Q, Lazouskaya V, He Q, Jin Y 2010, 'Effect of particle shape on colloid retention and release in saturated porous media', *J Environ Qual*, vol. 39, no. 2, Mar-Apr, pp. 500-8.

75. Salerno B, Flamm M, Logan B, Velegol D 2006, 'Transport of Rodlike Colloids through Packed Beds', *Environmental Science & Technology*, vol. 40, no. 20, pp. 6336-40.

76. Seymour MB, Chen G, Su C, Li Y 2013, 'Transport and retention of colloids in porous media: does shape really matter?', *Environ Sci Technol*, vol. 47, no. 15, Aug 6, pp. 8391-8.

77. Knappenberger T, Aramrak S, Flury M 2015, 'Transport of barrel and spherical shaped colloids in unsaturated porous media', *J Contam Hydrol*, vol. 180, Sep, pp. 69-79.

78. Xu S, Qian L, Saiers J 2008, 'Straining of nonspherical colloids in saturated porous media', *Environmental Science & Technology*, vol. 42, no. 3, pp. 771-8.

79. Torres-Díaz I, Jerri HA, Benczédi D, Bevan MA 2019, 'Shape Dependent Colloidal Deposition and Detachment', *Advanced Theory and Simulations*, vol. 2, no. 9, pp. 1-9.

80. Vahidkhah K, Bagchi P 2015, 'Microparticle shape effects on margination, near-wall dynamics and adhesion in a three-dimensional simulation of red blood cell suspension', *Soft Matter*, vol. 11, no. 11, Mar 21, pp. 2097-109.

81. Bradford SA, Bettahar M, Simunek J, van Genuchten MT 2004, 'Straining and Attachment of Colloids in Physically Heterogenous Porous Media', *Vadose Zone Journal*, vol. 3.

82. Aramrak S, Flury M, Harsh JB, Zollars RL, Davis HP 2013, 'Does colloid shape affect detachment of colloids by a moving air-water interface?', *Langmuir*, vol. 29, no. 19, May 14, pp. 5770-80.

83. Stempniewicz MM, Zhipeng C, Yanhua Z, Komen EMJ 2018, 'Resuspension models for monolayer and multilayer deposits of graphite dust', *Annals of Nuclear Energy*, vol. 120, pp. 186-97.

84. Kuznar ZA, Elimelech M 2007, 'Direct microscopic observation of particle deposition in porous media: Role of the secondary energy minimum', *Colloids and Surfaces A: Physicochemical and Engineering Aspects*, vol. 294, no. 1-3, pp. 156-62.

85. Bradford SA, Torkzaban S 2008, 'Colloid Transport and Retention in Unsaturated Porous Media: A Review of Interface-, Collector-, and Pore-Scale Processes and Models', *Vadose Zone Journal*, vol. 7, no. 2, pp. 667-81.

86. Torkzaban S, Walker SL, Bradford SA 2009, 'Reply to comment by William P. Johnson et al. on "Transport and fate of bacteria in porous media: Coupled effects of chemical conditions and pore space geometry"', *Water Resources Research*, vol. 45, no. 9, pp. 1-3.

87. Johnson WP, Pazmino E, Ma H 2010, 'Direct observations of colloid retention in granular media in the presence of energy barriers, and implications for inferred mechanisms from indirect observations', *Water Res*, vol. 44, no. 4, Feb, pp. 1158-69.

88. Shen C, Jin Y, Zhuang J, Li T, Xing B 2019, 'Role and importance of surface heterogeneities in transport of particles in saturated porous media', *Critical Reviews in Environmental Science and Technology*, vol. 50, no. 3, pp. 244-329.

89. Butt H-J, Cappella B, Kappl M 2005, 'Force measurements with the atomic force microscope: Technique, interpretation and applications', *Surface Science Reports*, vol. 59, no. 1-6, pp. 1-152.

90. Israelachvili J, Min Y, Akbulut M, Alig A, Carver G, Greene W, Kristiansen K, Meyer E, Pesika N, Rosenberg K, Zeng H 2010, 'Recent advances in the surface forces apparatus (SFA) technique', *Reports on Progress in Physics*, vol. 73, no. 3, pp. 1-16.

91. Li X, Zhang P, Lin CL, Johnson WP 2005, 'Role of Hydrodynamic Drag on Microsphere Deposition and Re-entrainment in Porous Media under Unfavorable Conditions', *Environ Sci Technol*, vol. 39, no. 11, pp. 4012-20.

92. Kutsovsky YE, Scriven LE, Davis HT, Hammer BE 1996, 'NMR imaging of velocity profiles and velocity distributions in bead packs', *Physics of Fluids*, vol. 8, no. 4, pp. 863-71.

93. Lee JH, Kaplan JB, Lee WY 2008, 'Microfluidic devices for studying growth and detachment of Staphylococcus epidermidis biofilms', *Biomedical Microdevices*, vol. 10, no. 4, Aug, pp. 489-98.

94. Douville NJ, Zamankhan P, Tung YC, Li R, Vaughan BL, Tai CF, White J, Christensen PJ, Grotberg JB, Takayama S 2011, 'Combination of fluid and solid mechanical stresses contribute to cell death and detachment in a microfluidic alveolar model', *Lab on a Chip*, vol. 11, no. 4, Feb 21, pp. 609-19.

95. Lin N, Valiei A, McKay G, Nguyen D, Tufenkji N, Moraes C 2022, 'Microfluidic Study of Bacterial Attachment on and Detachment from Zinc Oxide Nanopillars', *ACS Biomaterials Science and Engineering*, vol. 8, no. 7, Jul 11, pp. 3122-31.

96. Lazouskaya V, Wang LP, Or D, Wang G, Caplan JL, Jin Y 2013, 'Colloid mobilization by fluid displacement fronts in channels', *J Colloid Interface Sci*, vol. 406, Sep 15, pp. 44-50.

97. Chequer L, Bedrikovetsky P, Carageorgos T, Badalyan A, Gitis V 2019, 'Mobilization of Attached Clustered Colloids in Porous Media', *Water Resources Research*, vol. 55, no. 7, pp. 5696-714.

98. May R, Li Y 2013, 'The effects of particle size on the deposition of fluorescent nanoparticles in porous media: Direct observation using laser scanning cytometry', *Colloids and Surfaces A: Physicochemical and Engineering Aspects*, vol. 418, pp. 84-91.

99. Tufenkji N, Elimelech M 2005, 'Breakdown of Colloid Filtration Theory: Role of the Secondary Energy Minimum and Surface Charge Heterogeneities', *Langmuir*, vol. 21, no. 3, pp. 841-52.

100. Tufenkji N, Elimelech M 2004, 'Deviation from the Classical Colloid Filtration Theory in the Presence of Repulsive DLVO Interactions', *Langmuir*, vol. 20, no. 25, pp. 10818-28.

101. Johnson WP, Li X, Tong M, Ma H 2009, 'Comment on "Transport and fate of bacteria in porous media: Coupled effects of chemical conditions and pore space geometry" by Saeed Torkzaban et al', *Water Resources Research*, vol. 45, no. 9, pp. 1-3.

102. Bradford SA, Torkzaban S 2015, 'Determining Parameters and Mechanisms of Colloid Retention and Release in Porous Media', *Langmuir*, vol. 31, no. 44, Nov 10, pp. 12096-105.

103. Rasmuson A, Pazmino E, Assemi S, Johnson WP 2017, 'Contribution of Nano- to Microscale Roughness to Heterogeneity: Closing the Gap between Unfavorable and Favorable Colloid Attachment Conditions', *Environ Sci Technol*, vol. 51, no. 4, Feb 21, pp. 2151-60.

104. Pazmino E, Trauscht J, Johnson WP 2014, 'Release of colloids from primary minimum contact under unfavorable conditions by perturbations in ionic strength and flow rate', *Environ Sci Technol*, vol. 48, no. 16, Aug 19, pp. 9227-35.

105. Duffadar R, Kalasin S, Davis JM, Santore MM 2009, 'The impact of nanoscale chemical features on micron-scale adhesion: crossover from heterogeneity-dominated to mean-field behavior', *J Colloid Interface Sci*, vol. 337, no. 2, Sep 15, pp. 396-407.

106. Tong M, Johnson WP 2006, 'Excess Colloid Retention in Porous Media as a Function of Colloid Size, Fluid Velocity, and Grain Angularity', *Environmental Science & Technology*, vol. 40, pp. 7725-31.

107. VanNess K, Rasmuson A, Ron CA, Johnson WP 2019, 'A Unified Force and Torque Balance for Colloid Transport: Predicting Attachment and Mobilization under Favorable and Unfavorable Conditions', *Langmuir*, vol. 35, no. 27, Jul 9, pp. 9061-70.

108. Henry C, Minier J-P 2014, 'Progress in particle resuspension from rough surfaces by turbulent flows', *Progress in Energy and Combustion Science*, vol. 45, pp. 1-53.

109. Sümer B, Sitti M 2008, 'Rolling and Spinning Friction Characterization of Fine Particles Using Lateral Force Microscopy Based Contact Pushing', *Journal of Adhesion Science and Technology*, vol. 22, no. 5-6, pp. 481-506.

110. Dominik C, Tielens AGGM 1997, 'The Physics of Dust Coagulation and the Structure of Dust Aggregates in Space', *The Astrophysical Journal*, vol. 480, no. 2, pp. 647-73.

111. Dominik C, Tielens AGGM 1995, 'Resistance to rolling in the adhesive contact of two elastic spheres', *Philosophical Magazine A*, vol. 72, no. 3, pp. 783-803.

112. Ding W, Howard AJ, Peri MDM, Cetinkaya C 2007, 'Rolling resistance moment of microspheres on surfaces: contact measurements', *Philosophical Magazine*, vol. 87, no. 36, pp. 5685-96.

113. Shave MK, Balciunaite A, Xu Z, Santore MM 2019, 'Rapid Electrostatic Capture of Rod-Shaped Particles on Planar Surfaces: Standing up to Shear', *Langmuir*, vol. 35, no. 40, Oct 8, pp. 13070-7.

114. Xu Z, Niu WA, Rivera SL, Tuominen MT, Siegrist MS, Santore MM 2021, 'Surface Chemistry Guides the Orientations of Adhering E. coli Cells Captured from Flow', *Langmuir*, vol. 37, no. 25, Jun 29, pp. 7720-9.

115. Ma H, Bolster C, Johnson WP, Li K, Pazmino E, Camacho KM, Anselmo AC, Mitragotri S 2020, 'Coupled influences of particle shape, surface property and flow hydrodynamics on rod-shaped colloid transport in porous media', *J Colloid Interface Sci*, vol. 577, Oct 1, pp. 471-80.

116. McNew CP, Kananizadeh N, Li Y, LeBoeuf EJ 2017, 'The attachment of colloidal particles to environmentally relevant surfaces and the effect of particle shape', *Chemosphere*, vol. 168, Feb, pp. 65-79.

117. Cooley M, Sarode A, Hoore M, Fedosov DA, Mitragotri S, Sen Gupta A 2018, 'Influence of particle size and shape on their margination and wall-adhesion: implications in drug delivery vehicle design across nano-to-micro scale', *Nanoscale*, vol. 10, no. 32, Aug 16, pp. 15350-64.

118. Li K, Ma H 2021, 'High Fluid Velocity and Narrow Channels Enhance the Influences of Particle Shape on Colloid Retention in Saturated Groundwater Systems Under Favorable Deposition Conditions', *Frontiers in Water*, vol. 3.

119. Mody NA, King MR 2005, 'Three-dimensional simulations of a platelet-shaped spheroid near a wall in shear wall', *Physics of Fluids*, vol. 17, no. 11.

120. Jackson SP 2007, 'The growing complexity of platelet aggregation', *Blood*, vol. 109, no. 12, pp. 5087-95.

121. Ekiel-Jezewska ML, Sadlej K, Wajnryb E 2008, 'Friction of rodlike particles adsorbed to a planar surface in shear flow', *J Chem Phys*, vol. 129, no. 4, Jul 28, p. 041104.

122. Villagran Olivares MC, Benito JG, Unac RO, Vidales AM 2021, 'Kinetic Monte Carlo method applied to micrometric particle detachment mechanisms by aerodynamic forces', *J Phys Condens Matter*, vol. 34, no. 7, Nov 23.

123. Iimura K, Watanabe S, Suzuki M, Hirota M, Higashitani K 2009, 'Simulation of entrainment of agglomerates from plate surfaces by shear flows', *Chemical Engineering Science*, vol. 64, no. 7, pp. 1455-61.

124. Nguyen D, Rasmuson A, Thalberg K, Niklasson Bjo¨rn I 2014, 'Numerical modelling of breakage and adhesion of loose fine-particle agglomerates', *Chemical Engineering Science*, vol. 116, pp. 91-8.

125. Torkzaban S, Bradford SA 2016, 'Critical role of surface roughness on colloid retention and release in porous media', *Water Res*, vol. 88, Jan 1, pp. 274-84.

126. Bhagat AM, Goswami PS 2022, 'Effect of rough wall on drag, lift, and torque on an ellipsoidal particle in a linear shear flow', *Physics of Fluids*, vol. 34, no. 8.

127. Bhattacharjee S, Ko CH, Elimelech M 1998, 'DLVO Interaction between Rough Surfaces', *Langmuir*, vol. 14, no. 12, pp. 3365-75.

Appendix A

Supplementary Data for Chapter 5

This section contains the supplementary data for the paper titled: ‘Detachment of irregular-shape particles under unfavourable conditions: visualisation and modelling’.

Supplementary Material for

Detachment of irregular-shape particles under unfavourable conditions: visualisation and modelling

Heng Zheng Ting [a], Zhao Feng Tian [a], Pavel Bedrikovetsky [b]

[a] *School of Electrical and Mechanical Engineering, The University of Adelaide, Adelaide 5000, SA, Australia*

[b] *Australian School of Petroleum and Energy Resources, The University of Adelaide, Adelaide 5000, SA, Australia*

1. Drag and moment shape factors

The drag shape factor for oblate spheroids, $f_{d,Sphd}$ and cylinders, $f_{d,Cyl}$ are given as:

$$f_{d,Sphd} = (0.8707\alpha^2 + 0.7908\alpha + 0.05844)\,(\alpha + 0.008453)^{-1} \quad \text{(S1)}$$

$$f_{d,Cyl} = (0.8306\alpha^2 + 0.8525\alpha + 0.03278)\,(\alpha + 0.00294)^{-1} \quad \text{(S2)}$$

Similarly, the moment shape factors for oblate spheroids, $f_{M,Sphd}$ and cylinder, $f_{M,Cyl}$ particles are (Ting et al. 2021):

$$f_{M,\,Sphd} = (1.296\alpha^2 + 0.1509\alpha + 0.03718)(\alpha^2 + 0.0843\alpha + 0.0002284)^{-1} \quad \text{(S3)}$$

$$f_{M,Cyl} = (0.05955\alpha^2 + 1.337\alpha + 0.3813)(\alpha + 0.1358)^{-1} \quad \text{(S4)}$$

2. DLVO interaction potential and SEI

By SEI, the interaction potential between an oblate spheroid at varying distances from an infinite flat plate is expressed as (Bhattacharjee & Elimelech 1997):

$$U_{Sphd} = 2\pi \int_0^a \left[E\left(H - b\sqrt{1 - \frac{r^2}{a^2}} \right) - E\left(H + b\sqrt{1 - \frac{r^2}{a^2}} \right) \right] r dr \quad \text{(S5)}$$

Similarly, for a cylinder and an infinite flat plat, the interaction potential is expressed as (Wu et al. 2013):

$$U_{Cyl} = \pi a^2[E(D) - E(D + 2b)] \quad \text{(S6)}$$

The interparticle interactions arising from van der Waals, electric double layer and Born repulsion are given as (Gregory 1975; Israelachvili 2011; Mahmood et al. 2001):

$$E_{vdw} = -\frac{A_h}{12\pi h^2}, \quad \text{(S7)}$$

$$E_{edl} = 32\varepsilon_o\varepsilon_r\kappa\gamma_1\gamma_2\left(\frac{k_BT}{ze}\right)^2 \exp(-\kappa h), \quad \text{(S8)}$$

$$E_{born} = \frac{A_h\sigma^6}{360\pi h^8}, \quad \text{(S9)}$$

A_h is the Hamaker constant, ε_o is the dielectric permittivity of vacuum, ε_r is the relative dielectric permittivity of the solvent, k_B the Boltzmann constant, T temperature, z valency, ζ zeta potential, σ the atomic collision constant and e the charge of an electron. κ is the inverse Debye length and $\gamma = \tanh\left(\frac{ze\zeta_j}{4k_BT}\right)$.

3. **Streamlines for oblate spheroids**

The CFD simulations allow the streamlines around the oblate spheroid to be visualised. Note the presence of a wake and recirculation region in front and behind the α = 0.5 spheroid that is minimal in the spheroid with α = 0.05.

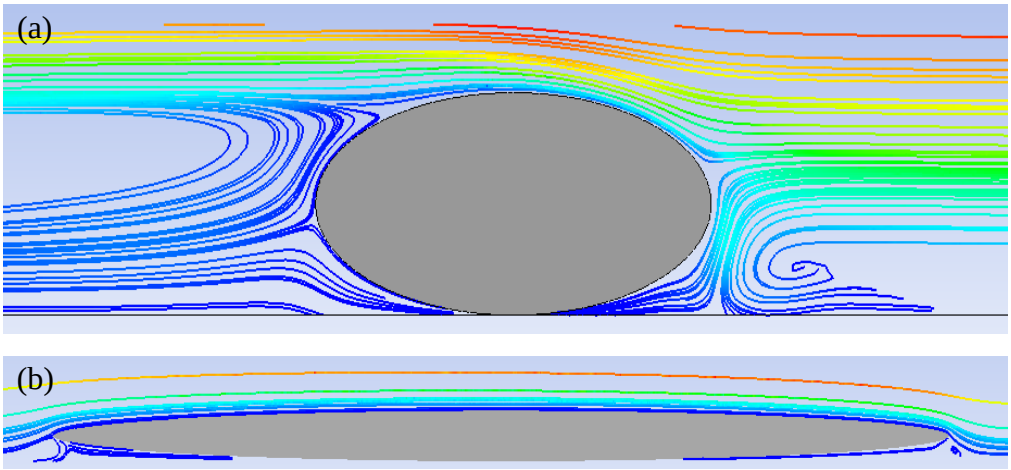

Figure S1: Comparison of the streamlines for (a) α=0.5 and (b) α = 0.05 spheroids both at Re = 50.

4. Variation of moment shape factor with Re_p

Figure S2 shows the minor dependence of the moment shape factor with increasing Re_p. Particle with $\alpha \geq 0.25$ tends to deviate more with increasing Re_p.

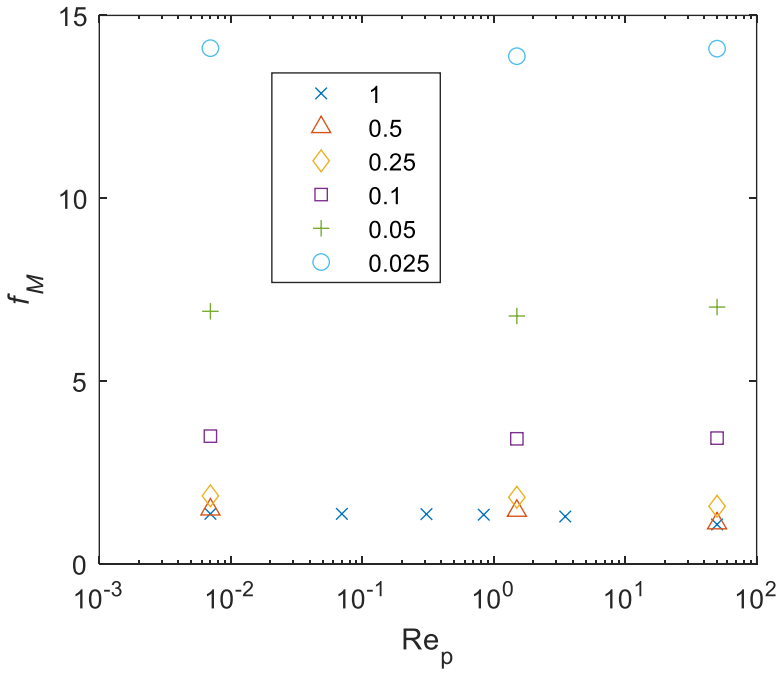

Figure S2: Variation of the moment shape factor, f_M for spheroids with particle Reynolds number. The shape factors are plotted for six different aspect ratios ranging from $0.025 \leq \alpha \leq 1$.

5. Impact of considering Re_p for shape factors

The shape factors (S1-S4) approximate the resultant drag and moment reasonably well even for Re_p > 0.1. The corrected curves were plotted by interpolating the f_d and f_M values as presented in Figure 3 and Figure S2.

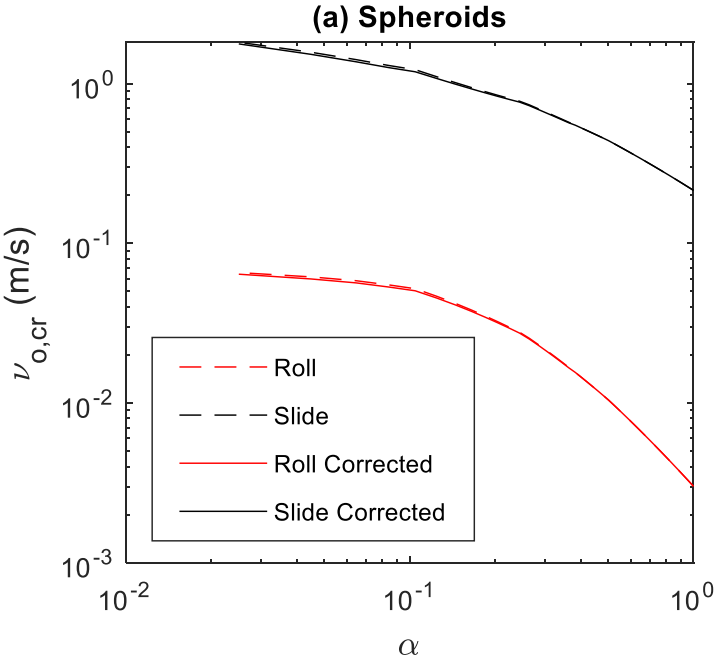

Figure S3: Impact of correcting shape factor when Re_p > 0.1 for R_{equi} = 3 µm, 0.3 M NaCl, pH 7, latex on glass. The 'corrected' lines are calculated by implementing the newly calculated f_d for Re_p > 0.1, which accounts for Re_p.

6. DLVO Energy and Force profile for laboratory conditions (latex)

The DLVO energy and force profile are plotted based on Eqns S5-S9 and corresponds to the salinity and pH conditions use for Experiment 1 and 2.

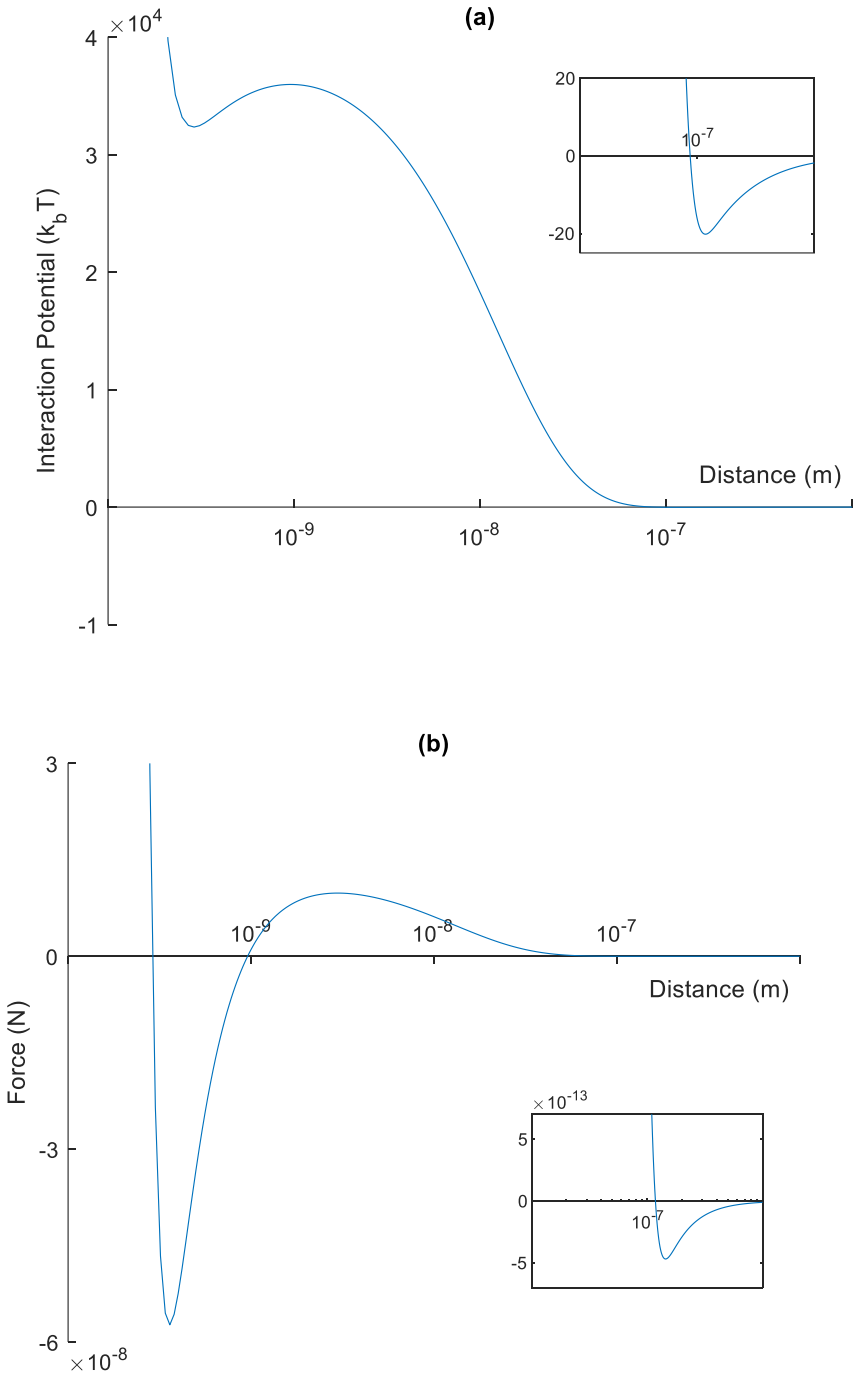

Figure S4: DLVO (a) energy and (b) force profile for 5 μm radius sphere latex particles on glass, in DI and pH 11. The salinity and pH corresponds to the conditions used in the direct visualisation lab.

7. Observation of transition behaviour in kaolinite

An example of two direct visualisation images compared side by side from Experiment 2 that details the transition behaviour.

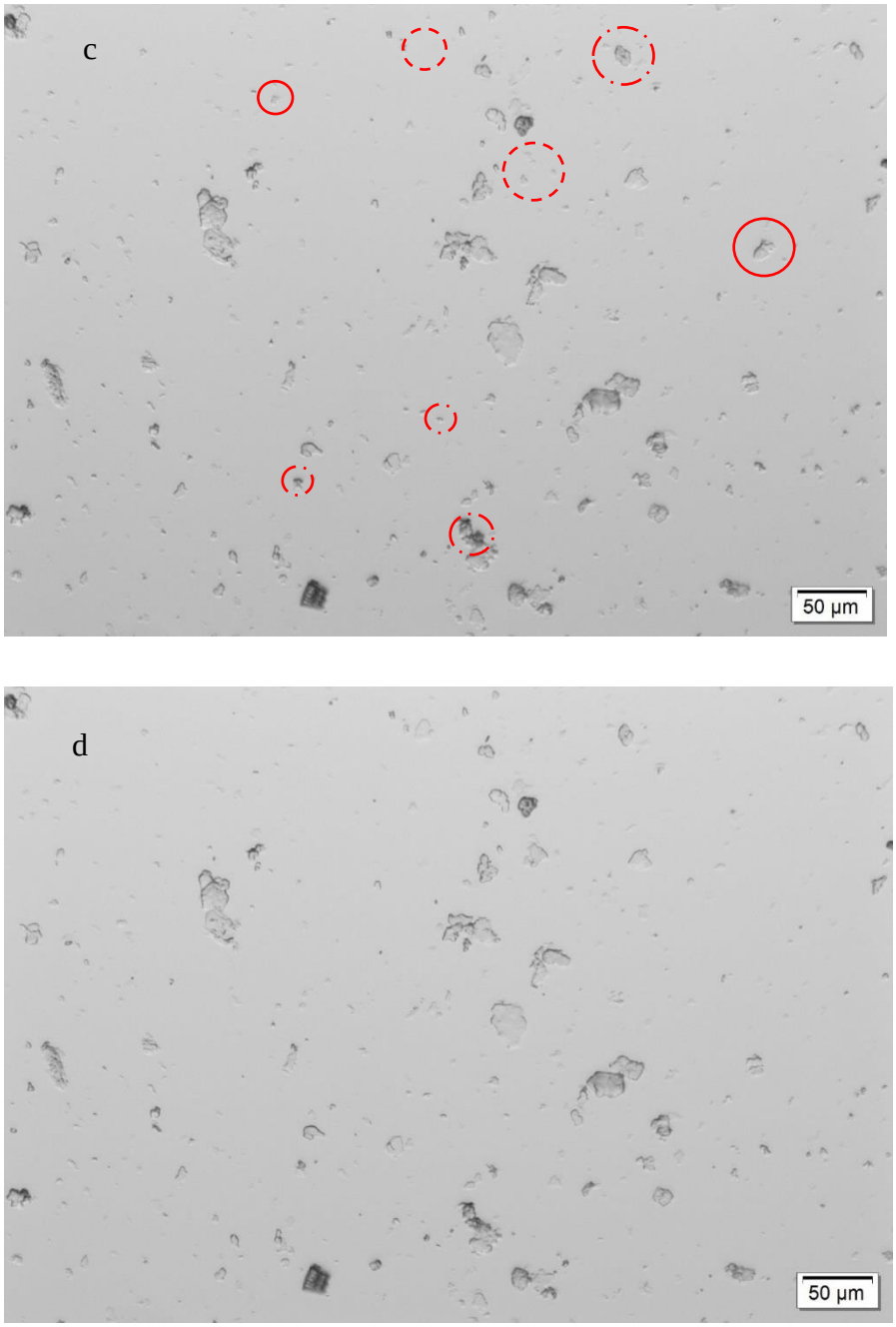

Figure S5: Comparison of two kaolinite visualisation images from step c to d in Experiment 2. During the transition stage, translation (shifting), detachment and reattachment were all observed. The red circles in (c) indicate that a change would occur in that position in (d), whether through translation (—·—), detachment (—) or reattachment (- - -).

8. **Experiment 2 velocity increments**

The visualisation of kaolinite detachment was done by increasing the flow averaged velocities, v in stepwise increments as detailed:

Table S1: Flow averaged velocities used for Experiment 3

Step	$\boldsymbol{v}$ (m/s)
o	0
a	2×10^{-5}
b	5×10^{-5}
c	2×10^{-4}
d	5×10^{-4}
e	2×10^{-3}
f	5×10^{-3}
g	2×10^{-2}
h	1×10^{-1}
i	5×10^{-1}
j	1

9. **References**

Bhattacharjee, S & Elimelech, M 1997, 'Surface Element Integration: A Novel Technique for Evaluation of DLVO Interaction between a Particle and a Flat Plate', *Journal of Colloid and Interface Science*, vol. 193, pp. 273-285.

Gregory, J 1975, 'Interaction of unequal double layers at constant charge', *Journal of Colloid and Interface Science*, vol. 51, no. 1, pp. 44-51.

Israelachvili, JN 2011, *Intermolecular and Surface Forces*, 3rd edn, Elsevier Inc., Amsterdam.

Mahmood, T, Amirtharajah, A, Sturm, T & Dennett, K 2001, 'A micromechanics approach for attachment and detachment of asymmetric colloidal particles', *Colloids and Surfaces*, vol. 177, no. 2-3, pp. 99-110.

Ting, HZ, Bedrikovetsky, P, Tian, ZF & Carageorgos, T 2021, 'Impact of shape on particle detachment in linear shear flows', *Chemical Engineering Science*, vol. 241.

Wu, L, Gao, B, Tian, Y, Munoz-Carpena, R & Zigler, KJ 2013, 'DLVO interactions of carbon nanotubes with isotropic planar surfaces', *Langmuir*, vol. 29, no. 12, Mar 26, pp. 3976-3988.

Appendix B

Supplementary Data for Chapter 6

This section contains the supplementary data for the paper titled: ‘Image interpretation for kaolinite detachment from solid substrate: Type curves, stochastic model’.

Supplementary Material for

Image interpretation for kaolinite detachment from solid substrate: type curves, stochastic model

Heng Zheng Ting [a], Yutong Yang [b], Zhao Feng Tian [a], Themis Carageorgos [b], Pavel Bedrikovetsky [b]

[a] *School of Mechanical Engineering, The University of Adelaide, Adelaide 5000, SA, Australia*

[b] *Australian School of Petroleum and Energy Resources, The University of Adelaide, Adelaide 5000, SA, Australia*

S1. DLVO and SEI formulation

1.1. Surface Element Integration for oblate spheroids

The Surface Element Integration (SEI) method evaluates the respective DLVO interaction energy between the oblate spheroids of various aspect ratios with the flat glass surface. For an oblate spheroid, the interaction potential, U_{Sphd} is expressed as [1, 2]:

$$U_{Sphd} = 2\pi \int_0^a \left[E\left(H - b\sqrt{1-\frac{r^2}{a^2}}\right) - E\left(H + b\sqrt{1-\frac{r^2}{a^2}}\right)\right] r dr. \quad \text{(S1)}$$

Referring to Fig. S1, we used a radial coordinate system originating from the particle centre, defined by the *r* and *Z* axis. *H* is the distance of the centre of the particle from the plate surface. *h* is the local distance of a surface element from the flat plate. *a* is the semi-major axis of the spheroid, *b* is the semi-minor axis of the spheroid.

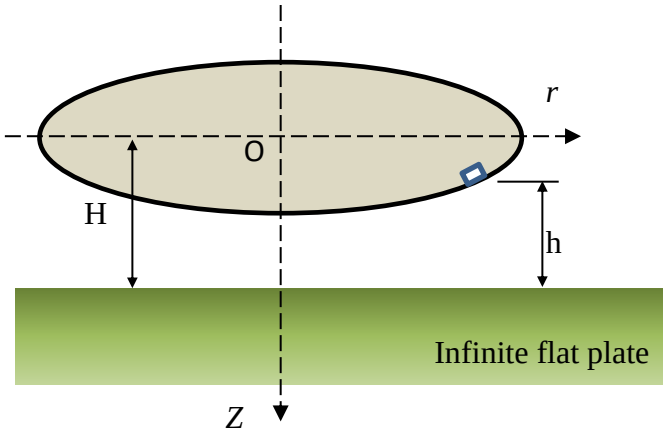

Fig. S1. SEI configuration for the oblate spheroid and an infinite flat plate with radial coordinate systems.

1.2. Interaction potential between two infinite flat plate

SEI scales the interaction between two infinite flat plates to an oblate spheroid. The van der Waals, $E_{vdw,}$ electric double layer, $E_{edl,}$ and Born repulsion, E_{born} interaction energy per unit area of two infinite flat plate separated by a distance, h is given as [3-5]:

$$E_{vdw} = -\frac{A_h}{12\pi h^2}, \tag{S2}$$

$$E_{edl} = 32\varepsilon_o\varepsilon_r\kappa\gamma_k\gamma_g\left(\frac{k_BT}{ze}\right)^2\exp(-\kappa h), \tag{S3}$$

$$E_{born} = \frac{A_h\sigma^6}{360\pi h^8}, \tag{S4}$$

A_h is the Hamaker constant (1.35×10^{-20} J) for a kaolinite-water-glass system calculated using the Lifshitz theory [3], ε_o is the permittivity of vacuum (8.85×10^{-12} $C^2N^{-1}m^{-2}$), ε_r is the relative permittivity of water (78.46). κ is the inverse Debye length, γ_k and γ_g are the reduced surface potential for the kaolinite and glass, respectively (=tanh($ze\zeta/4k_BT$). ζ is the zeta potential, z is the ion valency, e (1.6×10^{-19} C) is the charge of an electron, T is the absolute temperature and σ is the atomic collision coefficient (5Å).

S2. Poiseuille shear flow

To match the modelling with the lab, the shear rate, $\dot{\gamma}_o$, in the microfluidic cell needs to be determined. This is because the formulae for hydrodynamic forces (Eqns. 5-7) were expressed in terms of $\dot{\gamma}_o$ rather than velocity, *v*. $\dot{\gamma}_o$ is a function of the particle centre velocity, v_o and the semi-minor axis of the oblate spheroid, *b*, such that $v_o = \dot{\gamma}_o\, b$. The Poiseuille flow equation (Eqn. S5) [6] was used to calculate the particle centre velocity based on the known area- averaged velocity, *v*. *l* is the height of the microfluidic channel (450 μm).

$$v_o = 6v\left(\frac{b}{l}\right)\left[1 - \left(\frac{b}{l}\right)\right]. \tag{S5}$$

S3. Measurement of the semi-major axis, *a* of kaolinite particles/aggregates.

The distribution of *a* for kaolinites can be measured from the flow visualisation experiments using image processing. *a* was calculated by determining the '*MajorAxisLength*' property (divided by two) in MATLAB's Image Processing Toolbox (R2021b). The histogram was best fitted with a lognormal distribution curve of mean, μ = -13.00 and standard deviation, σ = 0.55.

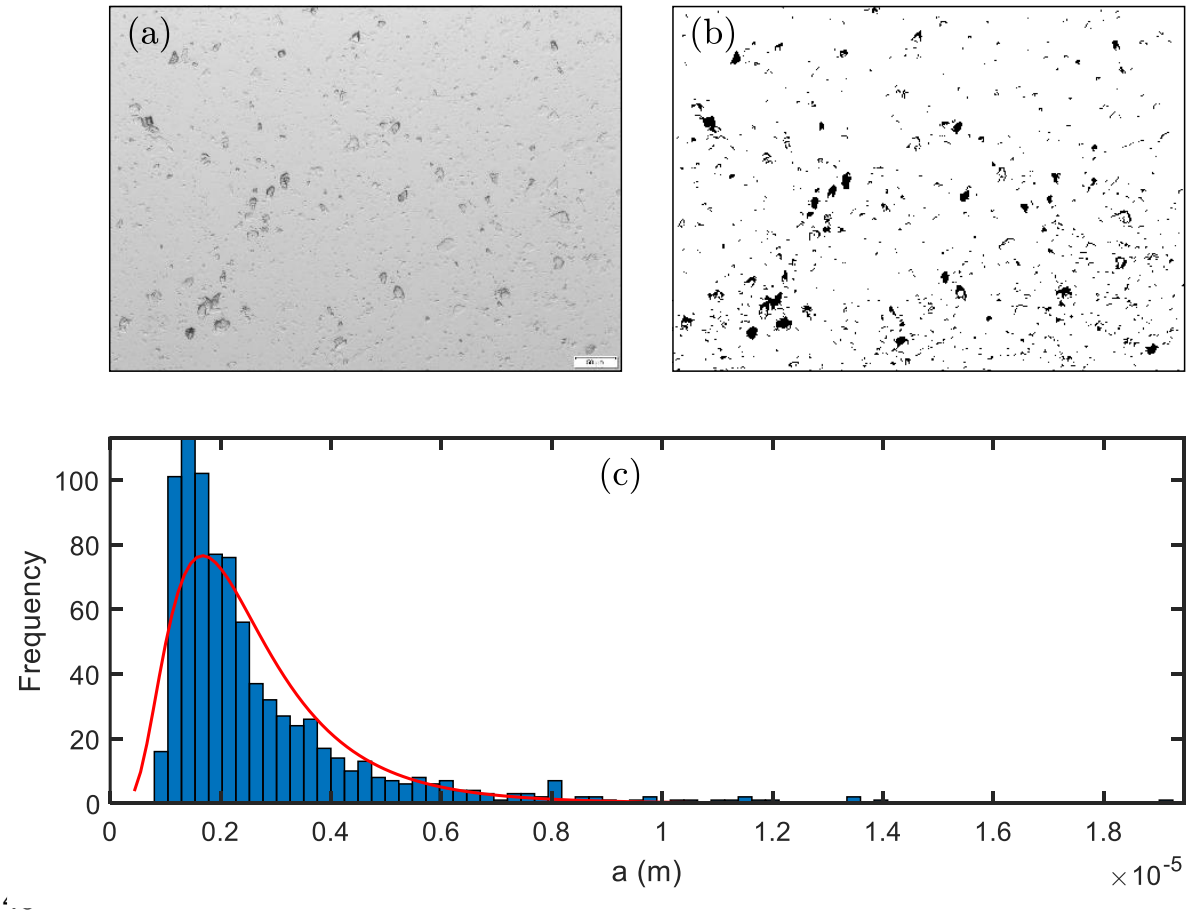

Fig. S2. Determination of the probability distribution function for the semi-major axis, a of kaolinite particles using image processing. (a) The original microscope image taken from a flow visualisation spot (DI, pH 11, v=0 m/s). The enclosed scale (bottom right) is the length of 50 μm. (b) Image binarisation to discretise the kaolinite particles/aggregates. (c) Histogram of a fitted with a lognormal distribution (mean, $\overline{x}$ = -13.00; standard deviation, σ = 0.55) curve in red.

S4. Zeta potential measurements for glass and kaolinite

The zeta potential measurements from the Zetasizer were curved fitted such that the zeta potentials, ζ (in mV) for the glass and kaolinite are given as:

$$\zeta_g = 1.0048\left(1 - e^{-(-1.3112pH+21.371)IS}\right)(-1.2696pH + 47.952) + (-0.125pH - 54.4117) \quad \text{(S6)}$$

$$\zeta_z = 0.998\left(1 - e^{-(-1.8526pH+24.5370)IS}\right)(0.6022pH + 21.677) + (-1.9666pH - 32.826) \quad \text{(S7)}$$

IS refers to the salinity in units of M NaCl.

S5. Velocity increments for the direct visualisation tests.

Table S1 details the flowrate and velocity used for each velocity increment during Test 1 and 2 under favourable conditions. Similarly, Table S2 lists the flowrate and velocity increments for Tests 3 and 4 under unfavourable conditions.

Table S1. Flowrate and velocity increments used for Tests 1 & 2.

Step no.	Flowrate, Q (ml/min)	Velocity, v (m/s)
0	0.00	0
1	5.17	0.0383
2	6.02	0.0446
3	7.21	0.0534
4	8.82	0.0653
5	11.19	0.0829
6	15.12	0.112
7	22.06	0.1634
8	37.54	0.2781
9	96.28	0.7132

Table S2. Flowrate and velocity increments used for Tests 3 & 4.

Step no.	Flowrate, Q (ml/min)	Velocity, v (m/s)
0	0	0
1	2.70×10^{-3}	2.00×10^{-5}
2	6.75×10^{-3}	5.00×10^{-5}
3	2.70×10^{-2}	2.00×10^{-4}
4	6.75×10^{-2}	5.00×10^{-4}
5	0.270	2.00×10^{-3}
6	0.675	5.00×10^{-3}
7	6.75	5.00×10^{-2}
8	13.5	0.1
9	67.5	0.5
10	135	1

S6. Direct visualisation images for Test 3

Fig. S3 shows the additional set of images for the flow visualisation from Test 3. The two staged detachment behaviour is observed in that there is minimal detachment between steps 3 to 6.

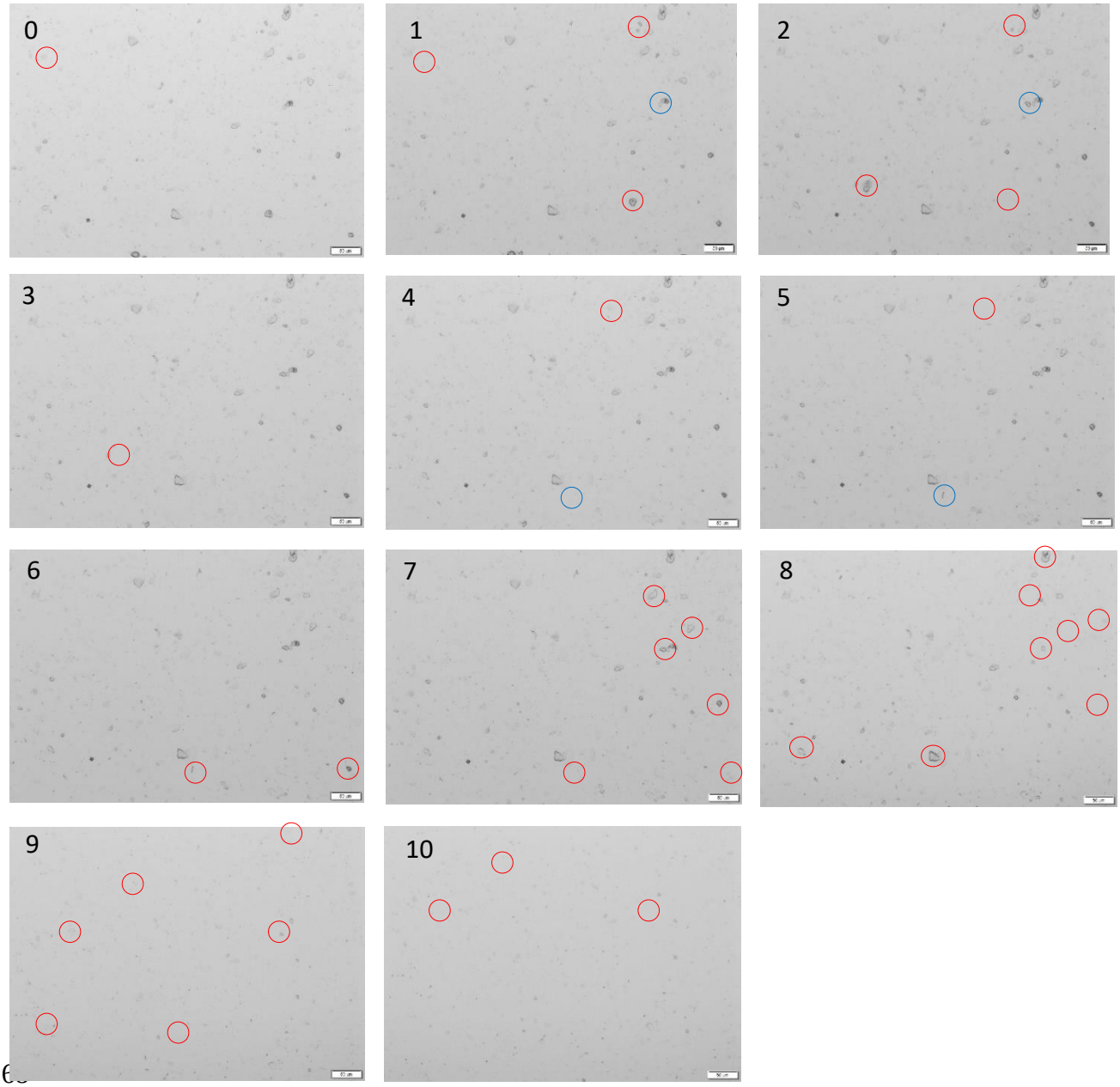

Fig. S3. Images from test 3 with velocity increments over 10 steps (0.01 M, pH 11, 300 ppm kaolinite particles). The red and blue circles highlight the kaolinite particles that will either detach or reattach respectively in the next frame/velocity increment. The circles do not mark all the detachments and reattachments but only highlight obvious examples.

References

1. Bhattacharjee S, Chen J, Elimelech M. DLVO interaction energy between spheroidal particles and a flat surface. Colloids and Surfaces A: Physicochemical and Engineering Aspects. 2000;165:143-56.

2. Ting HZ, Bedrikovetsky P, Tian ZF, Carageorgos T. Impact of shape on particle detachment in linear shear flows. Chemical Engineering Science. 2021;241.

3. Israelachvili JN. Intermolecular and Surface Forces. 3rd ed. Amsterdam: Elsevier Inc.; 2011.

4. Gregory J. Interaction of unequal double layers at constant charge. Journal of Colloid and Interface Science. 1975;51(1):44-51.

5. Mahmood T, Amirtharajah A, Sturm T, Dennett K. A micromechanics approach for attachment and detachment of asymmetric colloidal particles. Colloids and Surfaces. 2001;177(2-3):99-110.

6. Sharma M, Chamoun H, Sarma D, Schechter R. Factors Controlling the Hydrodynamic Detachment of Particles from Surfaces. Journal of Colloid and Interface Science. 1992;149(1):121-34.

Appendix C

Supplementary Data for Chapter 7

This section contains the supplementary data for the paper titled: ‘Detachment of inclined spheroidal particles from flat substrates’.

Supplementary Materials for

Detachment of inclined spheroidal particles from flat substrates

Heng Zheng Ting [a], Yutong Yang [b], Zhao Feng Tian [a], Themis Carageorgos [b], Pavel Bedrikovetsky [b]

[a] *School of Mechanical Engineering, The University of Adelaide, Adelaide 5000, SA, Australia*

[b] *Australian School of Petroleum and Energy Resources, The University of Adelaide, Adelaide 5000, SA, Australia*

S1. Latex stretching equipment

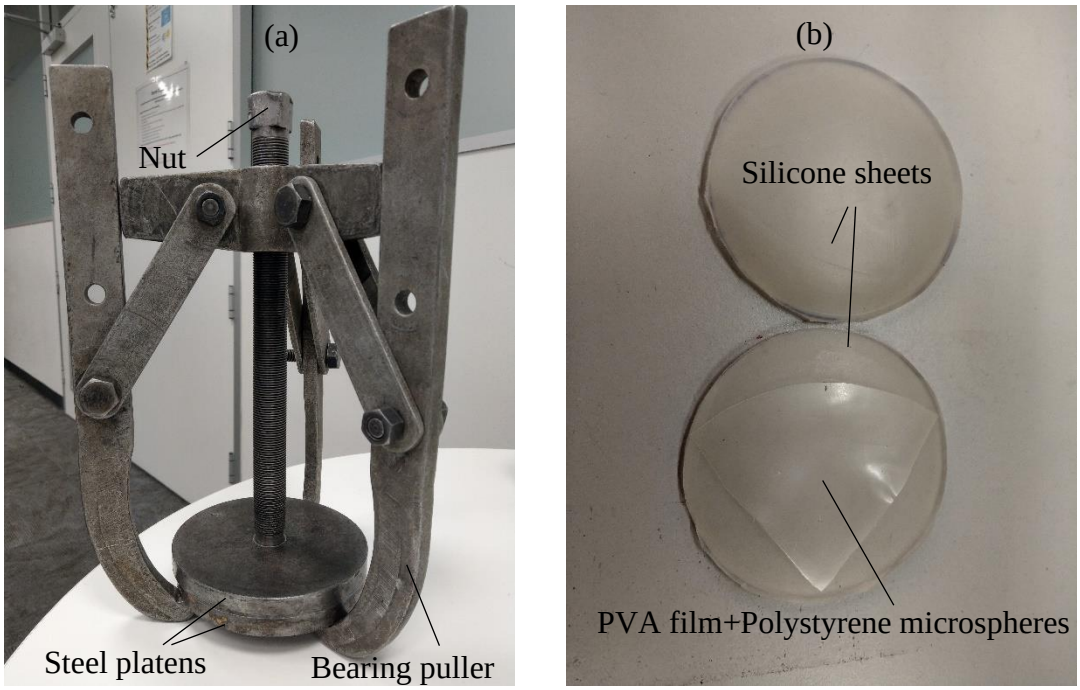

Fig. S1. Apparatus and materials used for polystyrene latex stretching. (a) Bearing puller and double steel platens assembly used to apply the compression force required for the deformation of the polystyrene microspheres. (b) Two 3mm thick silicone sheets with a quarter segment of the PVA film matrix containing the polystyrene latex particles.

Tightening the nut on the bearing puller presses the two steel platens firmly together, which provides the required compression force to deform the PVA film and the polystyrene microspheres. The silicone sheets serve to distribute the compression pressure such that the deformation in the spheres is equal in both the centre and the edge of the platens [1].

S2. Determination of the deposition orientation angle, φ

The orientation angles observed in the visualisation experiments are quantified through image processing. Since the visualisation experiments were done in a top-down configuration, the microscope image captured is the grey shaded region as shown in Fig. S2.

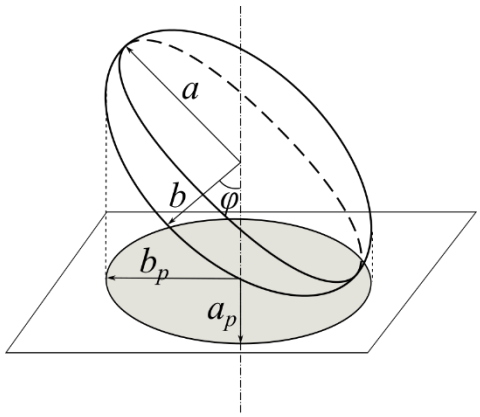

Fig. S2. Projection of an oblate spheroid at an orientation angle to a flat substrate.

By determining the semi-major, a_p and semi-minor axis, b_p of the *projected* ellipse (grey region), the orientation angle can be determined through the following correlation.

$$\left(b_p/a_p\right)^2 = \cos^2\varphi + \left(r_e/a_p\right)^6 \sin^2\varphi\,. \tag{S1}$$

We assume that a_p is equal to a, while $b \leqslant b_p \leqslant a$. Hence, when $b_p = b$, $\varphi = 90°$ and when $b_p = a = a_p$, $\varphi = 0°$. Eqn. (S1) was solved numerically through MATLAB to determine the orientation angle φ. a_p and b_p are equal to half of the 'MajorAxisLength' and 'MinorAxisLength' property calculated using MATLAB image processing.

Note that r_e is also required in the calculation of the orientation angle. We used the mean value of the sphere radius, such that r_e=1.55 μm for S1 and r_e=2.965 μm for S2. The projection angle is very sensitive to r_e, which we assumed to be constant, when in reality, they are distributed. This introduces a potential source of error into the calculation of the critical detachment velocity.

S3. Probability distribution of a and φ

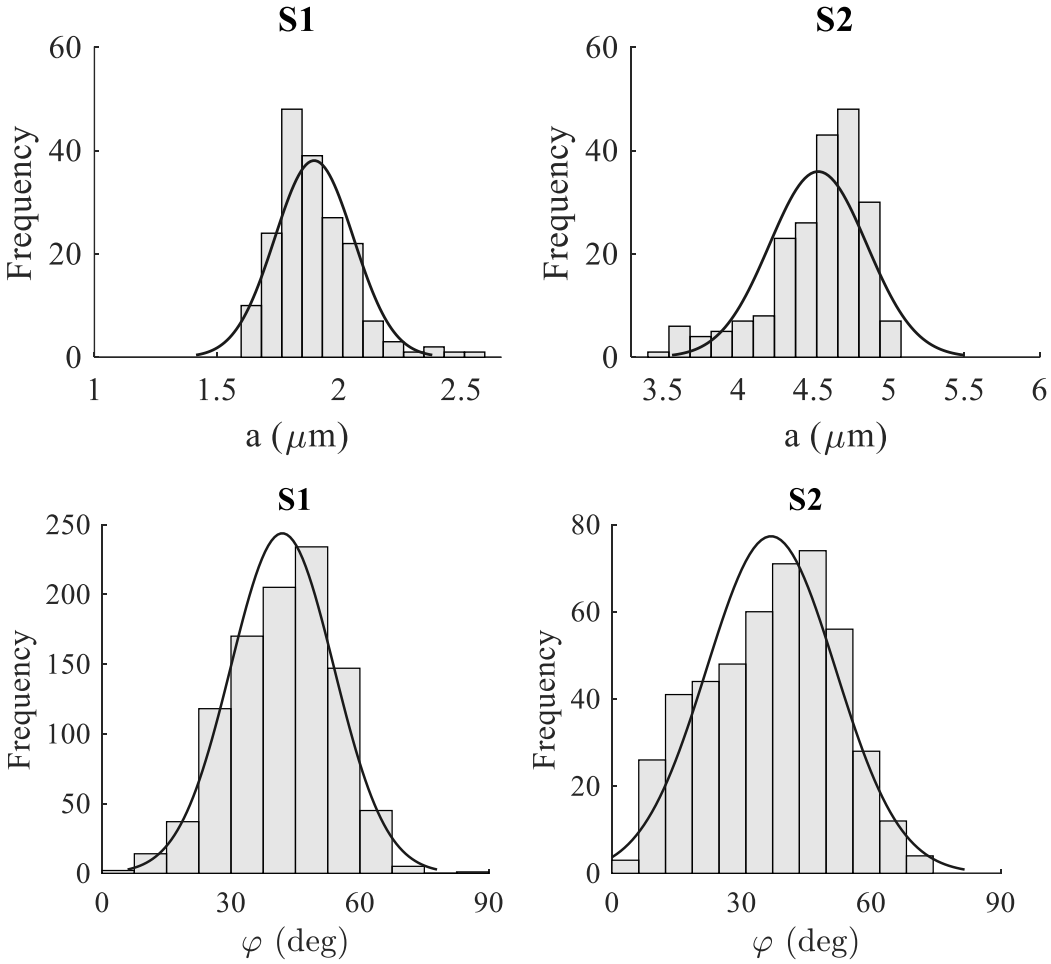

Fig. S3. Distribution of the semi-major particle axis, a (first row) and the orientation angle, φ (second row) for the manufactured oblate spheroid samples: S1 and S2. The distributions were calculated by image processing of SEM and direct visualisation images, respectively. The histograms are fitted with normal distribution curves, with a corresponding mean and standard deviation detailed in Table 1 of the main text.

S4. Extra set of visualisations (S1)

0) v = 0 m/s

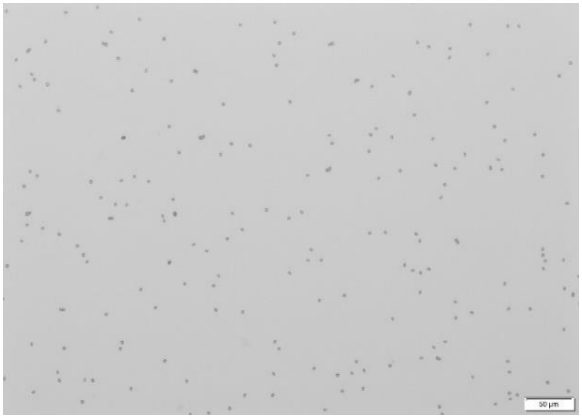

1) v=2×10^{-5} m/s;

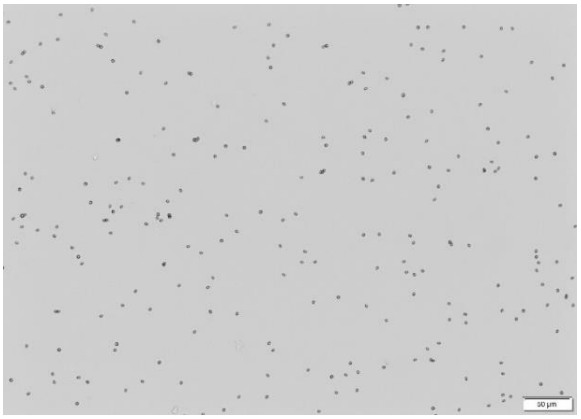

9) v=0.1 m/s;

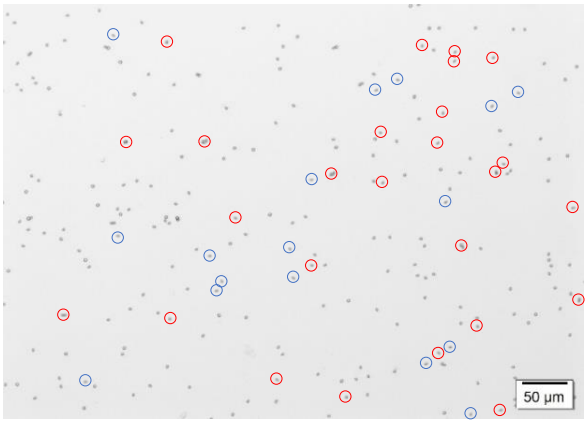

10) v=0.5 m/s;

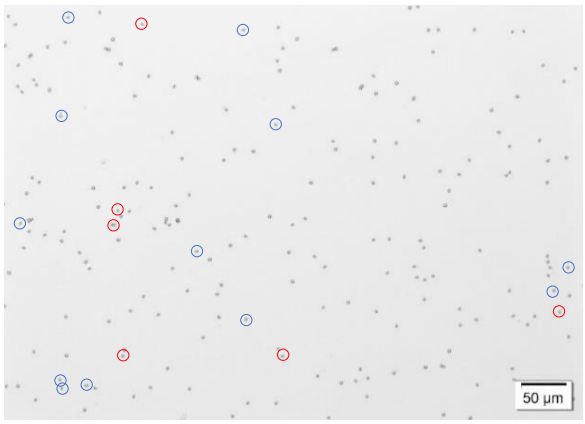

11) v=1 m/s;

Fig. S4. Visualisation of S1 oblate spheroids (r_e = 1.55 µm) with increasing flow velocity. Conditions were kept at a constant 0.3 M NaCl and pH 3. Flow direction is from up to down. Blue circles represent particles that will be reoriented in the next frame. Similarly, the red circles highlight all the particles that will detach in the next frame. Images between steps 1 to 9 were not presented here as no changes were observed.

S5. SEI calculations

For the particle wall configuration as presented in Fig. 6, the variables required in Eqn. (5) can be evaluated using the following equations:

$$\hat{\mathbf{n}}\cdot\hat{\mathbf{k}} = M[\sin\theta\sin\phi\sin\varphi(1+r^2 d\cos^2\theta)+\cos\theta\cos\varphi(1-r^2 d\sin^2\theta)], \tag{S2}$$

$$M = (1+r^4 d^2\sin^2\theta\cos^2\theta)^{-\frac{1}{2}} \tag{S3}$$

$$d = (a^{-2}-b^{-2}), \tag{S4}$$

$$Z = r(\sin\theta\sin\phi\sin\varphi+\cos\theta\cos\varphi) \tag{S5}$$

$$r = \left(\frac{\sin^2\theta\cos^2\phi}{a^2}+\frac{\sin^2\theta\sin^2\phi}{a^2}+\frac{\cos^2\theta}{b^2}\right)^{-1/2}. \tag{S6}$$

Similarly, to evaluate the interaction energy per unit area between two infinite flat plates, E, separated by a distance, h, the interaction is taken as the sum of the van der Waals, electrical double layer and the Born repulsion force such that:

$$E_{vdw} = -\frac{A_h}{12\pi h^2}, \tag{S7}$$

$$E_{edl} = 32\varepsilon_o\varepsilon_r\kappa\gamma_1\gamma_2\left(k_BT/z_ve_c\right)^2\exp(-\kappa h), \tag{S8}$$

$$E_{born} = \frac{A_h\sigma_c^{\,6}}{360\pi h^8}. \tag{S9}$$

Here, A_h is the Hamaker constant, ε_o and ε_r is the permittivity in a vacuum (8.85×10^{-12} $C^2N^{-1}m^{-2}$) and the relative permittivity of water (78.46), respectively. κ is the inverse Debye length, γ_1 and γ_2 ($\gamma_i=tanh(ze\zeta_i/4k_BT)$ is the reduced surface potential for the polystyrene latex particle and the glass, respectively. ζ is the zeta potential, z_v is the ion valency, e_c (1.6×10^{-19} C) is the charge of an electron, T is the absolute temperature (in Kelvin) and σ_c is the atomic collision coefficient (5Å).

S6. SEI code validation

The SEI equations were validated against the work of Bhattacharjee et al. [2]. For a prolate spheroid with semi-major axis of 40 nm and semi-minor axis of 20 nm, the same curves were reproduced for the van der Waals interaction, as shown in Fig. S5.

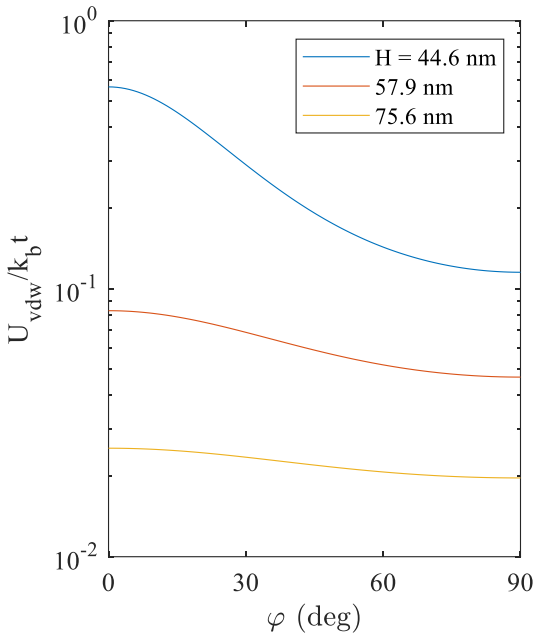

Fig. S5. van der Waals interaction of a prolate spheroid and an infinite flat plate with different orientation angles, at three different distances of separation between the particle centre and the plate. The Hamaker constant was 1×10^{-20} J and the spheroid had a semi-major axis of 40 nm and a semi-minor axis of 20 nm.

S7. Hertz Theory for Elliptical Contact

For the case when $\varphi = 0°$ (side-on configuration), the Hertz contact theory for circular contact can be used, where:

$$l_n = \left(\frac{3F_a r_1}{4E^*} \right)^{1/3} . \tag{S10}$$

In the case of a sphere, r_1 is the radius of the sphere [3]. For an oblate spheroid at $\varphi = 0°$, r_1 is the *inverse* of the principal curvatures at the contact point, given by Eqns. (S14) or (S15).

For cases where $\varphi \neq 0°$, the contact area becomes elliptical, with the semi-major, a_c and semi-minor, b_c radius of contact given by [3, 4]:

$$a_c = \left(\frac{3F_a[K(e) - E(e)]}{2\pi e^2 E^* A} \right)^{1/3}, \tag{S11}$$

$$b_c = a_c \sqrt{1 - e^2}\ . \tag{S12}$$

Here, e is the eccentricity that relates a_c to b_c. $K(e)$ and $E(e)$ are the complete elliptic integrals of the first and second kind, respectively. For our study, where the rotation is around the X-axis, $l_n = b_c$.

The equivalent Young's modulus is calculated as:

$$E^* = \left[\frac{\left(1 - \nu_1^2\right)}{E_1} + \frac{\left(1 - \nu_2^2\right)}{E_2} \right]^{-1}. \tag{S13}$$

The principal curvatures at the point of contact are defined by [5]:

$$\kappa_1 = \frac{a}{a^2 \sqrt{1 + \left(a^2 \big/ b^2 - 1 \right) z^2 \big/ b^2}}, \tag{S14}$$

$$\kappa_2 = \frac{a}{a^2 \left[1 + \left(a^2 \big/ b^2 - 1 \right) z^2 \big/ b^2 \right]^{3/2}}, \tag{S15}$$

where z is the z-coordinate (body-fixed coordinate) at the contact point. Referring to Fig. 6, rotation of the particle about the X-axis means that the contact point occurs only along the ridge (Y-Z plane) of the spheroid (where ϕ = 90°). Rotating the particle between $0° \leqslant \varphi \leqslant 90°$ is equivalent to varying θ between 0° to 90°. Therefore, z is related to φ, such that:

$$z = \cos\varphi \left(\frac{\sin^2 \varphi}{a^2} + \frac{\cos^2 \varphi}{b^2} \right)^{-1/2} \tag{S16}$$

$z = b$ when $\varphi = 0°$ and $z = 0$ when $\varphi = 90°$.

The principal orthogonal radius of curvature, r_i, is the inverse of curvature ($r_i = 1/\kappa_i$). For $\varphi = 0°$, $\kappa_1 = \kappa_2$ and consequently, there is only one principal orthogonal radius of curvature.

Following Ref. [4], the parameters required to evaluate the contact radii are expressed as:

$$A = {}^{1}\!/_{2r_1}; B = {}^{1}\!/_{2r_2} \tag{S17}$$

$$\frac{1}{\left[K(e)-E(e)\right]}\left[\frac{E(e)}{1-e^2}-K(e)\right]=\frac{B}{A} \tag{S18}$$

$$K(e)=\int_0^{\pi/2}\frac{d\vartheta}{\sqrt{1-e^2\cos^2\vartheta}}; E(e)=\int_0^{\pi/2}\sqrt{1-e^2\cos^2\vartheta}\,d\vartheta \tag{S19}$$

An excellent example showing the application and solving of the Eqns. (S11), (S12) and (S17)-(S19) is presented by Barber [4], pp. 37-38.

S8. Hydrodynamic Impact

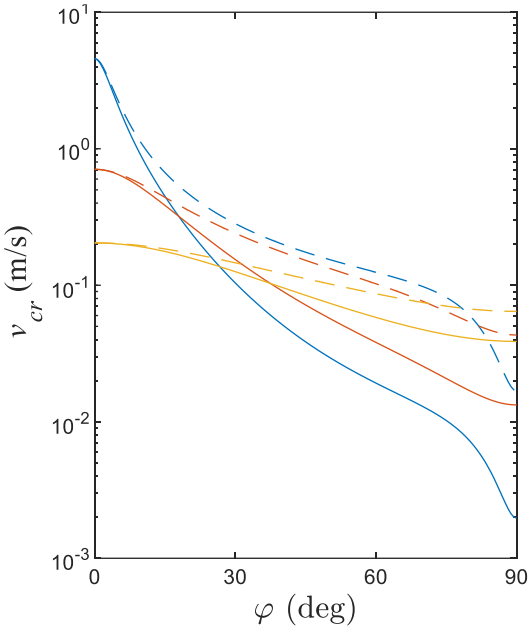

Fig. S6. Impact of considering the variation of drag moment with orientation angle. Blue, red and yellow represents α = 0.25, 0.5 and 0.75 respectively. Dashed lines are plotted by only considering variation in adhesion force with orientation angle and letting $f_{M,\varphi}$ = 1 for all angles. Solid lines are plotted to account for both the variation of adhesion force and the drag moment. The particle volume was kept constant at r_e= 3 μm. The particle was subjected to favourable conditions of 0.3 M NaCl and pH 3. The lever arm was calculated using Hertz theory for elliptical contact in both the dashed and solid curves.

It is apparent from Fig. S6 that the variation in the moment of drag, M with φ can significantly affect the detachment of the spheroidal particles, particularly at high orientation angles. Approximately an order of magnitude difference is observed in the detachment velocity when φ = 90°.

S9. Zeta Potential Measurements

Table S1. Zeta potential, ζ_p measurements for various polystyrene latex samples.

Sample No.	r_e (µm)	Sample	ζ_p (mV)
1	3	S1	-3.80
2		S3	-12.33
3		Polybead Microspheres 3 µm	-29.27
5	6	S2	-6.71
6		S4	-5.10
7		Polybead Microspheres 6 µm	-15.00

It is apparent that the stretching procedure has a significant impact on the zeta potential of the particles, even when comparing between the processed and unprocessed spheres. This could potentially be due to the residual PVA that remains on the particle [6]. The PVA film procedure consistently reduces the zeta potential of the particles.

S10. Visualisation velocity increments

Table S2. Flow rates and velocities used in each step during the visualisation experiment.

Steps	Flowrate, Q (ml/min)	Velocities, v (m/s)
0	0	0
1	2.70×10^{-3}	2×10^{-5}
2	6.75×10^{-3}	5×10^{-5}
3	2.70×10^{-2}	2×10^{-4}
4	6.75×10^{-2}	5×10^{-4}
5	2.70×10^{-1}	2×10^{-3}
6	6.75×10^{-1}	5×10^{-3}
7	2.70	0.02
8	6.75	0.05
9	13.50	0.10
10	67.50	0.50
11	135.00	1.00
12	210.00	1.56

S11. CFD data for spheroids of various aspect ratios and orientation angles.

Table S3-S5 presents the drag, lift and moment exerted by the linear shear flow on the various oblate spheroid configurations. The total drag force is the sum of its components: the form and friction drag. Note the sign change in the lift force from positive to negative with increasing orientation angle. Negative lift shows that the force acts vertically downwards, towards the substrate. Also note the significant increase in the magnitude of the lift force when the particle is inclined. Yet, the contribution of the lift towards the resultant M is still negligible (i.e. the change in the direction of lift only yielded a maximum deviation of 0.23% in M). r_e = 3 μm for all spheroids, while changing the α to 0.25, 0.5 or 0.75. The simulation was configured so that the spheroids always touch at a point to the substrate regardless of the rotation.

Table S3. CFD data for the drag, lift and moment exerted on an oblate spheroid with α = 0.25.

φ	Form Drag (N)	Friction Drag (N)	Total Drag Force (N)	Lift Force (N)	Moment (N m)	$f_{M,\varphi}$
0	2.29E-11	1.03E-10	1.26E-10	1.68E-13	2.79E-16	1.000
30	7.95E-11	1.26E-10	2.07E-10	-6.66E-11	7.60E-16	2.720
60	2.05E-10	1.20E-10	3.26E-10	-6.63E-11	1.81E-15	6.485
90	2.73E-10	1.06E-10	3.80E-10	1.17E-12	2.39E-15	8.536
120	2.04E-10	1.20E-10	3.26E-10	6.44E-11	1.81E-15	6.474
150	7.93E-11	1.27E-10	2.07E-10	6.58E-11	7.58E-16	2.714

Table S4. CFD data for the drag, lift and moment exerted on an oblate spheroid with α = 0.5.

φ	Form Drag (N)	Friction Drag (N)	Total Drag Force (N)	Lift Force (N)	Moment (N m)	$f_{M,\varphi}$
0	3.74E-11	1.00E-10	1.38E-10	2.17E-13	3.88E-16	1.000
22.5	5.09E-11	1.06E-10	1.57E-10	-2.13E-11	5.12E-16	1.317
45	8.53E-11	1.12E-10	1.98E-10	-3.07E-11	8.29E-16	2.134
67.5	1.22E-10	1.13E-10	2.36E-10	-2.23E-11	1.13E-15	2.914
90	1.38E-10	1.12E-10	2.51E-10	6.06E-13	1.27E-15	3.257
112.5	1.22E-10	1.13E-10	2.36E-10	2.12E-11	1.13E-15	2.912
135	8.53E-11	1.12E-10	1.98E-10	2.99E-11	8.28E-16	2.131
157.5	5.09E-11	1.06E-10	1.57E-10	2.07E-11	5.11E-16	1.316

Table S5. CFD data for the drag, lift and moment exerted on an oblate spheroid with α = 0.75.

φ	Form Drag (N)	Friction Drag (N)	Total Drag Force (N)	Lift Force (N)	Moment (N m)	$f_{M,\varphi}$
0	5.11E-11	1.06E-10	1.57E-10	2.77E-13	5.47E-16	1.000
22.5	5.65E-11	1.08E-10	1.65E-10	-8.12E-12	5.98E-16	1.095
45	6.97E-11	1.11E-10	1.81E-10	-1.16E-11	7.25E-16	1.326
67.5	8.34E-11	1.13E-10	1.97E-10	-8.51E-12	8.53E-16	1.561
90	8.92E-11	1.14E-10	2.03E-10	4.27E-13	9.07E-16	1.660
112.5	8.34E-11	1.13E-10	1.97E-10	7.69E-12	8.53E-16	1.561
135	6.97E-11	1.11E-10	1.81E-10	1.09E-11	7.24E-16	1.325
157.5	5.65E-11	1.08E-10	1.65E-10	7.52E-12	5.98E-16	1.094

S12. Magnitude of gravitational and buoyancy force.

In considering the gravitational/buoyancy forces, F_g:

$$F_g = \frac{4}{3}\pi r_e^3 (\rho_p - \rho_w) g, \tag{S20}$$

where ρ_p and ρ_w are the latex particle and brine density, respectively. Latex particles have a density of ρ_p = 1.05 g/cm^3 while the 0.3 M NaCl brine solution at 20°C has ρ_w= 1.0105 g/cm^3 [7]. g is the gravitational acceleration (9.8 m s^{-2}). For the r_e = 3 μm latex particles used throughout this study, the resultant buoyancy force, $F_g = 5.87 \times 10^{-14}$ N (one magnitude less than lift). The omission of the gravitational/buoyancy force is therefore justified.

References

1. Ahn SJ, Ahn KH, Lee SJ. Film squeezing process for generating oblate spheroidal particles with high yield and uniform sizes. Colloid and Polymer Science. 2016;294(5):859-67.

2. Bhattacharjee S, Chen J, Elimelech M. DLVO interaction energy between spheroidal particles and a flat surface. Colloids and Surfaces A: Physicochemical and Engineering Aspects. 2000;165:143-56.

3. Johnson KL. Contact mechanics: Cambridge University Press; 1985.

4. Barber JR. Contact Mechanics. Switzerland: Springer; 2018.

5. Harris WF. Curvature of ellipsoids and other surfaces. Ophthalmic & Physiological Optics. 2006;26(5):497-501.

6. Gomez-Flores A, Bradford SA, Wu L, Kim H. Interaction energies for hollow and solid cylinders: Role of aspect ratio and particle orientation. Colloids and Surfaces A: Physicochemical and Engineering Aspects. 2019;580.

7. Haynes WM, editor. CRC Handbook of Chemistry and Physics. 95 ed. Oakville: CRC Press LLC; 2014.